

Studies in Single Photon Emission Imaging

Jeremy M. C. Brown

B. App. Sc. (Phys), B. Sc. Hons. (Phys)



School of Physics and Astronomy, Monash University

March 26, 2015

Contents

Contents	i
Abstract	v
General Declaration	vii
Acknowledgements	ix
1 Introduction	1
1.1 Mechanical Collimation	1
1.2 Compton Collimation	2
1.3 Thesis Overview	8
I Monte Carlo Radiation Transport Modelling	11
2 Monte Carlo Method, Geant4 and Electromagnetic Physics Models	13
2.1 Monte Carlo Method	13
2.2 Geant4: A Toolkit for Simulating the Passage of Particles Through Matter	15
2.3 Photon, Electron and Positron Physics Models of Geant4	15
2.4 Summary	41
3 A Low Energy Bound Atomic Electron Compton Scattering Model for Geant4	43
II Development of a Hybrid Single Photon Emission Imaging System	57
4 A Pixelated Emission Detector for RadiOisotopes (PEDRO)	59
5 Towards Optimal Collimator Design for the PEDRO Hybrid Imaging System	67
6 Laplacian Erosion: An Image Deblurring Technique for Multi-Plane Gamma-Cameras	81
III Fundamental Study of Advanced Compton Imaging	93
7 Towards Quantification of Advanced Compton Imaging	95

7.1	Introduction	95
7.2	Advanced Compton Imager Simulation, Image Recovery and Performance Assessment	96
7.3	Results	100
7.4	Discussion	106
7.5	Conclusion	107
8	Concluding Remarks	109
	Bibliography	113
	Appendices: Geant4 Collaboration Papers	123
	Appendix A	125
	Appendix B	137

Copyright Notices

Notice 1

Under the Copyright Act 1968, this thesis must be used only under the normal conditions of scholarly fair dealing. In particular no results or conclusions should be extracted from it, nor should it be copied or closely paraphrased in whole or in part without the written consent of the author. Proper written acknowledgement should be made for any assistance obtained from this thesis.

Notice 2

I certify that I have made all reasonable efforts to secure copyright permissions for third-party content included in this thesis and have not knowingly added copyright content to my work without the owner's permission.

Abstract

This thesis presents a number of studies into Single Photon Emission Imaging (SPEI) that can be grouped into three main sections: Monte Carlo Radiation Transport Modelling, Development of a Hybrid SPEI System and Fundamental Study of Advanced Compton Imaging.

The first section of this thesis, Monte Carlo Radiation Transport Modelling, presents an overview of the Monte Carlo radiation transport modelling toolkit Geant4 and a newly derived low energy Compton scattering model, the Monash University Compton scattering model. This Compton scattering model was developed to address the limitation present in the majority of Monte Carlo bound atomic electron Compton scattering models: incorrect determination of the ejected direction of Compton electrons due to the non-zero momentum of the bound atomic electron. A theoretical foundation that ensures the conservation of energy and momentum in the relativistic impulse approximation was utilised to develop energy and directional algorithms for both the scattered photon and ejected Compton electron from first principles. Assessment of this model was undertaken in two steps: comparison with respect to two Compton scattering classes of Geant4 adapted from Ribberfors' work, and experimental comparison with respect to Compton electron kinetic energy spectra obtained from the Compton scattering of 662 keV photons off the K-shell of gold. It was shown that this new Compton scattering model was a viable replacement for the majority of computational models that have been adapted from Ribberfors' work. Additionally, this model was shown to be able to reproduce the Compton scattering triply differential cross-section Compton electron kinetic energy spectra of 662 keV photons K-shell scattering off of gold to within experimental uncertainty.

The second section of this thesis, Development of a Hybrid SPEI System, presents the development of a novel hybrid collimated SPEI system: the Pixelated Emission Detector for RadiOisotopes (PEDRO). The PEDRO is a conceptual proof of principle hybrid SPEI system that was designed to explore and quantify the relationship between spatial resolution and sensitivity, inherent in SPEI, over the energy range of 30 keV to 511 keV. This system was originally intended to be constructed from a Compton camera stack located behind a coded mask composed of a mix of pinholes, slats and/or open areas. A total of three studies are presented in this section that outline the development of: 1) a Geant4 application to be used for optimisation of PEDRO with respect to a robust metric, 2) an automated routine for the optimisation of large-area slits in the outer regions of a coded mask for PEDRO which has a central region allocated for pinholes, and 3) a novel experimentally motivated image deblurring technique for multi-plane Gamma cameras such as PEDRO. These three studies illustrated two main points: 1) it may indeed be possible to overcome the trade-off between spatial resolution and sensitivity inherent in SPEI through hybrid Compton-mechanical collimation, and 2) the multi-plane nature of hybrid collimation

systems can be capitalised on to reduce the level of image blurring associated with collimator opening geometry and, in turn, improve recovered image quality.

Finally, the third section of this thesis, Fundamental Study of Advanced Compton Imaging, presents a preliminary study into the fundamental limits of recoil electron tracking enhanced Compton collimation, or Advanced Compton Imaging, for photon energies below 2 MeV. A custom Geant4 application of an idealised detection system was developed and four different detection materials were tested over a wide range of electron tracking resolutions. Increased image performance and point source convergence was observed with respect to standard Compton imaging regardless of recoil electron tracking accuracy in all tested materials across the investigated energy range. Additionally, the rate of point source convergence with respect to standard Compton imaging was discovered to be maximised for electron tracking accuracies of 45° to 60° Full Width at Tenth Maximum (FWTM) for photons of incident energy greater than 500 keV. Further study with more detailed simulation and image recovery frameworks is required to assess the validity of these observed trends.

General Declaration

Declaration for thesis based or partially based on conjointly published or unpublished work

In accordance with Monash University Doctorate Regulation 17.2 / Doctor of Philosophy and Master of Philosophy regulations the following declarations are made:

I hereby declare that this thesis contains no material which has been accepted for the award of any other degree or diploma at any university or equivalent institution and that, to the best of my knowledge and belief, this thesis contains no material previously published or written by another person, except where due reference is made in the text of this thesis.

This hybrid thesis includes four original papers published in peer reviewed journals. Two of the four published full-length papers have myself as the first author. This hybrid thesis is split into three parts: Monte Carlo Radiation Transport Modelling (Part I), Development of a Hybrid Single Photon Emission Imaging System (Part II), and Fundamental Study of Advanced Compton Imaging (Part III).

The original project of this thesis focused on the development of a novel hybrid emission imaging system, the Pixelated Emission Detector for Radioisotopes (PEDRO). This novel imaging system, which as a key project of the Monash Centre for Synchrotron Science (MCSS), was attempting to overcome the trade-off between spatial resolution and sensitivity that is present in Single Photon Emission Imaging (SPEI) below 750 keV. My participation in this PEDRO project resulted in three peer reviewed journal publications, on one of which I am first author, that are presented in Part II. However, due to the dissolution of MCSS, which resulted in the associated relocation of both original PhD supervisors and loss of access to crucial infrastructure for the project, this thesis was refocused 18 months in with new PhD supervisors.

The second project of this thesis was inspired by the findings of the first 18 months of candidature exploring the potential of hybrid collimation in SPEI. This second project, for which I was the sole architect and participant, explored the fundamental limits of an emerging imaging modality in SPEI: Advanced Compton Imaging. A single first-author peer reviewed journal publication and a preliminary investigation have resulted from this project. These two investigations constitute Chapter 3 in Part I, and Chapter 7 in Part III. The work in Chapter 3 has since been integrated into the Monte Carlo radiation transport modelling toolkit Geant4 and, as a result, has generated two additional publications of which I am a co-author. These two sets of supporting publications can be found in Appendices A and B.

The ideas, development and writing up of two of the four published papers in the thesis were the principal responsibility of myself, the candidate, working within the School of Physics under the supervision of Dr Matthew R. Dimmock, Dr John E. Gillam and Professor David M. Paganin. In the other two published papers the inclusion of co-authors reflects the fact that the work came from active collaboration between researchers and acknowledges input into team-based research.

In the case of Chapters 3 to 6 my contribution to the work involved the following:

Thesis Chapter	Publication Title / Publication Status	Nature and Extent of Candidate's Contribution
3	A Low Energy Bound Atomic Electron Compton Scattering Model for Geant4: <i>Published</i>	Developed the theoretical model, developed/wrote the Geant4 physics class, undertook the simulations and comparison, and wrote up the paper
4	A Pixelated Emission Detector for RadiOistopes (PEDRO): <i>Published</i>	Co-developed the Geant4 application, assisted with simulations and analysis, and proofread the paper
5	Towards Optimal Collimator Design for the PEDRO Hybrid Imaging System: <i>Published</i>	Co-developed the automated routine and image reconstruction code, assisted with simulations and analysis, and proofread the paper
6	Laplacian Erosion: An Image Deblurring Technique for Multi-Plane Gamma-Cameras: <i>Published</i>	Developed the technique, extended the Geant4 application, undertook the simulations and analysis, and wrote up the paper

Jeremy M. C. Brown

Acknowledgements

In my opinion, what gets someone through a PhD is not the project, but the people around them. As such, I would like to thank all of my colleagues and friends who have “lived” this experience with me over the years. I tried to list you all, but once I got to around a hundred names I thought it better to follow the approach of the memorable Dr Ben Farmer: *“I am loath to begin a long list of acknowledgements out of fear that I will forget something or someone important, and somehow it is worse to be left off a long list rather than a short one. I will therefore keep this brief, and simply offer my sincere apologies to all whom I omit.”*

First and foremost, I would like to thank my three supervisors Matthew Dimmock, John Gillam and David Paganin. I doubt I would have completed these processes without the advice, freedom and support that I have received from you three over the years. In particular, I would like to thank John for sticking with me after leaving Monash to follow his own career. I also acknowledge Chris Hall who was one of my original supervisors that left Monash early on during my PhD candidature.

My time in the School of Physics has been an experience. I would like to thank a large number of the academic and professional staff, past and present, with specific emphasis on Julia Barnes, Alexis Bishop, Marcus Kitchen, Rod Mackie, Daniele Pelliccia, Jean Pettigrew and Robert Seefeld. Marcus, I am very grateful for your advice and support over the last 18 months. Hopefully our gamble will pay off soon, provided we can finally get our hands on some detectors. I also acknowledge the financial support I have received via the Faculty of Science Dean’s Postgraduate Research Scholarship from Monash University.

During my candidature I was privileged enough to be invited to join the Geant4 collaboration. From this collaboration I would like to thank Sebastien Incerti and Vladimir Ivanchenko for their advice and collaboration over the last two years. Sebastien your friendship was a key factor in my reconsidering quitting this PhD and leaving academia in early 2013, thank you.

I am grateful for the support I have received from all of my friends over the years. However, I would like to name a few key people whom without I would probably not be here today: Katie Auchettl, Georgia Brown, Tessa Charles, Russell Cooper, Sam Eastwood, Ben Farmer, Anthony Heath, Jack Hellerstedt, Elliot Hutchison, Martijn Jasperse, Ben Kay, Nat Lampe, Andrew Leong, Kaye Morgan, Goran Panjkovic, Narissa Strybosch, David Urban, Neil Wilson and Wan Zahidi Zakwan.

Finally, I would like to thank Jessica Crawshaw. Your presence during the last few months of writing up this document has made life significantly more enjoyable, thank you.

Introduction

The low energy interaction cross-sections of photons, in comparison to charged particles such as electrons and positrons, make them the primary particle of interest in emission imaging. Emission imaging utilises the information gained through the measurement of incoherent photon interactions to estimate their origin. Knowledge of the energy transfer and location of these interactions, in combination with the emission imaging system's geometry, enable the incident photon trajectory to be estimated. An agglomeration of a sufficient number of photon trajectories allows for the recovery of an image and / or spectra of emitted radiation from a region, or object, of interest.

Single Photon Emission Imaging (SPEI) is a specialised subset of emission imaging applied across the fields of nuclear assay, homeland security, pre-clinical nuclear medicine and X / γ -ray astronomy. Two primary methods of collimation exist in SPEI: mechanical and Compton. A review of these primary collimation methods and a discussion of their context with respect to the present thesis follow in Sections 1.1, 1.2 and 1.3.

1.1 Mechanical Collimation

Mechanical collimation is the predominant collimation method employed in SPEI for imaging photons of energy below a few hundred keV [17, 51]. An illustration of the basic principles of a Mechanically Collimated Imaging System (MCIS) are outlined in Figure 1.1. MCISs employ a direct or coded aperture, composed of a highly attenuating material, to restrict the solid angle of radiation incident upon the surface of a position-resolving, or position-and-energy-resolving, radiation detector [4, 17, 51]. In Figure 1.1(a), three photons of a characteristic energy are emitted from a radioactive source in the direction of a MCIS. Two of the photons strike the mechanical collimator and are stopped from reaching the radiation detector. The other photon passes unopposed through the opening in the collimation and is photoelectrically absorbed, depositing all of its energy within the active volume of the radiation detector (Figure 1.1(b)) [26, 50]. An estimate of the incident trajectory and emission location of the photon, a Line of Response (LoR), can be formed using the coordinates of the coded aperture centre, \mathbf{r}_1 , and photon's photoelectric absorption location, \mathbf{r}_2 (Figure 1.1(c)) [17, 51]. \mathbf{r}_1 and \mathbf{r}_2 define the parametric equation set of the LoR, with its volume being defined by the geometry of the coded aperture and the spatial resolution of the

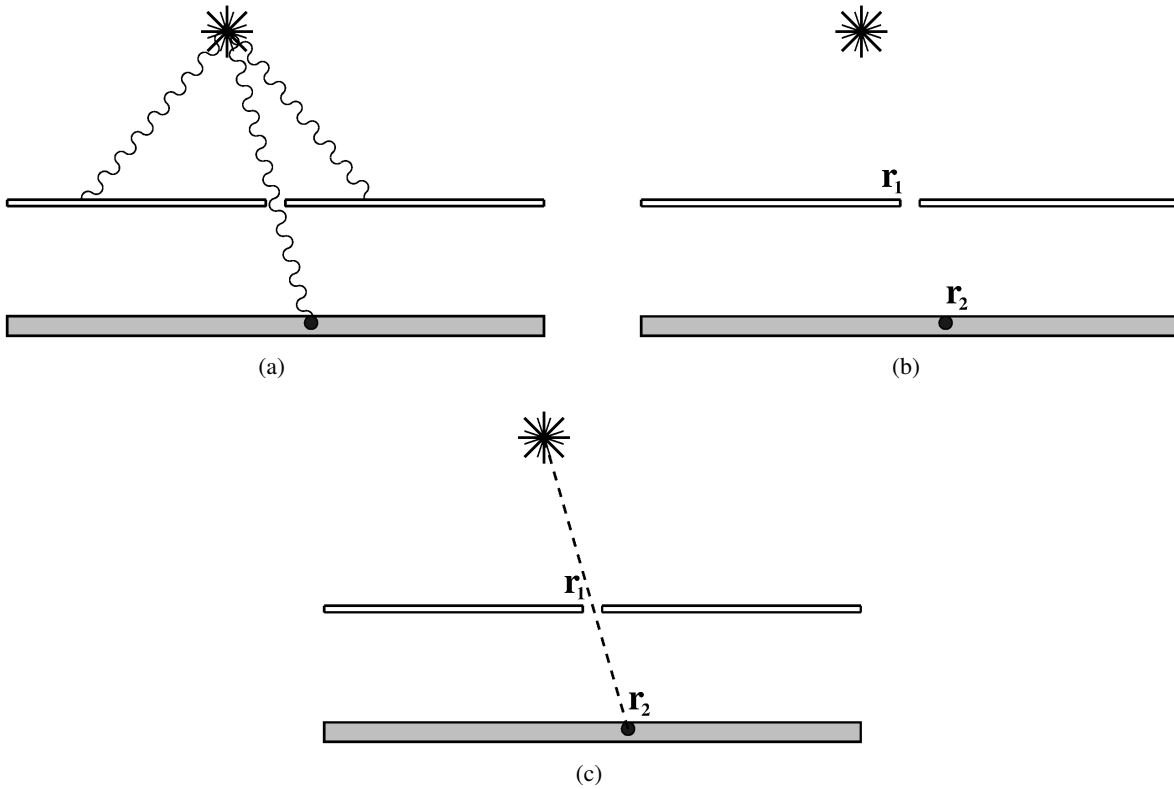


Figure 1.1: An overview of mechanical collimation and the construction of Lines of Response (LoRs).

radiation detector. The back-projection of these LoRs into the image space is the foundation of image reconstruction for mechanically collimated devices [17, 51].

The level of precision with which the incident trajectory and emission location of a photon can be estimated, or the level of information that the event possesses, is inversely proportional to the width of the LoR. Minimising the coded aperture open cross-section, and maximising the spatial resolution of the radiation detector will increase the average level of information that each event possesses [62, 63]. However, when the open cross-section of a coded aperture is decreased to reduce the volume of LoRs, increasing the level of information per event, the solid angle to which emitted radiation can pass through and interact with the radiation detector also decreases, lowering the system sensitivity [62, 63]. This trade off between event information, impacting the image spatial resolution, and sensitivity is the limiting factor of mechanical collimation [44, 57].

1.2 Compton Collimation

Compton scattering is the name given to the fundamental process of inelastic scattering between a high energy photon and an electron. Arthur Holly Compton first quantified the kinematics of this process for a non-bound electron at rest, known as the free electron approximation, for the incident photon energy (ω), photon scattering angle (θ) and scattered photon energy (ω'). The result of this work is now known as the

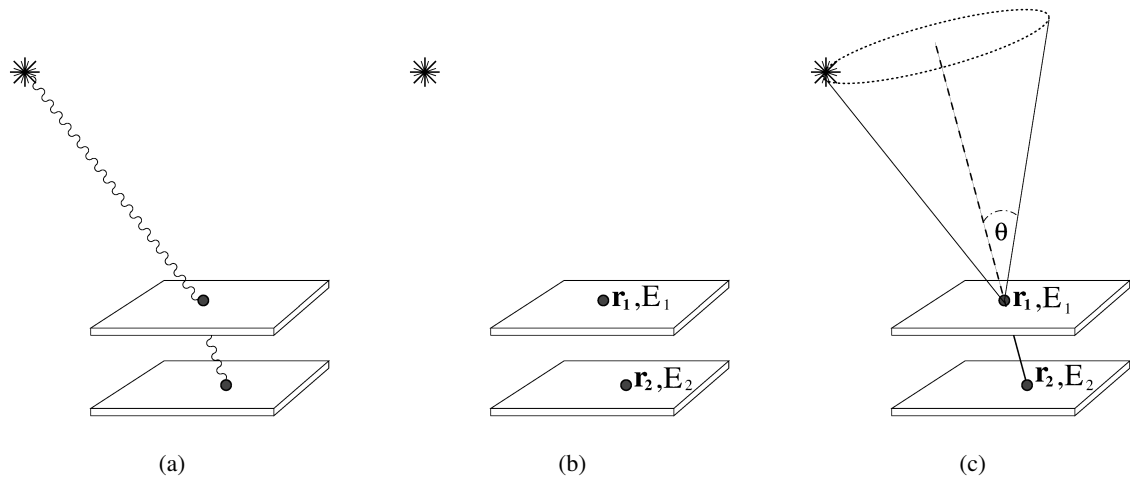


Figure 1.2: An illustration of how the incident photon trajectory can be estimated from the energy and location of each incoherent interaction within a two-detection-plane CIS.

Compton scattering formula:

$$\frac{\omega'}{\omega} = \frac{1}{1 + (\omega/m)(1 - \cos \theta)} \quad (1.1)$$

where m is the rest mass of an electron in natural units [18]. Compton collimation utilises this physical process to estimate the incident trajectory and emission location of an X- or γ -ray without physically restricting the solid angle of detection [96]. A more detailed description of Compton scattering is contained in Section 2.

Compton Imaging Systems (CISs) are typically comprised of either a single or stack of position and energy resolving radiation detectors [9, 15, 47, 52, 81, 85, 86, 89, 107]. As the incident photon travels through the active volume of the system, it may scatter a number of times and then possibly be photoelectrically absorbed. Through electronic means, it is possible to estimate the order of these interaction events and determine the path of an incident photon through a CIS's active detection volume [73, 103, 109]. In standard Compton collimation the incident photon trajectory, and emission location, can only be estimated if the following conditions are met:

- the photon undergoes two or more incoherent interactions that can be individually resolved within the active volume of the CIS, and
- the incident photon energy is known, or calculable from three or more detected incoherent interaction locations [30, 80].

An illustration of how the incident trajectory and emission location of a photon can be estimated from the energy deposited and interaction locations within a two detection plane CIS is outlined in Figure 1.2. In Figure 1.2(a), a photon is emitted from a radioactive source in the direction of a CIS

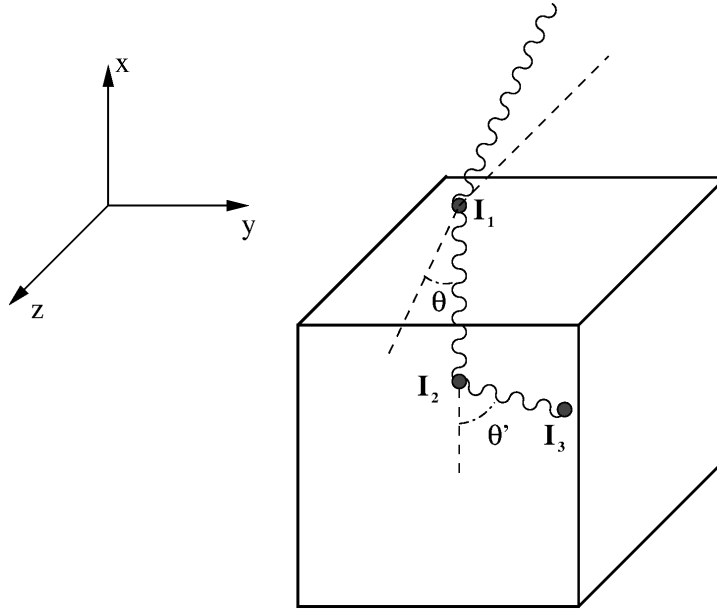


Figure 1.3: The most basic interaction sequence of a photon, double Compton scattering and photoelectric absorption, that has sufficient information for polarised Compton collimation.

and interacts twice within its active volume. Here the photon Compton scatters in the first detection plane, and is then photoelectrically absorbed in the second. For this interaction sequence, the CIS would indicate two interaction locations at \mathbf{r}_1 and \mathbf{r}_2 with measured quantities E_1 and E_2 corresponding to the energy transferred from the incident photon to the detection material through incoherent interaction processes (Figure 1.1(b)). In an ideal detection system, i.e. perfect energy resolution, the sum of these two energies would equal that of the incident photon ω . If timing information is disregarded, the application of Compton kinematics could recover the interaction order and determine the polar Compton scattering angle (θ) at the first interaction. With the available information, the range of possible incident trajectories, and emission locations, of the photon can be constrained to the surface of a cone known as a Cone of Response (CoR) (Figure 1.2(c)).

Only being able to estimate the polar Compton scattering angle severely limits the level of information per reconstructed event sequence that a standard CIS CoR carries [2, 8, 57]. Even under ideal conditions, the information obtained from a standard CoR is less than from an LoR. At present, three different advanced Compton collimation methods are being developed around the world. Each of these advanced Compton collimation methods - namely polarisation [8], mechanical encoding [57] and recoil electron tracking [2, 35, 74, 90] - are exploring physically motivated methods to limit the azimuthal range of the cone-surface. Limitation of the azimuthal angular range of a CoR will increase the utility of each event, improving the spatial resolution and contrast of images recovered from CIS. The level of improvement is directly proportional to the level of azimuthal angular restriction.

1.2.1 Polarised Compton Collimation

Polarised Compton collimation capitalises on the fact that photons are more likely to Compton scatter in a direction perpendicular to their plane of polarisation [24, 26]. A minimum of three incoherent interactions of a photon, within the active region of a CIS, is required to perform polarised Compton collimation [8]. The following overview will focus on the most basic photon interaction sequence that allows for the azimuthal restriction of a CoR.

Figure 1.3 illustrates the most basic interaction sequence of a photon that has sufficient information for polarised Compton collimation: double Compton scattering and photoelectric absorption. At the site of the first interaction (\mathbf{I}_1), the incident photon undergoes Compton scattering. During this process, the photon will be partially polarised in the direction perpendicular to the scattering plane [8]. The photon then continues to propagate through the active volume of the CIS and Compton scatters at a second site (\mathbf{I}_2). As the photon is polarised, there is an increased probability that it will scatter in a direction perpendicular to its plane of polarisation [26]. Photoelectric absorption is the third and final interaction (\mathbf{I}_3) of the photon seen in Figure 1.3, depositing all remaining photon energy into the active volume of the CIS.

The incident photon azimuthal angle at \mathbf{I}_1 can be estimated by working backwards through the interaction sequence utilising the relationship between photon polarisation and Compton scattering [8, 24]. Due to the probabilistic nature of the photon-matter interaction combined with measurement uncertainty of the plane of polarisation, an azimuthal Probability Density Function (PDF) can be determined which modulates the CoR. The azimuthal PDF is dependent on the incident photon energy and the first two Compton scattering angles (θ and θ' seen in Figure 1.3) [8].

Polarised Compton collimation has one major advantage over other advanced Compton collimation methods: it can be integrated into any CIS at the gamma tracking level (i.e. there is no need to change the hardware configuration). However, in comparison to the other two advanced Compton collimation methods, mechanical encoding and recoil electron tracking, the resultant enhancement is less [8, 74]. Boggs' idealised investigation into polarised Compton collimation illustrated the very strict conditions required to achieve a noticeable CoR azimuthal restriction [8]. The two major findings from that investigation were:

- maximum azimuthal restriction occurs when both the first and second Compton scattering angle of the photon are equal to $\pi/2$, and
- the level of azimuthal restriction is inversely proportional to incident photon energy, where optimal performance was seen when $\omega < 500$ keV.

When the energy dependence of the incident photon on the interaction cross-section, Compton cross-section and Klein–Nishina cross-section are also considered, it is clear that the probability for measuring an appropriate event sequence for polarised Compton collimation is low.

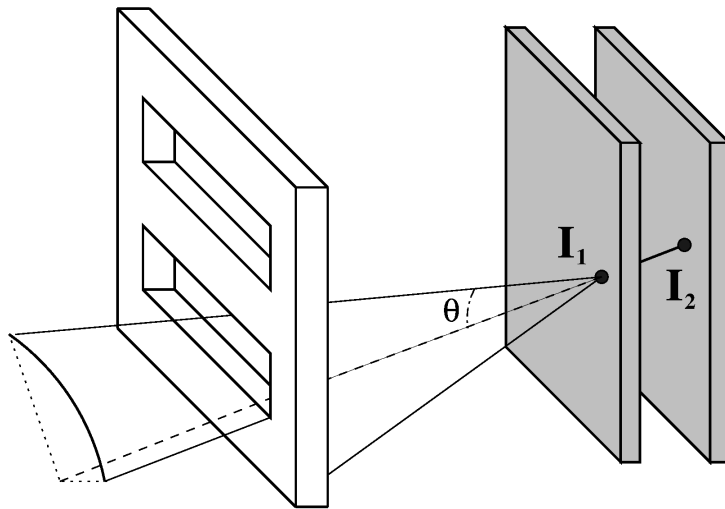


Figure 1.4: An illustration of how mechanical encoding can restrict the polar and azimuthal range of a CoR from a CIS.

1.2.2 Mechanically Encoded Compton Collimation

Mechanically encoded Compton collimation, more commonly known as hybrid collimation, combines mechanical and Compton collimation in an attempt to overcome the trade off between spatial resolution and sensitivity, inherent in SPEI [57]. Potentially composed of a stack of position and energy resolving radiation detectors located behind a coded aperture, hybrid imagers are expected to improve sensitivity over mechanical collimation while retaining high spatial resolution [57]. These systems are able to improve the information conveyed in a single event sequence through the modulation of the CoR by the open cross-section of the collimator.

An illustration of how mechanical encoding can restrict both the polar and azimuthal range of a CoR can be seen in Figure 1.4. As outlined in Figure 1.2, a CoR can be constructed from the energy and interaction locations of a photon within the active region of the detector stack. These CoRs will intersect the coded aperture and only the regions through which the CoR can freely pass can be backprojected into image space. The extent of CoR restriction, and improvement in information per event, is primarily defined by the coded aperture design. At present the extent to which hybrid collimation can overcome this trade off between spatial resolution and sensitivity in SPEI remains largely unexplored.

1.2.3 Recoil electron tracking enhanced Compton collimation

Recoil electron tracking enhanced Compton collimation utilises information derived from the primary electron ejected during the interaction of a photon within the active region of a CIS. In the free electron approximation, the target electron of a Compton scattering event recoils in the same plane as the scattered photon [26]. If the path of these Compton electrons can be tracked through the CIS, it is possible to restrict the azimuthal range of a CoR centred around a plane defined by the scattered photon and Compton electron ejection vectors. The measurement accuracy of the Compton electron ejection vector defines

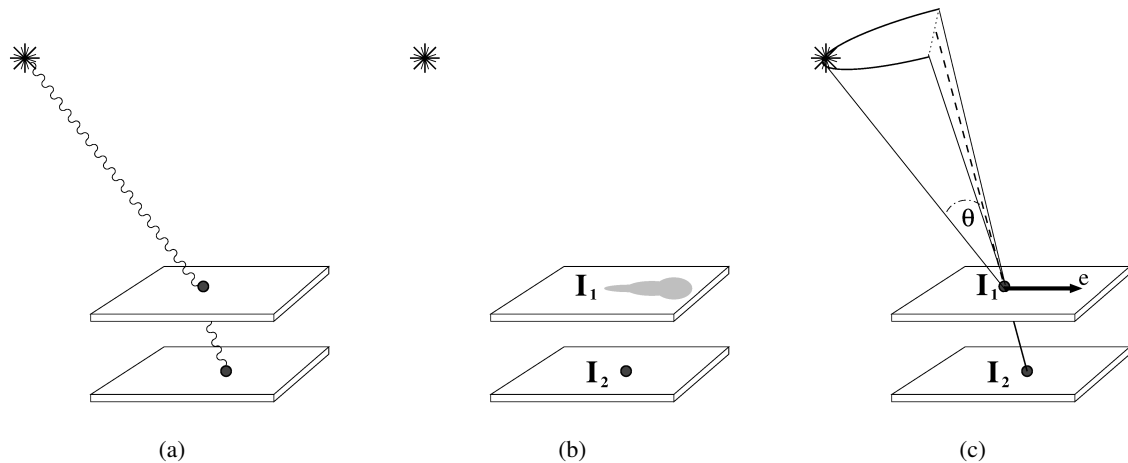


Figure 1.5: An illustration of how tracking Compton electrons can limit the azimuthal range of a CoR from the incoherent interaction of a photon within a two-detection-plane CIS.

the extent to which the azimuthal range can be restricted [2, 90, 108]. CISs which utilise the additional information gathered through recoil electron tracking are referred to as Advanced Compton Imaging Systems (ACISs).

Figure 1.5 outlines the basic principles of recoil electron tracking enhanced Compton collimation. In Figure 1.5(a) the emitted photon interacts twice within the active region of the ACIS, undergoing Compton scattering in the first detection plane, and then photoelectric absorption in the second. Unlike the overview of Compton collimation shown in Figure 1.2, here the first detection plane has a high enough spatial resolution to measure the charge cloud created as the Compton electron travels through its active volume (Figure 1.5(b)). Through analysis of the Compton electron charge cloud, the ejection direction of the Compton electron can be estimated [35, 74]. An azimuthally restricted CoR can be constructed using the energy deposited and location of each photon interaction site, in combination with the measured Compton electron vector. The azimuthal centre of this CoR is in the opposite direction to the measured Compton electron vector, where the extent of restriction is proportional to the measurement uncertainty of the Compton electron vector [2, 90].

Of the three advanced Compton collimation methods, recoil electron tracking does not suffer from the same limitations as the other two methods if a radiation detector of sufficient spatial resolution is available. Unlike polarisation Compton collimation, for which a highly specific photon interaction sequence is required, recoil electron tracking enhanced Compton collimation can be applied to any interaction sequence with more than two interactions if the direction of the first Compton electron can be determined. Also, the lack of a coded aperture gives the advanced collimation method a significant advantage over mechanically encoded Compton collimation. At present the fundamental limits of recoil electron tracking enhanced Compton collimation still remain largely unexplored.

1.3 Thesis Overview

This thesis presents a number of studies into SPEI utilising the Monte Carlo radiation transport modelling toolkit (MCRTM) Geant4 [1, 3] as a test platform. The following document is segmented into three sections: Monte Carlo Modelling of Radiation Transport (Part I), Development of a Hybrid SPEI System (Part II) and Fundamental Study of Advanced Compton Imaging (Part III). This is followed by a set of overarching concluding remarks in Chapter 8 that sum up the findings of all three parts.

1.3.1 Monte Carlo Modelling of Radiation Transport (Part I)

Part I is composed of two chapters that present an overview of the selected simulation test platform and development of a high precision low energy electromagnetic physics model intended for studies in SPEI. Chapter 2, contains an overview of the principles of MCRTM and gives an introduction to Geant4 with a specific focus on photon and electron transport modelling. Chapter 3 presents a study, published in Nuclear Instruments and Methods in Physics Research B in August of 2014, that outlines the development of a newly derived low energy Compton scattering model, the Monash University Compton scattering model. This Compton scattering model was developed to address the limitation present in the majority of Monte Carlo bound atomic electron Compton scattering models: incorrect determination of the ejected direction of Compton electrons due to the non-zero momentum of the bound atomic electron [10]. This model acted as the basis for the final study of this thesis, see Part III, and has since been implemented by the author of this thesis in Geant4 version 9.6 as the default high accuracy low energy Compton scattering model.

1.3.2 Development of a Hybrid SPEI System (Part II)

Part II is composed of three studies relating to the development of a novel hybrid collimated SPEI system: the Pixelated Emission Detector for RadiOisotopes (PEDRO). The PEDRO is a conceptual proof of principle hybrid SPEI system that was designed to explore and quantify the relationship between spatial resolution and sensitivity, inherent in SPEI, over the energy range of 30 keV to 511 keV. This system was originally intended to be constructed from a Compton camera stack, five Silicon Double Sided Strip Detectors (DSSDs) and a CdZnTe Hybrid Pixel Detector (HPD), located behind a coded mask composed of a mix of pinholes, slats and/or open areas conceptually similar to that seen in Figure 1.4. Chapter 4 presents the first of these studies on PEDRO, published in Nuclear Instruments and Methods in Physics Research A at the end of 2009, that developed a Geant4 computation framework to explore the optimal detector spacing of the system operating only as a Compton camera for incident 140 keV photons. The findings of this study were utilised in the second study seen in Chapter 5, published in IEEE Transaction on Nuclear Science during the middle of 2011, that explores optimising a coded aperture mask designed for the PEDRO imaging system at the same incident photon energy (140 keV). The third and final chapter, Chapter 6, presents the development of a novel experimentally motivated image deblurring technique for

multi-plane Gamma cameras, like that of PEDRO, which was published in IEEE Transactions on Nuclear Science at the end of 2013.

1.3.3 Fundamental Study of Advanced Compton Imaging (Part III)

Finally, Part III is composed of a preliminary study into the fundamental limits of recoil electron tracking enhanced Compton collimation, or Advanced Compton Imaging. After the abrupt end of the PEDRO project mid-way through the second year of PhD candidature, a new direction was taken focused around the developing field (in SPEI) of Advanced Compton Imaging. This decision was taken due to the promising results that are presented in Part II regarding the significant improvement in performance of hybrid collimation with respect to standard mechanical collimation through CoR modulation. As this new SPEI modality was relatively young, the study presented in Chapter 7 was undertaken in an attempt to quantify the fundamental limits of recoil electron tracking enhanced Compton collimation. This study also motivated the development of the Monash University Compton scattering model, presented in Chapter 3, to improve the physical accuracy of the selected simulation test platform, Geant4, for Advanced Compton Imaging studies.

Part I

Monte Carlo Radiation Transport Modelling

Monte Carlo Method, Geant4 and Electromagnetic Physics Models

Monte Carlo Radiation Transport Modelling (MCRTM) is a computational tool utilised by a large number of fields to evaluate the interaction and effect of radiation in a defined environment. The following chapter presents an overview of the Monte Carlo method and its application to radiation transport modelling (Section 2.1), an introduction to Geant4 (Section 2.2), the Monte Carlo radiation transport modelling toolkit selected as the test platform, and an in-depth description of the photon, electron and positron transport models utilised in this thesis (Section 2.3). This chapter is intended to illustrate the scientific rigour that was put into the development of these selected physics models by the Geant4 collaboration, and highlight their validity for studies into SPEI.

2.1 Monte Carlo Method

2.1.1 Overview

Monte Carlo methods are ideal for studying systems with many variable components. Most of these systems are typically too complex to model with analytic algorithms due to the cascading dependence of each component and/or their interaction with one another. Monte Carlo methods capitalise on the fact that the majority of these system can be broken down in small subsections, typically to the level of their individual components, which can be modelled through a combination of mathematical algorithms and/or sampling of probabilistic distributions. Systems that are said to be memoryless, i.e. a stochastic system which is dependent only on the current state and not the sequence of states that precedes it, are able to implement the sampling of these components in a Monte Carlo Markov chain to statistically model their evolution over time [28].

System components, typically probabilistic processes, can be separated into two main categories: discrete and continuous. Discrete processes contain a number of quantised states, x_i , with each state x having probability $p = p(x_i)$. Continuous processes do not have quantised states, instead they vary continuously over the entire observable range with some probability density $f(x)$ of measuring an event x . Here $f(x)$ represents the density function of continuous process that is either taken from theoretical models or tabulated data from experimental observations. For each process, a cumulative distribution

function $F(x)$ represents the probability of finding the process of interest in state x , where:

$$F(x) = \sum_{x_i} p(x_i), \quad x_i \leq x \text{ (Discrete)}, \quad (2.1)$$

$$F(x) = \int_{-\infty}^x f(x)dx, \text{ (Continuous)}. \quad (2.2)$$

Inversion of these distribution functions enables the state of either type of probabilistic process to be sampled using randomly sampled values from a uniformly distributed pseudo-random number generator bound over a range of 0 to 1. For given a random number r , the state of the x can be sampled via:

$$F^{-1}(r) = x, \quad (2.3)$$

where $F^{-1}(r)$ is the inverse distribution function of the process. Given enough trials (Ω), the shape of the distribution of sampled states will converge to the distribution function $F(x)$, i.e.:

$$F(x) = \int_{\Omega} F^{-1}(r)dr. \quad (2.4)$$

2.1.2 Radiation Transport Modelling: Ray-Traced Random Walks

The complexity of the radiation interaction within an environment is dependent on a large number of different factors, all of which are typically probabilistic in nature. A few of the more obvious factors include;

- particle type,
- particle energy,
- orientation, material composition and geometry of objects within the defined environment,
- external electromagnetic fields.

Construction of a single transport equation for a given particle type that includes the variable components listed above is nontrivial [56]. It is more straight-forward to solve the transport of a particle through the uses of small steps (discrete or random) where at each step location the state of the particle within the defined environment is determined [12, 13, 87]. At the location of each step the particle type, momentum and charge is used in combination with the composition, shape and density of the intersecting materials along the path, since its last interaction, to construct a “decision tree” [13]. This decision tree is constructed from a sequence of branching operations that represents the possible outcomes of the particle’s interaction at that step location [28]. The sampled outcome of this decision tree is then used to update the state of the particle and its surrounding environment. Subsequently, a new step is sampled at a distance along the ray corresponding to the updated particle’s net momentum vector [56]. This process continues until either the particle’s momentum reaches zero, or it leaves the defined volume [87]. This “ray-traced

random walk” implementation of the Monte Carlo method is the foundation of the Geant4 Monte Carlo radiation transport modelling toolkit [1].

2.2 Geant4: A Toolkit for Simulating the Passage of Particles Through Matter

Geant4, a toolkit for simulating the passage of particles through matter, is the result of a world wide collaboration of over 100 scientists and software engineers spanning the last 20 years [1, 3]. The original project proposed to the CERN Detector Research and Development Committee (DRDC), RD44, was the outcome of two combined studies from CERN and KEK to explore how modern computing technology could improve Geant3 [23]. To achieve the development philosophy outlined in RD44, “the simulation of any physics process at any energy can be easily plugged into Geant by any user”, Geant4 was developed utilising the C++ programming language and an object oriented design [23].

Since the development of the original implementation of Geant4, a total of nine additional versions have been released. With each release the core tracking, geometry and hits collection architecture has been incrementally improved and optimised. At the same time new particle types and physics models, including electromagnetic, hadronic and optical processes, spanning energies of a few eV to hundreds of TeV have been added to increase the functionality of Geant4 [94]. The main advantage which Geant4 possesses over other Monte Carlo radiation transport modelling programs/toolkits is the sheer number of particle types and physics models offered. With these additional models Geant4 has expanded its applicability from its original focus of particle and nuclear physics experiments to include: hadron therapy [22, 77], imaging science [36, 48], radiobiology [16, 43], space science [31, 78], synchrotron science [59, 88] and nuclear medicine [11, 37].

2.3 Photon, Electron and Positron Physics Models of Geant4

In this thesis all Geant4 applications were developed either utilising the `G4EmStandardPhysics_option4` physics constructor (`G4EMSP04`), or a custom Livermore physics constructor that, was for all intents and purposes, identical to `G4EMSP04` before its release [94]. Of the available Geant4 physics constructors [95], `G4EMSP04` was developed by the electromagnetic and low energy electromagnetic physics working groups from the most accurate electromagnetic physics models contained within Geant4 [95]. Specific care was taken when developing this physics constructor to utilise models that factor in atomic shell structure effects which have a significant impact on particle transport at energies below 10 MeV [94].

Table 2.1 contains a list of all of the kinematic photon, electron and positron physics processes and their respective model classes that `G4EMSP04` employs below 10 MeV. These models sample their interaction cross-sections from a combination of experimental and theoretical databases [6, 20, 71, 72, 94]. The total energy dependent cross-section for a given particle, over a possible elemental range from $Z = 1$

Photon	
Compton scattering	G4LowEPComptonModel
Rayleigh scattering	G4LivermoreRayleighModel
Photoelectric absorption	G4LivermorePhotoElectricModel
Gamma conversion	G4PenelopeGammaConversionModel
Electron and Positron	
Single / Multiple Elastic Scattering	G4UrbanMscModel
Bremsstrahlung	G4SeltzerBergerModel
Electron-Positron Annihilation	G4eplusAnnihilation

Table 2.1: Sub 10 MeV photon, electron and positron kinematic physics models of G4EMSP04 physics constructor.

to $Z = 100$, is derived through combination of each physical model's individual interaction cross-sections [94].

The remainder of this chapter is dedicated to describing the fundamental physical interactions of particles within these models after the random sampling of a target atom and interaction process has occurred. Each of these derived models utilise Feynman slash notation (otherwise known as Dirac slash notation) in natural units, i.e. $c = 1$ and $\hbar = 1$, and are represented via Feynman diagrams in momentum space with time running from bottom to top.

2.3.1 Photon Physics Models

Compton Scattering

As stated in Section 1.2, Compton scattering is the name given to the fundamental process of inelastic scattering of a high energy photon off of an electron. The Compton scattering physics class employed in the G4EMSP04 physics constructor, G4LowEPComptonModel, was developed as part of this thesis (see Chapter 3). The model was developed to address the limitation present in the majority of Monte Carlo bound atomic electron Compton scattering models: incorrect determination of the ejected direction of Compton electrons due to the non-zero momentum of the bound atomic electron [10].

In a Monte Carlo framework, the most accurate method that currently exists to simulate the angular distribution of Compton scattered photons is a parameterised function constructed from the product of the Incoherent Scattering Function (ISF) [42] and Klein-Nishina distribution (KN) [32, 39, 49, 82, 94]:

$$\frac{d\sigma}{d\Omega} = \text{ISF}(\omega, \theta, Z) \text{KN}(\omega, \theta) \quad (2.5)$$

where ω is the energy of the incident photon, θ is the scattering angle of the photon and Z is the atomic number of the target atom.

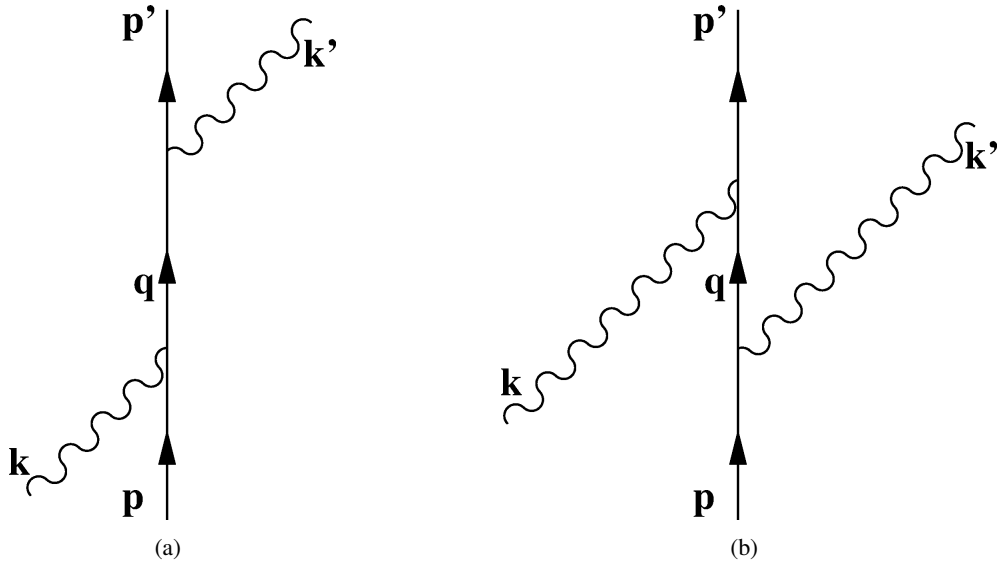


Figure 2.1: The two lowest order single Compton scattering Feynman diagrams in momentum space. A photon of incident energy ω strikes an electron and is absorbed. This photon is then re-emitted at a lower energy ω' where the net momentum change of the photon is transferred to the target electron.

The ISF function approximates an effective incoherent scattering amplitude, proportional to the effective atomic number of the atom, of an incident photon wave packet off a given electron within an isolated atom [42]. In its simplest form, under the assumption that ω is significantly greater than the spectrum of possible electronic excitation energies of the target atom [79], the Waller-Hartree theory gives the incoherent scattering function:

$$\text{ISF}(\mathbf{q}, Z) = \sum_{m=1}^Z \sum_{n=1}^Z \langle \Psi_0 | \exp[i\mathbf{q} \cdot (\mathbf{r}_m - \mathbf{r}_n)] | \Psi_0 \rangle - |\langle \Psi_0 | \sum_{m=1}^Z \exp(i\mathbf{q} \cdot \mathbf{r}_m) | \Psi_0 \rangle|^2, \quad (2.6)$$

where $\mathbf{q} = 2\omega \sin(\theta/2)$ is the momentum transfer to an electron, Z is the atomic number, Ψ_0 is the total radially symmetric ground-state wavefunction of the target atom, and $\mathbf{r}_{m,n}$ are the instantaneous positions of the m th and n th electrons within the target atom [42, 79]. The relationship shown in Equation 2.6 evaluates the effective atomic number of the target atom seen by the incident photons for a given ω and θ .

Single Compton scattering can be represented in momentum space via the two Feynman diagrams seen in Figure 2.1. Here, the Quantum Electrodynamics (QED) canonical quantised photon-electron scattering cross-section can be expressed as:

$$\sigma = (2\pi)^2 \frac{\epsilon\omega}{|p \cdot k|} \mathbf{S}_f \mathbf{S}_i \delta(p' + k' - p - k) |\langle f | \hat{M} | i \rangle|^2 \quad (2.7)$$

where:

- p and p' are the four-momentum of the ingoing and outgoing electron of mass m ,
- k and k' are the four-momentum of the incident and outgoing photon with polarisations ε and ε' ,
- $\varepsilon = p^0$, $\varepsilon' = p'^0$, $\omega = k^0$ and $\omega' = k'^0$,
- \mathbf{S} is the generalised summation symbol indicating the integration over momenta and summation over spins and polarisations, and
- $\langle f | \hat{M} | i \rangle$ is the transition probability amplitude for the initial (i) to final (f) state of the system [45].

Application of the Feynman rules of QED in momentum space to these two diagrams result in an S-matrix (\hat{S}_{fi}), equal to the transition matrix $\delta(p' + k' - p - k) \langle f | \hat{M} | i \rangle$, of the form [45]:

$$\begin{aligned} \hat{S}_{fi} &= \delta(p' + k' - p - k) \langle f | \hat{M} | i \rangle \\ &= \delta(p' + k' - p - k) \frac{ie^2 m}{8\pi^2 \sqrt{\varepsilon \varepsilon' \omega \omega'}} \bar{u}(\mathbf{p}') \\ &\times \left[\not{\varepsilon}' \frac{i(\not{p}' + \not{k}') - m}{(p' + k')^2 + m^2} \not{\varepsilon} + \not{\varepsilon} \frac{i(\not{p} - \not{k}') - m}{(p - k')^2 + m^2} \not{\varepsilon}' \right] u(\mathbf{p}) \end{aligned} \quad (2.8)$$

where $u(\mathbf{p})$ and $\bar{u}(\mathbf{p}')$ are the incident and outgoing field operators in momentum space, and m is the rest mass of the electron. Conservation of momentum, i.e. the δ -function seen in Equations 2.7 and 2.8, in combination with the fact that both particles are free in the initial and final states simplifies the expressions for momentum transfers in Figure 2.1 to:

$$\kappa = -p \cdot k = -p' \cdot k', \quad (2.9)$$

$$\kappa' = -p \cdot k' = -p' \cdot k, \quad (2.10)$$

and:

$$\frac{\omega'}{\omega} = \frac{1 - \beta \cos \alpha}{1 + (\omega/\varepsilon)(1 - \cos \theta) - \beta \cos \alpha} \quad (2.11)$$

where $|\mathbf{p}| = \beta\varepsilon$, $\varepsilon = \gamma m$, $\gamma = (1 - \beta^2)^{-1/2}$, α and α' are the angles between the incident electron and the incident and outgoing photon, θ is the angle between the incident and outgoing photon, and β is the incident electron velocity in natural units. With this Equation 2.8 simplifies to:

$$\begin{aligned} \hat{S}_{fi} &= \delta(p' + k' - p - k) \frac{ie^2 m}{8\pi^2 \sqrt{\varepsilon \varepsilon' \omega \omega'}} \bar{u}(\mathbf{p}') \\ &\times \left[\not{\varepsilon} \frac{i(\not{p} - \not{k}') - m}{2\kappa'} \not{\varepsilon}' - \not{\varepsilon}' \frac{i(\not{p}' + \not{k}') - m}{2\kappa} \not{\varepsilon} \right] u(\mathbf{p}). \end{aligned} \quad (2.12)$$

As the initial and final spins states are never experimentally observed, \mathbf{S}_i is averaged over the initial spins states and \mathbf{S}_f is summed over the final spin states and integrated over the final energy-momentum space τ_f . These spin sums are undertaken utilising the projection operators:

$$\Lambda_{\pm}(p) = \frac{1}{2m}(m \pm i\not{p}) \quad (2.13)$$

and the completeness relation:

$$\Lambda_+(p) + \Lambda_-(p) = 1. \quad (2.14)$$

Combining Equations 2.7 and 2.12 gives:

$$\sigma = \left(\frac{e^2}{4\pi}\right)^2 \frac{1}{2\kappa\epsilon'\omega'} \int d\tau_f \delta(p' + k' - p - k) X \quad (2.15)$$

where:

$$\begin{aligned} X &= \sum_{spins} \left| \bar{u}(\mathbf{p}') \left[\not{\epsilon}' \frac{i(\not{p} - \not{k}') - m}{2\kappa} \not{\epsilon} - \not{\epsilon}' \frac{i(\not{p} + \not{k}) - m}{2\kappa'} \not{\epsilon} \right] u(\mathbf{p}) \right|^2, \\ &= \frac{m^2}{4} \text{Tr} \left(\left[\frac{1}{\kappa} \not{\epsilon}' (i\not{p} + i\not{k} - m) \not{\epsilon} - \frac{1}{\kappa'} \not{\epsilon}' (i\not{p} - i\not{k}' - m) \not{\epsilon}' \right] \Lambda_-(p) \right. \\ &\quad \left. \times \left[\frac{1}{\kappa} \not{\epsilon} (i\not{p} + i\not{k} - m) \not{\epsilon}' - \frac{1}{\kappa'} \not{\epsilon}' (i\not{p} - i\not{k}' - m) \not{\epsilon} \right] \Lambda_-(p') \right). \end{aligned} \quad (2.16)$$

After expansion and simplification this trace can be written:

$$X = \frac{m^2}{\kappa^2} A + \frac{m^2}{\kappa'^2} B - \frac{m^2}{\kappa\kappa'} (C + D) \quad (2.17)$$

where:

$$A = \frac{1}{4} \text{Tr} [\not{\epsilon}' (ip - m + ik) \not{\epsilon} \Lambda_-(p) \not{\epsilon} (ip - m + ik) \not{\epsilon}' \Lambda_-(p')], \quad (2.18)$$

$$B = \frac{1}{4} \text{Tr} [\not{\epsilon} (ip - m - ik') \not{\epsilon}' \Lambda_-(p) \not{\epsilon}' (ip - m - ik') \not{\epsilon} \Lambda_-(p')], \quad (2.19)$$

$$C = \frac{1}{4} \text{Tr} [\not{\epsilon}' (ip - m + ik) \not{\epsilon} \Lambda_-(p) \not{\epsilon}' (ip - m - ik') \not{\epsilon} \Lambda_-(p')], \quad (2.20)$$

$$D = \frac{1}{4} \text{Tr} [\not{\epsilon} (ip - m - ik') \not{\epsilon}' \Lambda_-(p) \not{\epsilon} (ip - m + ik) \not{\epsilon}' \Lambda_-(p')]. \quad (2.21)$$

Equations 2.18 through 2.21 can be evaluated through the repeated application of the identity [34, 45]:

$$\begin{aligned} \text{Tr}(\phi_1 \cdots \phi_n) &= a_1 \cdot a_2 \text{Tr}(\phi_3 \cdots \phi_n) - a_1 \cdot a_3 \text{Tr}(\phi_2 \phi_4 \cdots \phi_n) \\ &\quad + \cdots + a_1 \cdot a_n \text{Tr}(\phi_2 \cdots \phi_{n-1}) \end{aligned} \quad (2.22)$$

and then substituted into Equation 2.17 to yield [45]:

$$X = \frac{1}{2} \left(\frac{\kappa}{\kappa'} + \frac{\kappa'}{\kappa} \right) - 1 + 2(\boldsymbol{\varepsilon} \cdot \boldsymbol{\varepsilon}')^2 + \left[\frac{(\boldsymbol{\varepsilon} \cdot \mathbf{p})^2 (\boldsymbol{\varepsilon}' \cdot \mathbf{p}')^2}{\kappa^2} + \frac{(\boldsymbol{\varepsilon}' \cdot \mathbf{p})^2 (\boldsymbol{\varepsilon} \cdot \mathbf{p}')^2}{\kappa'^2} \right] + 4 \left[\left(\frac{\boldsymbol{\varepsilon} \cdot \mathbf{p} \boldsymbol{\varepsilon}' \cdot \mathbf{p}}{\kappa} - \frac{\boldsymbol{\varepsilon} \cdot \mathbf{p}' \boldsymbol{\varepsilon}' \cdot \mathbf{p}}{\kappa'} \right) \boldsymbol{\varepsilon} \cdot \boldsymbol{\varepsilon}' - \frac{\boldsymbol{\varepsilon} \cdot \mathbf{p} \boldsymbol{\varepsilon} \cdot \mathbf{p}' \boldsymbol{\varepsilon}' \cdot \mathbf{p} \boldsymbol{\varepsilon}' \cdot \mathbf{p}'}{\kappa \kappa'} \right]. \quad (2.23)$$

With the trace above, it is now possible to evaluate Equation 2.15 for the relativistic cross-section per unit solid angle of a photon scattering off of an electron into the differential angle between θ and $\theta + d\theta$, and ϕ and $\phi + d\phi$. To achieve this let:

$$d\tau_f = d^3 p' d^3 k' = d^3 p' \omega'^2 d\omega' d\Omega \quad (2.24)$$

such that Equation 2.15 becomes:

$$\frac{d\sigma}{d\Omega} = \left(\frac{e^2}{4\pi} \right)^2 \frac{1}{2\kappa\epsilon'\omega'} \int d^3 p' \omega'^2 d\omega' \delta(p' + k' - p - k) X, \quad (2.25)$$

$$\frac{d\sigma}{d\Omega} = \left(\frac{e^2}{4\pi} \right)^2 \frac{1}{2\kappa\epsilon'\omega'} \int \omega'^2 d\omega' \delta(\epsilon' + \omega' - \epsilon - \omega) X, \quad (2.26)$$

where the integration over $d^3 p'$ results in the replacement of \mathbf{p}' with $\mathbf{p} + \mathbf{k} - \mathbf{k}'$ due to the δ -function over the system's three momenta. Application of the identity [34]:

$$\int dx \delta(f(x)) g(x) = \sum \left. \frac{g(x)}{\left| \frac{df}{dx} \right|} \right|_{\text{zero of } f(x)} \quad (2.27)$$

to the integral over ω' further simplifies Equation 2.26 to:

$$\frac{d\sigma}{d\Omega} = \left(\frac{e^2}{4\pi} \right)^2 \frac{1}{2\kappa\epsilon'\omega'} \omega'^2 \frac{d\omega'}{d(\omega' + \epsilon')} X \quad (2.28)$$

where $f(x) = \epsilon' + \omega' - \epsilon - \omega$ and $g(x) = \omega'^2 X$. Here ω' is regarded as a function of θ , ϕ , and the initial system state, enabling the derivative to be treated as constant [45]. Starting with:

$$\begin{aligned} \epsilon'^2 &= m^2 + (\mathbf{p} + \mathbf{k} - \mathbf{k}')^2 \\ &= \epsilon^2 + \omega^2 + \omega'^2 + 2\beta\omega\epsilon \cos \alpha - 2\beta\epsilon\omega' \cos \alpha' - 2\omega\omega' \cos \theta, \end{aligned} \quad (2.29)$$

the inverse of the derivative on the right side of Equation 2.28 can be determined through the use of Equation 2.11 and the relationship $\cos \alpha' = \cos \alpha \cos \theta + \sin \alpha \sin \theta \cos \phi$, which expresses α' in terms of α , θ and ϕ [45], such that:

$$\frac{d(\omega' + \epsilon')}{d\omega'} = 1 + \frac{\omega' - \beta\epsilon \cos \alpha' - \omega \cos \theta}{\epsilon'} = \frac{\epsilon\omega}{\epsilon'\omega'} (1 - \beta \cos \alpha). \quad (2.30)$$

Substitution of Equation 2.30 into Equation 2.28 yields the relativistic form of the differential cross-section per unit solid angle for Compton scattering:

$$\begin{aligned}\frac{d\sigma}{d\Omega} &= \frac{1}{2\epsilon^2} \left(\frac{e^2}{4\pi}\right)^2 \left(\frac{\omega'}{\omega}\right)^2 \frac{X}{(1 - \beta \cos \alpha)^2} \\ &= \left(\frac{\omega'}{\omega}\right)^2 \frac{r_0^2 X}{2\gamma^2(1 - \beta \cos \alpha)^2}\end{aligned}\quad (2.31)$$

where $r_0 = e^2/(4\pi m)$ is the classic electron radius. This equation can be further simplified into the Klein-Nishina cross-section, the differential cross-section per unit solid angle for Compton scattering off an electron at rest, when the momentum of the incident electron is set to zero, i.e. $p = (m, 0, 0, 0)$:

$$\frac{d\sigma}{d\Omega} = \frac{r_0^2}{4} \left(\frac{\omega'}{\omega}\right)^2 \left(\frac{\omega}{\omega'} + \frac{\omega'}{\omega} - 2 + 4(\boldsymbol{\varepsilon} \cdot \boldsymbol{\varepsilon}')^2\right) \quad (2.32)$$

where now $\beta = 0$, $\gamma = 1$, $k = m\omega$, $k' = m\omega'$ and Equation 2.11 reduces to:

$$\frac{\omega'}{\omega} = \frac{1}{1 + (\omega/m)(1 - \cos \theta)}. \quad (2.33)$$

Rayleigh Scattering

Rayleigh scattering, or electron resonance scattering, is the elastic scattering process of photons off bound atomic electrons described in the Feynman momentum space diagrams seen in Figure 2.2 [26, 45]. The G4EMSP04 Rayleigh scattering model, G4LivermoreRayleighModel [94], follows the approach of Cullen [19] that samples the angular distribution of Rayleigh scattered photons from a parameterised function consisting of the production of the square of the Atomic Form Factor (AFF) and differential Thomson cross-section per electron (DTC) [41, 94]:

$$\frac{d\sigma}{d\Omega} = \text{AFF}^2(\omega, \theta, Z) \text{DTC}(\theta) \quad (2.34)$$

where ω is the energy of the incident photon, θ is the scattering angle of the photon and Z is the atomic number of the target atom.

The AFF^2 term approximates an effective coherent scattering amplitude, proportional to the atomic number of the atom, of an incident photon wave packet off an isolated atom as a whole [42]. The AFF is given by:

$$\text{AFF}(\mathbf{q}, Z) = \sum_{n=1}^Z \langle \Psi_0 | \exp[i\mathbf{q} \cdot \mathbf{r}_n] | \Psi_0 \rangle \quad (2.35)$$

where $\mathbf{q} = 2\omega \sin(\theta/2)$ is the momentum transfer vector and Ψ_0 is the total radially symmetric ground-state wavefunction of the target atom and \mathbf{r}_n is the radius vector from the nucleus to the n th electron [42].

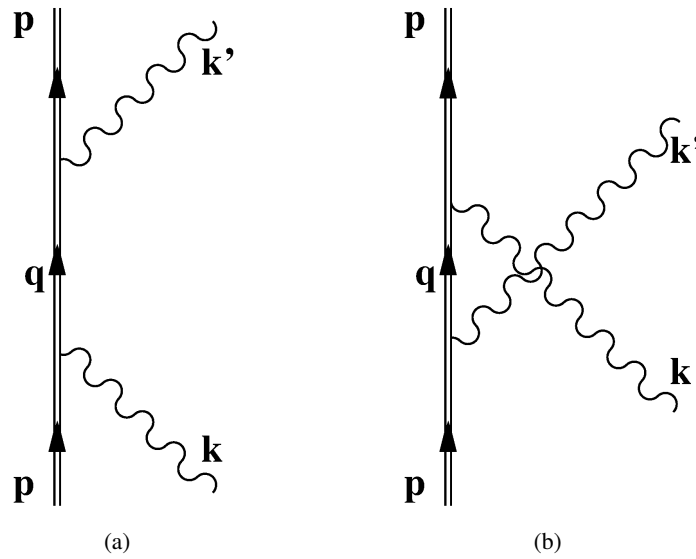


Figure 2.2: The two lowest order single Rayleigh scattering Feynman diagrams in momentum space. A photon of incident energy ω is absorbed by a bound atomic electron, represented by two solid parallel lines, exciting it to a higher discrete level or the continuum. The electron then transitions back to its original state, emitting a photon of the same energy ω .

Thomson scattering is the non-relativistic limit of Compton scattering where the energy of the incident photon is considered small, $\omega \ll m$ [45]. In this elastic scattering system $\omega' = \omega$, which simplifies Equation 2.32 to:

$$\frac{d\sigma}{d\Omega} = r_0^2 |\boldsymbol{\varepsilon} \cdot \boldsymbol{\varepsilon}'|^2 \quad (2.36)$$

where $\boldsymbol{\varepsilon}$ and $\boldsymbol{\varepsilon}'$ are the incident and outgoing photon polarisations, and $r_0 = e^2/(4\pi m)$ is the classical electron radius. In the unpolarised case, Equation 2.36 simplifies to the more commonly known version for the DTC [26, 45]:

$$\frac{d\sigma}{d\Omega} = r_0^2 \frac{1 + \cos^2 \theta}{2}. \quad (2.37)$$

Photoelectric Absorption

Photoelectric absorption is the total absorption process of a photon by a bound atomic electron [25]. The momentum of this photon-electron interaction is conserved through the emission of the target electron, or photo-electron, and the recoil of the residual atom [26]. This interaction process is only possible if the incident photon energy ω is greater than the binding energy of the target electron E_B [25]. G4EMSP04's photoelectric absorption model, G4LivermorePhotoElectricModel, utilises a parameterised version of the Sauter-Gavrila K-Shell distribution [29], which is simplified to zero order in αZ [94], to sample the polar ejection angle. Here α is the fine structure constant and Z is the atomic number of the target atom.

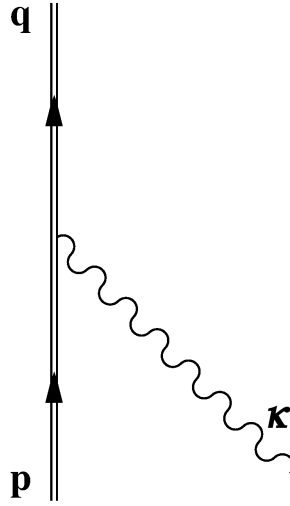


Figure 2.3: The lowest order Photoelectric absorption Feynman diagram in momentum space. A photon of incident energy ω is absorbed by a bound atomic electron, represented by two solid parallel lines, exciting it to the continuum.

Photoelectric absorption can be represented in momentum space via the Feynman diagram seen in Figure 2.3. The Sauter-Gavrila total relativistic K-shell differential cross-section for a hydrogen-like ion of atomic number Z , in the Born approximation and correct to first order in αZ , may be expressed as the sum of the two K-shell electrons and two possible spin directions of the final state photo-electron [29]:

$$\frac{d\sigma}{d\Omega} = \frac{(2\pi)^2 \alpha}{\kappa} \sum_{\sigma_1, \sigma_2} |T_{i \rightarrow f}|^2 \quad (2.38)$$

where the transition matrix ($T_{i \rightarrow f}$) is given by:

$$T_{i \rightarrow f} = \int \bar{u}_2(\mathbf{p}) \boldsymbol{\gamma} u_1(\mathbf{p} - \boldsymbol{\kappa}) d^3 p \quad (2.39)$$

for a photon of incident momentum $\boldsymbol{\kappa}$, energy κ and polarisation \mathbf{s} (where $\boldsymbol{\kappa} \cdot \mathbf{s} = 0$, $\mathbf{s}^2 = 1$ and \mathbf{s} is the four-component quantity $(\mathbf{s}, 0)$), and a K-shell electron of:

- ground-state spinor wavefunction $u_1(\mathbf{p})$ with energy $m(1 - \alpha^2 Z^2)^{\frac{1}{2}}$ (m to first order), and
- final-state spinor wavefunction $\bar{u}_2(\mathbf{p})$ of energy E , velocity β and asymptotic momentum \mathbf{k} inside the solid angle $d\Omega$.

Here, the electron's initial and final states, to first order in αZ , are related by:

$$E = m + \kappa, \quad (2.40)$$

$$E = \frac{m}{(1 - \beta^2)^{\frac{1}{2}}}, \quad (2.41)$$

$$k = E\beta, k^2 + m^2 = E^2, k^2 - \kappa^2 = 2m\kappa, k^2 + \kappa^2 = 2E\kappa. \quad (2.42)$$

In the Born approximation to first order of αZ the ground-state spinor can be written as:

$$u_1(\mathbf{p}) = \frac{1}{(4\pi)^{\frac{1}{2}}} \left[G(p) + iF(p)\gamma_0\boldsymbol{\gamma} \cdot \frac{\mathbf{p}}{p} \right] \chi_1 \quad (2.43)$$

where γ_0 and $\boldsymbol{\gamma} = (\gamma_1, \gamma_2, \gamma_3)$ are gamma matrices in the Dirac representation, and χ_1 is one of the constant spinors $(1, 0, 0, 0)$ or $(0, 1, 0, 0)$ according to the ground-state's magnetic quantum number of $\pm 1/2$ [29]. The functions $G(p)$ and $F(p)$ can be expressed in the following forms:

$$G(p) = \left(\frac{32(\alpha Z m)^5}{\pi} \right)^{\frac{1}{2}} \left(1 + \frac{\pi\alpha Z}{8m} p \right) \frac{1}{(p^2 + (\alpha Z m)^2)^2}, \quad (2.44)$$

$$F(p) = \left(\frac{8(\alpha Z m)^5}{\pi} \right)^{\frac{1}{2}} \frac{p}{m} \frac{1}{(p^2 + (\alpha Z m)^2)^2}, \quad (2.45)$$

accurate to first order in αZ [14, 29]. Substitution of these two functions into Equation 2.43 simplifies to:

$$u(\mathbf{p}) = N_1 \left[\frac{1}{(p^2 + (\alpha Z m)^2)^2} \chi_1 + \frac{\alpha Z}{2\pi^2} \phi(p) \chi_1 + \frac{i}{2m} \frac{1}{(p^2 + (\alpha Z m)^2)^2} \gamma_0 \boldsymbol{\gamma} \cdot \mathbf{p} \chi_1 \right], \quad (2.46)$$

where:

$$N_1 = \frac{1}{\pi} (8(\alpha Z m)^5)^{\frac{1}{2}} \text{ and } \phi(p) = \frac{\pi^3}{4} \frac{p}{m} \frac{1}{(p^2 + (\alpha Z m)^2)^2}. \quad (2.47)$$

The final-state spinor wavefunction $\bar{u}_2(\mathbf{p})$, which satisfies the Dirac equation in momentum space, can be written:

$$\bar{u}_2(\mathbf{p})(i\mathbf{p} + m) = ie \int \bar{u}_2(\mathbf{p}) \mathbf{A}(\mathbf{q} - \mathbf{p}) d^3 q \quad (2.48)$$

where \mathbf{p} is the four-component quantity (\mathbf{p}, E) and \mathbf{A} is the potential four-vector $(0, iA_0)$. Application of the Born approximation to this continuous spinor, i.e. the outgoing electron wavefunction, results in the second-order expression [29]:

$$\begin{aligned} \bar{u}_2 = N_2^* \bar{\chi}_2(\mathbf{k}) & \left[\delta(\mathbf{p} - \mathbf{k}) - ie \mathbf{A}(\mathbf{k} - \mathbf{p}) \frac{i\mathbf{p} - m}{p^2 - k^2 - i\epsilon} + (ie)^2 \int \mathbf{A}(\mathbf{k} - \mathbf{q}) \right. \\ & \left. \times \frac{i\mathbf{q} - m}{q^2 - k^2 - i\epsilon} \mathbf{A}(\mathbf{q} - \mathbf{p}) d^3 q \frac{i\mathbf{p} - m}{p^2 - k^2 - i\epsilon} \right] \end{aligned} \quad (2.49)$$

where $\bar{\chi}_2(\mathbf{k})$ is the momentum space spinor for a free electron of momentum \mathbf{k} and a certain spin direction, \mathbf{q} is the four-component quantity (\mathbf{q}, iE) and ϵ is a real positive infinitesimal quantity introduced to avoid the poles during integration. N_2 has been introduced due to the change in normalisation from \mathbf{k} scale to that of energy and solid angle, and its magnitude is independent of the existence of the external field, such that:

$$|N_2|^2 = kE \quad (2.50)$$

where k and E are related in Equation 2.42 . Now let the Columb potential in Equation 2.49 be replaced with a screened potential, i.e.:

$$eA_0(\mathbf{q}) = -\frac{\alpha Z}{2\pi^2} \frac{1}{q^2 + \mu^2} \quad (2.51)$$

such that the final-state spinor may be written in the form:

$$\begin{aligned} \bar{u}_2 = N_2^* \bar{\chi}_2(\mathbf{k}) & \left[\delta(\mathbf{p} - \mathbf{k}) - \frac{\alpha Z}{2\pi^2} \frac{\gamma_0}{[(\mathbf{p} - \mathbf{k})^2 + \mu^2]} \frac{\mathbf{ip} - m}{(p^2 - k^2 - i\epsilon)} + \left(\frac{\alpha Z}{2\pi^2} \right)^2 \right. \\ & \left. \times \int \frac{\gamma_0}{[(\mathbf{q} - \mathbf{k})^2 + \mu^2]} \frac{\mathbf{iq} - m}{(q^2 - k^2 - i\epsilon)} \frac{\gamma_0}{[(\mathbf{q} - \mathbf{p})^2 + \mu^2]} d^3 q \frac{\mathbf{ip} - m}{(p^2 - k^2 - i\epsilon)} \right] \end{aligned} \quad (2.52)$$

where μ is the magnetic permeability constant [29]. With Equations 2.47 and 2.52, and after simplification, the transition matrix $T_{i \rightarrow f}$ can be split into four terms:

$$T_{i \rightarrow f} = T_{0 \ i \rightarrow f} + T_{1 \ i \rightarrow f} + T_{2 \ i \rightarrow f} + T_{3 \ i \rightarrow f} \quad (2.53)$$

where:

$$T_{0 \ i \rightarrow f} = N_1 N_2^* \frac{\bar{\chi}_2 \mathbf{s}}{[(\mathbf{k} - \boldsymbol{\kappa})^2 + (\alpha Z m)^2]^2} \left[1 + \frac{i}{2m} (\mathbf{k} - \boldsymbol{\kappa}) \boldsymbol{\gamma}_0 \boldsymbol{\gamma} + \frac{\alpha Z}{2\pi^2} \phi(|\mathbf{k} - \boldsymbol{\kappa}|) \right] \chi_1, \quad (2.54)$$

$$T_{1 \ i \rightarrow f} = -\frac{\alpha Z}{2\pi^2} N_1 N_2^* (\bar{\chi}_2 \boldsymbol{\gamma}_0 \mathbf{I} \mathbf{s} \chi_1), \quad (2.55)$$

$$T_{2 \ i \rightarrow f} = -\frac{\alpha Z}{2\pi^2} N_1 N_2^* \frac{i}{2m} (\bar{\chi}_2 \boldsymbol{\gamma}_0 \mathbf{J} \mathbf{s} \boldsymbol{\gamma}_0 \boldsymbol{\gamma} \chi_1), \quad (2.56)$$

$$T_{3 \ i \rightarrow f} = \left(\frac{\alpha Z}{2\pi^2} \right)^2 N_1 N_2^* (\bar{\chi}_2 \boldsymbol{\gamma}_0 \mathbf{K} \mathbf{s} \chi_1), \quad (2.57)$$

for which:

$$I = \int \frac{\mathbf{ip} - m}{[(\mathbf{p} - \mathbf{k})^2 + \mu^2][(\mathbf{p} - \boldsymbol{\kappa})^2 + (\alpha Z m)^2]^2 (p^2 - k^2 - i\epsilon)} d^3 p, \quad (2.58)$$

$$J = \int \frac{\mathbf{ip} - m}{[(\mathbf{p} - \mathbf{k})^2 + \mu^2][(\mathbf{p} - \boldsymbol{\kappa})^2 + (\alpha Z m)^2]^2 (p^2 - k^2 - i\epsilon)} (\mathbf{p} - \boldsymbol{\kappa}) d^3 p \quad (2.59)$$

and:

$$\begin{aligned} K = & \int \int \frac{1}{[(\mathbf{q} - \mathbf{k})^2 + \mu^2]} \frac{\mathbf{iq} - m}{(q^2 - k^2 - i\epsilon)} \frac{\gamma_0}{[(\mathbf{q} - \mathbf{p})^2 + \mu^2]} \\ & \times \frac{\mathbf{ip} - m}{(p^2 - k^2 - i\epsilon)} \frac{1}{[(\mathbf{p} - \boldsymbol{\kappa})^2 + (\alpha Z m)^2]^2} d^3 p d^3 q. \end{aligned} \quad (2.60)$$

Evaluation of Equations 2.53 to 2.60 for the summation of $T_{0\ i \rightarrow f}$ over all possible transitions from the K-shell to the continuum final-state of asymptotic momentum \mathbf{k} yields:

$$\sum_{\sigma_1, \sigma_2} |T_{0\ i \rightarrow f}|^2 = \frac{|N_1 N_2|^2}{Em} \frac{1}{(\mathbf{k} - \boldsymbol{\kappa})^8} \left[\Theta_0 + \frac{\alpha Z}{\pi^2} (\mathbf{k} - \boldsymbol{\kappa})^4 \text{Re} \sum_{\lambda=1}^4 \Theta_\lambda \right] \quad (2.61)$$

to first order in αZ with:

$$\Theta_0 = \frac{1}{4} \text{Tr} \left[\mathbf{s} \gamma_0 (\mathbf{ia} + b) (\mathbf{il} - m) \gamma_0 (\mathbf{ia}' - b) \mathbf{s} (\mathbf{ik} - m) \right], \quad (2.62)$$

$$\Theta_\lambda = \frac{1}{4} \text{Tr} \left[R_\lambda (\mathbf{il} - m) \gamma_0 (\mathbf{ia}' - b) \mathbf{s} (\mathbf{ik} - m) \right], \quad (2.63)$$

where b , the four-component quantity $\mathbf{a}(\mathbf{a}, ia_0)$ and R_λ are given by:

$$\mathbf{a} = \frac{1}{2m} (\mathbf{k} - \boldsymbol{\kappa}) + \frac{(\mathbf{k} - \boldsymbol{\kappa})^2}{4m^2 \kappa} \boldsymbol{\kappa}, \quad a_0 = \frac{(\mathbf{k} - \boldsymbol{\kappa})^2}{4m^2 \kappa} E - 1, \quad (2.64)$$

$$b = \frac{(\mathbf{k} - \boldsymbol{\kappa})^2}{4m\kappa}, \quad (2.65)$$

$$\begin{aligned} R_1 &= \mathbf{s} \phi(|\mathbf{k} - \boldsymbol{\kappa}|), \quad R_2 = -\gamma_0 I^{(0)} \mathbf{s}, \\ R_3 &= -\frac{i}{2m} \gamma_0 J^{(0)} \mathbf{s} \gamma_0 \boldsymbol{\gamma}, \quad R_4 = -\frac{1}{4m^2 \kappa} \gamma_0 L \gamma_0 (\mathbf{it} - m) \mathbf{s}. \end{aligned} \quad (2.66)$$

Here, $I^{(0)}$ and $J^{(0)}$ are Equations 2.58 and 2.59 evaluated to zero order in $\alpha Z m$, \mathbf{k} is the momentum four-vector (\mathbf{k}, ik_0) of a free particle in motion ($k_0 = (\mathbf{k}^2 + m^2)^{\frac{1}{2}} = E$), \mathbf{l} is the momentum four-vector of a free particle at rest $(0, im)$, \mathbf{t} denotes the four-component quantity $(\boldsymbol{\kappa}, iE)$ and \mathbf{a}' denotes the four-component quantity $(\mathbf{a}, -ia_0)$ [29]. After the laborious task of evaluating the traces of Equations 2.62 and 2.63, and in turn evaluating Equation 2.61 (see [29]), the differential K-shell photoelectric cross-section for the K-Shell, correct to first order in αZ , can be given in the form:

$$\frac{d\sigma}{d\Omega} = \frac{4}{m^2} \alpha^6 Z^5 \frac{\beta^3 (1 - \beta^2)^3}{[1 - (1 - \beta^2)^{\frac{1}{2}}]^5} \left[P \left(1 - \frac{\pi \alpha Z}{\beta} \right) + \pi \alpha Z Q \right] \quad (2.67)$$

where:

$$\begin{aligned} P &= \frac{\sin^2 \theta \cos^2 \varphi}{(1 - \beta \cos \theta)^4} - \frac{1 - (1 - \beta^2)^{\frac{1}{2}}}{2(1 - \beta^2)} \frac{\sin^2 \theta \cos^2 \varphi}{(1 - \beta \cos \theta)^3} \\ &+ \frac{[1 - (1 - \beta^2)^{\frac{1}{2}}]^2}{4(1 - \beta^2)^{\frac{3}{2}}} \frac{\sin^2 \theta}{(1 - \beta \cos \theta)^3} \end{aligned} \quad (2.68)$$

$$\begin{aligned}
Q = & \frac{[1 - (1 - \beta^2)^{\frac{1}{2}}]^{\frac{1}{2}}}{2^{\frac{7}{2}}\beta^2(1 - \beta \cos \theta)^{\frac{5}{2}}} \left[\frac{4\beta^2}{(1 - \beta^2)^{\frac{1}{2}}} \frac{\sin^2 \theta \cos^2 \varphi}{1 - \beta \cos \theta} + \frac{4\beta}{1 - \beta^2} \cos \theta \cos^2 \varphi \right. \\
& - 4 \frac{1 - (1 - \beta^2)^{\frac{1}{2}}}{1 - \beta^2} (1 + \cos^2 \varphi) - \beta^2 \frac{1 - (1 - \beta^2)^{\frac{1}{2}}}{1 - \beta^2} \frac{\sin^2 \theta}{1 - \beta \cos \theta} \\
& \left. + 4\beta^2 \frac{1 - (1 - \beta^2)^{\frac{1}{2}}}{(1 - \beta^2)^{\frac{3}{2}}} - 4\beta \frac{[1 - (1 - \beta^2)^{\frac{1}{2}}]^2}{(1 - \beta^2)^{\frac{3}{2}}} \cos \theta \right] \\
& + \frac{1 - (1 - \beta^2)^{\frac{1}{2}}}{4\beta^2(1 - \beta \cos \theta)^2} \left[\frac{\beta}{1 - \beta^2} - \frac{2}{1 - \beta^2} \cos \theta \cos^2 \varphi + \frac{1 - (1 - \beta^2)^{\frac{1}{2}}}{(1 - \beta^2)^{\frac{3}{2}}} \cos \theta \right. \\
& \left. - \beta \frac{1 - (1 - \beta^2)^{\frac{1}{2}}}{(1 - \beta^2)^{\frac{3}{2}}} \right] \tag{2.69}
\end{aligned}$$

and θ and φ are the polar and azimuthal photo-electron ejection angles respectively [29].

Pair Production / Gamma Conversion

Pair production, often referred to as Gamma conversion, is the conversion process of a photon of minimum energy 1.022 MeV, within the field of a charged particle, into an electron-positron pair [26]. In this interaction, the sum of the rest mass and kinetic energies of the electron and positron, and the kinetic energy of the recoil charged particle/nucleus, in which the field of the interaction occurred, is equal to the incident photon energy (i.e. conservation of energy and momentum) [38]. G4EMSP04's pair production model, G4PenelopeGammaConversionModel, utilises a parameterised version of the Bethe-Heitler formula to sample the solid angle of emission and energy of the electron-positron pair, created in the field of a nucleus, with Coulomb corrections outlined in Davies et al. [21, 94].

Pair production in an external field, i.e. the field of an atomic nucleus, can be represented in momentum space via the Feynman diagram shown in Figure 2.4. Here, the canonically quantised pair production cross-section can be expressed as:

$$\sigma = (2\pi)^2 \mathbf{S}_f \bar{\mathbf{S}}_i \delta(\epsilon_+ + \epsilon_- - \omega) |\langle f | \hat{M} | i \rangle|^2 \tag{2.70}$$

where:

- p_- and p_+ are the four-momentum of the outgoing electron and positron of mass m and velocities β_- and β_+ ,
- k is the four-momentum of the incident photon with polarisation ε ,
- $\epsilon_+ = p_+^0$, $\epsilon_- = p_-^0$ and $\omega = k^0$,
- \mathbf{S} is the generalised summation symbol indicating the integration over momenta and summation over spins and polarisations, and
- $\langle f | \hat{M} | i \rangle$ is the transition probability amplitude for the initial (i) to final (f) state of the system [45].

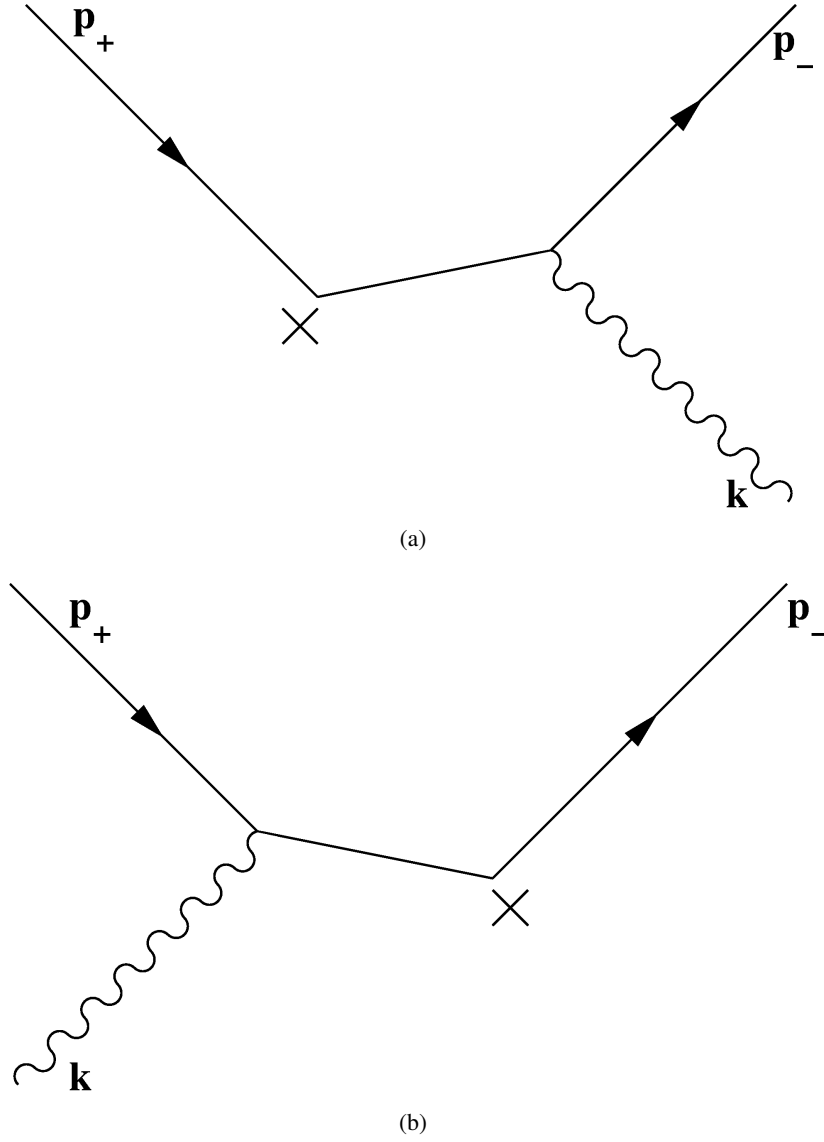


Figure 2.4: The two lowest order external field pair production Feynman diagrams in momentum space. A photon of incident energy ω undergoes conversion into an electron-positron pair of momentum p_- and p_+ within an external field (denoted by the cross in each image).

Application of the Feynman rules of QED in momentum space to the two diagrams seen in Figure 2.4 result in an S-matrix (\hat{S}_{fi}), equal to the transition matrix $\delta(\epsilon_+ + \epsilon_- - \omega) \langle f | \hat{M} | i \rangle$, of the form in [45]:

$$\begin{aligned}
 \hat{S}_{fi} &= \delta(\epsilon_+ + \epsilon_- - \omega) \langle f | \hat{M} | i \rangle \\
 &= \frac{ie^2}{(2\pi)^2} \frac{m}{\sqrt{\epsilon_+ \epsilon_-} 2\omega} \int \bar{u}(\mathbf{p}_-) \left[\not{\epsilon} \frac{i(\not{p}_- - \not{k}) - m}{(p_- - k)^2 + m^2} \not{n} + \not{n} \frac{i(\not{k} - \not{p}_+) - m}{(k - p_+)^2 + m^2} \not{\epsilon} \right] \\
 &\quad \times u(\mathbf{p}_+) \phi(\mathbf{q}) \delta(\mathbf{p}_+ + \mathbf{p}_- + \mathbf{q} - \mathbf{k}) d^3q
 \end{aligned} \tag{2.71}$$

where $\bar{u}(\mathbf{p}_-)$ and $u(\mathbf{p}_+)$ are the electron and positron field operators in momentum space, and n is a time-like unit vector (i.e. $n^2 = -1$). Here, the external field $\phi(\mathbf{q})$ is the Coulomb field of a nucleus of

charge Z :

$$\phi(\mathbf{q}) = \frac{Ze}{(2\pi)^{\frac{3}{2}} |\mathbf{q}|^2} \quad (2.72)$$

in the first Born approximation, i.e. the lowest order of αZ , where $\mathbf{q} = \mathbf{k} - \mathbf{p}_+ - \mathbf{p}_-$ [7, 45]. Substitution of Equation 2.72 into Equation 2.71 and its integration after simplification via the momentum delta function $\delta(\mathbf{p}_+ + \mathbf{p}_- + \mathbf{q} - \mathbf{k})$, in combination with the identity $\alpha = e^2/(4\pi)$, yields:

$$\begin{aligned} \hat{S}_{fi} = i\alpha \frac{\sqrt{\alpha Z^2}}{(2\pi)^2} \delta(\epsilon_+ + \epsilon_- - \omega) \frac{m}{\sqrt{\epsilon_+ \epsilon_- \omega}} \frac{1}{|\mathbf{q}|^2} \bar{u}(\mathbf{p}_-) \left[\not{\epsilon} \frac{i(\not{p}_- - \not{k}) - m}{2p_- \cdot k} \not{p} \right. \\ \left. + \not{p} \frac{i(\not{k} - \not{p}_+) - m}{2p_+ \cdot k} \not{\epsilon} \right] u(\mathbf{p}_+). \end{aligned} \quad (2.73)$$

Substitution of this result into Equation 2.70 after summation over the positron spin states (\mathbf{S}_i), summation over the electron spin states (\mathbf{S}_f), and integrating over the final energy-momentum space τ_f gives:

$$\sigma = (2\pi)^2 \frac{\alpha Z^2}{4\pi^4} r_0^2 \int \frac{m^4}{\epsilon_+ \epsilon_- \omega} \frac{1}{|\mathbf{q}|^4} \frac{1}{(2m)^2} d\tau_f \delta(\epsilon_+ + \epsilon_- - \omega) X. \quad (2.74)$$

Here, the trace X results from the summation over the electron and positron spin directions and can be written:

$$X = (2m)^2 \text{Tr}[Q\Lambda_+(p_+)\bar{Q}\Lambda_-(p_-)] \quad (2.75)$$

where:

$$Q(p_-, p_+) = \not{\epsilon} \frac{i(\not{p}_- - \not{k}) - m}{-2p_- \cdot k} \not{p} + \not{p} \frac{i(\not{k} - \not{p}_+) - m}{-2p_+ \cdot k} \not{\epsilon} \quad (2.76)$$

and:

$$\Lambda_{\pm}(p) = \frac{1}{2m}(m \pm i\not{p}). \quad (2.77)$$

Evaluation of this trace can be simplified through the application of the special gauge $\epsilon^0 = 0$ and, after some working, see [7, 38, 45], becomes:

$$\begin{aligned} X = -2 \left[\left(\frac{p_- \cdot \epsilon}{p_- \cdot k} \right)^2 (4\epsilon_+^2 - \mathbf{q}^2) + \left(\frac{p_+ \cdot \epsilon}{p_+ \cdot k} \right)^2 (4\epsilon_-^2 - \mathbf{q}^2) + 2 \frac{p_- \cdot \epsilon p_+ \cdot \epsilon}{p_- \cdot k p_+ \cdot k} \right. \\ \left. \times (4\epsilon_+ \epsilon_- + \mathbf{q}^2) + \left(2 - \frac{\mathbf{q}^2}{p_- \cdot k p_+ \cdot k} + \frac{p_+ \cdot k}{p_- \cdot k} + \frac{p_- \cdot k}{p_+ \cdot k} \right) \right]. \end{aligned} \quad (2.78)$$

With the trace above, it is now possible to evaluate Equation 2.70 for the differential cross-section for pair production by a linear polarised photon in the Coulomb field of a nucleus of charge Z for the emission of the electron into the solid angle $d\Omega_-$ and positron into the solid angle $d\Omega_+$. To achieve this let:

$$d\tau_f = d^3 p_+ d^3 p_- = |\mathbf{p}_+| \epsilon_+ d\epsilon_+ d\Omega_+ |\mathbf{p}_-| \epsilon_- d\epsilon_- d\Omega_- \quad (2.79)$$

such that Equation 2.70 becomes:

$$d\sigma = -\frac{\alpha Z^2}{(2\pi)^2} r_0^2 \int \frac{m^2}{|\mathbf{q}|^4} \frac{|\mathbf{p}_+| |\mathbf{p}_-|}{\omega} X d\Omega_+ d\Omega_- d\epsilon_+ d\epsilon_- \delta(\epsilon_+ + \epsilon_- - \omega) \quad (2.80)$$

where $|\mathbf{p}_+| = \beta_+\epsilon_+$ and $|\mathbf{p}_-| = \beta_-\epsilon_-$. Application of Equation 2.27 to the integral over ϵ_- simplifies Equation 2.80 to:

$$d\sigma = -\frac{\alpha Z^2}{(2\pi)^2} r_0^2 \frac{m^2}{|\mathbf{q}|^4} \frac{|\mathbf{p}_+||\mathbf{p}_-|}{\omega} X d\Omega_+ d\Omega_- d\epsilon_+ \quad (2.81)$$

such that the substitution of Equation 2.78 yields the compact form of the Bethe-Heitler formula [7]:

$$d\sigma = -\frac{\alpha Z^2}{(2\pi)^2} r_0^2 \frac{m^2}{|\mathbf{q}|^2} \frac{|\mathbf{p}_+||\mathbf{p}_-|}{\omega} 2 \left[\left(2\epsilon_+ \frac{p_- \cdot \boldsymbol{\varepsilon}}{p_- \cdot k} + 2\epsilon_- \frac{p_+ \cdot \boldsymbol{\varepsilon}}{p_+ \cdot k} \right)^2 - \mathbf{q}^2 \left(\frac{p_- \cdot \boldsymbol{\varepsilon}}{p_- \cdot k} - \frac{p_+ \cdot \boldsymbol{\varepsilon}}{p_+ \cdot k} \right)^2 + \left(2 - \frac{\mathbf{q}^2}{p_- \cdot k p_+ \cdot k} + \frac{p_+ \cdot k}{p_- \cdot k} + \frac{p_- \cdot k}{p_+ \cdot k} \right) \right] d\Omega_+ d\Omega_- d\epsilon_+. \quad (2.82)$$

2.3.2 Electron and Positron Physics Models

Single / Multiple Elastic Scattering

Elastic electron and positron scattering by an atom occurs, primarily, due to the electrostatic interaction of the screened nuclear Coulomb field with the deflected particle [26, 58]. The G4EMSP04 single/multiple electron/positron scattering model, G4UrbanMscModel [94], utilises Lewis' condensed approach based on the integro-differential diffusion equation for multiple scattering in a homogeneous medium [53, 102].

In Urban's adaption of Lewis' framework, the multiple scattering process can be completely described by the transport mean free paths (λ_k):

$$\frac{1}{\lambda_k} = 2\pi n_a \int_{-1}^1 [1 - P_k(\cos \theta)] \frac{d\sigma}{d\Omega} d(\cos \theta) \quad (2.83)$$

where $d\sigma/d\Omega$ is the differential scattering cross-section, P_k is the k -th Legendre polynomial, n_a is the number of atoms per volume and λ_k are functions of particle energy in a given material. Here, the mean property of multiple scattering depends only on the first and second moments of the mean free paths [102]. From Equation 2.83, the mean free value of the geometric path length z , in the first moment λ_1 , is given by:

$$\langle z \rangle = \lambda_1 \left[1 - \exp\left(-\frac{t}{\lambda_1}\right) \right] \quad (2.84)$$

where t is the true path length determined by the particle type, energy, and interaction process [53]. At the end of the true path length step t , the mean value of the scattering angle θ of the particle can be given, in terms of $\cos \theta$, by:

$$\langle \cos \theta \rangle = \exp\left(-\frac{t}{\lambda_1}\right) \quad (2.85)$$

with variance of:

$$\sigma_{var}^2 = \langle \cos^2 \theta \rangle - \langle \cos \theta \rangle^2 = \frac{1 + 2 \exp(-2\kappa\tau)}{3} - \exp(-2\tau) \quad (2.86)$$

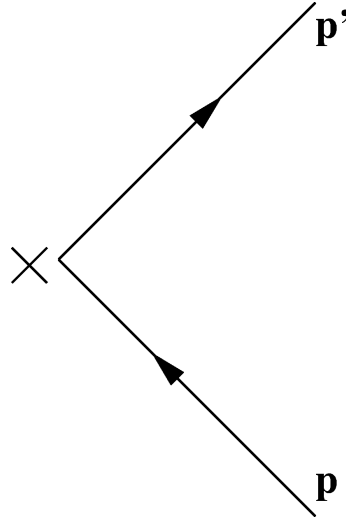


Figure 2.5: The lowest order external field elastic electron/positron scattering Feynman diagram in momentum space.

where $\tau = t/\lambda_1$, $\kappa = \lambda_1/\lambda_2$ and λ_2 is the second moment of the transport mean free paths [33, 102]. Additionally, if the initial particle direction is parallel to the z axis, the square of the mean lateral displacement is given by:

$$\langle x^2 + y^2 \rangle = \frac{4\lambda_1^2}{3} \left[\tau - \frac{\kappa + 1}{\kappa} + \frac{\kappa}{\kappa - 1} \exp(-\tau) - \frac{1}{\kappa(\kappa - 1)} \exp(-\kappa\tau) \right] \quad (2.87)$$

with the correlation strength between the final lateral position and particle direction for the true path length step t :

$$\langle xv_x + yv_y \rangle = \frac{2\lambda_1}{3} \left[1 - \frac{\kappa}{\kappa - 1} \exp(-\tau) + \frac{1}{\kappa(\kappa - 1)} \exp(-\kappa\tau) \right] \quad (2.88)$$

where v_x and v_y are the $x - y$ components of the directional unit vector [102]. In the case of the elastic scattering of electrons and positrons in Geant4, the differential scattering cross-section, $d\sigma/d\Omega$, seen in Equation 2.83, is the screened Rutherford differential cross-section in the first Born approximation [54, 55, 102].

Elastic electron scattering in an external field, i.e. the field of an atomic nucleus, can be represented in momentum space via the Feynman diagram seen in Figure 2.5. Here, the canonical quantised elastic electron scattering cross-section can be expressed as:

$$\sigma = (2\pi)^2 \frac{1}{\beta} \mathbf{S}_f \overline{\mathbf{S}}_i \delta(\epsilon' - \epsilon) |\langle f | \hat{M} | i \rangle|^2 \quad (2.89)$$

where:

- p and p' are the four-momentum of the incoming and outgoing electron of mass m and velocity β ,
- $\epsilon = p^0$ and $\epsilon' = p'^0$,

- \mathbf{S} is the generalised summation symbol indicating the integration over momenta and summation over spins and polarisations, and
- $\langle f | \hat{M} | i \rangle$ is the transition probability amplitude for the initial (i) to final (f) state of the system [45].

Application of the Feynman rules of QED in momentum space to the diagram seen in Figure 2.5 results in a S-matrix (\hat{S}_{fi}), equal to the transition matrix $\delta(\epsilon' - \epsilon) \langle f | \hat{M} | i \rangle$, of the form [45]:

$$\begin{aligned} \hat{S}_{fi} &= \delta(\epsilon' - \epsilon) \langle f | \hat{M} | i \rangle \\ &= \delta(\epsilon' - \epsilon) \frac{e}{\sqrt{2\pi}} \sqrt{\frac{m^2}{\epsilon'\epsilon}} \int \bar{u}(\mathbf{p}') \phi(\mathbf{q}) u(\mathbf{p}) \delta(p' - p - q) d^4q \end{aligned} \quad (2.90)$$

where $u(\mathbf{p})$ and $\bar{u}(\mathbf{p}')$ are the incoming and outgoing electron field operators in momentum space. In Urban's adaption of Lewis' framework for electrons and positrons, the external field $\varphi_\mu(x)$ is the screened Coulomb field of a nucleus of charge Z :

$$\varphi_\mu(x) = n_\mu \frac{Ze}{4\pi r} \exp(-\lambda r) = \frac{n_\mu}{(2\pi)^{\frac{3}{2}}} \int \phi(\mathbf{q}) \delta(q^0) \exp(iq \cdot x) d^4q, \quad (2.91)$$

where $\lambda = m\alpha Z^{1/3}$, α is the fine structure constant, n is a time-like unit vector (i.e. $n^2 = -1$), and [54, 55]:

$$\phi(\mathbf{q}) = \frac{Ze}{(2\pi)^{\frac{3}{2}} [\lambda^2 + |\mathbf{q}|^2]}. \quad (2.92)$$

Substitution of $\phi(\mathbf{q})$ into Equation 2.90 and integration, after simplification via the momentum delta function $\delta(p' - p - q)$, yields [34]:

$$\hat{S}_{fi} = \delta(\epsilon' - \epsilon) \frac{Ze^2}{(2\pi)^2} \frac{m}{\sqrt{\epsilon'\epsilon}} \frac{1}{\lambda^2 + |\mathbf{p}' - \mathbf{p}|^2} \bar{u}(\mathbf{p}') \not{h} u(\mathbf{p}). \quad (2.93)$$

Insertion of this expression into Equation 2.83 in combination with the summation over the incoming (\mathbf{S}_i) and outgoing (\mathbf{S}_f) electron spin states, and integrating over the final energy-momentum space τ_f gives¹:

$$d\sigma = \frac{Z^2 e^4 m^2}{4\pi^2 \beta} \int \frac{1}{\sqrt{\epsilon'\epsilon} (|\mathbf{p}' - \mathbf{p}|^2 + \lambda^2)^2} |\bar{u}(\mathbf{p}') \not{h} u(\mathbf{p})|^2 \delta(\epsilon' - \epsilon) d\tau_f. \quad (2.94)$$

With this result it is now possible to begin evaluating the relativistic electron elastic scattering differential cross-section of an electron into the differential solid angle $d\Omega$. In such a system the electron spins are not observed, thus we sum over the final state spins such that:

$$\begin{aligned} \frac{1}{2} \sum_{\text{Spins}} |\bar{u}(\mathbf{p}') \not{h} u(\mathbf{p})|^2 &= -2(n\Lambda_-(p)n\Lambda_-(p')) \\ &= \frac{1}{2m} (2(n \cdot p)^2 + p \cdot p' + m^2) \\ &= \gamma^2 \left(1 - \beta^2 \sin^2 \frac{\theta}{2} \right) \end{aligned} \quad (2.95)$$

¹At this point it is possible to switch to the calculation of the elastic scattering of positrons from a screened Coulomb potential by replacing $|\bar{u}(\mathbf{p}') \not{h} u(\mathbf{p})|^2$ with $|\bar{v}(\mathbf{p}') \not{h} v(\mathbf{p})|^2$ where $v(\mathbf{p}')$ and $\bar{v}(\mathbf{p})$ are the incoming and outgoing positron field operators in momentum space [45].

where θ is the scattering angle of the electron [45]. Additionally, for an electron scattered elastically at angle θ [34]:

$$|\mathbf{p}' - \mathbf{p}| = 2|\mathbf{p}| \sin \frac{\theta}{2}. \quad (2.96)$$

Now let:

$$d\tau_f = d^3 p' = |\mathbf{p}'| \epsilon' d\epsilon' d\Omega \quad (2.97)$$

and substitute Equations 2.95 and 2.96 into Equation 2.94 to give:

$$\begin{aligned} \frac{d\sigma}{d\Omega} &= \frac{Z^2 e^4 m^2}{4\pi^2 \beta} \int \frac{2\gamma^2 (1 - \beta^2 \sin^2 \frac{\theta}{2})}{\left((2|\mathbf{p}| \sin \frac{\theta}{2})^2 + \lambda^2 \right)^2} \frac{|\mathbf{p}'| \epsilon'}{\sqrt{\epsilon' \epsilon}} d\epsilon' \delta(\epsilon' - \epsilon) \\ &= \frac{Z^2 e^4 m^2 \beta'}{4\pi^2 \beta} \int \frac{2\gamma^2 (1 - \beta^2 \sin^2 \frac{\theta}{2})}{\left((2\beta \epsilon \sin \frac{\theta}{2})^2 + \lambda^2 \right)^2} \frac{\epsilon'^2}{\sqrt{\epsilon' \epsilon}} d\epsilon' \delta(\epsilon' - \epsilon) \end{aligned} \quad (2.98)$$

where $|\mathbf{p}'| = \beta' \epsilon'$ and $|\mathbf{p}| = \beta \epsilon$. After application of the identity in Equation 2.27, in combination with the fact that for an elastically scattered electron $|\mathbf{p}| = |\mathbf{p}'|$, $\beta = \beta'$, $\epsilon = \epsilon'$ and $\epsilon = \gamma m$, the screened Rutherford scattering cross-section in the first Born approximation may be written:

$$\frac{d\sigma}{d\Omega} = \frac{Z^2 e^4}{2\pi^2} \frac{\epsilon^3 (1 - \beta^2 \sin^2 \frac{\theta}{2})}{\left(4\beta^2 \epsilon^2 \sin^2 \frac{\theta}{2} + \lambda^2 \right)^2}. \quad (2.99)$$

Bremsstrahlung Radiation

Bremsstrahlung radiation, or braking radiation, is the name given to the physical phenomenon of the emission of a low energy photon during acceleration/deflection of a charged particle by another charged particle or nucleus [38, 45]. G4EMSP04's Bremsstrahlung model, G4SeltzerBergerModel, utilises two different approaches to sample the single differential cross-section for the photon energy ($d\sigma/dk$) and double differential cross-section for the emission direction relative to the incident momentum of the electron/positron ($d\sigma/[dkd\Omega]$) [94]. The single differential cross-section is constructed from the sum of the contribution of Bremsstrahlung produced in the field of the atomic nucleus ($d\sigma_n/dk$) and field of the Z atomic electrons ($d\sigma_e/dk$):

$$\frac{d\sigma}{dk} = \frac{d\sigma_n}{dk} + Z \frac{d\sigma_e}{dk} \quad (2.100)$$

where $d\sigma_n/dk$ and $d\sigma_e/dk$ are constructed from interpolation of the published tables of Pratt et al. [76] and Seltzer et al. [84]. For the double differential cross-section, a parameterised version of the double differential cross-section reported by Tsai is utilised [97, 98]. All of the atomic nucleus and

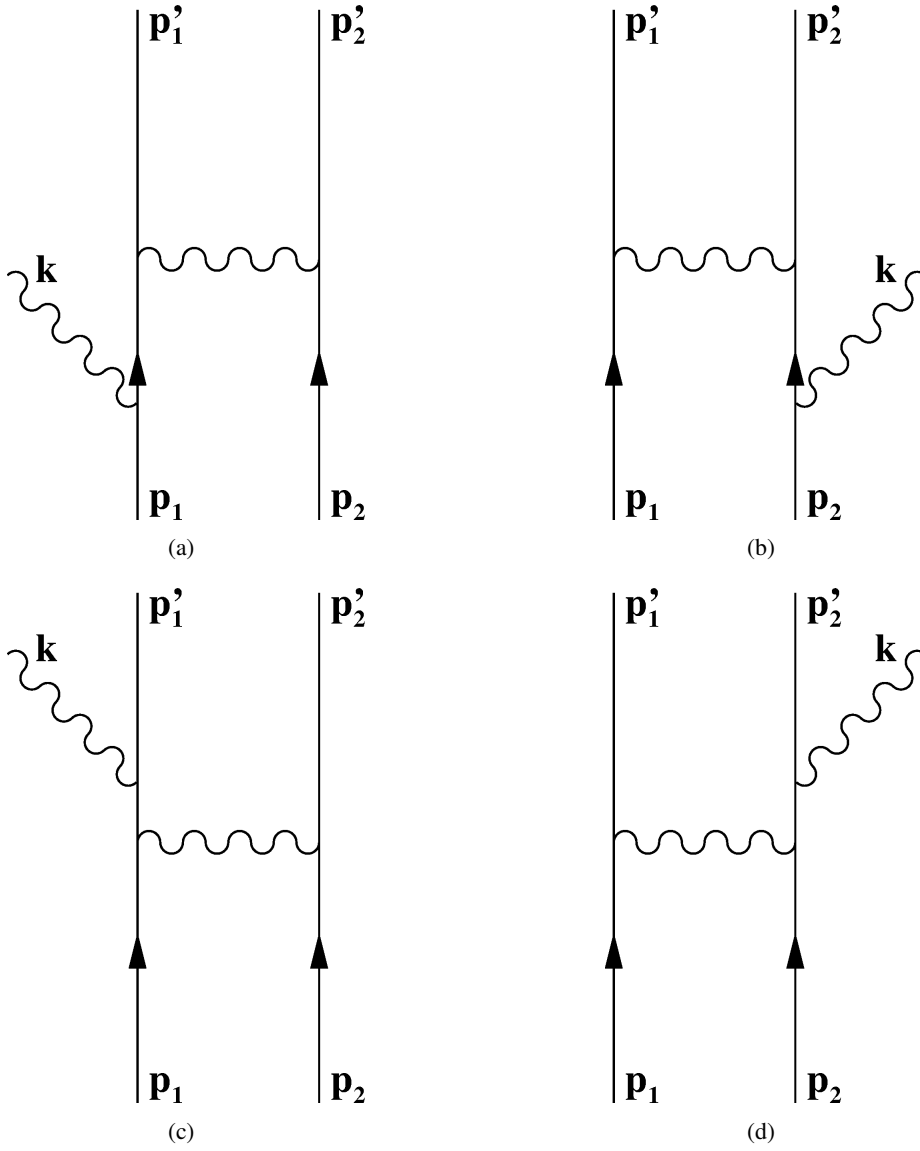


Figure 2.6: The four lowest order momentum space Bremsstrahlung electron-electron collision Feynman diagrams. Two electrons of incident momentum p_1 and p_2 scatter off one another resulting in the emission of a photon of energy ω .

atomic electron single/double differential Bremsstrahlung cross-sections have been developed from the fundamental framework of Bethe and Heitler [7, 38, 83, 84, 97, 98, 99].

Bremsstrahlung emission from electron-electron collisions, i.e. electron atomic-electron scattering, can be represented in momentum space via the Feynman diagrams seen in Figure 2.6. Here, the electron-electron Bremsstrahlung cross-section can be expressed as:

$$\sigma = (2\pi)^2 \frac{\epsilon_1 \epsilon_2}{\sqrt{(p_1 \cdot p_2)^2 - m^4}} \delta(p'_1 + p'_2 + k - p_1 - p_2) |\langle f | \hat{M} | i \rangle|^2 \quad (2.101)$$

where:

- p_1 and p'_1 are the four-momentum of the first incoming and outgoing electron of mass m and velocity β_1 ,
- p_2 and p'_2 are the four-momentum of the second incoming and outgoing electron of mass m and velocity β_2 ,
- k is the outgoing four-momentum of the Bremsstrahlung photon of polarisation ε and energy $\omega = k^0$,
- $\epsilon_1 = p_1^0$, $\epsilon'_1 = p'_1{}^0$, $\epsilon_2 = p_2^0$ and $\epsilon'_2 = p'_2{}^0$,
- \mathbf{S} is the generalised summation symbol indicating the integration over momenta and summation over spins and polarisations, and
- $\langle f | \hat{M} | i \rangle$ is the transition probability amplitude for the initial (i) to final (f) state of the system [45].

Application of the Feynman rules of QED in momentum space to the diagrams seen in Figure 2.6 result in a S-matrix (\hat{S}_{fi}), equal to the transition matrix $\delta(\epsilon' - \epsilon) \langle f | \hat{M} | i \rangle$, of the form² [45]:

$$\begin{aligned}
\hat{S}_{fi} &= \delta(p'_1 + p'_2 + k - p_1 - p_2) \langle f | \hat{M} | i \rangle \\
&= \delta(p'_1 + p'_2 + k - p_1 - p_2) \frac{e^3}{(2\pi)^{\frac{7}{2}}} \frac{m^2}{\sqrt{2\omega\epsilon_1\epsilon'_1\epsilon_2\epsilon'_2}} \\
&\times \left[\bar{u}(\mathbf{p}'_2) \gamma_\mu u(\mathbf{p}_2) \frac{1}{(p'_2 - p_2)^2} \bar{u}(\mathbf{p}_1) C^\mu(p'_1, p_1) u(\mathbf{p}_1) \right. \\
&- \bar{u}(\mathbf{p}'_1) \gamma_\mu u(\mathbf{p}_2) \frac{1}{(p'_1 - p_2)^2} \bar{u}(\mathbf{p}'_2) C^\mu(p'_2, p_1) u(\mathbf{p}_1) \\
&- \bar{u}(\mathbf{p}'_2) \gamma_\mu u(\mathbf{p}_1) \frac{1}{(p'_2 - p_1)^2} \bar{u}(\mathbf{p}'_1) C^\mu(p'_1, p_2) u(\mathbf{p}_2) \\
&\left. + \bar{u}(\mathbf{p}'_1) \gamma_\mu u(\mathbf{p}_1) \frac{1}{(p'_1 - p_1)^2} \bar{u}(\mathbf{p}'_2) C^\mu(p'_2, p_2) u(\mathbf{p}_2) \right] \quad (2.102)
\end{aligned}$$

where:

$$C^\mu(p', p) = \gamma^\mu \frac{i(\not{p} + \not{k}) - m}{(p+k)^2 + m^2} \not{\epsilon} + \not{\epsilon} \frac{i(\not{p}' - \not{k}) - m}{(p'-k)^2 + m^2} \gamma^\mu \quad (2.103)$$

and γ^μ is a set of 4 by 4 gamma matrices [45]. Substitution of Equation 2.102 into Equation 2.101, summation over final spin and polarisation states, and averaging over initial spin and polarisation states yields:

$$d\sigma = \frac{\alpha r_0^2}{(2\pi)^2} \frac{\beta'_1 \epsilon'_1 \omega d\omega}{\epsilon'_2 \sqrt{(p_1 \cdot p_2)^2 - m^4}} \frac{d\epsilon'_1}{d(\epsilon'_1 + \epsilon'_2 + \omega)} X d\Omega'_1 d\Omega_k \quad (2.104)$$

where integration over the delta function of momentum and energy eliminated p'_2 and replaced $d^3 p'_1 = \beta'_1 \epsilon'^2_1 d\Omega'_1$ with:

²At this point it is possible to switch to the calculation of the Bremsstrahlung cross-section for positron-electron collisions by replacing $p_2 \rightarrow -p'_+$ and $p'_2 \rightarrow -p_+$.

$$\beta'_1 \epsilon'_1{}^2 d\Omega'_1 \frac{d\epsilon'_1}{d(\epsilon'_1 + \epsilon'_2 + \omega)} \quad (2.105)$$

and:

$$X = \left[\frac{x(p'_1 p_1, p'_1 p_1)}{[(p'_1 - p_1)^2]^2} + \frac{x(p'_2 p_2, p'_1 p_1)}{(p'_2 - p_2)^2 (p'_1 - p_1)^2} - \frac{x(p'_1 p_2, p'_1 p_1)}{(p'_1 - p_2)^2 (p'_1 - p_1)^2} \right. \\ \left. - \frac{x(p'_2 p_1, p'_1 p_1)}{(p'_2 - p_1)^2 (p'_1 - p'_1)^2} + (p_1 \leftrightarrow p_2) \right] + (p'_1 \leftrightarrow p'_2). \quad (2.106)$$

Here:

$$\begin{aligned} x(p'_1 p_1, p'_1 p_1) &= \text{Tr} \left[\gamma_\mu \Lambda_-(p_1) \gamma_\nu \Lambda_-(p'_1) \right] \\ &\quad \times \text{Tr} \left[C^\mu(p'_2, p_2) \Lambda_-(p_2) \overline{C^\nu(p'_2, p_2)} \Lambda_-(p'_2) \right], \\ x(p'_2 p_2, p'_1 p_1) &= \text{Tr} \left[\gamma_\mu \Lambda_-(p_2) \overline{C^\nu(p'_2, p_2)} \Lambda_-(p'_2) \right] \\ &\quad \times \text{Tr} \left[C^\mu(p'_1, p_1) \Lambda_-(p_1) \gamma_\nu \Lambda_-(p'_1) \right], \\ x(p'_1 p_2, p'_1 p_1) &= \text{Tr} \left[\gamma_\mu \Lambda_-(p_2) \overline{C^\nu(p'_2, p_2)} \Lambda_-(p'_2) C^\mu(p'_2, p_1) \Lambda_-(p_1) \gamma_\nu \Lambda_-(p'_1) \right], \\ x(p'_2 p_1, p'_1 p_1) &= \text{Tr} \left[\gamma_\mu \Lambda_-(p'_2) \overline{C^\nu(p_2, p'_2)} \Lambda_-(p_2) C^\mu(p_2, p'_1) \Lambda_-(p'_1) \gamma_\nu \Lambda_-(p_1) \right] \end{aligned} \quad (2.107)$$

where the bar indicates that the gamma matrices in that expression are to be written in reverse order, $\Lambda_-(p) = (m - i\not{p})/2m$, and $(p \leftrightarrow q)$ means the previous expression with p and q interchanged [45]. Evaluation of the general form of this dimensionless trace X , i.e. Equation 2.106, was first successfully achieved by Votruba [106]. This is a lengthy task and will not be repeated in this thesis.

Bremsstrahlung produced in the field of the atomic nucleus can be represented in momentum space via the Feynman diagrams seen in Figure 2.7. Here, the canonical quantised Bremsstrahlung cross-section in the field of the atomic nucleus can be expressed as:

$$\sigma = \frac{(2\pi)^2}{\beta} \mathbf{S}_f \overline{\mathbf{S}}_i \delta(\epsilon' + \omega - \epsilon) |\langle f | \hat{M} | i \rangle|^2 \quad (2.108)$$

where:

- p and p' are the four-momentum of the incoming and outgoing electron of mass m and velocity β ,
- k is the outgoing four-momentum of the Bremsstrahlung photon of polarisation ε and energy $\omega = k^0$,
- $\epsilon = p^0$ and $\epsilon' = p'^0$
- \mathbf{S} is the generalised summation symbol indicating the integration over momenta and summation over spins and polarisations, and

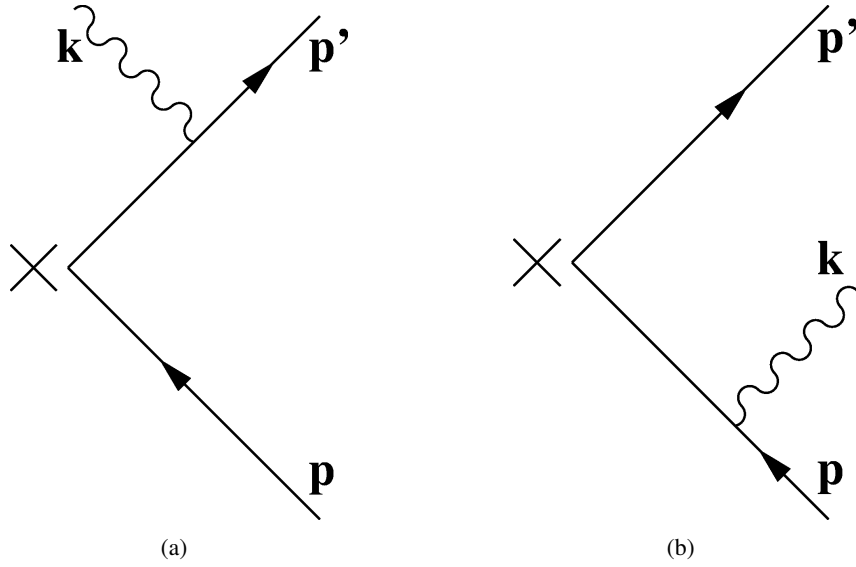


Figure 2.7: The two lowest order momentum space Feynman diagrams of Bremsstrahlung in an external field. The path of an electron of incident momentum p is accelerated/deflected to p' off an external potential, indicated by the cross in each diagram, resulting in the emission of a photon of energy ω .

- $\langle f | \hat{M} | i \rangle$ is the transition probability amplitude for the initial (i) to final (f) state of the system [45].

The momentum space diagrams for electron Bremsstrahlung in the field of an atomic nucleus (seen in Figure 2.7) can be transformed into those for pair production in the field of an atomic nucleus, contained in Figure 2.4, through the application of the substitution law [7, 45]. The substitution law states: “If two diagrams M' and M differ only in one external line, such that this line is an **outgoing** photon, electron, or positron line in M' and an **ingoing** photon, electron or positron line, respectively, in M , then the S -matrix (\hat{S}_{fi}) elements associated with M' and M are related as follows:

M'	M		
k' out	k in	$k' \leftrightarrow k$	$e' \leftrightarrow e$
p' out	q in	$p' \leftrightarrow -q$	$u(p') \leftrightarrow v(q)$
q' out	p in	$q' \leftrightarrow -p$	$v(q') \leftrightarrow u(p)$

In case of circular polarisation: right-circular \leftrightarrow left-circular polarisation” [45]. Thus, if the external field is assumed to be the Coulomb field of a nucleus of charge Z (i.e. Equation 2.72), the pair production cross-section seen in Equation 2.74 can be transformed through the substitution of $k \rightarrow -k$, $p_- \rightarrow p'$ and $p_+ \rightarrow -p$ to give³:

$$d\sigma = \frac{(2\pi)^2}{\beta} \frac{\alpha Z^2}{4\pi^4} r_0^2 \int \frac{m^4}{\epsilon' \epsilon \omega} \frac{1}{|\mathbf{q}|^4} \frac{1}{(2m)^2} \frac{1}{2} X d^3 p' d^3 k \delta(\epsilon' + \omega - \epsilon) \quad (2.109)$$

³At this point it is possible to switch to the calculation of the positron Bremsstrahlung cross-section in the field of an atomic nucleus by replacing $p \rightarrow -p'_+$ and $p' \rightarrow -p_+$.

and Equation 2.78 becomes:

$$X = 2 \left[\left(\frac{p' \cdot \varepsilon}{p' \cdot k} \right)^2 (4\epsilon^2 - \mathbf{q}^2) + \left(\frac{p \cdot \varepsilon}{p \cdot k} \right)^2 (4\epsilon'^2 - \mathbf{q}^2) - 2 \frac{p' \cdot \varepsilon p \cdot \varepsilon}{p' \cdot k p \cdot k} \right. \\ \left. \times (4\epsilon' \epsilon - \mathbf{q}^2) + \left(2 + \frac{q^2}{p' \cdot k p \cdot k} - \frac{p \cdot k}{p' \cdot k} - \frac{p' \cdot k}{p \cdot k} \right) \right] \quad (2.110)$$

where the Bremsstrahlung cross-section differs due to velocity of the incident particle, replacement of $-\Lambda_+(p_+)$ by $\Lambda_-(p)$, the density of the final states, and a factor of a half as the sum over the spins of the positron p_+ is replaced by an average of the spins of the electron p [7, 38, 45]. With some basic working, almost identical to that of Equations 2.78 to 2.82, Equations 2.109 and 2.110 yield the compact form of the Bethe-Heitler Bremsstrahlung cross-section (see Jauch and Rohrlich [45]):

$$d\sigma = \frac{\alpha Z^2}{(2\pi)^2} r_0^2 \frac{m^2}{|\mathbf{q}|^4} \frac{|\mathbf{p}'|}{|\mathbf{p}|} \frac{d\omega}{\omega} d\Omega' d\Omega_k \\ \times \left[\left(2\epsilon\omega \frac{p' \cdot \varepsilon}{p' \cdot k} - 2\epsilon'\omega \frac{p \cdot \varepsilon}{p \cdot k} \right)^2 + \omega^2 \mathbf{q}^2 \left(\frac{p' \cdot \varepsilon}{p' \cdot k} - \frac{p \cdot \varepsilon}{p \cdot k} \right)^2 \right. \\ \left. + \omega^2 \left(2 + \frac{\mathbf{q}^2}{p' \cdot k p \cdot k} - \frac{p \cdot k}{p' \cdot k} - \frac{p' \cdot k}{p \cdot k} \right) \right]. \quad (2.111)$$

Electron-Positron Annihilation

Electron-positron annihilation is the process where an electron and positron, its anti-particle, collide and emit two photons of total energy $2m = 1.022$ MeV. In the simplest case, the momentum of the centre of mass of the two-body system is zero and the two photon quanta are emitted back to back with the same energy of $m = 0.511$ MeV [26]. G4EMSP04's electron-positron annihilation model, G4eplusAnnihilation [94], utilises Heitler's in flight electron-positron annihilation differential cross-section model [38].

Electron-positron annihilation can be represented in momentum space via the Feynman diagrams presented in Figure 2.8. Here, the electron-positron annihilation cross-section can be expressed as:

$$\sigma = \frac{(2\pi)^2 \epsilon_+ \epsilon_-}{\sqrt{(p \cdot q)^2 - m^4}} \mathbf{S}_f \bar{\mathbf{S}}_i \delta(k_1 + k_2 - p - q) |\langle f | \hat{M} | i \rangle|^2 \quad (2.112)$$

where:

- $p = (\epsilon_-, \mathbf{p})$ and $q = (\epsilon_+, \mathbf{q})$ are the momentum four-vectors of the incident electron and positron of masses m and velocities β_- and β_+ ,
- $k_1 = (\omega_1, \mathbf{k}_1)$, ε_1 and $k_2 = (\omega_2, \mathbf{k}_2)$, ε_2 are the momentum and polarisation four-vectors of the emerging photons,
- \mathbf{S} is the generalised summation symbol indicating the integration over momenta and summation over spins and polarisations, and
- $\langle f | \hat{M} | i \rangle$ is the transition probability amplitude for the initial (i) to final (f) state of the system [45].

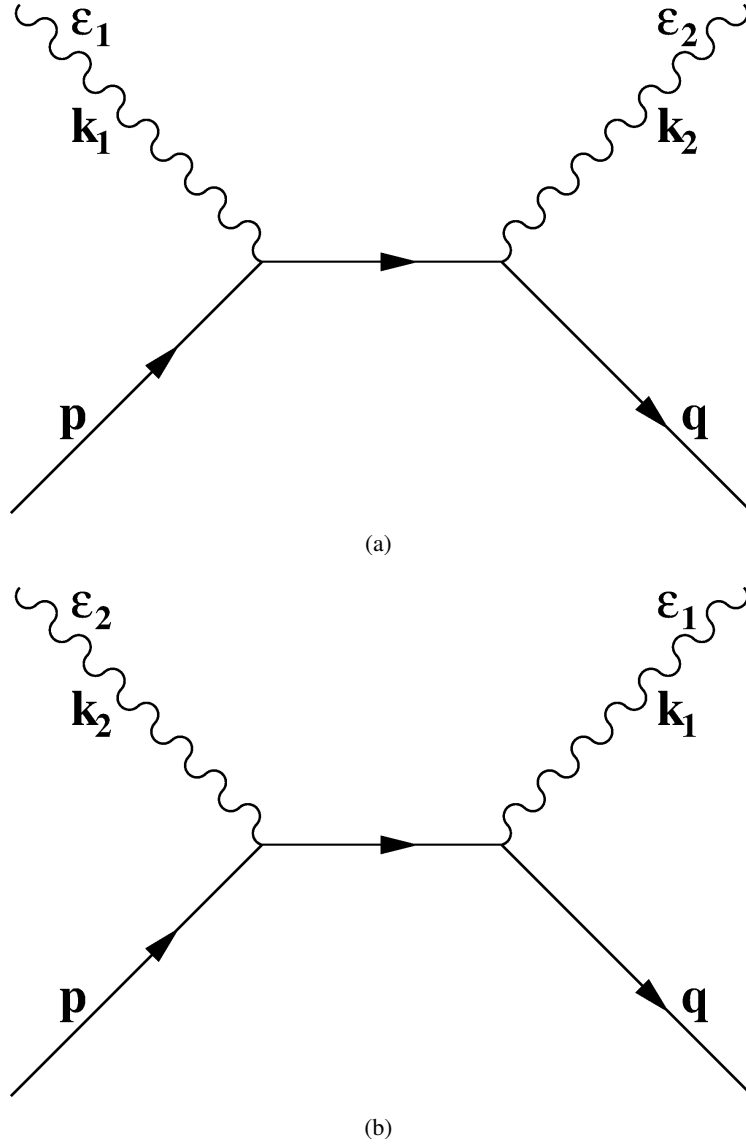


Figure 2.8: The two lowest order momentum space Feynman diagrams of electron-positron annihilation. An electron of incident momentum p and a positron of incident momentum q collide resulting in their annihilation and emission of two photons with momentum and polarisation k_1, k_2 , and ϵ_1 and ϵ_2 .

Application of the Feynman rules of QED in momentum space to the diagrams seen in Figure 2.8 result in an S-matrix (\hat{S}_{fi}), equal to the transition matrix $\delta(k_1 + k_2 - p - q) \langle f | \hat{M} | i \rangle$, of the form [45]:

$$\begin{aligned}
 \hat{S}_{fi} &= \delta(k_1 + k_2 - p - q) \langle f | \hat{M} | i \rangle \\
 &= \delta(k_1 + k_2 - p - q) \frac{-ie^2}{(2\pi)^2} \frac{m}{\sqrt{\epsilon_+ \epsilon_-} 2\omega_1 \omega_2} \bar{v}(\mathbf{q}) \left[\frac{\epsilon_2 (i\not{p} - i\not{k}_1 - m) \epsilon_1}{2p \cdot k_1} \right. \\
 &\quad \left. + \frac{\epsilon_1 (i\not{p} - i\not{k}_2 - m) \epsilon_2}{2p \cdot k_2} \right] u(\mathbf{p}).
 \end{aligned} \tag{2.113}$$

Substitution of the result above into Equation 2.112 and averaging over the incident electron-positron

spins yields:

$$d\sigma = \frac{\alpha^2}{4\omega_1\omega_2\sqrt{(p \cdot q)^2 - m^4}} \int d\tau_f X \delta(k_1 + k_2 - p - q) \quad (2.114)$$

such that:

$$-X = \frac{m^2}{\kappa_1^2} A + \frac{m^2}{\kappa_2^2} B + \frac{m^2}{\kappa_1\kappa_2} (C + D) \quad (2.115)$$

and:

$$A = (\varepsilon_2(ip - m - ik_1)\varepsilon_1\Lambda_-(p)\varepsilon_1(ip - m - ik_1)\varepsilon_2\Lambda_+(q)), \quad (2.116)$$

$$B = (\varepsilon_1(ip - m - ik_2)\varepsilon_2\Lambda_-(p)\varepsilon_2(ip - m - ik_2)\varepsilon_1\Lambda_+(q)), \quad (2.117)$$

$$C = -(\varepsilon_2(ip - m - ik_1)\varepsilon_1\Lambda_-(p)\varepsilon_2(ip - m - ik_2)\varepsilon_1\Lambda_+(q)), \quad (2.118)$$

$$D = -(\varepsilon_1(ip - m - ik_2)\varepsilon_2\Lambda_-(p)\varepsilon_1(ip - m - ik_1)\varepsilon_2\Lambda_+(q)), \quad (2.119)$$

where $-\kappa_1 = p \cdot k_1$, $-\kappa_2 = p \cdot k_2$, $\Lambda_-(p) = (m - ip)/2m$ and $\Lambda_+(q) = (m - iq)/2m$. The trace X , along with A , B , C and D , resembles Equation 2.17, and Equations 2.18 to 2.21 respectively, that contains the trace from the S-matrix for Compton scattering. In fact, under the substitutions:

$$p \rightarrow p, p' \rightarrow -q, \varepsilon \rightarrow \varepsilon_1, \varepsilon' \rightarrow \varepsilon_2, k \rightarrow -k_1, k' \rightarrow k_2 \quad (2.120)$$

the expressions for A , B , C and D are identical. Thus with the appropriate substitutions of Equation 2.120 the trace X for polarised and \bar{X} for unpolarised photons can be written:

$$X = \frac{1}{2} \left(\frac{\kappa_1}{\kappa_2} + \frac{\kappa_2}{\kappa_1} \right) + 1 - 2(\varepsilon_1 \cdot \varepsilon_2)^2 - 2 \left[\frac{(\varepsilon_1 \cdot p)^2 (\varepsilon_2 \cdot q)^2}{\kappa_1^2} + \frac{(\varepsilon_2 \cdot p)^2 (\varepsilon_1 \cdot q)^2}{\kappa_2^2} \right] - 4 \left[\left(\frac{\varepsilon_1 \cdot p \varepsilon_2 \cdot q}{\kappa_1} + \frac{\varepsilon_1 \cdot q \varepsilon_2 \cdot p}{\kappa_2} \right) \varepsilon_1 \cdot \varepsilon_2 + \frac{\varepsilon_1 \cdot p \varepsilon_2 \cdot p \varepsilon_1 \cdot q \varepsilon_2 \cdot q}{\kappa_1 \kappa_2} \right], \quad (2.121)$$

$$\bar{X} = \sum_{\text{pol}} X = 2 \left(\frac{\kappa_1}{\kappa_2} + \frac{\kappa_2}{\kappa_1} \right) + 4 \left(\frac{m^2}{\kappa_1} + \frac{m^2}{\kappa_2} \right) - 2 \left(\frac{m^2}{\kappa_1} + \frac{m^2}{\kappa_2} \right)^2. \quad (2.122)$$

With these two traces it is now possible to evaluate the differential cross-section for positron annihilation in flight. To achieve this let:

$$d\tau_f = d^3k_2 d^3k_1 = d^3k_2 \omega_1^2 d\omega_1 d\Omega_1 \quad (2.123)$$

and integrate Equation 2.114 over d^3k_2 replacing every instance of k_2 by $p + q - k_1$ to give [45]:

$$d\sigma = \frac{\alpha^2}{4\omega_1\omega_2\sqrt{(p \cdot q)^2 - m^4}} \int \omega_1^2 d\omega_1 \delta(\epsilon_1 + \epsilon_2 - \omega_1 - \omega_2) X d\Omega_1. \quad (2.124)$$

Application of the integral identity in Equation 2.27 further simplifies Equation 2.124 such that:

$$d\sigma = \frac{\alpha^2 \omega_1}{4\omega_2 \sqrt{(p \cdot q)^2 - m^4}} \frac{d\omega_1}{d(\omega_1 + \omega_2)} X d\Omega_1. \quad (2.125)$$

Here, ω_2 is a function of ω_1 . Through the conservation of energy and momentum, we have:

$$\omega_2^2 = \mathbf{p}^2 + \mathbf{q}^2 + \omega_1^2 + 2[|\mathbf{p}||\mathbf{q}| \cos \phi - \omega_1(|\mathbf{p}| \cos \theta'_1 + |\mathbf{q}| \cos \theta_1)] \quad (2.126)$$

where ϕ , θ , and θ' are the angles between p and q , k_1 and q , and k_1 and p [45]. Projection of the momentum parallel and perpendicular to k_1 gives:

$$\begin{aligned} \omega_1 + \omega_2 \cos \Theta &= |\mathbf{q}| \cos \theta_1 + |\mathbf{p}| \cos \theta'_1, \\ \omega_2 \sin \Theta &= |\mathbf{q}| \sin \theta_1 + |\mathbf{p}| \sin \theta'_1 \end{aligned} \quad (2.127)$$

where Θ is the angle between \mathbf{k}_1 and \mathbf{k}_2 . In a system where θ_1 , θ'_1 and the initial state is constant, i.e. \mathbf{p} , \mathbf{q} and ϕ are set, the derivative of Equation 2.126 in combination with Equation 2.127 gives:

$$\frac{d(\omega_1 + \omega_2)}{d\omega_1} = 1 - \cos \Theta. \quad (2.128)$$

Substitution of this result into Equation 2.125 gives the differential cross-section for positron annihilation in flight:

$$d\sigma = \frac{1}{4} r_0^2 \frac{\omega_1}{\omega_2} \frac{m^2 X d\Omega_1}{\sqrt{(p \cdot q)^2 - m^4} (1 - \cos \Theta)} \quad (2.129)$$

where X can be substituted with \bar{X} for the unpolarised case.

2.4 Summary

This chapter has presented an introduction to the selected simulation test platform Geant4 and gives an in-depth description of its high accuracy low energy photon, electron and positron transport models. Particular care was taken to prove the fundamental validity of each of these low energy electromagnetic physics models as their accuracy dictates the accuracy of the studies presented in Parts II and III. In fact, to ensure the accuracy of Geant4 for the SPEI study into Advanced Compton Imaging in Part III, a new low energy bound atomic electron Compton scattering model was developed. This new Compton scattering model, the Monash University model, is presented in Chapter 3.

A Low Energy Bound Atomic Electron Compton Scattering Model for Geant4

A low energy bound atomic electron Compton scattering model for Geant4

J. M. C. Brown, M. R. Dimmock, J. E. Gillam and D. M. Paganin

Published in Nuclear Instruments and Methods in Physics Research B, Volume 338, Pages 77–88, 2014

DOI: 10.1016/j.nimb.2014.07.042

Reproduced here with kind permission from Elsevier Inc.

Declaration for Thesis Chapter 3

Declaration by candidate

In the case of Chapter 3, the nature and extent of my contribution to the work was the following:

Nature of Contribution	Extent of Contribution (%)
Developed the theoretical model, developed/wrote the Geant4 physics class, G4LowEPComptonModel, undertook the simulations and comparison, and wrote up the paper	90 %

The following co-authors contributed to the work. If co-authors are students at Monash University, the extent of their contribution in percentage terms is stated:

Name	Nature of Contribution	Extent of Contribution (%)
M. R. Dimmock	Provided supervisory advice, aided proofreading and drafting	
J. E. Gillam	Provided supervisory advice, aided proofreading and drafting	
D. M. Paganin	Provided supervisory advice, aided proofreading and drafting	

The undersigned hereby certify that the above declaration correctly reflects the nature and extent of the candidate's and co-authors' contributions to this work.

Candidate's Signature:

Date: / /

Main Supervisor's Signature:

Date: / /



Contents lists available at ScienceDirect

Nuclear Instruments and Methods in Physics Research B

journal homepage: www.elsevier.com/locate/nimb

A low energy bound atomic electron Compton scattering model for Geant4

J.M.C. Brown^{a,*}, M.R. Dimmock^b, J.E. Gillam^{c,d}, D.M. Paganin^a^a School of Physics, Monash University, Victoria 3800, Australia^b Department of Medical Imaging and Radiation Science, School of Biomedical Science, Monash University, Victoria 3800, Australia^c IFIC CSIC Universitat de Valencia, Valencia E-46071, Spain^d Health Sciences, University of Sydney, NSW 2006, Australia

ARTICLE INFO

Article history:

Received 2 February 2014

Received in revised form 16 June 2014

Accepted 31 July 2014

Available online 29 August 2014

Keywords:

Compton scattering

Geant4

Radiation transport modelling

Monte Carlo method

ABSTRACT

A two-body fully relativistic three-dimensional scattering framework has been utilised to develop an alternative Compton scattering computational model to those adapted from Ribberfors' work for Monte Carlo modelling of Compton scattering. Using a theoretical foundation that ensures the conservation of energy and momentum in the relativistic impulse approximation, this new model, the Monash University Compton scattering model, develops energy and directional algorithms for both the scattered photon and ejected Compton electron from first principles. The Monash University Compton scattering model was developed to address the limitation of the Compton electron directionality algorithms of other computational models adapted from Ribberfors' work. Here the development of the Monash University Compton scattering model, including its implementation in a Geant4 low energy electromagnetic physics class, G4LowEPComptonModel, is outlined. Assessment of the performance of G4LowEPComptonModel was undertaken in two steps: (1) comparison with respect to the two standard Compton scattering classes of Geant4 version 9.5, G4LivermoreComptonModel and G4PenelopeComptonModel, and (2) experimental comparison with respect to Compton electron kinetic energy spectra obtained from the Compton scattering of 662 keV photons off the K-shell of gold. Both studies illustrate that the Monash University Compton scattering model, and in turn G4LowEPComptonModel, is a viable replacement for the majority of computational models that have been adapted from Ribberfors' work. It was also shown that the Monash University Compton scattering model is able to reproduce the Compton scattering triply differential cross-section Compton electron kinetic energy spectra of 662 keV photons K-shell scattering off of gold to within experimental uncertainty.

© 2014 Elsevier B.V. All rights reserved.

1. Introduction

The process of Compton scattering [1] is of interest in a large number of different fields, ranging from γ -ray astronomy [2–4] to pre-clinical medical imaging [5–7]. Ribberfors' Compton scattering model, the Double Differential Compton scattering Cross-Section (DDCS) in the Relativistic Impulse Approximation (RIA) [8], has served as a basis for the majority of Monte Carlo Compton scattering models employed today [9–12]. Developed using a framework based on Quantum Electrodynamics (QED), its accuracy has been validated through the comparison of simulation and experiment [9]. This framework was developed to include the effects of scattering off an atomic bound electron, binding energy and pre-collision

momentum of the target electron on the relationship of energy and angle dependence of the scattered photon [8]. The Doppler broadening of the scattered photon's energy distribution as a function of scattering angle contributes to noticeable differences between the free-electron assumption and reality for photon energies below 5 MeV.

Of the available Monte Carlo radiation transport programs, Geant4 [13,14], one of the most widely employed, has been released since 2008 with a number of classes that account for the effects of Doppler broadening in low energy Compton scattering [15]. These low energy Compton scattering classes, G4LivermoreComptonModel and G4PenelopeComptonModel, are based on adaptations of Ribberfors' Compton scattering model [9,12]. The limitation of these computational models, and others adapted from Ribberfors' Compton scattering model in a similar way, is that only the components of the pre-collision momentum of the electron contained within the two-dimensional plane defined by the

* Corresponding author.

E-mail address: j.m.c.brown@monash.edu (J.M.C. Brown).

incident and scattered photon, termed the photon plane, are incorporated into their scattering frameworks. As a result, both computational models are forced to constrain the ejected direction of the Compton electron into the photon plane. Each of the two Geant4 Compton scattering classes utilise different methods to estimate the polar ejection angle of the Compton electron. G4LivermoreComptonModel utilises a free-electron assumption, and G4PenelopeComptonModel assumes that the Compton electron is emitted in the direction of the photon's momentum transfer vector in an attempt to conserve energy and momentum of the system [11,12].

Alternative models to Ribberfors' DDCS have been developed and even expanded to the Triply Differential Compton scattering Cross-Section (TDCS), including the dependence of the ejection direction of the Compton electron [16–21]. These models have primarily explored the numerical calculation of K-shell Compton scattering cross-sections for numerous materials over an energy range of a few keV [16,17,20] to 1 MeV [20]. Of the wide range of different approaches in both the RIA and Independent Particle Approximation (IPA), one of the most promising is that described in the seminal paper from Kaliman et al. [17]. This paper outlines the development of a numerical framework for the TDCS calculation in a full relativistic second-order S-matrix QED IPA which was compared to experimental data for the K-shell Compton scattering of 662 keV photons in gold. While this model was consistent with the data to within experimental uncertainty [17], the present work approaches Compton scattering from a simple first principles framework in an attempt to limit the dependence on sampling from interpolated n-dimensional pre-calculated datasets.

The present work outlines the development and testing of the Monash University Compton scattering model. The model employs a two-body fully relativistic three-dimensional scattering framework, to avoid the previously discussed limitations of those computational models adapted from Ribberfors' Compton scattering framework, to model the ejection direction of the Compton electron. The development of a relativistic three-dimensional two-body scattering model and its implementation to a Geant4 low energy electromagnetic physics class, G4LowEPComptonModel, can be found in Section 2. Section 3 presents a comparison of G4LowEPComptonModel to the two standard Compton scattering classes of Geant4 version 9.5 for three different test elements over an energy range of 10 keV to 10 MeV. Section 4 presents an experimental comparison of G4LowEPComptonModel for calculation of the TDCS for 662 keV photons Compton scattering off gold with respect to the experimental data presented in Ljubičić et al. [22]. A discussion and an overall conclusion of the present work follows in Sections 5 and 6 respectively.

2. The Monash University Compton scattering model

The development of the Monash University Compton scattering model can be separated into two sections: the theoretical development of a relativistic three dimensional two-body scattering model, and its implementation to a Geant4 low energy electromagnetic physics class, G4LowEPComptonModel. A preliminary version of the Monash University Compton scattering model was originally presented at the IEEE Nuclear Science Symposium and Medical Imaging Conference in 2011 [23]. Since the submission of this proceeding, see [23], the physical framework has been redeveloped from first principles and implemented as a Geant4 low energy electromagnetic physics class.

2.1. Scattering model

The Monash University Compton scattering model utilises special-relativistic transforms to incorporate the effects of an atomic

bound non-stationary electron in a formalism similar to unpolarised inverse Compton scattering [24]. The scattering diagram seen in Fig. 1 outlines the basic principles of Compton scattering with an electron of non-zero pre-collision momentum.

Extension of the framework to Compton scattering off an atomic bound electron is possible through the relativistic impulse approximation [8,25]. Implementation of this approximation simplifies the relationship between pre-collision and post-collision momenta of the system to:

$$\mathbf{P} + \mathbf{Q} = \mathbf{P}' + \mathbf{Q}' \quad (1)$$

where \mathbf{P} , \mathbf{P}' , \mathbf{Q} and \mathbf{Q}' are the four-momenta for the incident photon, scattered photon, target electron, and recoil electron respectively. The four-momenta of the incident photon, target electron, scattered photon and recoil electron can be expressed in spherical coordinates as:

$$\mathbf{P} = \frac{\epsilon}{c}(1, 1, 0, 0), \quad (2)$$

$$\mathbf{Q} = \gamma m(c, u, \alpha, \beta), \quad (3)$$

$$\mathbf{P}' = \frac{\epsilon'}{c}(1, 1, \theta, 0), \quad (4)$$

$$\mathbf{Q}' = \gamma' m(c, u', \phi, \psi), \quad (5)$$

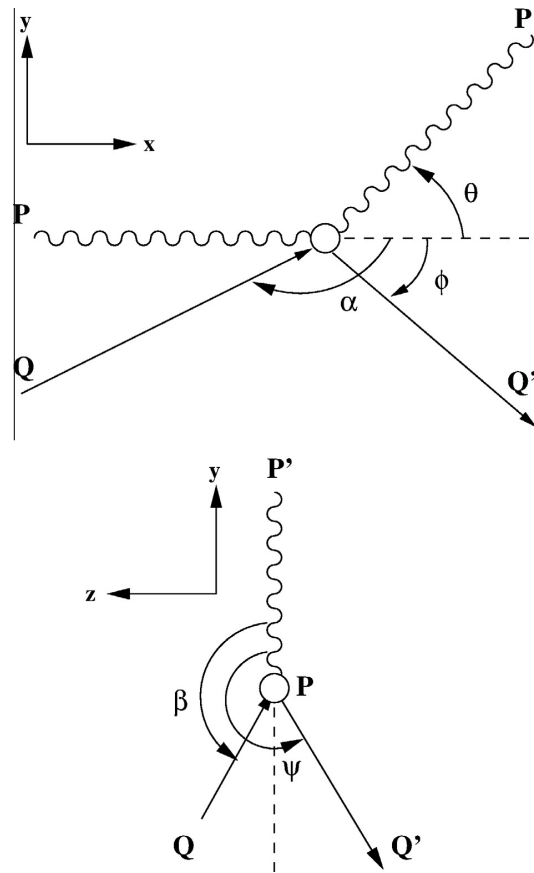


Fig. 1. A scattering diagram of atomic bound electron Compton scattering. \mathbf{P} is the incident photon momentum, \mathbf{Q} the electron pre-collision momentum, \mathbf{P}' the scattered photon momentum and \mathbf{Q}' the recoil electron momentum.

where ϵ is the energy of the incident photon, ϵ' is the energy of the scattered photon, c is the speed of light, m is the rest mass of an electron, u is the speed of the target electron, u' is the speed of the recoil electron, $\gamma = (1 - (u^2/c^2))^{-1/2}$ and $\gamma' = (1 - (u'^2/c^2))^{-1/2}$.

Monte Carlo modelling of Compton scattering in an atomic bound electron system requires that the incident photon four-momentum (\mathbf{P}) and target atom be known. Using this information, Probability Density Functions (PDFs) can be created from the scattering function corrected Klein–Nishina formula and the target atom's Compton profile [10,26,27]. These PDFs then allow for the recoil photon angle (θ) and electron pre-collision four-momentum (\mathbf{Q}) to be sampled. No orientation of the target atom is assumed, thus the incident angles of the electron's pre-collision four-momentum into the scattering plane, α and β , are randomly sampled within a uniform distribution. With these sampled values, only the scattered photon energy and ejected Compton electron kinetic energy and angles, ϕ and ψ , remain unknown. Sections 2.1.1 and 2.1.2 derive an expression for the scattered photon energy and recoil electron energy and direction within the electromagnetic potential field of the atom respectively.

2.1.1. Scattered photon energy

An expression for ϵ' can be derived from Eq. (1). Following Lightman et al. [28], the unwanted vector \mathbf{Q} is isolated to one side of the equation and squared:

$$\mathbf{Q}'^2 = (\mathbf{P} + \mathbf{Q} - \mathbf{P}')^2. \quad (6)$$

Since $\mathbf{Q}^2 = \mathbf{Q}'^2$ and $\mathbf{P}^2 = \mathbf{P}'^2 = 0$, Eq. (6) yields:

$$\mathbf{P} \cdot \mathbf{P}' = \mathbf{P} \cdot \mathbf{Q} - \mathbf{P}' \cdot \mathbf{Q} \quad (7)$$

where:

$$\mathbf{P} \cdot \mathbf{P}' = \frac{\epsilon\epsilon'}{c^2}(1 - \cos\theta), \quad (8)$$

$$\mathbf{P} \cdot \mathbf{Q} = \frac{\gamma m \epsilon}{c}(c - u \cos\alpha), \quad (9)$$

$$\mathbf{P}' \cdot \mathbf{Q} = \frac{\gamma' m \epsilon'}{c}(c - u \cos\theta \cos\alpha - u \sin\theta \sin\alpha \cos\beta). \quad (10)$$

Substitution of Eqs. (8)–(10) into Eq. (7) gives:

$$\epsilon' = \frac{\gamma m c (c - u \cos\alpha)}{1 - \cos\theta + \frac{\gamma m c (c - u \cos\theta \cos\alpha - u \sin\theta \sin\alpha \cos\beta)}{\epsilon}} \quad (11)$$

which is the three-dimensional Compton scattering formula, a direct extension of the two-dimensional inverse Compton scattering formula (Eq. (33.8) in Rindler [24]).

2.1.2. Compton electron energy and direction

With information regarding the energy of the incident photon, target electron, and now the scattered photon, the kinetic energy of the recoil electron within the electromagnetic potential field of the atom can be determined through the conservation of energy. The scattering system's energy pre- and post-collision obeys:

$$E'_k = \epsilon + E_k - \epsilon' \quad (12)$$

where E_k is the kinetic energy of the target electron, E'_k is the kinetic energy of the recoil electron and ϵ' is the energy of the scattered photon.

From here on the present work moves away from what has previously been achieved with a relativistic three-dimensional scattering framework, and derives two expressions for the recoil electron direction in spherical coordinates, ϕ and ψ , in the relativistic impulse approximation. As in Section 2.1.1, an expression for

the recoil electron direction in spherical coordinates can be derived through manipulation of Eq. (1). Utilising the Lightman et al. method [28], the following two equations can be formed through the isolation of \mathbf{Q} and \mathbf{P} and then squaring each equation:

$$\mathbf{Q}^2 = (\mathbf{P}' + \mathbf{Q}' - \mathbf{P})^2, \quad (13)$$

$$\mathbf{P}^2 = (\mathbf{P}' + \mathbf{Q}' - \mathbf{Q})^2. \quad (14)$$

As $\mathbf{Q}^2 = \mathbf{Q}'^2$ and $\mathbf{P}^2 = \mathbf{P}'^2 = 0$, Eqs. 13 and 14 simplify to:

$$\mathbf{P} \cdot \mathbf{P}' = \mathbf{P}' \cdot \mathbf{Q}' - \mathbf{P} \cdot \mathbf{Q}', \quad (15)$$

$$\mathbf{P}' \cdot \mathbf{Q} = \mathbf{P}' \cdot \mathbf{Q}' + \mathbf{Q}^2 - \mathbf{Q} \cdot \mathbf{Q}' \quad (16)$$

where:

$$\mathbf{P}' \cdot \mathbf{Q}' = \frac{\gamma' m \epsilon'}{c}(c - u' \cos\theta \cos\phi - u' \sin\theta \cos\psi \cos\phi), \quad (17)$$

$$\mathbf{P} \cdot \mathbf{Q}' = \frac{\gamma' m \epsilon}{c}(c - u' \cos\phi), \quad (18)$$

$$\mathbf{Q} \cdot \mathbf{Q}' = \gamma\gamma' m^2 (c^2 - uu' \cos\alpha \cos\phi - uu' \sin\beta \sin\alpha \sin\theta \sin\phi - uu' \cos\beta \sin\alpha \cos\theta \sin\phi). \quad (19)$$

Substitution of Eqs. (8)–(10), (17)–(19) and $\mathbf{Q}^2 = m^2 c^2$ into Eqs. 15 and 16 gives, after simplification:

$$c(\epsilon' - \epsilon) = \frac{\epsilon\epsilon'}{\gamma' m c}(1 - \cos\theta) + \epsilon' u' \sin\theta \cos\psi \sin\phi + (\epsilon' u' \cos\theta - \epsilon u') \cos\phi, \quad (20)$$

$$\begin{aligned} \gamma' m \epsilon' = & m^2 c^2 (\gamma\gamma' - 1) - (\gamma\gamma' m^2 uu' \cos\alpha - \frac{\gamma' m \epsilon' u'}{c} \cos\theta) \cos\phi \\ & - (\gamma\gamma' m^2 uu' \cos\beta \sin\alpha - \frac{\gamma' m \epsilon' u'}{c} \sin\theta) \cos\psi \sin\phi \\ & + \frac{\gamma' m \epsilon'}{c}(c - u \cos\theta \cos\alpha - u \sin\theta \cos\beta \sin\alpha) \\ & - \gamma\gamma' m^2 uu' \sin\beta \sin\alpha \sin\psi \sin\phi. \end{aligned} \quad (21)$$

Now let:

$$A = \epsilon' u' \sin\theta, \quad (22)$$

$$B = \epsilon' u' \cos\theta - \epsilon u', \quad (23)$$

$$C = c(\epsilon' - \epsilon) - \frac{\epsilon\epsilon'}{\gamma' m c}(1 - \cos\theta), \quad (24)$$

$$D = \frac{\gamma' m \epsilon'}{c}(c - u \cos\theta \cos\alpha - u \sin\theta \cos\beta \sin\alpha) + m^2 c^2 (\gamma\gamma' - 1) - \gamma' m \epsilon', \quad (25)$$

$$E = (\gamma\gamma' m^2 uu' \cos\alpha - \frac{\gamma' m \epsilon' u'}{c} u' \cos\theta), \quad (26)$$

$$F = (\gamma\gamma' m^2 uu' \cos\beta \sin\alpha - \frac{\gamma' m \epsilon' u'}{c} \sin\theta), \quad (27)$$

$$G = \gamma\gamma' m^2 uu' \sin\beta \sin\alpha, \quad (28)$$

then Eqs. 20 and 21 become:

$$\cos\psi \sin\phi = \frac{C - B \cos\phi}{A}, \quad (29)$$

$$G \sin\psi \sin\phi = H + I \cos\phi, \quad (30)$$

where $H = D - \frac{FC}{A}$ and $I = \frac{FB}{A} - E$. Squaring Eq. (29), applying the trigonometric identity $\cos^2\psi = 1 - \sin^2\psi$, and then substituting the result into the squared form of Eq. (30) yields:

$$G^2 \left(1 - \left(\frac{C - B \cos \phi}{A \sin \phi} \right)^2 \right) \sin^2 \phi = (H + I \cos \phi)^2. \quad (31)$$

Further manipulation of Eq. (31), application of the trigonometric identity $\sin^2 \phi = 1 - \cos^2 \phi$ and letting $x = \cos \phi$ yields the final form of the equation:

$$Wx^2 + Yx + Z = 0 \quad (32)$$

where:

$$W = (FB - EA)^2 + G^2 A^2 + G^2 B^2, \quad (33)$$

$$Y = 2 \left((AD - FC)(FB - EA) - G^2 BC \right), \quad (34)$$

$$Z = (AD - FC)^2 + G^2 (C^2 - A^2). \quad (35)$$

The quadratic form of Eq. (32) means the polar angle of the recoil electron, ϕ , is given via:

$$\cos \phi = \frac{-Y \pm \sqrt{Y^2 - 4WZ}}{2W} \quad (36)$$

where either of the two solutions of $\cos \phi$ are possible if they satisfy the requirement that $|\cos \phi| \leq 1$. With a known value of polar angle, ϕ , the corresponding azimuthal angle, ψ , of the recoil electron can be determined by:

$$\cos \psi = \frac{C - B \cos \phi}{A \sin \phi}. \quad (37)$$

Treatment of the electromagnetic field potential of the atom's influence on the ejected Compton electron's kinetic energy and direction in the relativistic impulse approximation is a complicated issue. At present, G4LowEPComptonModel utilises two assumptions, the same as those applied by G4LivermoreComptonModel and G4PenelopeComptonModel, regarding the ejected Compton electron's kinetic energy and direction. First, the assumption is made that the kinetic energy of the Compton electron can be simplified to:

$$E_{CE} = \epsilon - \epsilon' - E_B \quad (38)$$

where E_{CE} is the kinetic energy of the Compton electron and E_B is the binding energy of the target electron [11]. Second, assuming that each atom is spherically symmetric, the influence of the electromagnetic field potential on the ejected Compton electron direction is assumed to be minimal.

2.2. An overview of G4LowEPComptonModel

The G4LowEPComptonModel class was developed using the guidelines outlined by the Geant4 Low Energy Electromagnetic Physics Working Group. An outline of the computational process of G4LowEPComptonModel is presented in Fig. 2. Previously developed computational algorithms from G4LivermoreComptonModel were used in the first three flowchart steps of the computation process of the G4LowEPComptonModel to sample several parameters:

1. Target atomic element in a composite material.
2. Photon scattering angle from the target element Klein-Nishina cross-section.
3. Shell and momentum of an electron in the target element.

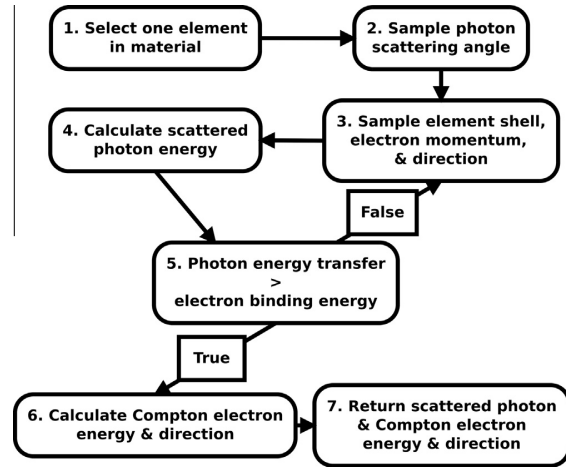


Fig. 2. Computational process of the G4LowEPComptonModel.

Step 4 (in Fig. 2) implements Eq. (11) in Section 2.1.2 to determine the energy of the scattered photon. The remaining processes of the G4LowEPComptonModel continue on to:

5. Check that the energy of the photon energy-momentum transfer exceeds the target electron binding energy.
6. Calculate the Compton electron energy and ejection direction in spherical coordinates using Eqs. (36) and (37).
7. Alter the energy and direction of the scattered photon, to those calculated in Step 4, and add the ejected Compton electron to the particle list of the event.

If the condition outlined in Step 5 has not been met, the computational process resets to Step 3 and an iteration flag is increased. As with G4LivermoreComptonModel, an upper limit of 1000 iterations has been set. In the event that the number of iterations for a single Compton scattering interaction exceeds this upper limit, the interaction is aborted and the photon's energy and direction are unchanged.

3. Comparison of the Monash University Compton scattering model to the two standard Compton scattering classes of Geant4 version 9.5

Carbon (C), copper (Cu) and lead (Pb) were selected to compare G4LowEPComptonModel to the two established Compton scattering classes of Geant4 version 9.5: G4LivermoreComptonModel, and G4PenelopeComptonModel. From here on these three classes will be referred to as Monash, Livermore and Penelope. The three materials were selected as they occupy the 2nd, 4th and 6th rows of the periodic table, sampling across the range of common terrestrial elements. A simulation geometry of a mono-energetic pencil beam of photons incident onto a slab of high density material was employed. Photon energies were simulated over an energy range of 10 keV to 10 MeV (see Table 1). Each simulation was run until 10 million Compton scattering events of the incident pencil beam were recorded. Analysis of these simulations has been split into two sections: scattered photon and ejected Compton electron kinetic energy spectra, and Compton electron

Table 1

Simulated photon energies over an energy range of 10 keV to 10 MeV for carbon (C), copper (Cu) and lead (Pb).

Material	Simulated photon energies (keV)
Carbon (C)	10, 25, 50, 75
	100, 250, 500, 750
	1000, 2500, 5000, 7500, 10,000
Copper (Cu)	50, 75,
	100, 250, 500, 750
Lead (Pb)	1000, 2500, 5000, 7500, 10,000
	125, 250, 500, 750
	1000, 2500, 5000, 7500, 10,000

directionality. Both sections utilised the Normalised Cross-Correlation Coefficient (NCCC) to assess the difference between classes. The NCCC is defined as:

$$\text{NCCC} = \frac{|\sum_{i=0}^n S_1(i)S_2(i)|}{\left[\sum_{i=0}^n (S_1(i)^2)\right]^{1/2} \left[\sum_{i=0}^n (S_2(i)^2)\right]^{1/2}} \quad (39)$$

where $S_1(i)$ and $S_2(i)$ represent the two n -dimensional arrays under comparison [30]. NCCC values of greater than 0.995, 0.999 and 1.0 indicate a fair, good and exact level of correlation between two n -dimensional arrays [30].

3.1. Scattered photon and ejected Compton electron energy spectra

The scattered photon (solid lines) and ejected Compton electron (dashed lines) energy spectra from each class for lowest energy and 1000 keV photon simulations of C, Cu and Pb targets can be seen in Figs. 3–5. For the lowest energy spectra, Figs. 3(a), 4(a) and 5(a), the scattered photon spectra contain two distinct “horns” and the Compton electron energy spectra resemble an exponential like drop off, from left to right, with a single “horn” on the right hand side. Embedded within the far right of the scattered photon spectra “horns” are a number of distinct steps. These steps are due to the atomic electron binding potential and that, in bound atomic electron Compton scattering, the energy transfer from the incident photon to a target electron must be greater than its binding energy. In the 1000 keV spectra, Figs. 3(b), 4(b) and 5(b), the aforementioned “horns” that were previously on the far right in the scattered photon spectra have become incorporated into a “step-like” edge and the Compton electron energy spectra have spread out with an additional distinct peak now present at the left hand side of each spectrum. These new left hand side peaks in the Compton electron energy spectra are also due to the impact of atomic electron binding potential. With the exception of the Penelope 10 keV scattered photon energy spectra for C, where a lower continuum between the two “horns” is present (Fig. 3(a)), all three classes display a high level of agreement with one another.

Fig. 6 contains the NCCC for the comparison of Monash vs Livermore, Monash vs Penelope and Livermore vs Penelope for the scattered photon (red markers) and Compton electron (blue markers) energy spectra. With the exception of incident photon energies below 50 keV in C, the NCCC of Livermore and Penelope indicates a fair to good level of correlation for both the scattered photon and Compton electron energy spectra. An identical result can be seen for the NCCC of Monash and Penelope scattered photon and Compton electron energy spectra. Finally, the NCCC of both the Monash and Livermore scattered photon and Compton electron energy spectra fall within the good level of correlation range for all tested energies and materials with the exception of incident photon energies below 50 keV in C.

All three classes have shown a fair to good level of correlation between scattered photon and Compton electron energy spectra with the exception of Penelope for photon energies below 50 keV

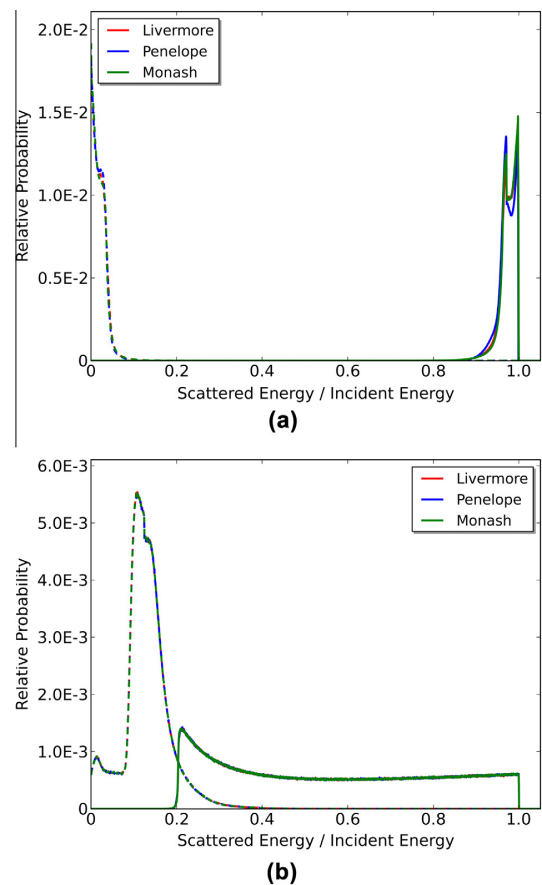


Fig. 3. Comparison of the scattered photon (solid lines) and Compton electron (dashed lines) energy spectra from 10 keV (a) and 1000 keV (b) photons scattering off carbon.

incident onto C. The observed good level of correlation between Monash and Livermore in comparison to Penelope is due to the different method applied for sampling the pre-collision momentum of atomic bound electrons. Both Monash and Livermore sample the pre-collision momentum of the bound atomic electron from interpolated Compton profiles calculated by Biggs et al. in 1975 [27,29]. Conversely, Penelope utilises the analytic Compton profiles outlined in [11].

3.2. Compton electron directionality

Figs. 7–9 contain the Compton electron polar (solid lines) and azimuthal (dashed lines) ejection angle distributions from each class for the lowest energy and 1000 keV photon simulations of C, Cu and Pb targets. The azimuthal angle with respect to the photon plane is displayed and the range of the relative probability has been constrained to maximise the resolution of features in the ejected Compton electron polar angle distributions. Inspection of the Compton electron polar and azimuthal angular distributions yields the following observations:

- Livermore’s and Penelope’s polar distributions are constrained to a region from 0 to $\pi/2$ radians.
- Monash’s polar angle distributions span 0 to π radians.

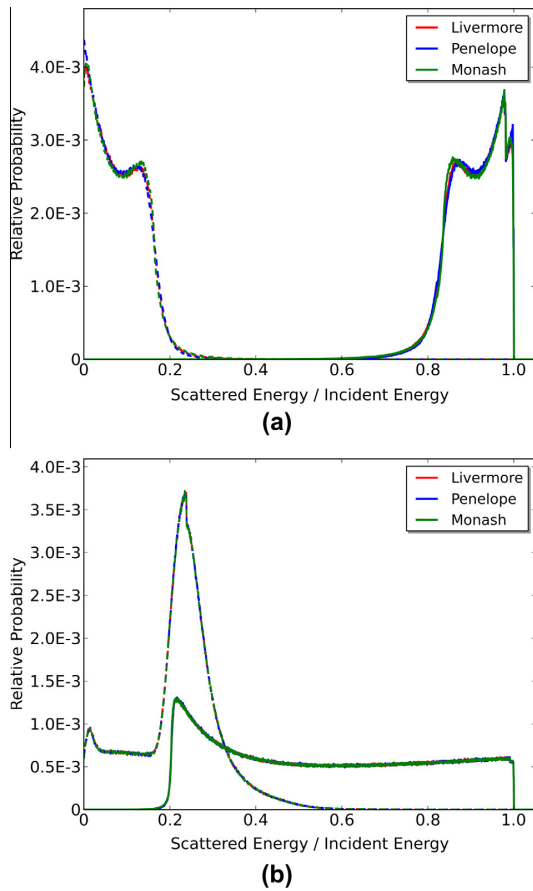


Fig. 4. Comparison of the scattered photon (solid lines) and Compton electron (dashed lines) energy spectra from 50 keV (a) and 1000 keV (b) photons scattering off copper.

- Livermore's and Penelope's azimuthal angle distributions are constrained at 0 radians.
- Monash's azimuthal angle distributions span 0 to $\pi/2$ radians.
- Monash's Compton electron ejection direction distribution becomes less forward focused with the increase of atomic number.
- Monash's Compton electron ejection direction distribution becomes more forward focused with the increase of incident photon energy.
- Livermore and Penelope's polar and azimuthal angle distributions display a high level of agreement, with the exception of Figs. 7(a), 9(a) and 9(b),
- At higher incident photon energies Monash's Compton electron ejection direction distributions approach those of Livermore and Penelope.

Livermore and Penelope utilise different methods to estimate the ejection direction of the Compton electron (see Section 1). The observed difference between Livermore's and Penelope's polar angle distributions is due to the performance of the free-electron approximation in a bound electron scattering system. This approximation leads to incorrect estimates of the Compton electron polar ejection angle and artefacts such as the Pb K-shell peak seen between 0.4 and 0.5 radians in Fig. 9(b). Penelope avoids artefacts

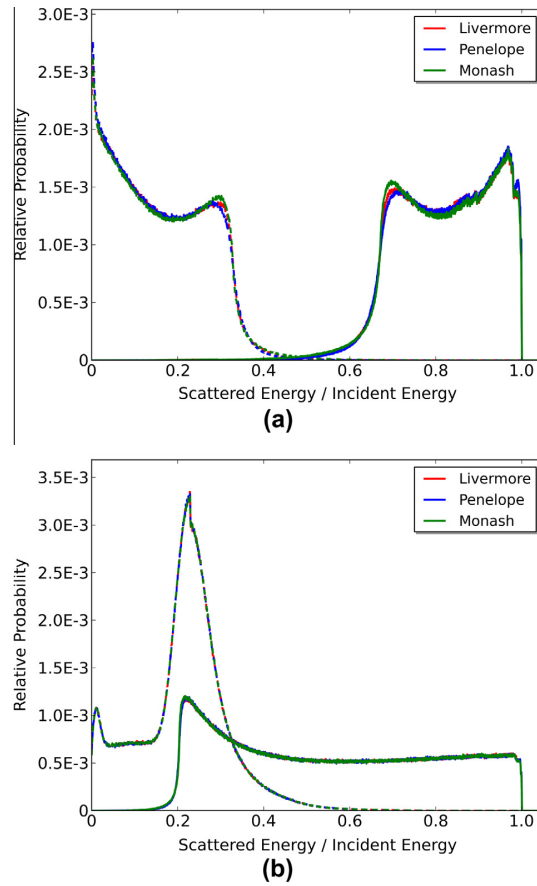


Fig. 5. Comparison of the scattered photon (solid lines) and Compton electron (dashed lines) energy spectra from 125 keV (a) and 1000 keV (b) photons scattering off lead.

due to electron binding effects as it assumes that the Compton electron is emitted in the direction of the photon's momentum transfer vector [11,12]. However, both approaches are restricted adaptations of Ribberfors' Compton scattering framework as they then limit the ejected direction of the Compton electron to the photon plane.

The relationship of the incident photon energy and atomic number on Monash's Compton electron ejection direction distribution is analogous to the influence of electron pre-collision momentum on the energy broadening (Doppler broadening) of the scattered photon. Both of these phenomena are due to the interaction of the pre-collision momentum of the electron and momentum transfer of the photon. In the case of Doppler broadening, the energy broadening of the scattered photon for a set photon scattering angle is due to the projection of the pre-collision momentum vector of the electron onto the photon scattering vector [8]. In the case of the Compton electron ejection direction distribution, the narrowing or broadening of the distribution is due to the addition of the electron pre-collision momentum component, perpendicular to the photon plane, to the photon momentum transfer vector.

Quantification of the differences in polar (red markers) and azimuthal (blue markers) ejection angle distributions between Monash and Geant4's two standard Compton scattering classes, for the tested energies and elements outlined in Table 1, was

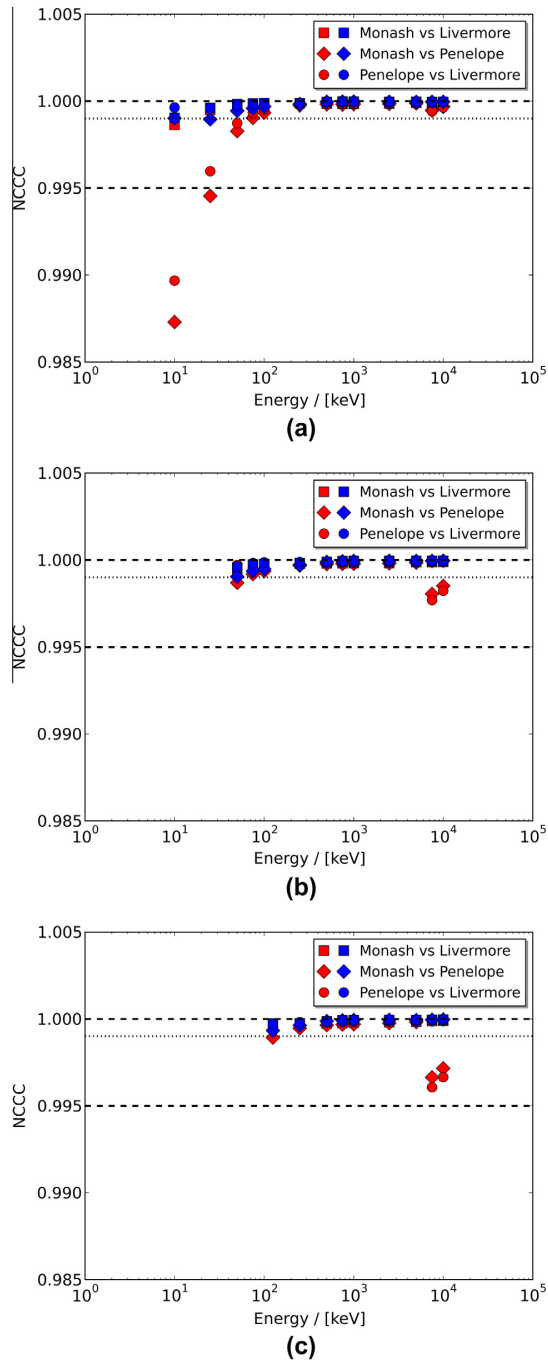


Fig. 6. NCCC of the scattered photon (red markers) and Compton electron (blue markers) energy spectra across the tested energy range between all three classes for carbon (a), copper (b) and lead (c). The dashed and dotted black lines represent the fair and good level of correlation ranges respectively. (For interpretation of the references to colour in this figure caption, the reader is referred to the web version of this article.)

undertaken using the NCCC. Fig. 10 contains the NCCC for the comparison of Monash vs Livermore, Monash vs Penelope and Livermore vs Penelope for the polar and azimuthal ejection angle

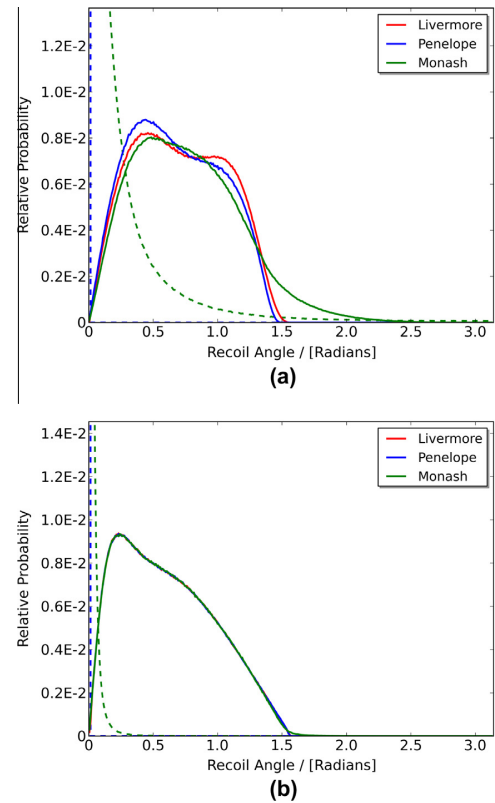


Fig. 7. Comparison of the polar (solid lines) and azimuthal (dashed lines) ejection angle distributions from 10 keV (a) and 1000 keV (b) photons scattering off carbon.

distributions. Inspection of Fig. 10 supports the previous observations from Figs. 7–9. As the incident photon energy increases for all three tested elements, the polar angle distribution of Monash approaches those of Livermore and Penelope. Also, as the atomic number of the target element increases, the NCCC of Monash and the two standard Geant4 Compton scattering classes' azimuthal angle distributions decreases. However, over the tested energy range for each material, the NCCC of azimuthal angular distributions between Monash and the two standard Geant4 Compton scattering classes does not approach unity.

4. Comparison of the Monash University Compton scattering model with experiment data

Comparison of the Monash Compton scattering model with experiment data was undertaken against TDCS measurements by Ljubičić et al. [22]. Ljubičić et al. utilised a triple coincidence experiment, see Fig. 11, to measure the K-shell TDCS Compton electron kinetic energy spectra of gold for two unique scattered photon and ejected Compton electron angle combinations. The experiment was constructed of two NaI(Tl) scintillators, a Si(Li) semiconductor detector, a highly collimated 662 keV ^{57}Co photon beam and a 2 cm by 2 cm 5 mg/cm² gold foil, D1 and D2, D3, S, and T respectively in Fig. 11. The two NaI(Tl) scintillator detectors, D1 and D2, act as the scattered photon and K-shell X-ray fluorescence detectors respectively. D1 was operated in spectroscopic mode with a Full Width at Half Maximum (FWHM) energy resolution of 7% at 662 keV and D2 was operated in counting mode. The Si(Li) semiconductor detector, D3 in Fig. 11, was used to determine the kinetic energy

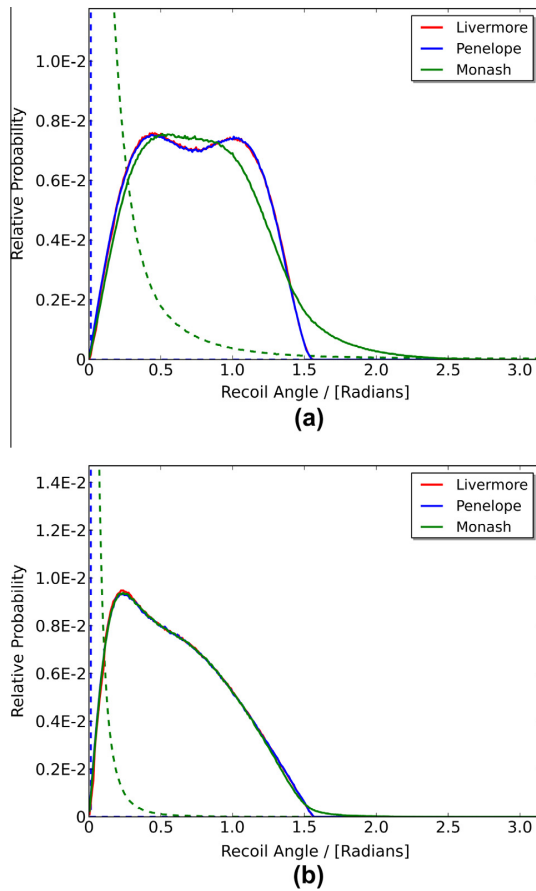


Fig. 8. Comparison of the polar (solid lines) and azimuthal (dashed lines) ejection angle distributions from 50 keV (a) and 1000 keV (b) photons scattering off copper.

of the ejected Compton electron. The spectral binning of D3 was set to the effective FWHM energy resolution of 20 keV. The two-dimensional spectral data from D1 and D3, measured within a coincidence timing window of 40 ns, was filtered utilising a 160 keV window centred around $E_{CE} + \epsilon' = \epsilon - E_{BK}$, where E_{BK} is the K-shell electron binding energy of gold.

A Geant4 simulation of a beam of 1×10^{12} 662 keV photons incident on a 1.0 mm thick gold plate ($\rho = 19.3 \text{ g/cm}^3$) was constructed to emulate the triple coincidence experiment in Fig. 11. For each 662 keV photon K-shell Compton scattering event, the scattered photon and ejected Compton electron angles and energies were recorded. This data was run through a system response algorithm which accounted for the detector energy blurring and angular measurement uncertainties outlined in [22]. TDCS Compton electron kinetic energy spectra were generated from the filtered data to match the two scattering situations [22], where $\theta = 90^\circ, \phi = 24^\circ, \psi = 180^\circ$, and $\theta = 60^\circ, \phi = 37^\circ, \psi = 180^\circ$, and is shown in comparison to the experimental data in Fig. 12.

Fig. 12(a) contains a comparison between the simulated and experimental TDCS data for the scattering situation where $\theta = 90^\circ, \phi = 24^\circ$ and $\psi = 180^\circ$. These two spectra each contain a single photopeak at around 290 keV and show a high level of agreement below 350 keV. The difference between these two spectra above 350 keV can be attributed to a combination of multiple scattered photo and Compton electrons within the gold foil and detector casing into D3, contributing to false coincidence events, that could

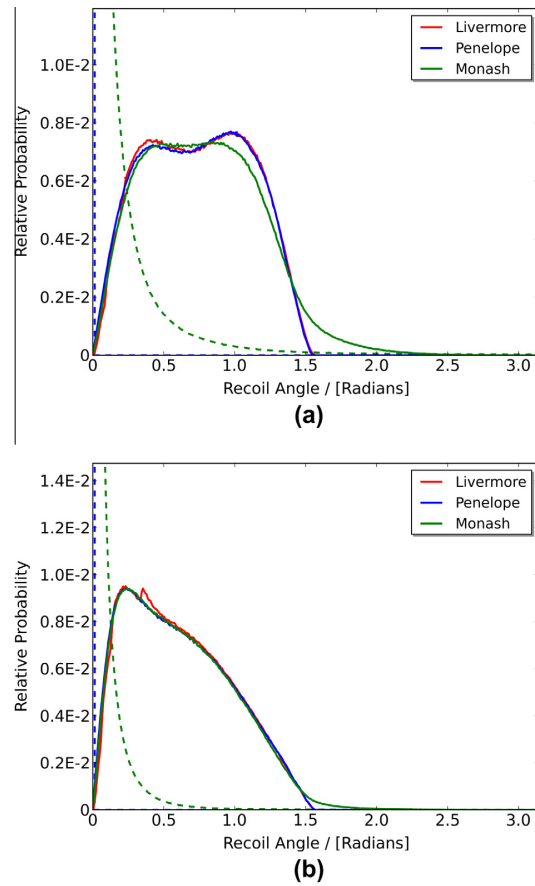


Fig. 9. Comparison of the polar (solid lines) and azimuthal (dashed lines) ejection angle distributions from 125 keV (a) and 1000 keV (b) photons scattering off lead.

not be corrected for in Ljubičić et al. [22]. Fig. 12(b) shows the data for the scattering situation where $\theta = 60^\circ, \phi = 37^\circ$ and $\psi = 180^\circ$. Out of the two sets of spectra only the Monash spectra possess a clear photopeak, centred at 180.5 keV, resulting in a minimal level of agreement between the two. The high level of statistical fluctuation observed in the experimental spectra was attributed to the methodology employed to compensate for the multiple scattering of photo and Compton electrons [22]. As a result, drawing a direct comparison between the experimental data and the Monash University Compton scattering model for this specific scattering situation is not statistically significant.

Further examination of Fig. 12(b) shows that the maximum cross-section is present at 230 keV and 180.5 keV for the experimental and Monash spectra respectively. In this specific scattering situation, where $\theta = 60^\circ$, a free-electron Compton scattering framework [1] (after the subtraction of the K-shell binding energy of gold) predicts that the ejected Compton electron would have a kinetic energy of 179.5 keV indicated by the vertical dashed black line in Fig. 12(b). While the Monash spectra's maximum cross-section corresponds to this value within 1 keV, a difference of 50 keV is present with respect to the experimental spectrum. The spike observed at 170 keV in the experimental cross-section data, which is within one spectral bin width to the predicted Compton electron ejection energy (20 keV), gives rise to the notion that the observed counts above 200 keV are solely due to the combination of multiple scattering of photo and Compton electrons within the gold foil and

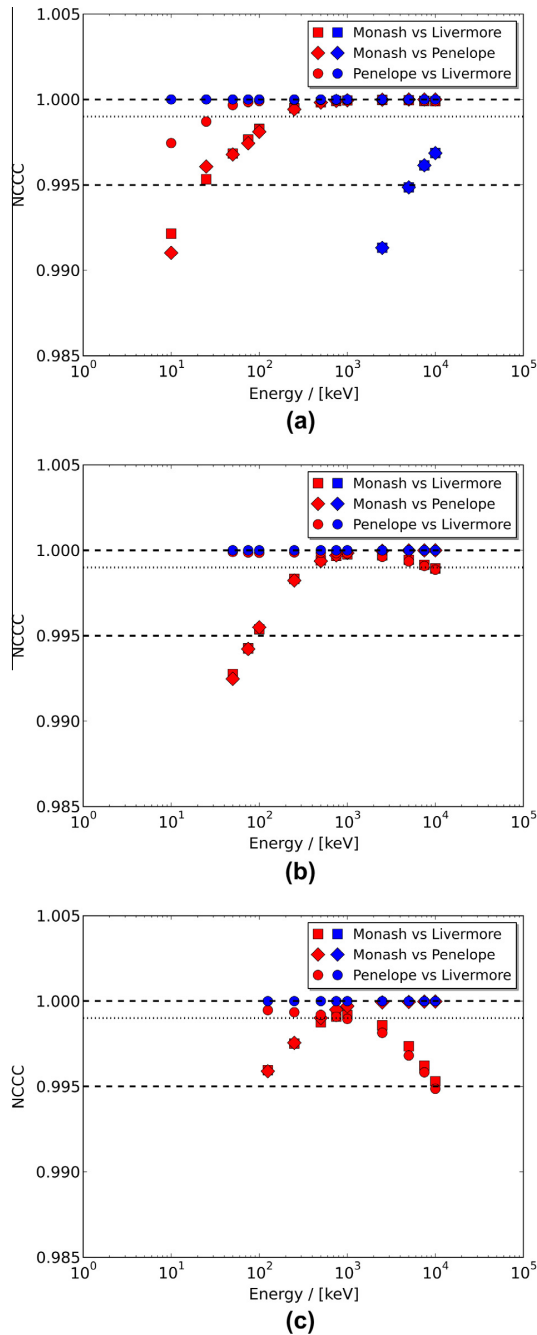


Fig. 10. NCCC of the polar (red markers) and azimuthal (blue markers) ejection angle distributions across the tested energy range between all three classes for carbon (a), copper (b) and lead (c). The dashed and dotted black lines represent the fair and good level of correlation ranges respectively. (For interpretation of the references to colour in this figure caption, the reader is referred to the web version of this article.)

detector casing into D3. However, due to the significant experimental uncertainties [17,22], the resultant spectra in Fig. 12 from the Monash University Compton scattering model simulations are consistent with the experimental data.

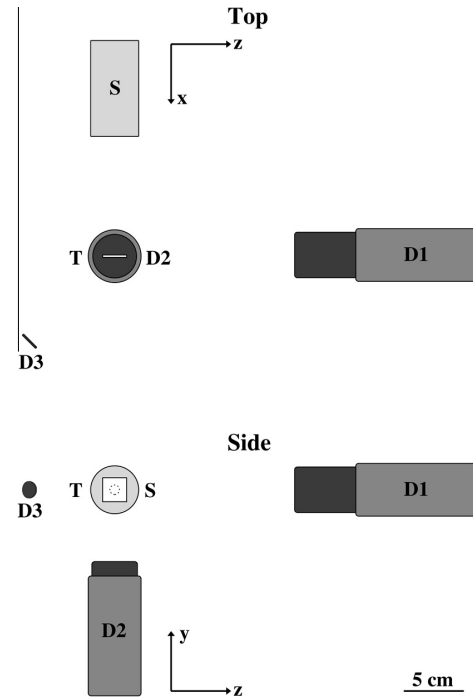


Fig. 11. A schematic of the triple coincidence experiment utilised by Ljubičić et al. to measure the K-shell Compton scattering TDCS of 662 keV photons off of gold [22].

5. Discussion

A comparison of the Monash University Compton scattering model was undertaken with respect to adapted computational versions of Ribberfors' Compton scattering model. Over an energy range of 10 to 10000 keV for three elements, C, Cu and Pb, Monash was compared to the two standard Compton scattering classes of Geant4 version 9.5, Livermore and Penelope, that have been adapted from the photon scattering algorithms of Ribberfors' framework [11,12,29]. Section 3 illustrated a fair to good level of correlation between the photon scattering algorithms of all three Compton scattering classes. All three classes also displayed a fair to excellent level of correlation between Compton electron kinetic energy distributions for all three elements for incident photon energies above 25 keV. This was not the case for the polar and azimuthal angle distributions of the ejected Compton electron. As the incident energy of the photon increased, the difference between the polar and azimuthal angle distributions of the ejected Compton electron of Monash in comparison to Livermore and Penelope decreased. However, neither the polar or azimuthal angle distribution NCCCs approach a value indicating even a fair level of correlation over the tested energy range.

The difference seen in Section 3 between the Compton electron algorithms of Monash in comparison to Livermore and Penelope was not unexpected. The Monash scattering model was developed to avoid the limitations of computational Compton scattering models adapted from Ribberfors' framework in simulating the ejection direction of the Compton electron. An example of how ensuring the conservation of energy and momentum in the relativistic impulse approximation can affect the simulation of Compton scattering can be seen in Fig. 13. This figure contains the two-dimensional log intensity histograms of ejected Compton electron angles for Pb at 125 keV of all three classes. Here, the Livermore (Fig. 13(b))

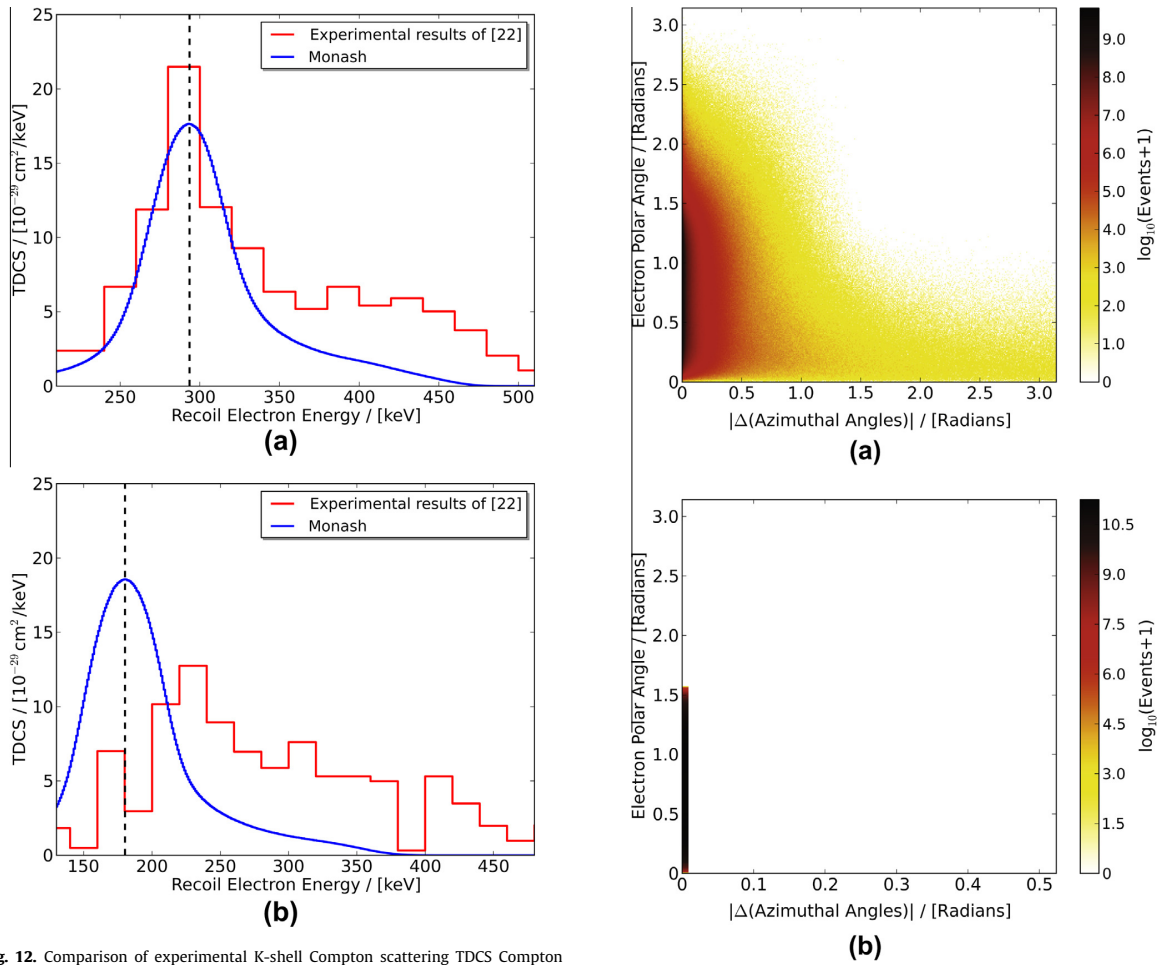


Fig. 12. Comparison of experimental K-shell Compton scattering TDCS Compton electron kinetic energy spectra to simulations undertaken utilising the Monash Compton scattering model. The two sets of spectra present the specific Compton scattering situations where $\theta = 90^\circ, \phi = 24^\circ, \psi = 180^\circ$, (a), and $\theta = 60^\circ, \phi = 37^\circ, \psi = 180^\circ$, (b). A vertical dashed black line can be seen in each set of spectra that indicates the predicted ejected Compton electron kinetic energy from the free-electron Compton scattering framework [1].

and Penelope (Fig. 13(c)) Compton electron ejection angle distributions are constrained to a slither along an azimuthal angle of 0 radians. The results reported in Section 3 showed that this trend was constant regardless of target material or incident photon energy. Inspection of Monash's Compton electron ejection angle distribution (Fig. 13(a)) shows that the ejection direction of the Compton electron is not constrained to an azimuthal ejection angle of 0 radians, but is distributed through a range of 0 to $\pi/2$ radians. Section 3 reported that the distribution of the azimuthal ejection angle of the Compton electron was dependent on the atomic number of the target atom and incident photon energy.

As stated in Section 4, the Monash University Compton scattering model is consistent with the experimental data from Ljubičić et al. within experimental uncertainty [17,22]. This same experimental data set was utilised by Kaliman et al. [17] to explore the accuracy of one of the most promising Compton scattering models,

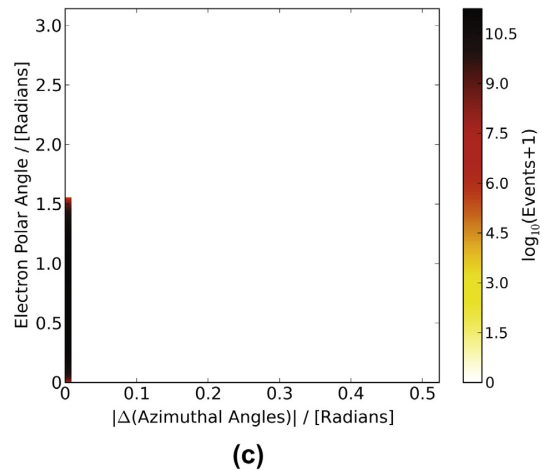


Fig. 13. The Monash (a), Livermore (b) and Penelope (c) model two-dimensional log intensity histograms of the ejected Compton electron angles for Pb at 125 keV.

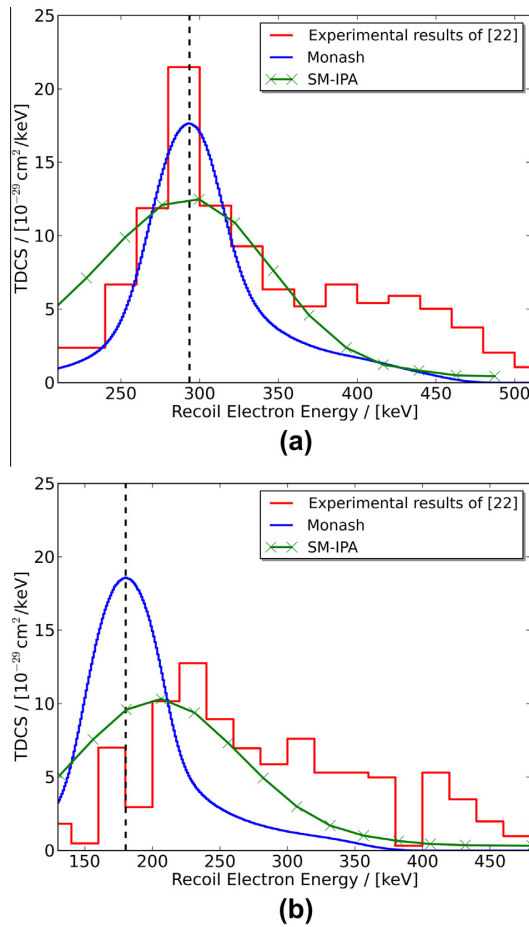


Fig. 14. Comparison of the Monash Compton scattering model and Kaliman et al. [17] full relativistic second-order S-matrix QED IPA (SM-IPA) with respect to experimental K-shell Compton scattering TDCS Compton electron kinetic energy spectra for 662 keV photons in gold. The two sets of spectra present the specific Compton scattering situations where $\theta = 90^\circ, \phi = 24^\circ, \psi = 180^\circ$, (a), and $\theta = 60^\circ, \phi = 37^\circ, \psi = 180^\circ$, (b). A vertical black can be seen in each set of spectra that indicates the predicted ejected Compton electron kinetic energy from the free-electron Compton scattering framework [1].

their full relativistic second-order S-matrix QED IPA TDCS model, for K-shell scattering [17]. Fig. 14 contains a comparison of the Monash Compton scattering model and Kaliman et al.'s full relativistic second-order S-matrix QED IPA (SM-IPA) with respect to experimental data from Ljubičić et al. Inspection of these two data sets shows that for Fig. 14(a) the Monash model more accurately reproduces the measured experimental spectra, while in Fig. 14(b) it is the SM-IPA model that appears more accurate. Further support for the Monash Compton scattering model is that in each case the maximum cross-section of its spectrum falls within 1 keV of the free-electron Compton scattering frameworks predicted Compton electron ejection energy. A noticeable difference between these values, indicated by a vertical dashed black line in each spectrum, and the maximum cross-section of the SM-IPA model is present in both sets of spectra. This difference is also present in Fig. 7 of Kaliman et al. [17] from which the spectral data was extracted. However, for each of these two data sets, both models

are consistent with the experimental data within uncertainty [17,22].

The increased complexity of the G4LowEPComptonModel class resulted in an inverse relationship between atomic number and average CPU time per event. An increase in average CPU time per event was observed which varied from 0% to 10% over the range of simulated photon energies for each material. An approximate 5% increase in simulation time was also observed in the first implementation of the Livermore Compton scattering model (G4LECS) in comparison to the standard Compton scattering models of Geant4 at the time of publication [29]. As in [29], this level of reduction in simulation efficiency can be argued to be worth the increase in overall accuracy for the simulation of low energy photon transport.

As of version 9.6 (released November 2012), the Monash University Compton scattering model, G4LowEPComptonModel, became part of the Geant4 Monte Carlo radiation transport toolkit. Over the next few years additional improvements to G4LowEP-ComptonModel are planned:

- The addition of photon polarisation through the inclusion of existing Geant4 algorithms.
- Updating Biggs' electron momentum density functions and Compton profiles using Dirac–Hartree–Fock wavefunctions from GRASP2K [31,32].
- The development of algorithms to model the influence of the atomic electromagnetic field potential in the relativistic impulse approximation.

Further experimental validation of both the photon and Compton electron energy and angular distributions as a function of incident photon energy and target material is also planned utilising a similar design to Ljubičić et al. [22] and Bell et al. [33].

6. Conclusion

A Geant4 low energy electromagnetic physics class, G4LowEP-ComptonModel, was developed and compared to the two established Compton scattering classes of Geant4 version 9.5: G4LivermoreComptonModel, and G4PenelopeComptonModel. The Monash scattering model was developed using a theoretical foundation that ensured the conservation of energy and momentum in the relativistic impulse approximation to avoid relying on approximations employed by the two Geant4 established Compton scattering classes utilised in modelling the ejection direction of the Compton electron. Comparison of the scattered photon energy distributions of all three Compton scattering models has shown a fair to good level of correlation over the tested energy range for the three selected elements: carbon, copper and lead. In addition, a fair to good level of correlation was also observed between the Compton electron energy spectra of all three classes for energies > 50 keV. As expected, a difference was observed between the polar and azimuthal ejection angle distributions of G4LowEPComptonModel in comparison to the two established Compton scattering classes of Geant4 version 9.5 due to the breakdown of both Geant4 classes Compton electron ejection direction algorithms below 10 MeV. Further improvements to the Monash University Compton scattering model and G4LowEPComptonModel, with rigorous experimental validation, are currently underway.

The Monash University Compton scattering model was:

- Shown to be a viable alternative to those computational models adapted from Ribberfors' Compton scattering framework.
- Experimentally consistent with the triply differential Compton scattering cross-section data presented in Ljubičić et al. [22].

Acknowledgements

The authors are grateful to Dr. S. Incerti of CNRS/IN2P3/CENBG, Bordeaux, France, and Professor V. Ivantchenko of M.V. Lomonosov Moscow State University, Moscow, Russia for their discussion and guidance in the adaption of the Monash Compton scattering model into the Geant4 low-energy electromagnetic class G4LowEPComptonModel. The authors would also like to acknowledge Dr. G. Ruben of CSIRO, Melbourne, Australia for his helpful comments and suggestions. J. E. Gillam was supported by a CSIC 'Juan de la Cierva' program. This work was supported by the Multi-modal Australian ScienceS Imaging and Visualisation Environment (MAS-SIVE) (www.massive.org.au).

References

- [1] A.H. Compton, *Phys. Rev.* 21 (1923) 483–502.
- [2] S.E. Boggs et al., *Astron. Astrophys. Suppl. Ser.* 145 (2000) 311–321.
- [3] A. Zoglauer et al., *Proc. SPIE* 4851 (2003) 1302–1309.
- [4] A. Akyüz et al., *New Astron.* 9 (2004) 127–135.
- [5] D.W. Wilson et al., *IEEE Trans. Med. Imaging* 19 (2000) 412–422.
- [6] M.R. Dimmock et al., *Nucl. Instrum. Methods Phys. Res. A* 612 (2009) 133–137.
- [7] C.V. Nguyen et al., *IEEE Trans. Nucl. Sci.* 58 (2011) 639–650.
- [8] R. Ribberfors, *Phys. Rev. B* 12 (1975) 2067–2074.
- [9] Y. Namito et al., *Nucl. Instrum. Methods Phys. Res. A* 349 (1994) 489–494.
- [10] D.E. Cullen et al., *Nucl. Instrum. Methods Phys. Res. B* 101 (1995) 499–510.
- [11] D. Brusa et al., *Nucl. Instrum. Methods Phys. Res. A* 379 (1996) 167–175.
- [12] F. Salvat, et al., *Proc. of a Workshop/Training Course*, OECD/NEA 5–7, Nov. 2001.
- [13] S. Agostinelli et al., *Nucl. Instrum. Methods Phys. Res. A* 506 (2003) 250–303.
- [14] J. Allison et al., *IEEE Trans. Nucl. Sci.* 53 (2006) 270–278.
- [15] F. Longo, et al., *IEEE Nucl. Sci. Symp. Conf. Rec.* N41–2, 2008.
- [16] P.M. Bergstrom Jr et al., *Phys. Rev. A* 48 (1993) 1134–1162.
- [17] Z. Kaliman et al., *Phys. Rev. A* 57 (1998) 2683–2691.
- [18] R.H. Pratt et al., *Nucl. Instrum. Methods Phys. Res. B* 261 (2007) 175–179.
- [19] V. Florescu et al., *Phys. Rev. A* 80 (2009) 033421.
- [20] L.A. Lajohn, *Phys. Rev. A* 81 (2010) 043404.
- [21] R.H. Pratt et al., *Radiat. Phys. Chem.* 79 (2010) 124–131.
- [22] A. Ljubičić, et al., *Proc. 1967 Symp. on Nucl. Beta Decay and Weak Interactions Zagreb (Yugoslavia)*, 285–293, 1969.
- [23] J.M.C. Brown, et al., *IEEE NSS MIC Symp. Record*, 1385–1389, 2011.
- [24] W. Rindler, *Introduction to Special Relativity*, 2nd Ed., Oxford Univ. Press, Oxford UK, 1991.
- [25] J.W.M. Du Mond, *Phys. Rev.* 33 (1929) 643–658.
- [26] O. Klein, Y. Nishina, *Z. Phys.* 52 (1929) 853–869.
- [27] F. Biggs et al., *At. Data Nucl. Data Tables* 16 (1975) 201–309.
- [28] A.P. Lightman et al., *Problem Book in Relativity and Gravitation*, Princeton University Press, Princeton, New Jersey USA, 1975.
- [29] R.M. Kippen, *New Astron. Rev.* 48 (2004) 221–225.
- [30] J. Hernández-Andrés et al., *J. Opt. Soc. Am. A* 18 (2001) 412–420.
- [31] P. Jönsson et al., *Comput. Phys. Commun.* 177 (2007) 597–622.
- [32] I.P. Grant, *Relativistic Quantum Theory of Atoms and Molecules*, Springer Science, Oxford UK, 2007.
- [33] F. Bell et al., *J. Phys. B: At. Mol. Opt. Phys.* 24 (1991) L533–L538.

Part II

Development of a Hybrid Single Photon Emission Imaging System

A Pixelated Emission Detector for RadiOisotopes (PEDRO)

A Pixelated Emission Detector for RadiOisotopes (PEDRO)

M. R. Dimmock, J. E. Gillam, T. E. Beveridge, J. M. C. Brown, R. A. Lewis and C. J. Hall

Published in Nuclear Instruments and Methods in Physics Research A, Volume 612, Pages 133–137, 2009

DOI: 10.1016/j.nima.2009.10.050

Reproduced here with kind permission from Elsevier Inc.

Declaration for Thesis Chapter 4

Declaration by candidate

In the case of Chapter 4, the nature and extent of my contribution to the work was the following:

Nature of Contribution	Extent of Contribution (%)
Co-developed the Geant4 application, assisted with simulations and analysis, and proofread the paper	20 %

The following co-authors contributed to the work. If co-authors are students at Monash University, the extent of their contribution in percentage terms is stated:

Name	Nature of Contribution	Extent of Contribution (%)
M. R. Dimmock	Lead development of the Geant4 application, coordinated the simulations and analysis, and wrote up the paper	
J. E. Gillam	Co-developed the Geant4 application, assisted with simulations and analysis, and proofread the paper	
T. E. Beveridge	Co-developed the Geant4 application and proofread the paper	
R. A. Lewis	Aided proofreading and drafting	
C. J. Hall	Provided supervisory advice, aided proofreading and drafting	

The undersigned hereby certify that the above declaration correctly reflects the nature and extent of the candidate's and co-authors' contributions to this work.

Candidate's Signature:

Date: / /

Project Leader's Signature:

Date: / /

Main Supervisor's Signature:

Date: / /



Contents lists available at ScienceDirect

Nuclear Instruments and Methods in Physics Research A

journal homepage: www.elsevier.com/locate/nima

A Pixelated Emission Detector for RadiOisotopes (PEDRO)

M.R. Dimmock^{a,b,*}, J.E. Gillam^{a,b,*}, T.E. Beveridge^{a,b}, J.M.C. Brown^{a,b}, R.A. Lewis^{a,b}, C.J. Hall^{a,b}^a School of Physics, Bldg. 19, Monash University, Victoria 3800, Australia^b Monash Center for Synchrotron Science, Bldg. 220, Monash University, Victoria 3800, Australia

ARTICLE INFO

Article history:

Received 15 May 2009
 Received in revised form
 9 September 2009
 Accepted 6 October 2009
 Available online 17 October 2009

Keywords:

Compton camera
 PEDRO
 SPECT

ABSTRACT

The Pixelated Emission Detector for RadiOisotopes (PEDRO) is a hybrid imager designed for the measurement of single photon emission from small animals. The proof-of-principle device currently under development consists of a Compton-camera situated behind a mechanical modulator. The combination of mechanical and electronic (hybrid) collimation should provide optimal detection characteristics over a broad spectral range ($30 \text{ keV} \leq E_\gamma \leq 511 \text{ keV}$), through a reduction in the sensitivity-resolution trade-off, inherent in conventional mechanically collimated configurations.

This paper presents GEANT4 simulation results from the PEDRO geometry operated only as a Compton camera in order to gauge its advantage when used in concert with mechanical collimation—regardless of the collimation pattern. The optimization of multiple detector spacing and resolution parameters is performed utilizing the Median Distance of Closest Approach (MDCA) and has been shown to result in an optimum distance, beyond which only a loss in sensitivity occurs.

© 2009 Elsevier B.V. All rights reserved.

1. Introduction

Single Photon Emission Imaging (SPEI) of small animal models [1] requires a detector configuration that provides both high spatial resolution and high sensitivity to emitted radiation in order to optimize the signal to noise ratio in the reconstructed image. However, the trade-off between spatial resolution and measurement statistics inherent in techniques such as pinhole imaging [2] renders the optimization of the design a difficult task. In an attempt to decouple this relationship, a number of novel detection schemes have been developed:

- Multiplexing and coded-aperture measurement [3,4].
- Synthetic collimation [5].
- Compton-kinematic imaging [6].

Systems which employ such approaches to collimation have been shown to improve the quality of the resulting image. Multiplexing collimation can provide enhanced sensitivity without affecting the resolution, particularly at photon energies $\leq 50 \text{ keV}$. Also at these low energies, a multi-resolution detector has been shown to allow implementation of the synthetic collimator approach [7], enhancing the reconstruction. Compton collimation allows increased sensitivity at high energies ($E_\gamma \geq 400 \text{ keV}$) as well as a greater degree of multi-energy imaging [8]. Simulations

investigating the combination of more than one of these methods show that further gains may also be achievable [9,10], however, these techniques are yet to be validated by experiment.

The Pixelated Emission Detector for RadiOisotopes (PEDRO) is a proof of principle hybrid imager being developed to investigate the combination of mechanical and electronic (hybrid) collimation for incident gamma rays in the energy range $30 \text{ keV} \leq E_\gamma \leq 511 \text{ keV}$. It consists of an interchangeable aperture array in front of a stack of Silicon (Si) detectors and a Cadmium Telluride (CdTe) detector. The aperture array has been designed to accommodate pinholes, slats or open-areas, as the optimal mechanical modulation for hybrid imaging between the above spectral extents is unclear.

The ability to maximize the system sensitivity at no loss to resolution will require the use of data for which each photon has interacted multiple times in the active detection volume. The response to such measurement is a cone-surface, the information from which is combined with that of the mechanical collimator for image reconstruction. Collimators with large open fractions (such as a slat collimator) will serve to truncate the cone-surface response of the Compton camera, while for smaller open-fraction collimators (such as multi-pinhole systems) the cone-surface will reduce the open area through which the photon must have passed. In either case, the use of Compton information reflects the sensitivity increase while the mechanical collimator governs the system resolution [11].

This investigation utilized a parallelized Geant4 Monte Carlo model [12] to investigate the detector stack as a Compton imager, by measuring the median spatial accuracy of the Compton

* Corresponding authors at: School of Physics, Bldg. 19, Monash University, Victoria 3800, Australia. Tel.: +61 3 9902 9757; fax: +61 3 9902 9817.

E-mail address: dimmock@physics.monash.edu.au (M.R. Dimmock).

cone-surface response at a specific location. The result is a measure of both the resolving power and aperture de-multiplexing capacity of Compton information applied to an aperture array such as a multi-pinhole collimator placed at this location.

When a gamma ray of incident energy (E_0) Compton scatters, the measured angle of scatter (θ_M) can be calculated from

$$\cos(\theta_M) = 1 + mc^2 \left(\frac{1}{E_0} - \frac{1}{E_0 - E_S} \right) \quad (1)$$

where mc^2 is the rest mass of the electron and E_S is the kinetic energy of the recoil electron in the scatter detector. The effect of the angular uncertainty, the difference between the True scatter angle (θ_T) and θ_M , can be quantified at the source location by a Cartesian distance function. This Distance of Closest Approach (DCA) [13] is independent of any image processing algorithm and given as

$$DCA = \|\mathbf{s} - \mathbf{p}\| \cdot \sin(\theta_T - \theta_M) \quad (2)$$

where $\mathbf{s} - \mathbf{p}$ is the vector between the scatter (\mathbf{s}) and source (\mathbf{p}) locations

In order to quantify the distance functions for different geometries, the DCA is calculated on a per event basis and a histogram is produced for each PEDRO configuration. As the DCA may be non-Gaussian, especially when dominated by Doppler broadening, the standard deviation is inappropriate as a measure of distribution width. Instead, the median of the DCA (MDCA) was calculated. As well as enabling inter-comparison of the different geometries, the MDCA can be used as an estimate of the ability to perform aperture de-multiplexing, as it is the distance within which 50% of the data is guaranteed to lie.

2. Detector model and simulation

The simulation of a Si scattering element and CdTe absorber has recently been shown to yield good results as a dual head Compton camera [14] for 140 keV incident gamma rays. The Compton cross-section for Si makes it an ideal scattering material [15]. The ratio of the Compton to total interaction is 94% at 140 keV and 99.7% at 511 keV. Between 1 and 17 mm of Si are required for optimal scattering at these respective energies. As the current operational thickness of each individual wafer is limited to approximately 2.0 mm [16], a modular stack of Si detectors must be utilized. While thick Si increases the interaction probability, the parallax error, governed by the depth of interaction resolution, also increases.

A Geant4 model has been developed that allows the user to optimize a modular detector geometry that consists of a number of Si Double Sided Strip Detectors (Si-DSSDs) and a pixelated CdTe detector. The free parameters include the strip widths, thicknesses and relative positioning of the Si-DSSDs and the pixelation and thickness of the CdTe. The source distribution, source energy and incident flux are similarly changeable. A variable multi-aperture array has also been included in the model. A schematic of this geometry including five Si-DSSD wafers is shown in Fig. 1. The centers along the x axis of the source (P), collimator (C), Si scatterers ($S_1 - S_5$) and CdTe absorber (A) are indicated by the broken lines.

In the model the timestamp, energy and position information generated from each interaction are stored in the hit collection (one for each detector component) for post processing. To simulate pixelation, the model bins the locations of each interaction stored in the hit collections to a user defined pixel size (in the y/z plane of Fig. 1) and half-thickness location (x in Fig. 1). The combined hit collection is then analyzed to determine if multiple interactions occurred within a single pixel. If this has

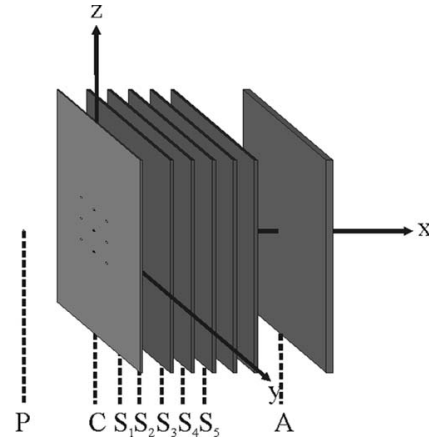


Fig. 1. A schematic representation of the PEDRO detector configuration described in the Geant4 simulation.

occurred, the energy deposited is summed and one of the hits removed. The energy can be determined with or without Doppler broadening and noise from the electronics response function can also be applied to the perfect measurements.

3. Preliminary simulation results

In this investigation, the open parameters of the experimental PEDRO as a Compton camera have been explored (the collimator was made transparent) to assess its advantage when used in concert with mechanical collimation—regardless of the collimation pattern. The dimensions of each of the Si-DSSDs were fixed at $60 \times 60 \times 0.25 \text{ mm}^3$ with 0.2 mm strip pitch. This allowed the detector spacing and energy resolution effects to be investigated without the MDCA being dominated by the position resolution. The CdTe back detector was modelled as a $60 \times 60 \times 2.0 \text{ mm}^3$ volume, with 0.2 mm pixelation. The source simulated was an isotropic, non-attenuating, 140 keV gamma-ray emitter (^{99m}Tc) placed 50.0 mm from the front of the first Si wafer ($S_1 - (T_S/2) - P = 50.0 \text{ mm}$, where T_S is the Si thickness). For each simulation, 1.5×10^8 photons were tracked. If the combined hits collection from an event was ≥ 2 , the cone surface generated was analyzed by calculating the MDCA.

The two main spatial degrees of freedom that affect the performance of the stack geometry are:

1. The distance between the front of the CdTe and the rear of the Si stack (D_{SA}), defined as

$$D_{SA} = \overline{S_5 A} = A - S_5 - \frac{(T_A + T_S)}{2} \quad (3)$$

where T_A is the CdTe thickness. D_{SA} was varied from 0.25 to 10 mm in 0.25 mm steps.

2. The distance from the center of one Si wafer to the center of the next wafer (ΔS), defined as

$$\Delta S = \overline{S_x S_{x+1}} = S_{x+1} - S_x - T_S. \quad (4)$$

ΔS was also varied from 0.25 to 10 mm in 0.25 mm steps.

When D_{SA} was scanned, ΔS was kept constant at 1.0 mm. When ΔS was scanned, D_{SA} was kept constant at 1.00 cm.

Fig. 2a presents the raw MDCA for all multiple interaction events as a function of D_{SA} and ΔS , without the inclusion of Doppler broadening or electronic noise in the model. The MDCA is large and

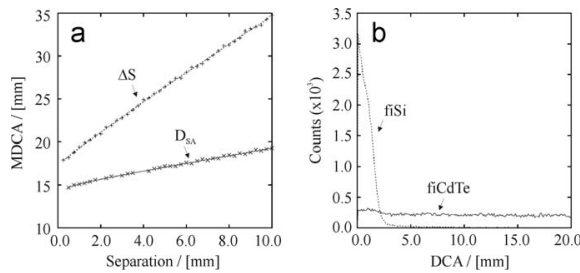


Fig. 2. (a) The MDCA for all multiple interaction events as a function of D_{SA} and ΔS . (b) The distance function from multiple-interaction events categorized for events where the primary interaction occurs in the Si of the CdTe.

shown to get worse as D_{SA} or ΔS increases. This appears counter intuitive as the accuracy with which the cone of response can be reconstructed should improve with separation between interactions.

Fig. 2 b shows the cause of the large MDCA. Gamma rays that interact first in the CdTe (termed fiCdTe events herein) produce an almost flat distance function and a large MDCA. Whereas, the distance function for those in which the primary interaction occurs in the Si (termed fiSi events herein) is much steeper and gives rise to a small MDCA. This result suggests that the majority of gamma-rays that interact in the CdTe first, travel a short distance before interacting in the CdTe a second time. Also there are a large number of fiCdTe events that contain poor information in the data set.

As D_{SA} or ΔS vary, so too do the source-to-primary (R_1) and primary-to-secondary (R_2) interaction distances, resulting in several competing factors. Firstly, the angular resolution is proportional to the inverse square of R_1 and R_2 [17]. Secondly, for a given constant angular uncertainty, the DCA increases linearly with R_1 —an effect transferred to the MDCA.

For fiCdTe events the linear increase, combined with the large angular uncertainty from the small R_2 dominates over the improvement in angular resolution. Therefore, most fiCdTe interactions should not be used for cone-surface formation. The possible exceptions are fiCdTe events that involve back scatter from the CdTe into one of the Si wafers. Experimentally, at 140 keV such interaction ordering is achieved through analysis of individual energy deposits. The scatter and recoil energy are well separated at both low (≤ 200 keV) and high (≥ 1 MeV) energies, while between these limits there is an ordering ambiguity for single scatter events.

In order to investigate these competing factors, the events that contributed to the MDCA distributions were split according to the Si detector in which the first interaction occurred, excluding fiCdTe events. Figs. 3a–d and e–h show these MDCA distributions as a function of increasing ΔS and D_{SA} , respectively. The sets of distributions are presented as pairs where:

- Fig. 3 a,e—The effects of Doppler broadening and electronic noise are excluded.
- Fig. 3 b,f—Doppler broadening is included through the Low Energy Compton Scattering (G4LECS) package in Geant4.
- Fig. 3 c,g—Electronic noise is approximated as a Gaussian distribution with 4.0 keV FWHM that is randomly sampled. For this energy and material the electronic noise can be considered as constant over the spectral range.
- Fig. 3 d,h—Both of the above contributions to energy resolution are incorporated.

In Fig. 3 a the Si-source distance for each layer is fixed while D_{SA} (Si-CdTe) is increased. This is equivalent to increasing \bar{R}_2 (the

average over all R_2 values) while \bar{R}_1 remains unchanged, resulting in a reduction of the angular uncertainty and hence MDCA. As the spectral resolution worsens (Figs. 3 b–d) the difference between Si layer distributions is reduced and they plateau faster due to an increase in the minimum angular uncertainty.

In Fig. 3 e both \bar{R}_1 (Si-source) and \bar{R}_2 (Si-CdTe) increase with ΔS for detectors S_2 – S_4 . However, for S_1 , \bar{R}_1 remains constant while \bar{R}_2 increases, analogous to Fig. 3 a. Conversely, for S_5 , \bar{R}_2 remains constant while \bar{R}_1 increases. Events that scatter in S_1 are shown to result in an MDCA that improves as ΔS increases. Events that scatter in S_5 show decreased resolution at the source location. The distributions for detectors S_2 – S_4 lie between these limits but follow the same general trend. As the spectral resolution worsens (Figs. 3 f–h), the gradient of the S_1 distribution, governed by the angular uncertainty, becomes positive and the magnitude increases with ΔS . The effect of a 5.1 keV (3σ) threshold associated with the 4.0 keV electronic noise was also investigated. The thresholding increased the MDCA proportionally by $\sim 4\%$ in all circumstances so the shapes of MDCA distributions in Figs. 3 d,h were unchanged yet the absolute values were seen to become worse.

The absolute sensitivities as a function of ΔS and D_{SA} are shown in Figs. 4a and b, respectively. All events with ≥ 2 interaction pixels were considered but split according to whether they were fiSi or fiCdTe. Each figure also shows the distributions following the inclusion of the 5.1 keV threshold (fiSi_{thresh} and fiCdTe_{thresh}). The sensitivity is shown to decrease as ΔS and D_{SA} increase, as expected. The 5.1 keV threshold results in a systematic drop in sensitivity of $\sim 18\%$ for both fiSi or fiCdTe as a function of ΔS and of $\sim 13\%$ and $\sim 20\%$ for fiSi or fiCdTe as a function of D_{SA} . The intrinsic efficiency of the geometry to fiSi events is $\sim 2.0\%$. However, it should be noted that the solid angle subtended by the closest Si wafer detectors is only 11% of 4π .

From these simulations, a number of preliminary conclusions can be drawn:

1. Cones reconstructed from fiCdTe events should not be used in imaging if considering Compton information.
2. Doppler broadening and electronic noise were accounted for and were shown to have comparable effects on the MDCA distributions.
3. The application of a 5.1 keV threshold at 140 keV resulted in a proportionate increase in MDCA, due to the rejection of small angle scatters ($\leq 30^\circ$), for this stack geometry.
4. Analysis of the MDCA over multiple parameters shows there is an upper separation (D_{SA}), beyond which purely a loss of efficiency occurs. For the position and energy resolution parameters presented, this value was shown to occur at 2.5 mm.

4. Experimental verification

Many variations of the detector geometry and collimator design are currently being simulated. However, to be useful these results must be validated experimentally. In order to conduct this validation, a version of the PEDRO imager is currently being constructed (Fig. 5a). The Si-DSSD-CdTe stack (Fig. 5 e) will be operated in an environment that can be cooled to -20°C . It will be housed inside an RF-shielded case (Fig. 5 d) with a thin entrance window. This in turn will be mounted inside an insulated box (Fig. 5 b) that will be purged with dry-Nitrogen gas to prevent condensation. The coolant is pumped through a pipe network held by the support stand (Fig. 5 c). The collimator will be mounted externally in a conduit through the insulated box wall. The RF-case, collimator and source-block will be positioned by guide rods that allow them to move independently from one another in the $\pm x$ direction.

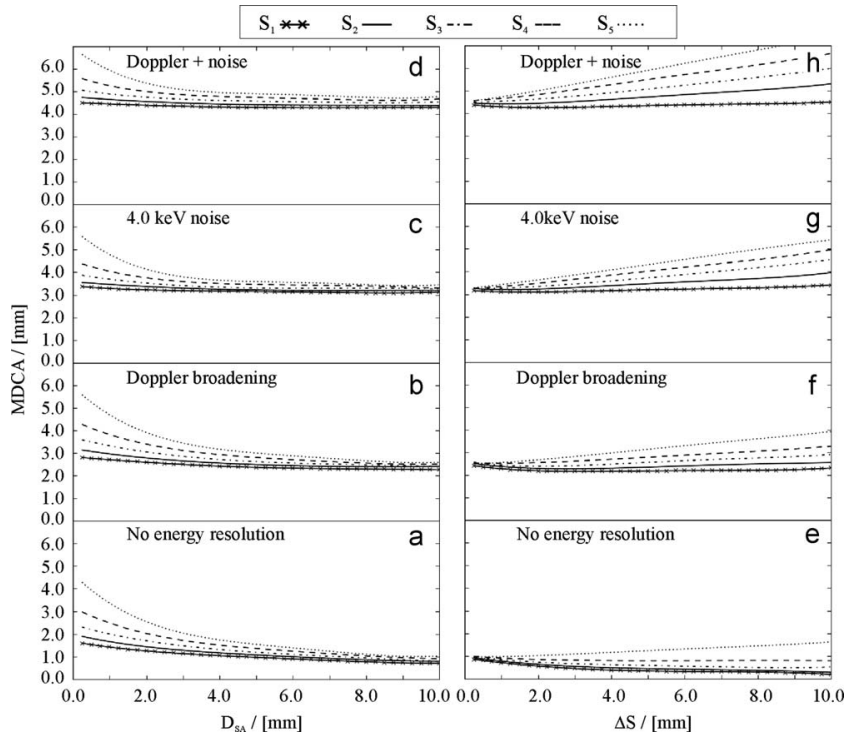


Fig. 3. MDCA distributions indexed by the Si detector in which the first interaction occurred. (a–d) The MDCA as a function of D_{SA} with no energy resolution, Doppler broadening, 4.0 keV electronic noise and both Doppler broadening and electronic noise included, respectively. (e–h) The MDCA as a function of ΔS with no energy resolution, Doppler broadening, 4.0 keV electronic noise and both Doppler broadening and electronic noise included, respectively.

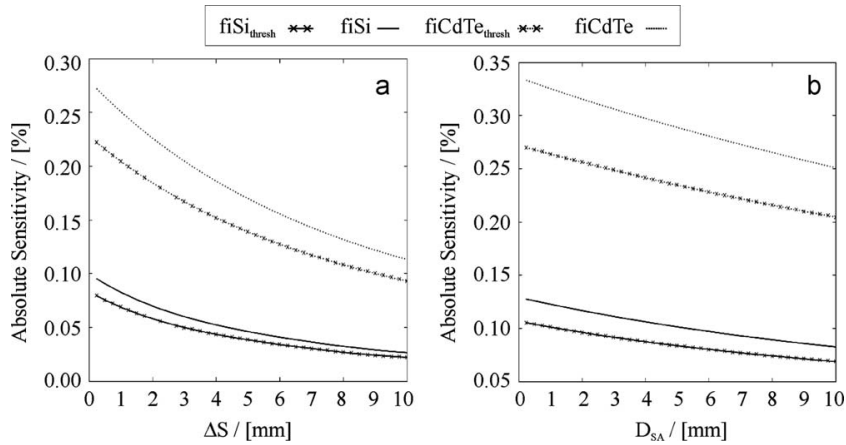


Fig. 4. (a) and (b) show the absolute sensitivities as a function of ΔS and D_{SA} , respectively. The events are split according to whether they are fiSi or fiCdTe. Each figure also shows the distributions following the inclusion of the 5.1 keV threshold ($fiSi_{thresh}$ and $fiCdTe_{thresh}$).

The scatter detectors are being constructed from seven layers of Si-DSSDs manufactured by Centro Nacional de Microelectrónica (CNM), Barcelona. The n-type wafers are made from high resistivity ($\sim 15 \text{ k}\Omega\text{cm}$) material and have an active volume of $32.0 \times 32.0 \times 0.8 \text{ mm}^3$. The contacts are segmented into 64 orthogonal strips with a 0.5 mm pitch and 0.1 mm inter-strip gaps, allowing the interaction positions of incident photons to be localized to the center of $0.4 \times 0.4 \times 0.8 \text{ mm}^3$ voxels. Each Si-DSSD

will be mounted on a motherboard and DC coupled to two Ideas VA64TA1 ASICs in a configuration similar to that described in Ref. [18]. The bias will be applied by operating the ASICs with a voltage gap corresponding to the bias potential ($\sim 150 \text{ V}$ on the n-side).

The Hybrid Pixel Detector (HPD) [19] currently being developed by the Cooperative Research Center for Biomedical Imaging Development (CRC-BID) consists of a $51.2 \times 51.2 \times 2.0 \text{ mm}^3$ CdTe crystal with a 256×256 pixelated anode. The crystal will be

bump-bonded to the 0.2 mm pitch ASIC. Each ASIC channel comprises a pre-amp, shaping amp, analogue-to-digital converter (ADC), histogramming memory, a controller and compensation network to modify amplifier gains.

The multiplexed outputs from both the VA64TA1 and HPD ASICs will be read out and controlled through the Generic Data Acquisition (GDAQ) system, also developed by CRC-BID. The GDAQ PCI card can hold up to three daughter cards, each of which contain two 12-bit 200 Msps ADCs. For the PEDRO-GDAQ implementation, the Altera Cyclone II FPGA on the GDAQ card will provide local interfaces and buffering and software (Jetpack), which has been developed in-house, will enable precise control and readout functionality for synchronized read out of coincidence events. Although this detector-readout configuration will yield optimal energy resolution results, the slow shaper and multiplexed readout of the VA64TA1 ASICs will limit the count rate to ~ 200 kHz.

Calculation of the aperture geometry requires the consideration of many experimental factors including the incident gamma ray energy (E_γ) and the material properties such as the mass-attenuation coefficient and K-edge. The PEDRO imager has been designed for $30 \text{ keV} \leq E_\gamma \leq 511 \text{ keV}$ and it is therefore not practicable to utilize a single geometry over this energy range. For initial validation an interchangeable aperture mounting structure has been constructed (Fig. 6). The maximum thickness of the holding structure, Fig. 6 a, supports 1.50 cm of Tungsten inserts, sufficient to yield a transmission $< 3\%(3\sigma)$ at 511 keV. Up

to nine apertures, consisting of pinholes, slats or open spaces (Fig. 6 c) can be mounted as inserts in the volume of the inner frame (Fig. 6 b). The final collimator (Fig. 6 c) is constructed from two identical structures, the upper and lower halves (Fig. 6 d). This versatile design will allow a full validation of the simulation.

5. Conclusion

A model has been generated that can be used for the optimization of PEDRO using the MDCA. The MDCA provides a measure of both the point spread function of a Compton camera and the ability of Compton information to distinguish between multiple pinholes in a coded-aperture device (given the central collimator position is coincident with the simulated source location). In a coded-aperture pinhole imager that does not use Compton information the level of image overlap increases with the distance between the collimator and the image-plane. Should a Compton camera be substituted as the detector in this situation then the MDCA is similarly dependant on the distance to the scatter-plane (\bar{R}_1). The MDCA reflects the ability to truncate the area (and hence pinhole-set) through which an incident photon must have passed. This provides a measure of the ability to demultiplex an arbitrary aperture array at a given location.

From this investigation into the PEDRO Compton camera it was concluded that cones reconstructed from fCdTe events should not be used for single scatter imaging. The inclusion of Doppler broadening and electronic noise were investigated and were shown to have comparable effects on the MDCA distributions. Analysis of the MDCA over multiple parameters shows there is an optimum D_{SA} , beyond which only a loss of efficiency occurs. For the position and energy resolution parameters presented, this value was shown to occur at 2.5 mm.

Due to fabrication cost the proof-of-principle detector configuration will have worse spatial resolution (0.8 mm thick Si and 0.4 mm strip width) than the simulation presented in this paper. This will change the gradient of the MDCA curves, yet an optimum separation (D_{SA}) is still expected. This paper presents a method by which an arbitrary geometry may be optimized for hybrid-collimation imaging, to be verified by trials with the experimental system.

Acknowledgments

This study has been supported by the Cooperative Research Center for Biomedical Imaging Development Ltd (CRC-BID), established and supported under the Australian Government's Cooperative Research Centers Programme.

References

- [1] F.J. Beekman, et al., Phys. Med. Biol. 49 (2004) 4579.
- [2] R.J. Jaszczak, et al., Phys. Med. Biol. 39 (1994) 425.
- [3] J. Qian, et al., Nucl. Instr. and Meth. A 594 (2008) 102.
- [4] S.R. Meikle, et al., IEEE Nucl. Sci. Symp. Conf. Rec. 3 (2000) 21.
- [5] D.W. Wilson, et al., IEEE Trans. Med. Imag. 19 (2000) 412.
- [6] S. Motomura, et al., IEEE Trans. Nucl. Sci. NS-54 (2007) 710.
- [7] S. Shokouhi, et al., Phys. Med. Biol. 54 (2009) 207.
- [8] L. Han, et al., Phys. Med. Biol. 53 (2008) 7029.
- [9] T.E. Peterson, et al., Nucl. Instr. and Meth. A. 505 (2003) 608.
- [10] W. Rogers, et al., US Patent No. 6881959, 2005.
- [11] L.J. Meng, et al., IEEE Trans. Nucl. Sci. NS-50 (2003) 1609.
- [12] S. Agostinelli, et al., Nucl. Instr. and Meth. A. 506 (2003) 250.
- [13] S.J. Wilderman, et al., IEEE Trans. Nucl. Sci. NS-4 (1997) 250.
- [14] L.J. Harkness, et al., Nucl. Instr. and Meth. A. 604 (2009) 351.
- [15] A. Studen, et al., Nucl. Instr. and Meth. A. 501 (2003) 273.
- [16] B.F. Philips, et al., IEEE Nucl. Sci. Symp. Conf. Rec. 1 (2001) 207.
- [17] C.E. Ordonez, et al., IEEE Trans. Nucl. Sci. NS-46 (1999) 1142.
- [18] H. Tajima, et al., IEEE Trans. Nucl. Sci. NS-51 (2004) 842.
- [19] S. Midgley, et al., Nucl. Instr. and Meth. A. 573 (2007) 129.

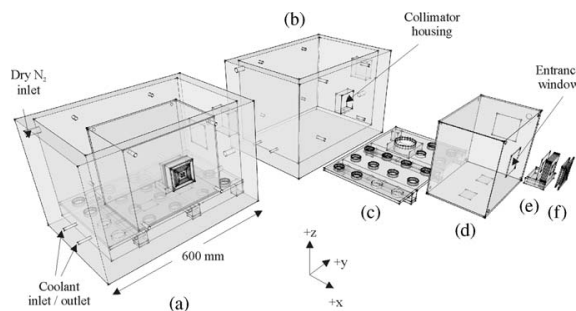


Fig. 5. The PEDRO imager experimental configuration. (b–f) The scale design drawings for the insulated-box, cooling-pipe stand, RF-shielded box, Si-DSSD-HPD stack and holding structure and collimator, respectively. The guide rods on which the collimator, RF-case and source block are mounted are not shown.

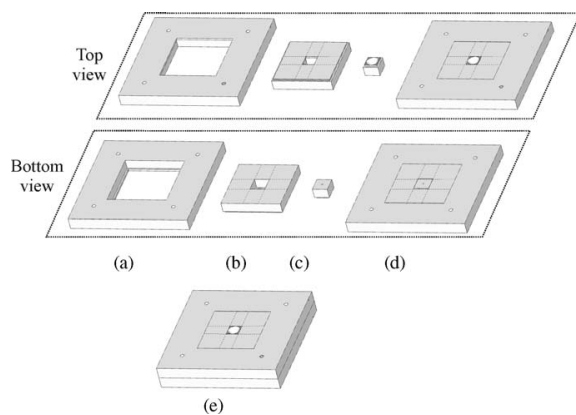


Fig. 6. The PEDRO modular collimator configuration. (a–e) The outer holding structure, inner frame, Tungsten aperture, half assembly and full assembly.

Towards Optimal Collimator Design for the PEDRO Hybrid Imaging System

Towards Optimal Collimator Design for the PEDRO Hybrid Imaging System

C. V. Nguyen, J. E. Gillam, J. M. C. Brown, D. V. Martin, D. A. Nikulin and M. R. Dimmock

Published in IEEE Transactions on Nuclear Science, Volume 58(3), Pages 639–650, 2011

DOI: 10.1109/TNS.2011.2134869

Reproduced here with kind permission from IEEE.

Declaration for Thesis Chapter 5

Declaration by candidate

In the case of Chapter 5, the nature and extent of my contribution to the work was the following:

Nature of Contribution	Extent of Contribution (%)
Co-developed the automated routine and image reconstruction code, assisted with simulations and analysis, and proofread the paper	20 %

The following co-authors contributed to the work. If co-authors are students at Monash University, the extent of their contribution in percentage terms is stated:

Name	Nature of Contribution	Extent of Contribution (%)
C. V. Nguyen	Lead the development of the automated routine and co-developed the image reconstruction code, coordinated the simulations and analysis, and wrote the paper	
J. E. Gillam	Co-developed the reconstruction code, and proofread the paper	
D. V. Martin	Co-developed the automated routine and proofread the paper	5 %
D. A. Nikulin	Provided computational technical support and proofread the paper	
M. R. Dimmock	Co-developed the automated routine and image reconstruction code, assisted with simulations and analysis, provided supervisory advice, and proofread the paper	

The undersigned hereby certify that the above declaration correctly reflects the nature and extent of the candidate's and co-authors' contributions to this work.

Candidate's Signature:

Date: / /

Project Leader's Signature:

Date: / /

Main Supervisor's Signature:

Date: / /

Towards Optimal Collimator Design for the PEDRO Hybrid Imaging System

Chuong V. Nguyen, John E. Gillam, Jeremy M. C. Brown, David V. Martin, Dmitri A. Nikulin, and Matthew R. Dimmock

Abstract—The Pixelated Emission Detector for RadiOisotopes (PEDRO) is a hybrid imaging system designed for the measurement of single photon emission from small animal models. The proof-of-principle device consists of a Compton-camera situated behind a mechanical collimator and is intended to provide optimal detection characteristics over a broad spectral range, from 30 to 511 keV. An automated routine has been developed for the optimization of large-area slits in the outer regions of a collimator which has a central region allocated for pinholes. The optimization was tested with a GEANT4 model of the experimental prototype. The data were blurred with the expected position and energy resolution parameters and a Bayesian interaction ordering algorithm was applied. Images were reconstructed using cone back-projection. The results show that the optimization technique allows the large-area slits to both sample fully and extend the primary field of view (FoV) determined by the pinholes. The slits were found to provide truncation of the back-projected cones of response and also an increase in the success rate of the interaction ordering algorithm. These factors resulted in an increase in the contrast and signal-to-noise ratio of the reconstructed image estimates. Of the two configurations tested, the cylindrical geometry outperformed the square geometry, primarily because of a decrease in artifacts. This was due to isotropic modulation of the cone surfaces, that can be achieved with a circular shape. Also, the cylindrical geometry provided increased sampling of the FoV due to more optimal positioning of the slits. The use of the cylindrical collimator and application of the transmission function in the reconstruction was found to improve the resolution of the system by a factor of 20, as compared to the uncollimated Compton camera. Although this system is designed for small animal imaging, the technique can be applied to any application of single photon imaging.

Index Terms—Compton scattering enhancement, multiple pinhole, PEDRO.

I. INTRODUCTION

SINGLE photon emission imaging devices are typically based on either mechanical [1]–[3] or electronic (Compton) [4] collimation. Mechanical collimators are composed of high

Z materials that modulate the photon flux incident on the detector. This allows a high resolution estimate of the radio-tracer distribution to be obtained at the expense of system sensitivity.

Electronic collimation requires no physical modulation of the incident flux. However, the resolution of the image estimate is limited by the detector position and energy resolutions and Doppler broadening. Typically, highly pixelated semiconductor detectors are utilized as they provide superior energy resolution over conventional scintillation detectors. Following a Compton scattered event an additional tracking or interaction ordering step is performed to determine the first and second interactions that define the cone of response (CoR). The subsequent back-projection of CoRs from many such events yields a high sensitivity, but generally low resolution, estimate of the radioisotope distribution.

The Pixelated Emission Detector for RadiOisotopes (PEDRO) [5] is a proof of principle hybrid imaging system being developed to investigate the combination of mechanical and electronic (hybrid) collimation [6]–[9]. The intended energy range for operation is from 30 to 511 keV. The optimization of this hybrid system should yield image estimates with both high resolution and high sensitivity. This will be achieved through reconstruction of both lines of response (LoRs) from well-defined pinholes in the center of the collimator and modulated CoRs from large-area apertures in the outer-regions. The aim of such an optimization is to increase the number of photons which impinge on the detector stack without polluting the pinhole projection data. It is expected that the modulated CoRs should complement the pinhole data, extending the field of view (FoV) and improve the iterative reconstructions. In order to achieve this goal, several constraints must be considered in the design of the large-area slits:

- The apertures must be able to focus the incident photons at pre-determined regions of the detector stack.
- The photons should be directed in a manner which maximizes the probability of a Compton scatter being the primary interaction mechanism.
- The overlap between the pinhole FoV and the large-area slit FoV should be maximized in order that the resulting images can be combined and/or quantitatively compared.

This paper focuses on collimator optimization for photons with an incident energy $e_0 = 140$ keV. The experimental prototype that is currently being tested is introduced in Section II. The 2D-optimization of slit geometries and the extension to 3D are described in Section III. This section also details the optimization procedure and the Compton reconstruction algorithm. Quantified results from Monte-Carlo simulations of the experimental prototype are presented in Sections IV and V. Finally, the results and directions for future work are provided in Section VI.

Manuscript received November 15, 2010; revised March 04, 2011; accepted March 21, 2011. Date of publication May 05, 2011; date of current version June 15, 2011. This work was supported by the Cooperative Research Center for Biomedical Imaging Development Ltd (CRC-BID), established and supported under the Australian Government's Cooperative Research Centers Program.

C. V. Nguyen and M. R. Dimmock are with the School of Physics, Monash University, Melbourne, VIC 3800, Australia and also with the Monash Node of the CRC for Biomedical Imaging Development, Melbourne, VIC 3800, Australia.

J. E. Gillam is with the Instituto de Fisica Corpuscular (IFIC), Universidad de Valencia-CSIC, Valencia, Spain.

J. M. C. Brown and D. V. Martin are with the School of Physics, Monash University, Melbourne, VIC 3800, Australia.

D. A. Nikulin is with the Monash Node of the CRC for Biomedical Imaging Development, Melbourne, VIC 3800, Australia.

Color versions of one or more of the figures in this paper are available online at <http://ieeexplore.ieee.org>.

Digital Object Identifier 10.1109/TNS.2011.2134869

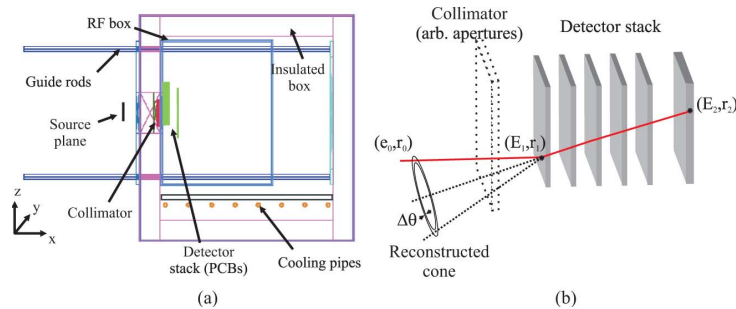


Fig. 1. (a) A schematic representation of the PEDRO experimental prototype. (b) A schematic illustration of the collimated Compton camera with an incoherent scatter with energy deposits E_1 and E_2 at two interaction locations r_1 and r_2 . The left-most layer is the collimator shown with dashed lines to represent any arbitrary aperture configuration. The next 5 layers are Si detectors. The final layer is a CdTe detector.

II. EXPERIMENTAL PEDRO

The experimental prototype (shown schematically in Fig. 1(a) being developed consists of an interchangeable aperture array positioned in front of a Compton camera. The Compton camera is composed of a stack of Silicon double-sided strip-detectors (Si-DSSDs) and a Cadmium Telluride (CdTe) hybrid-pixel detector (HPD). The aperture array has been designed to accommodate pinholes, slits and open-areas as the optimal configuration is as yet undetermined. Ideally, to maximise the detection efficiency of the PEDRO, many detector layers would be incorporated. However, due to the limit imposed by the budget for the project, only 5 Si-DSSDs and 1 HPD are used in the system.

Each of the 5 Si-DSSDs that comprises the stack was fabricated by Centro Nacional de Microelectronica. The active volume of each is $0.8 \times 31.9 \times 31.9 \text{ mm}^3$, which is segmented into 64 orthogonal strips on each side. The strips each have a width of $400 \mu\text{m}$ and gap of $100 \mu\text{m}$. The detectors are bonded to GM-IDEAS VA64TA Application Specific Integrated Circuits (ASICs) and are operated in a DC coupled configuration.

The HPD [10] is currently being developed at the Monash Centre for Synchrotron Science (MCSS), as part of a project being conducted by MCSS as a participant of the Cooperative Research Centre for Biomedical Imaging Development (CR-CBID). It consists of a $51.2 \times 51.2 \times 2.0 \text{ mm}^3$ CdTe crystal with a 256×256 pixelated anode. The crystal will be bump-bonded to the 0.2 mm pitch custom-designed ASIC.

The full-width-half-maximum (FWHM) of the detector energy resolution is dependent on the detector material, applied bias and incident energy. The FWHM is of the form $y = ax + b$, where x is the deposited energy in keV, and a and b are material-dependent parameters. In this work, the values of a and b are chosen to be 0.01 and 2.0 for Si detectors, and 0.015 and 4.0 for CdTe detector. These values were approximated from the distributions expected from the experimental prototype detectors.

The multiplexed outputs from both the VA64TA1 and HPD ASICs will be read out and controlled through the Generic Data Acquisition (GDAQ) system [11], also developed at MCSS. Software (DAX) has been developed in-house to enable precise control and readout functionality for synchronized coincidence data collection.

III. COLLIMATOR DESIGN OPTIMIZATION

The predominant interaction mechanism through which gamma rays interact in the detectors varies significantly with

the source energy and detector material. For incident photons where $e_0 \leq 50 \text{ keV}$ photoelectric absorption occurs primarily in the Si-DSSDs, minimizing the flux incident on the HPD. For $50 < e_0 \leq 100 \text{ keV}$, photons that interact in the Si-DSSDs will undergo either incoherent (Compton) scattering or photoelectric absorption, while those that interact in the CdTe will be predominantly photoelectrically absorbed. Therefore, the experimental configuration is optimal when operated as a multi-resolution Single Photon Emission Imaging (SPEI) device. For this mode of operation, small apertures (pinholes) are required to reconstruct a high-resolution estimate of the source by back-projection of LoRs into the imaging volume. The resolution of the reconstructed image depends on the size of the pinhole(s) and detector pixels, assuming full energy deposition. To increase the sensitivity of the system, many pinholes may be utilized. This typically results in the degree of multiplexing of the projection data increasing with distance from the collimator.

For incident photons with energies $100 e_0 \leq 700 \text{ keV}$, the probability of incoherent (Compton) scattering becomes dominant in the Si-DSSDs and the data consists of events where the primary interaction is either photo-electric absorption or Compton scattering. For the latter, Compton data can be used to help restrict the number of pinholes through which the incident photon may have passed via de-multiplexing [12]. As well as increasing the number or density of pinholes, the sensitivity can also be increased by the introduction of large-area apertures. This is only feasible if the primary interaction mechanism for photons that pass through these apertures is Compton scattering. The resulting CoRs measured are modulated by the aperture, limiting the range of possible incident photon trajectories and making each cone surface more informative. If a photon passes through a large-area aperture and a single interaction is recorded (due to the process of photoelectric absorption or the gamma ray scattering out of the stack), only a LoR can be back-projected. The axis of the line is defined between the center of the pixel and the aperture. The uncertainty of the line will be dominated by the size of the aperture and will be significantly more blurred than an equivalent LoR back-projected through a well-defined pinhole. The LoRs from pinholes give rise to high-resolution, low-sensitivity measurements while the large-area aperture CoRs yield higher-sensitivity, lower-resolution measurements in comparison. It should be noted that the ad-

dition of large-area apertures within the collimator needs careful consideration so that the high resolution pinhole data is not contaminated, but instead enhanced when combined with the CoRs.

For photons where $e_0 \geq 700$ keV, the photoelectric absorption cross-section is insignificant compared to that for Compton scattering and the optimization of the collimator becomes ambiguous. At these energies, it is likely that the inclusion of a collimator would degrade the image estimate as the edges of the apertures become transparent to the gamma rays and the collimator serves only as a scattering target.

Calculation of each aperture geometry is governed by many experimental factors, including e_0 and the material properties such as the mass-attenuation coefficient and K-edge location. The system will be operated over a broad energy range, so it is not practical to utilize a single geometry over this range as the level of scatter and penetration into the collimator increases with energy. To address this issue, an interchangeable aperture mounting structure has been constructed which is able to support a maximum thickness of 1.50 cm of Tungsten inserts, sufficient to limit the transmission at 511 keV to $< 3\%$ (3σ). Up to nine aperture arrays, consisting of pinholes, slats or open spaces, can be mounted as inserts in the volume. The work presented here assumes that the central region of the collimator is reserved for an arbitrary number of pinholes for forming a high resolution image. The optimization then determines the number, shape and position of large-area slits to be added to the outer collimator regions that maximize the system sensitivity or FoV. As stated previously, the quality of the image estimate generated from the detector data depends on the interaction sequence of each event. For the optimization of large-area slits, the most informative data can be obtained from photons that Compton scatter where both the primary and secondary interaction sites can be resolved. Events for which any of the first two interactions are not recorded and or resolved will decrease the signal-to-noise ratio (SNR) in the image estimate, unless appropriately weighted. This is because the back-projection axis from an unresolved Compton event would be oriented in the wrong direction, while the back-projected LoR from a photoelectric-absorption event would have a large uncertainty determined by the open-area of the slit. The two event categories described above will be referred to as resolved and unresolved measurements.

Optimisation parameters can include the FoV, sensitivity and ultimately the overall image quality. For the investigations presented herein, the openings of the slits were adjusted so that the following criteria were met:

- The FoV of the slit-set was constrained to at least fully sample the extents of the FoV of the pinholes. This criterion was selected in order that in future investigations, the difference in imaging performance between the slits and pinholes may be assessed.
- Provided criterion one held, the sensitivity of the detector array was maximized.

For the 3D realization of the collimator, the resultant image quality was also quantified.

A. Two-Dimensional Collimator Design

The first step towards developing an optimization routine was to generate a 2D ray-tracing version of the model illustrated

in Fig. 2(a). This was utilized to investigate the 2D geometric constraints of the experimental PEDRO configuration. The optimization then followed a multi-step procedure:

- 1) *Geometric configuration.* The geometries and locations of the source, detector stack and collimator are fixed. The values that were chosen to describe the experimental prototype are presented in Table I. For this investigation, the three pinholes were positioned at the corners of an equilateral triangle with side-length of 6.0 mm. In 2D, the pinhole dimensions were calculated from the projection onto the y -axis. This configuration then allowed the source projections to be determined. It should be noted that in all of the following discussion, the pinholes were used as place-holders. However, they were not made transparent to the incident photons. The source was a uniform circular distribution on the y - z plane. In 2D, this distribution was a projection onto the y -axis. The y - z dimensions of the HPD were fixed to be the same as the size of the pinhole-source projection at the x -location of the detector. To maintain the directionality of the collimator, a minimum thickness of Tungsten (L_W) through which any ray-traced photon trajectory must pass is defined by the user. For this investigation, L_W was fixed at 1.02 mm for which 95% (or 2σ) of 140 keV incident photons are stopped in the collimator.
- 2) *Upper limit of FoV.* A line from location **H** (Fig. 2(a)) at the top edge of the HPD is chosen to connect to the upper edge of the FoV (source). The line intersects the collimator walls at **A** and **B**. Locations **A** and **B** mark the limits of the upper and lower sides of the slit through which gamma rays can pass without impinging on the HPD. This location is chosen as photons that pass through the large-area slits and are incident on the HPD are likely to undergo photo-electric absorption. Such photons result in an unresolved event-type and contaminate the pinhole projection. Locations **C** and **D** lying on the vector **AB** are then selected at a distance from **A** and **B** equal to L_W as **AC** and **BD** become the edges of the slit.
- 3) *Lower limit of FoV.* Location **G** is the position of the top edge of the first Si-DSSD. Two vectors are then defined that connect **G** to **C** and **D** and intersect with the collimator walls at **E** and **F**. The geometry of the slit is now defined by locations **A**, **B**, **C**, **D**, **E** and **F**. This slit is the primary large-area aperture that maximizes the ratio of resolved to unresolved event types without polluting the pinhole projection data. The FoV of the aperture is defined by the vectors **HA** and **GE**.
- 4) *Utilization of remaining space.* More slits can be added to the remaining section of the collimator by starting new lines from location **H**. The addition of subsequent slits must not violate the condition that the minimum thickness of any ray-traced from the source and crossing the HPD is greater than L_W .
- 5) *Refinement of slit locations.* The locations of **A** or **B** of the slits can be adjusted for the desired final FoV of the source. Currently the locations are chosen by considering the slit-to-slit and slit-to-pinhole distances and selecting the set that produces the greatest transmission within the FoV of the source.

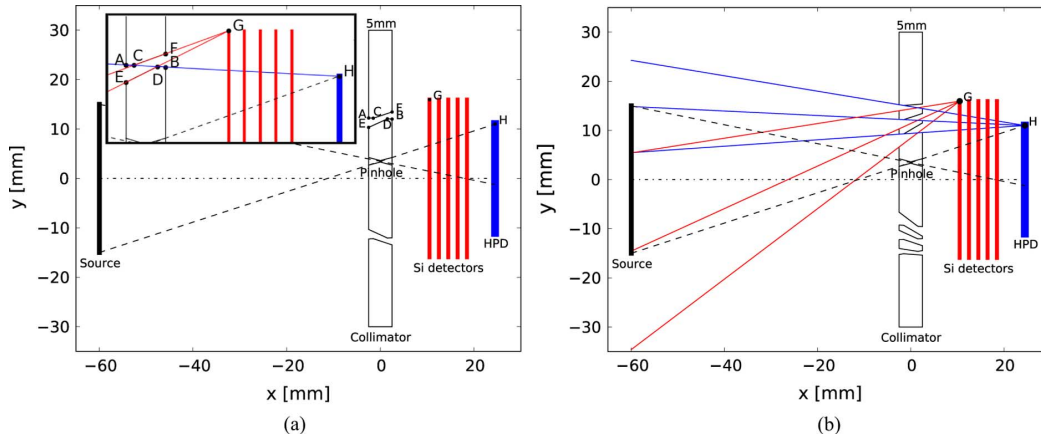


Fig. 2. (a) A schematic representation of the 2D ray-tracing collimator optimization. This was performed for a single large-area slit with 3 pinholes in an equilateral triangle configuration around the collimator center. The geometry of the slit is now defined by locations A, B, C, D, E and F, determined from the optimization. Inset is a zoomed view of the geometry of the slit and the ray tracing to form the slit. The limit-case lines connecting any point within the slit to G and H mark the regions of the detectors for which photons incident on the collimator can interact. Events for which the primary interaction of a Compton scatter sequence occurs in these regions are used for Compton back-projection. The oblique dashed lines show the projection of the source through one of the 3 pinholes on the collimator. The projections of the source through the 3 pinholes partially overlap in the centre region of the HPD. This is the reason why the lower end of the pinhole projection on the HPD goes below the centre line in this figure. (b) The extension of the optimization to show multiple large-area slits above and below the central region, pre-allocated for the pinholes.

TABLE I
THE GEOMETRIES OF EXPERIMENTAL COMPONENTS (SEE FIG. 2(a) AND (b))

	Size (y-z) [mm]	Pixel size (y-z) [mm]	Thickness (x) [mm]	Location (x) [mm]
Source	30.0 (dia.)	N/A	0.0	-60.0
Collimator	60.0 (dia.)	N/A	5.0	0.0
Si-DSSDs	31.9 × 31.9	0.2 × 0.2	0.8	9,11,13,15,17
HPD	20.7 × 20.7	0.5 × 0.5	2.0	23.0

Fig. 2(b) shows the extension of the design to a collimator with 3 slits on each of the upper and lower sides. The limiting cases of the ray tracing are shown on the upper part of the collimator. At each slit, two vectors that define the range of the FoV are defined between locations G and H and the upper and lower edges of the slit. The limit-case lines connecting any point within the slit to G and H mark the regions of the detectors for which photons incident on the collimator can interact. Events for which the primary interaction of a Compton scatter sequence occurs in these regions are used for Compton back-projection. The oblique dashed lines show the projection of the source through one of the 3 pinholes on the collimator. The projections of the source through the 3 pinholes partially overlap in the centre region of the HPD. This is the reason why the lower end of the pinhole projection on the HPD goes below the centre line in this figure.

The effective transmission ET_W as a function of emission location y and angle α (angle of photon emission from the source plane) of the optimized large-area slits, can be calculated from,

$$ET_W(y, \alpha) = \exp[-\mu_W^t L_W(y, \alpha)] \quad (1)$$

where $L_W(y, \alpha)$ is the total depth of Tungsten that the ray intersects with the collimator, and μ_W^t is the total linear attenuation coefficient for Tungsten at the source energy. For 140 keV photons, $\mu_W^t = 36.2 \text{ cm}^{-1}$. In the following discussions, μ will always refer to the linear attenuation coefficient. The effective

transmission outside the bounds of the collimator is neglected. The mean effective transmission (ET) from each emission location in y is given by,

$$\langle ET_W \rangle(y) = \frac{1}{\pi} \int_{-\pi/2}^{\pi/2} ET_W(y, \alpha) d\alpha. \quad (2)$$

After traversing the collimator, the modulated photon flux impinges on the Si-DSSD stack. The effective attenuation (EA) of the stack is given by,

$$EA_{Si}(y, \alpha) = 1 - \exp[-\mu_{Si}^t L_{Si}(y, \alpha)] \quad (3)$$

where $L_{Si}(y, \alpha)$ is the total depth of Si and μ_{Si}^t is the total linear attenuation coefficient of Si. For 140 keV, $\mu_{Si}^t = 0.35 \text{ cm}^{-1}$. The effective sensitivity (ES) of the system is proportional to the product of the collimator transmission and the attenuation in the Si-DSSD stack, given by,

$$\langle ES_{sys} \rangle(y) = \frac{1}{\pi} \int_{-\pi/2}^{\pi/2} ET_W(y, \alpha) EA_{Si}(y, \alpha) d\alpha. \quad (4)$$

If the sampled emission angles are binned (discretized), (2) and (4) become,

$$\langle ET_W \rangle(y) = \frac{1}{\pi} \sum_{i=0}^N ET_W(y, \alpha_i) \Delta\alpha \quad (5)$$

$$\langle ES_{sys} \rangle(y) = \frac{1}{\pi} \sum_{i=0}^N ET_W(y, \alpha_i) EA_{Si}(y, \alpha_i) \Delta\alpha \quad (6)$$

where $\Delta\alpha = \pi/N$, N is the number of angular bins and $\alpha_i = -\pi/2 + i\Delta\alpha$.

Fig. 3(a) presents an example of rays emitted from a point at the center of the source distribution ($y = 0$). The limits of the ray vectors show the range in α of the trajectories utilized to calculate the effective transmission at this location. All the rays

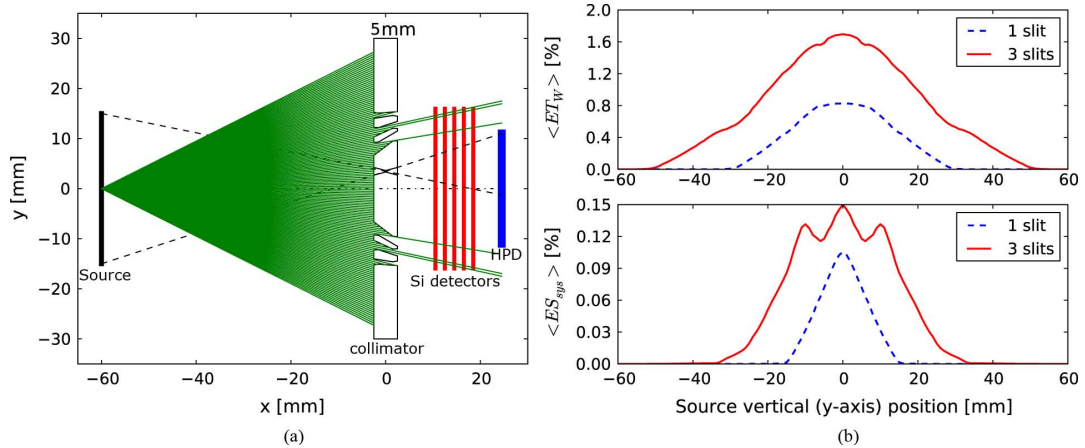


Fig. 3. (a) Illustration of ray tracing for 500 photons emitted from location $y = 0$. All the rays with an effective transmission below 5% are visualized as being stopped in the collimator. (b) Line-plots of the calculated effective transmission (upper) and system effective sensitivity (lower). Solid and dashed lines represent the distributions for the collimators with one and three slits, respectively. Note that the y -range in (b) is larger than that in (a). The FoV of the system for both the one and three slit geometries extends beyond the range of the distributed source. The magnitude and range of the sensitivity function is significantly larger for three slits with respect to the one slit geometry.

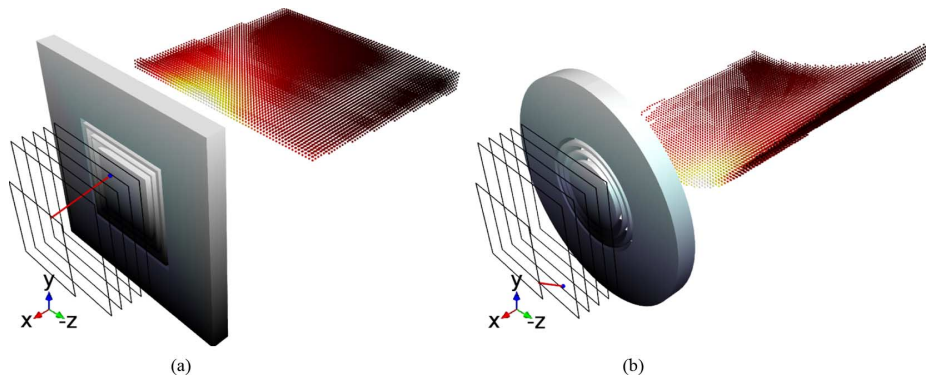


Fig. 4. (a) A 3D representation of the triple slit square collimator configuration. (b) A 3D representation of the triple slit cylindrical collimator configuration. The dots in front of the collimator represent the image voxels where the transmission $p_t = 1$. The shades of the dots represent the values of CoR at the voxels. The transparent squares represent the detector layers. The short straight line shows the recoil photon trajectory connecting the first (shown as solid dot) and second interactions forming the CoR.

with ET_W below 5% are shown to be stopped in the collimator.

Fig. 3(b) shows the distributions of $\langle ET_W \rangle$ and $\langle ES_{sys} \rangle$ as the number of slits included is increased. The distribution was calculated in 1.0 mm increments along the y -axis. At each location, 5000 photons were uniformly emitted within an angular range of 2π . When there are no slits in the collimator, $\langle ET_W \rangle$ and $\langle ES_{sys} \rangle$ are negligible. When changing from one slit to three slits, $\langle ET_W \rangle$ and $\langle ES_{sys} \rangle$ are significantly increased as expected. The FoV is also significantly increased with the extension to three slits.

B. Three-Dimensional Collimator Model in GEANT4

The optimized collimator, described in the previous section, was extended to 3D and modelled in GEANT4 [13]. The simulations incorporated all of the experimental components: detectors; motherboards; housing; RF-shielding; the collimator

and the source. In GEANT4, the collimator was constructed from two parts, an inner section reserved for pinholes and an outer part containing slits. The slits in the outer sections were formed using the G4BREPSolidPolyhedra class objects to avoid repeating solid subtractions that can cause errors in GEANT4 ray-tracing. This object class also made the extension from square to cylindrical configurations trivial as the input just required an increase in the number of sides of each polyhedron. Fig. 4(a) and (b) show the two 3D configurations modelled in GEANT4. The first collimator design was composed of three concentric square slits that were matched to the geometry of the Cartesian detector stack. The second was a cylindrical geometry, which better used the space surrounding the central pinhole region. In reality, the individual parts of the collimators need extra mechanical supports to be held together in place. A solution is to fill in slit spaces with a low density rigid plastic foam [15].

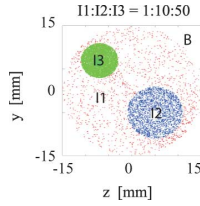


Fig. 5. The triple intensity planar phantom source distributions. The three circles (radius = 15.0, 6.0, and 4.0 mm) have relative intensities of 1:10:50. Region B is the background of the phantom with zero intensity. The source is on y - z plane.

To study the performance of both collimator configurations, simulations were performed with a distributed source of $e_0 = 140$ keV shown in Fig. 5. The source distribution was a triple intensity planar phantom consisting of three circular distributions $I1$, $I2$ and $I3$. The outer circle ($I1$) had a radius of 15.0 mm and the two inner circles had radii of 6.0 mm and 4.0 mm. The smallest radius of the circles was approximately 2 times the average gap of the slits, to account for the expected size of the point-spread-function (PSF). The three distributions had relative intensities of 1:10:50.

An additional study was performed to investigate the system PSF. A point-source which emitted 140 keV photons was positioned at the center of the FoV for geometries that included the Compton camera stack both with and without a physical collimator.

The reconstruction algorithm used for both the distributed and point source investigations is described in Section III-C.

C. Compton Reconstruction

Estimates of the source distributions were formed utilizing Compton-cone reconstruction with consideration of the transmission properties of the collimator. For an incident gamma ray emitted from location \mathbf{r}_0 , with energy e_0 , the Compton scatter angle θ_C at the first interaction is related to the energy deposited E_1 (see Fig. 1(b)) by,

$$\cos \theta_C = 1 + m_e c^2 \left(\frac{1}{e_0} - \frac{1}{e_1} \right) \quad (7)$$

where $e_1 = e_0 - E_1$ is the energy carried by the recoil photon after the interaction. For an ideal system, the scattering angle θ_C defines a CoR on which the photon emission location originated. For a finite imaging volume in a realistic system the intersection of the CoR with the imaging volume gives a probability distribution of the likelihood that the photon was emitted from each voxel in the volume. The probability density function Φ of the CoR can be generally expressed as:

$$\Phi(\mathbf{r}_v) = \frac{1}{4\pi} p_t(\mathbf{r}_v) \cdot p_{v1} \cdot p_C \cdot p(\mathbf{r}_{v1}, \wedge | \theta_C, E_1) \cdot p_{12} \cdot p_i \quad (8)$$

where \mathbf{r}_v is the location of an arbitrary voxel inside the imaging volume, \mathbf{r}_{v1} is the vector from \mathbf{r}_v to the cone apex \mathbf{r}_{11} , $p_t(\mathbf{r}_v)$ is the collimator transmission function, p_{v1} is the probability that the gamma ray from \mathbf{r}_v reaches the interaction location \mathbf{r}_{11} given it traverses the collimator, p_C is the probability that a Compton scatter occurs at \mathbf{r}_{11} , p_{12} is the probability that the photon reaches the second interaction location \mathbf{r}_{12} , p_i is the probability of an

interaction at \mathbf{r}_{12} and $p(\mathbf{r}_{v1}, \wedge | \theta_C, E_1)$ is the probability of the emission at \mathbf{r}_v Compton scattering at an angle θ_C resulting in a measured energy E_1 . \wedge denotes cone surface. The last of these probabilities is the double differential cross section, which can be approximated by,

$$p(\mathbf{r}_{v1}, \wedge | \theta_C, E_1) = \frac{1}{2\pi r_{v1}^2} p_\wedge(\theta_v | \theta_C) \cdot p(\theta_C) \quad (9)$$

where θ_v is the angle between \mathbf{r}_{v1} and the vector of the cone axis \mathbf{r}_{12} , $p(\theta_C)$ is the scattering function and $p_\wedge(\theta_v | \theta_C)$ is the CoR with angular uncertainty. The probability density function (PDF) of CoR can be approximated by [14],

$$p_\wedge(\theta_v | \theta_C) = \left[0.9 \exp\left(-\frac{(\theta_v - \theta_C)^2}{2\sigma^2}\right) + 0.1 \exp\left(-\frac{(\theta_v - \theta_C)^2}{2(3\sigma)^2}\right) \right] \quad (10)$$

where σ is chosen to be $\Delta\theta/2.35$. It should be noted that (10) is an approximation, both in the shape and the width of the function. This approximation is reasonable as long as Doppler broadening is the dominant factor in $\Delta\theta$.

In this study, image reconstruction is performed by CoR back-projection. In order to preserve the intensity, the sum of the contributions of all voxels for each CoR was normalized to 1.0. This implies that the source is contained by the image volume. Additional detailed description of the implementation of the Compton back-projection can be found in the Appendix.

IV. CONTRAST AND SIGNAL-TO-NOISE RESULTS

A. GEANT4 Simulation Results

The simulations were performed on the Nimrod/G computing cluster at Monash University [16]. The data were filtered to remove the histories for Rayleigh scatters and interactions that occurred in the collimator or housing as no *a-priori* knowledge of this information can be recorded experimentally. A total of 5.0×10^8 events were generated from the triple-intensity phantom. To provide realistic measurement data, uncertainties due to the nominal spatial and energy resolutions of the experimental detectors were added to the ideal data. The Compton interaction sequences were then randomized and re-ordered using a version of Bayesian reconstruction [17] where the source location was assumed to be at negative infinity on the x -axis.

Fig. 6(a) shows the statistics for Compton events as a function of event fold (the number of interactions in an event) for the square and cylindrical geometries. The cylindrical collimator yielded increases of 14.9% and 19.0% in the numbers of total and successfully ordered events, respectively, in comparison with the square collimator. An increase was achieved even though the open-fraction of the square collimator is greater. The percentage of successfully tracked events for the cylindrical geometry was 66.0%, compared to 63.7% for the square geometry. Although these rates were less than perfect, the majority of the unsuccessfully ordered events were not included in the image estimate as they were attenuated in transmission correction. Improved ordering could be achieved by incorporating the collimator geometry into the ordering algorithm, however it would be extremely computationally

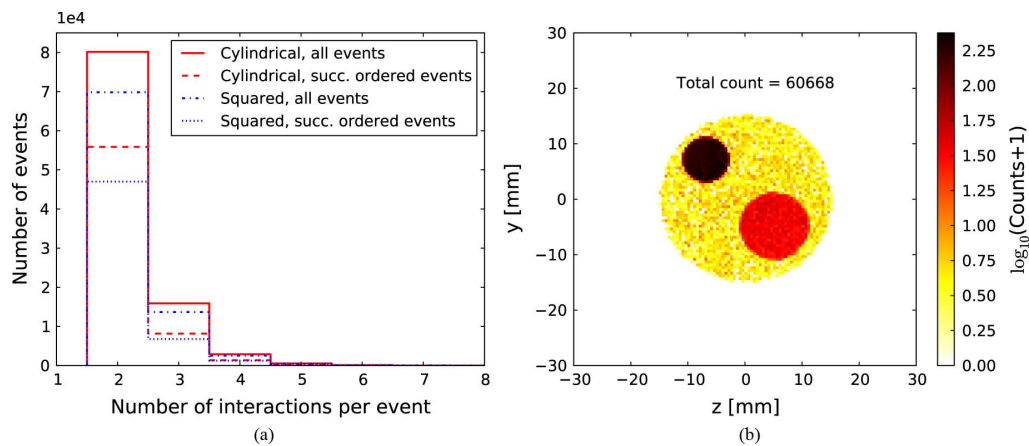


Fig. 6. (a) A plot showing the number of events as a function of the number of interactions in the event for the two collimator configurations. (b) A 2D histogram in log-scale showing the photon emission positions, at the source plane, for events that passed through the cylindrical collimator and interacted in the detector-stack.

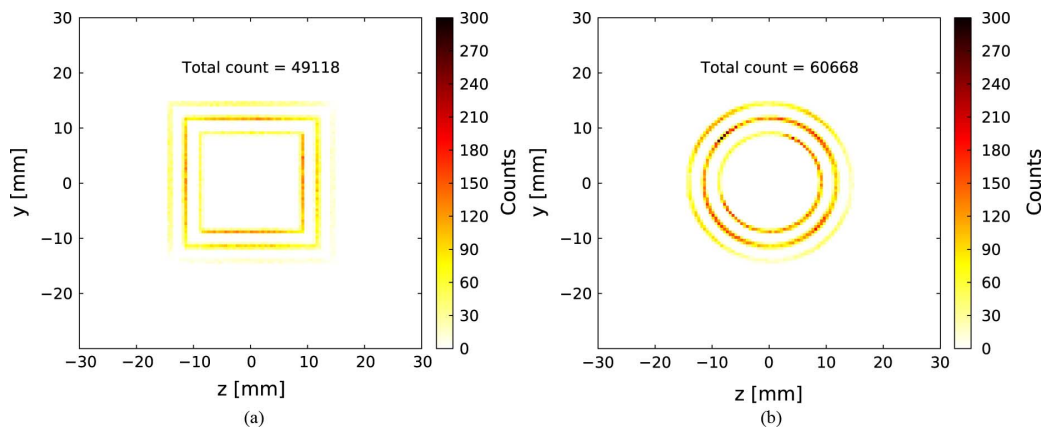


Fig. 7. 2D histograms of the positions at which the photon emission vectors intersect the collimator plane for all detected Compton scattered events for (a) the square and (b) the cylindrical geometries, respectively. The complex variation in intensity shown between (a) and (b) is due to the combination of the change in the number of emitted photons that intersect the different regions of the collimators as a function of distance from the center of the FoV and the asymmetric source distribution.

intensive to test every permutation and so this extension was not included. For the result shown in Fig. 6(a), the realistic resolved/unresolved ratios are 0.143 and 0.161 for squared- and cylindrical collimators, respectively. From a comparable simulation, where the outer region of the collimator was completely open, the mean resolved/unresolved ratio was calculated to be 0.190. The lower resolved/unresolved ratios can be attributed to multiple scatter events being clustered into single pixels and the inclusion of housing interactions in the collimator data set but not in the comparable simulation one. Fig. 6(b) shows the 2D event histogram of the photon emission positions, at the source plane, for events that passed through the cylindrical collimator and interacted in the detector-stack. The distribution closely resembles the phantom shown in Fig. 5, and shows that the FoV of the slits covers the entire distributed planar phantom. The equivalent distribution for the events that passed through the square-slit collimator is very similar and is therefore not shown.

Fig. 7(a) and (b) show 2D histograms of the positions at which the photon emission vectors intersect the collimator plane for all detected Compton scattered events for the square and cylin-

drical geometries, respectively. The narrow distributions closely reproduce the precise outlines of the collimator apertures. This agreement demonstrates the effectiveness of the design at minimizing the number of unresolved events—events for which the primary scatter occurs in the collimator—that compose the data set. The variation in intensity shown in Fig. 7(a) and (b) is due to the combination of several geometrically varying parameters. These parameters include the source emission in spherical coordinates, the “Cartesian nature” of the detector stack and the asymmetric source distribution. In addition, for the cylindrical slit geometry, the intensity of the histogram is maximum in the regions of corners of the squared detectors where there is greater intersection of the rays with the detector stack. From these distributions, the cylindrical collimator has been shown to outperform the square collimator.

B. Reconstruction Results

The event data described in Section IV-A were reconstructed utilizing the technique described in Section III-C. The intersection of each back-projected CoR with each voxel in

the imaging volume was calculated and summed. In order to reduce the computation time, p_{v1} , p_{12} and p_i were set to 1.0. Although these terms will ultimately effect the final image, their contribution is small compared to the other parameters that describe the $p_{\Lambda}(\theta_v | \theta_C)$. Also, they will have a similar effect on both the ideal (excluding energy and spatial uncertainties) and realistic (including energy and spatial uncertainties) images reconstructed for each test case. Therefore setting these three parameters to unity was deemed to have a minimal effect on the study of the collimator performance. For each case, both the ideal and realistic image estimates were reconstructed to investigate the subsequent change in performance. The effects of the collimator on the image reconstruction were also investigated by performing back-projections with and without the collimator transmission function. It should be noted that while the GEANT4 data was blurred with the expected levels of experimental position and energy resolutions and Bayesian interaction ordering, no attempt has yet been made to estimate the performance of the code with time uncertainty that would result in pile-up and random coincidence.

Fig. 8(a) and (b) show the image estimates, at the depth where the source was located ($x = -60$ mm), for data collected with the square collimator and without inclusion of the collimator transmission function (i.e., cone-surface back-projection). The back-projection results from ideal data are shown on the left, while those using realistic experimental factors are shown on the right. The source appears as a single unresolved distribution in both cases and the size of this distribution is shown to increase significantly with the application of the experimental factors. Under these conditions, the data from the cylindrical collimator also resulted in similar distributions and so is not presented.

Fig. 8(c) and (d) show image estimates from the same data as is presented in Fig. 8(a) and (b), however, the collimator transmission function has also been included in each back-projection. The resulting reconstructions have a significant reduction in the level of overall blur and the high intensity source distribution is now visible above the background. However, there are still significant artifacts in the horizontal and vertical directions, caused by preferential modulation of the back-projected CoRs. Fig. 8(e) and (f) show equivalent representations to those in Fig. 8(c) and (d), however the simulated data were generated with a cylindrical shaped collimator. The resulting back-projections for this configuration enable isotropic modulation of the CoRs which results in a substantial reduction in image artifacts. The high intensity profile can easily be differentiated from the other features and the intermediate intensity distribution can also be observed. Additionally, There is a reduction of about 2 times in image intensity from ideal back-projection (left) to realistic back-projection (right) in Fig. 8. This is because of the effect of the additional spatial and energy uncertainties on blurring of the back-projected PDF of each CoR and decreasing the success rate of the Bayesian tracking algorithm. The noise in the images shows that the image quality can be improved with more event data.

In order to quantify the quality of different image estimates the contrast and noise properties for the three features and the background were measured by overlaying the exact phantom. The labelled regions I1, I2, I3 and B on the phantom shown in

Fig. 5 are used as the template for the calculations, i.e., those regions are masked off when calculating the various contributions to contrast and SNR. As an example of the calculation, the contrast between regions I3 and I1 was obtained by dividing the difference of the mean intensities of regions I3 and I1 by the sum of the mean intensities, or $\langle I3 \rangle - \langle I1 \rangle / \langle I3 \rangle + \langle I1 \rangle$. Table II shows the contrast for each of the regions of the images reconstructed from data collected using the square collimator, with and without the inclusion of the collimator transmission function, and the cylindrical collimator with the inclusion of the transmission correction. In the table, B denotes the mean background level. For both the ideal and realistic data, the contrast between the intermediate intensity circle (I2) and the low intensity circle (I1) is completely dominated by the criss-cross artifacts. However, the contrast of $I3:I1$, $I2:I1$ and $I1:B$ increase significantly with the inclusion of the transmission function. When the cylindrical collimator is used, the contrast further increases in all cases for both the ideal and realistic data.

Table III shows the signal-to-noise-ratio (SNR). The SNR was calculated as $\langle I_N \rangle / \langle B \rangle$ for each distribution. In this instance the “signal” refers to mean intensities of the image regions where an emission was produced, when overlaying the exact phantom. Whereas the “noise” refers to the mean intensity of the image region from where no emissions were generated. For both collimator geometries, the SNR increases significantly with the inclusion of the transmission correction. The improvement in the SNR for the square collimator with the transmission function was 126%, on average. By moving from the square geometry to a cylindrical geometry, a further average increase of 31% was obtained. Repeat data sets were produced and the SNR values of calculated. The variations in SNR between the data sets was shown to be less than 10%.

V. SYSTEM POINT-SPREAD-FUNCTION (PSF)

A single point source was positioned in the center of the FoV in order to assess the affect of including large-area-apertures on the resolution of the system. Two configurations were considered, the Compton camera stack both with and without the cylindrical collimator. GEANT4 simulations were performed for which 1.0×10^7 event histories were generated. The total number of detected events were 1.57×10^6 and 4.7×10^4 , respectively. This means that the slit openings on the collimator enabled 3.0% of all possible events to be detected, however it should be remembered that the central region of the collimator was reserved for pinholes. If this central region were allocated further large-area-slits, this fraction would be much greater. In fact the number of events that would pass through the three central pinholes is only 2.3% of the data that passes through the slits in the outer regions.

Fig. 9(a) and (c) show the image estimate and slice at $y = 0.0$ for the system without a mechanical collimator. As with all the data presented in this work, all detected events were included and there was no minimum threshold applied to the acceptance angle or distance between scatters. The FWHM of the PSF was estimated to be at least 42.0 mm. Clearly, no modulation can be applied to the back-projected CoRs. Fig. 9(b) and (d) shown the image estimate and slice at $y = 0.0$ for the system with

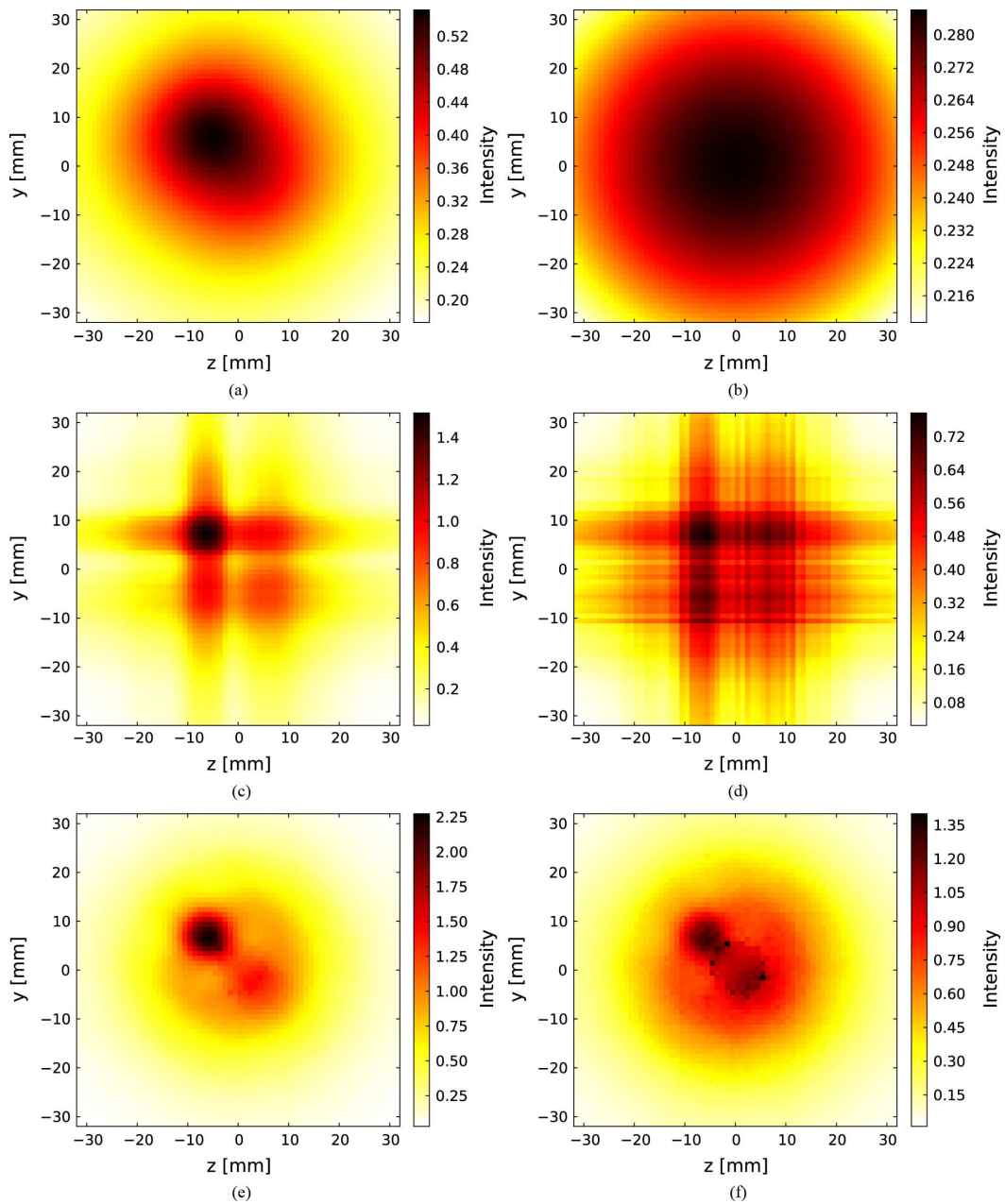


Fig. 8. Image estimates at the volume slice where the source was located. (a)-(d) were generated with data from the square collimator and (e)-(f) with data from the cylindrical collimator. The left column shows image estimates reconstructed from ideal data. The right column shows image estimates from data with experimental factors applied. (c) and (d) show the improvement achieved with the inclusion of the transmission function, with respect to (a) and (b). (e) and (f) show the further gains achieved through moving from a square to cylindrical geometry.

the cylindrical collimator. The modulation transmission function was applied to each CoR in back-projection. The FWHM of the realistic PSF in Fig. 9(d) is shown to be reduced to 2.0 mm, or by a factor of 20 with respect to the bare Compton camera. However, tails resulting from asymmetric modulation across the three concentric large-area-slits results in a broadening at the base of the distribution.

VI. CONCLUSION

The design of a hybrid collimator for the PEDRO prototype detector has been investigated. The aim was to find a realistic geometry that would enable optimized large-area slits to be included in the outer regions of a collimator to improve the sensitivity and increase the FoV. The constraints were to ensure that

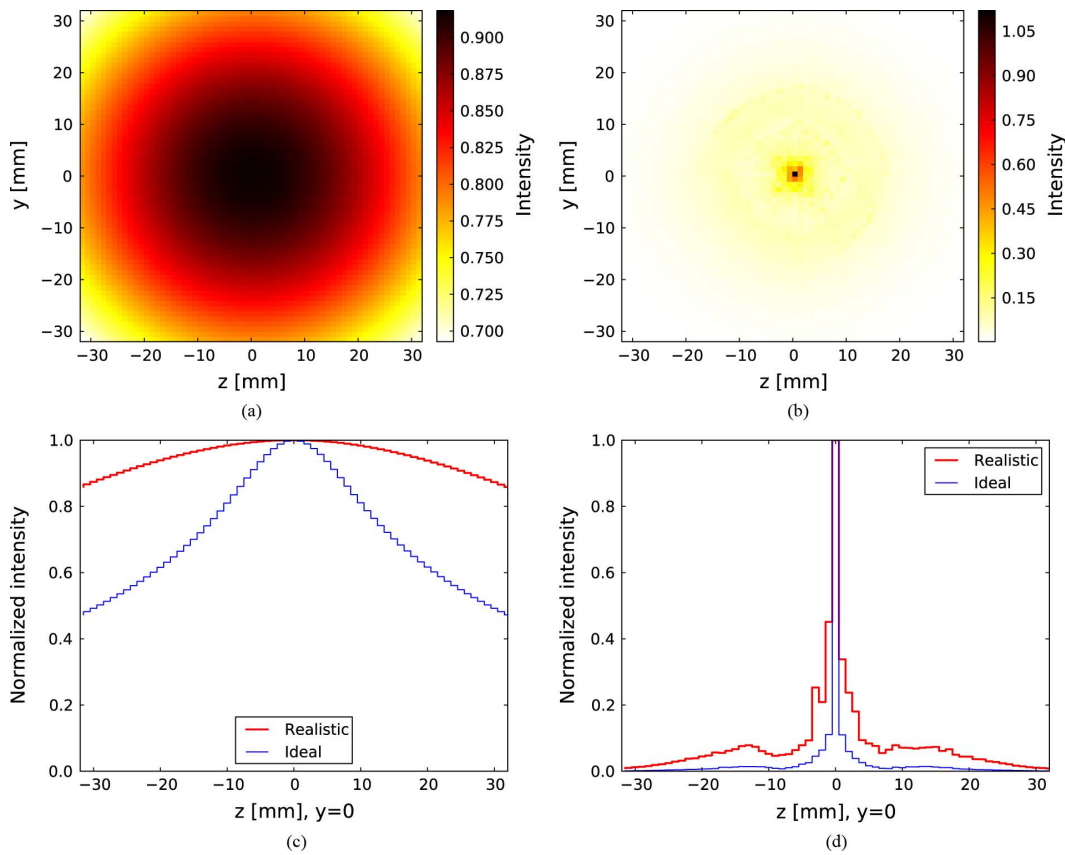


Fig. 9. Image estimates of the single point source obtained without any collimator (left) and with the cylindrical collimator (right). (a)-(b) are back-projection image estimates with realistic conditions. (c)-(d) are the distributions across the image estimates at $y = 0$, with both ideal and realistic conditions. With the cylindrical collimator, the FWHM of the realistic PSF in (d) is at least 20 times smaller than without the collimator.

TABLE II
IMAGE CONTRAST FOR THE SQUARE AND CYLINDRICAL COLLIMATORS.

		Square		Cylindrical	Phantom
		w/o trans.	w/ trans.		
Ideal	I3:I1	0.098	0.297	0.334	0.916
	I2:I1	-0.009	0.024	0.099	0.818
	I1:B	0.238	0.500	0.571	1.000
Realistic	I3:I1	0.002	0.134	0.171	0.916
	I2:I1	0.004	0.021	0.093	0.818
	I1:B	0.055	0.401	0.515	1.000

TABLE III
SNR FOR THE SQUARE AND CYLINDRICAL COLLIMATORS.

		Square		Cylindrical
		w/o trans.	w/ trans.	
Ideal	I3:B	1.975	5.546	7.342
	I2:B	1.595	3.149	4.467
	I1:B	1.623	3.003	3.664
Realistic	I3:B	1.122	3.001	4.412
	I2:B	1.125	2.439	3.769
	I1:B	1.117	2.340	2.126

the additional slits did not affect the image estimate that could be collected with the multi-pinhole configuration in the center of the aperture array.

It has been shown that the optimization technique developed allowed the large-area slits to not only fully sample the primary

FoV, but also to extend this to enable region-of-interest analysis. The algorithm also enables the user to adjust the optimized slits to trade-off the FoV and sensitivity.

Square- and cylindrical-slit geometries were tested and the effect of accounting for the collimator transmission functions was also investigated. For both geometries, the results have shown that the collimator transmission function modulated the back-projected CoRs into the imaging volume and significantly improved the image quality quantified by contrast and SNR. It was also found that a cylindrical geometry collimator outperformed a square geometry collimator. The isotropic modulation of the cone surfaces resulted in less artefacts and more highly resolved image estimates. Also, the cylindrical geometry provided increased sampling of the FoV due to more optimal positioning of the slits. From data collected with the cylindrical collimator and a single point source in the center of the FoV, the resolution of the system was improved by a factor of 20, as compared to the uncollimated Compton camera. Although a resolution of ≥ 2.0 mm is not sufficient for small animal imaging, it is expected that this high statistics data will be utilized to compliment the high resolution pinhole data and improve the reconstruction. It is also likely that further gains are possible. Also, techniques where resolutions of the order of ≥ 2.0 mm can be obtained

with relatively high statistics data sets are useful in other applications of SPEI.

Future work will involve both comparing and combining the pinhole data and large-area aperture Compton data in the framework of a maximum likelihood expectation maximization (ML-EM) reconstruction. A more realistic phantom for small animals, such as the Derenzo phantom, will be used to investigate the limits of image resolution and contrast that can be achieved for clusters of small features.

APPENDIX

Collimator Transmission Function: The slits on the collimator limit the cone back-projections as only certain gamma ray trajectories have a significant probability of traversing the Tungsten. The collimator transmission is given by,

$$p_t(\mathbf{r}_{\mathbf{v}1}) = \exp[-\mu_W^t L_W(\mathbf{r}_{\mathbf{v}1})] \quad (11)$$

where $L_W(\mathbf{r}_{\mathbf{v}1})$ is the length that $\mathbf{r}_{\mathbf{v}1}$ intersects with the collimator material. The collimator transmission function has values $0 \leq p_t(\mathbf{r}_{\mathbf{v}1}) \leq 1$, depending on the thickness of Tungsten traversed. To obtain $L_W(\mathbf{r}_{\mathbf{v}1})$, a 3D ray-tracing algorithm was implemented. Currently, to simplify the calculation, $p_t(\mathbf{r}_{\mathbf{v}1})$ was set to zero for $\forall L_W(\mathbf{r}_{\mathbf{v}1}) > 0$. The effect of the collimator transmission function is demonstrated in Fig. 4(a) and (b). The transmission function truncates the cone surface and therefore reduces the number of possible locations from which the source emission may have occurred. It was also found to improve the accuracy of the gamma-ray tracking algorithms as the majority of the false interaction orderings cannot be traced back through the collimator.

Detector Interaction Probabilities: The probability that a Compton scatter occurs in a detector is given by [18],

$$p_C = \frac{\mu_{Si}^C(e_0, Z)}{\mu_{Si}^t(e_0, Z)} \exp[-\mu_{Si}^t L_{Si}(\mathbf{r}_{\mathbf{v}1})] \quad (12)$$

where $\mu_{Si}^C(e_0, Z)$ is the incoherent scattering linear attenuation coefficient and $\mu_{Si}^t(e_0, Z)$ is the total attenuation coefficient. For a stack geometry such as PEDRO, the probability that the photon traversed all other detectors between the source and \mathbf{r}_1 can also be included. This probability is given by,

$$p_{v1} = \exp[-\mu_{Si}^t L_{Si}(\mathbf{r}_{\mathbf{v}1})]. \quad (13)$$

Following the initial scatter, the photon must then escape the primary interaction detector and traverse all other material intersected along \mathbf{r}_{12} . This probability is given by,

$$p_{12} = \exp[-\mu_{Si}^t L_{Si}(\mathbf{r}_{12})]. \quad (14)$$

Finally the photon must undergo a second interaction at \mathbf{r}_2 , with probability,

$$p_i = 1 - \exp[-\mu_{Si,HPD}^t L_{Si,HPD}^{hit}(\mathbf{r}_{12})] \quad (15)$$

where $\mu_{Si,HPD}^t$ and $L_{Si,HPD}^{hit}$ are the linear attenuation and depth of intersection of the detector, either Si or HPD, at the second interaction.

Scattering Distribution Function: Given a Compton scatter is recorded, the angular probability for unpolarized incident photons is governed by $p(\theta_C)$, the scattering corrected Klein-Nishina cross section [19], [20], given by,

$$p(\theta_C) = K \frac{d\sigma_{KN}}{d\Omega} \Big|_{\theta_C} \cdot \sin \theta_C \cdot S(x, Z) \quad (16)$$

where K is a normalization factor so that $\int_0^\pi p(\theta) d\theta = 1$, $S(x, Z)$ is incoherent scattering function with $x = \sin \theta / \lambda (\text{\AA})$ and $\lambda (\text{\AA}) = 12.39852 / e_0 (keV)$. $S(x, Z)$ is material dependent and its functional dependence can be found in [21], $d\sigma_{KN}/d\Omega|_{\theta_C}$ is Klein-Nishina cross section at θ_C given by,

$$\frac{d\sigma_{KN}}{d\Omega} \Big|_{\theta_C} = \frac{r_e^2}{2} \left(\frac{e_1}{e_0} \right)^2 \left(\frac{e_0}{e_1} + \frac{e_1}{e_0} - \sin^2 \theta_C \right) \quad (17)$$

where $r_e = e^2 / (4\pi\epsilon_0 m_e c^2) = 2.818 \times 10^{-15} \text{m}$ is the classical electron radius.

Angular Uncertainty Function: For an arbitrary gamma ray, \mathbf{r}_{01} has a magnitude r_{01} . Similarly, the first and second interaction positions \mathbf{r}_1 and \mathbf{r}_2 define a vector \mathbf{r}_{12} with magnitude r_{12} . The angular uncertainty due to detector spatial resolution is described in [22] as,

$$\Delta\theta_r = \frac{\Delta r_1}{r_{v1}} \sqrt{1 + \alpha^2 (1 + \beta^2) + 2\alpha \cos \theta_C} \quad (18)$$

where $\alpha = r_{v1}/r_{12}$, $\beta = \Delta r_2/\Delta r_1$, Δr_1 and Δr_2 are the spatial resolutions of the detectors in which the first and second interactions occurred (see Table I).

The angular uncertainty due to energy resolution can be obtained from the derivative of (7) with respect to the energy of the scattered photon e_1 [23]. The uncertainty is expressed as,

$$\Delta\theta_E = \frac{m_e c^2}{e_1^2 \sin \theta_C} \Delta E_T \quad (19)$$

where ΔE_T is the total energy uncertainty caused by Doppler Broadening (ΔE_D) and detector energy resolution (ΔE_R). The energy uncertainty due to Doppler Broadening can be approximated according to [24], [25],

$$\Delta E_D \approx \frac{e_1}{e_0} \sqrt{e_0^2 + e_1^2 - 2e_0 e_1 \cos \theta_C} \frac{\Delta p_z}{m_e c} \quad (20)$$

where $\Delta p_z/m_e c$ is the dimensionless FWHM of the Compton profile. From [26] and [24], $\Delta p_z/m_e c$ for Si and CdTe are equal to 0.95×10^{-2} and 2.03×10^{-2} , respectively.

Combined with the FWHM of the detector energy resolution ΔE_R , the total energy uncertainty becomes,

$$\Delta E_T = \sqrt{\Delta E_R^2 + \Delta E_D^2} \quad (21)$$

and the total angular uncertainty is:

$$\Delta\theta = \sqrt{\Delta\theta_r^2 + \Delta\theta_E^2}. \quad (22)$$

ACKNOWLEDGMENT

The authors wish to acknowledge Monash University for the use of their Nimrod software in this work.

REFERENCES

- [1] S. Metzler, R. Accorsi, A. Ayan, and R. Jaszczak, "Slit-slat and multi-slit-slat collimator design and experimentally acquired phantom images from a rotating prototype," *IEEE Trans. Nucl. Sci.*, vol. 57, pp. 125–134, 2010.
- [2] S. Meikle, P. Kench, A. Weisenberger, R. Wojcik, M. Smith, S. Majewski, S. Eberl, R. Fulton, A. Rosenfeld, and M. Fulham, "A prototype coded aperture detector for small animal SPECT," in *Nuclear Science Symp. Conf. Record*, 2002, vol. 3, pp. 1580–1584.
- [3] J. Qian, E. Bradley, S. Majewski, V. Popov, M. Saha, M. Smith, A. Weisenberger, and R. Welsh, "A small-animal imaging system capable of multipinhole circular/helical SPECT and parallel-hole SPECT," *Nucl. Instrum. Methods Phys. Res. A*, vol. 594, pp. 102–110, 2008.
- [4] S. Motomura, S. Enomoto, H. Haba, K. Igarashi, Y. Gono, and Y. Yano, "Gamma-ray Compton imaging of multitracer in biological samples using strip germanium telescope," *IEEE Trans. Nucl. Sci.*, vol. 54, pp. 710–717, 2007.
- [5] M. Dimmock, J. Gillam, T. Beveridge, J. Brown, R. Lewis, and C. Hall, "A pixelated emission detector for radioisotopes (PEDRO)," *Nucl. Instrum. Methods Phys. Res. A*, vol. 612, pp. 133–137, 2009.
- [6] N. Clinthorne, C. Ng, C. Hua, J. Gormley, J. Leblanc, S. Wilderman, and W. Rogers, "Theoretical performance comparison of a Compton-scatter aperture and parallel-hole collimator," in *Proc. Nuclear Science Symp.*, 1996, vol. 2, pp. 788–792.
- [7] B. Smith, "Reconstruction methods and completeness conditions for two Compton data models," *J. Opt. Society Amer. A*, vol. 22, pp. 445–459, 2005.
- [8] B. Smith and L. Denbina, "Cameras shapes for medical imaging Compton cameras," *Proc. SPIE*, vol. 7805, p. 780512, 2010.
- [9] D. Wilson, H. Barrett, and E. Clarkson, "Reconstruction of two-and three-dimensional images from synthetic-collimator data medical imaging," *IEEE Trans. Med. Imaging*, vol. 19, pp. 412–422, 2002.
- [10] S. Midgley, A. Berry, N. Benci, S. Morton, D. Phillips, P. Smith, S. Troja, and R. Lewis, "Hybrid pixel detector development for medical radiography," *Nucl. Instrum. Methods Phys. Res. A*, vol. 573, pp. 129–132, 2007.
- [11] A. Lynch, A. Berry, G. Panjkovic, and R. Lewis, "Generic data acquisition system for multi-dimensional radiation detectors," in *IEEE Nuclear Science Symp. Conf. Record, NSS'07*, 2008, vol. 1, pp. 478–481.
- [12] L. Meng, W. Rogers, N. Clinthorne, and J. Fessler, "Feasibility study of Compton scattering enhanced multiple pinhole imager for nuclear medicine nuclear science," *IEEE Trans. Nucl. Sci.*, vol. 50, pp. 1609–1617, 2003.
- [13] S. Agostinelli, J. Allison, K. Amako, J. Apostolakis, H. Araujo, P. Arce, M. Asai, D. Axen, S. Banerjee, and G. Barrand, "Geant4-a simulation toolkit," *Nucl. Instrum. Methods Phys. Res. A*, vol. 506, pp. 250–303, 2003.
- [14] S. Wilderman, J. Fessler, N. Clinthorne, J. LeBlanc, and W. Rogers, "Improved modeling of system response in list mode EM reconstruction of Compton scatter camera images," *IEEE Trans. Nucl. Sci.*, vol. 48, pp. 111–116, 2001.
- [15] D. S. Vickers, "Collimator for Radiation Detectors and Method of Use," U.S. patent 7612343, 2009.
- [16] D. Abramson, J. Giddy, and L. Kotler, "High performance parametric modeling with Nimrod/G: Killer application for the global grid?," in *Proc. Int. Parallel and Distributed Processing Symp. (IPDPS)*, Cancun, Mexico, May 2000, pp. 520–528.
- [17] G. Pratz and C. Levin, "Bayesian reconstruction of photon interaction sequences for high-resolution PET detectors," *Phys. Med. Biol.*, vol. 54, pp. 5073–5094, 2009.
- [18] S. Wilderman, N. Clinthorne, J. Fessler, C. Hua, and W. Rogers, "List mode EM reconstruction of Compton scatter camera images in 3-D," in *Proc. IEEE Nuclear Science Symp.*, vol. 3.
- [19] D. Cullen, "A simple model of photon transport," *Nucl. Instrum. Methods Phys. Res. A*, vol. 101, pp. 499–510, 1995.
- [20] T. Kragh, "Tradeoffs and Limitations in Statistically Based Image Reconstruction Problems," Ph.D. dissertation, The Univ. Michigan, Ann Arbor, 2002.
- [21] J. Hubbell, W. Veigele, E. Briggs, R. Brown, D. Cromer, and R. Howerton, "Atomic form factors, incoherent scattering functions, and photon scattering cross sections," *J. Phys. Chem. Ref. Data*, vol. 4, pp. 471–538, 1975.
- [22] C. Ordonez, W. Chang, and A. Bolozdynya, "Angular uncertainties due to geometry and spatial resolution in Compton cameras," *IEEE Trans. Nucl. Sci.*, vol. 46, pp. 1142–1147, 1999.
- [23] A. Zoglauer and G. Kanbach, "Doppler broadening as a lower limit to the angular resolution of next-generation Compton telescopes," in *Proc. Society of Photo-Optical Instrumentation Engineers (SPIE) Conf. Series*, 2003, vol. 4851, pp. 1302–1309.
- [24] G. Matscheko, G. Carlsson, and R. Ribberfors, "Compton spectroscopy in the diagnostic x-ray energy range: II. Effects of scattering material and energy resolution," *Phys. Med. Biol.*, vol. 34, pp. 199–208, 1989.
- [25] M. Hirasawa and T. Tomitani, "An analytical image reconstruction algorithm to compensate for scattering angle broadening in Compton cameras," *Phys. Med. Biol.*, vol. 48, pp. 1009–1026, 2003.
- [26] F. Biggs, L. Mendelsohn, and J. Mann, "Hartree-Fock Compton profiles for the elements," *Atomic Data Nucl. Data Tables*, vol. 16, pp. 201–309, 1975.

Laplacian Erosion: An Image Deblurring Technique for Multi-Plane Gamma-Cameras

Laplacian Erosion: An Image Deblurring Technique for Multi-Plane Gamma-Cameras

J. M. C. Brown, J. E. Gillam, D. M. Paganin and M. R. Dimmock

Published in IEEE Transactions on Nuclear Science, Volume 60(5), Pages 3333–3342, 2013

DOI: 10.1109/TNS.2013.2264946

Reproduced here with kind permission from IEEE.

Declaration for Thesis Chapter 6

Declaration by candidate

In the case of Chapter 6, the nature and extent of my contribution to the work was the following:

Nature of Contribution	Extent of Contribution (%)
Developed the technique, extended the Geant4 application, undertook the simulations and analysis, and wrote up the paper	90 %

The following co-authors contributed to the work. If co-authors are students at Monash University, the extent of their contribution in percentage terms is stated:

Name	Nature of Contribution	Extent of Contribution (%)
J. E. Gillam	Provided supervisory advice, aided proofreading and drafting	
D. M. Paganin	Provided supervisory advice, aided proofreading and drafting	
M. R. Dimmock	Provided supervisory advice, aided proofreading and drafting	

The undersigned hereby certify that the above declaration correctly reflects the nature and extent of the candidate's and co-authors' contributions to this work.

Candidate's Signature:

Date: / /

Main Supervisor's Signature:

Date: / /

Laplacian Erosion: An Image Deblurring Technique for Multi-Plane Gamma-Cameras

Jeremy M. C. Brown, John E. Gillam, David M. Paganin, and Matthew R. Dimmock

Abstract—Laplacian Erosion, an image deblurring technique for multi-plane Gamma-cameras, has been developed and tested for planar imaging using a GEANT4 Monte Carlo model of the Pixelated Emission Detector for Radioisotopes (PEDRO) as a test platform. A contrast and Derenzo-like phantom composed of ^{125}I were both employed to investigate the dependence of detection plane and pinhole geometry on the performance of Laplacian Erosion. Three different pinhole geometries were tested. It was found that, for the test system, the performance of Laplacian Erosion was inversely proportional to the detection plane offset, and directly proportional to the pinhole diameter. All tested pinhole geometries saw a reduction in the level of image blurring associated with the pinhole geometry. However, the reduction in image blurring came at the cost of signal to noise ratio in the image. The application of Laplacian Erosion was shown to reduce the level of image blurring associated with pinhole geometry and improve recovered image quality in multi-plane Gamma-cameras for the targeted radiotracer ^{125}I .

Index Terms—Image deblurring, mechanical collimation, single photon emission imaging.

I. INTRODUCTION

SINGLE Photon Emission Imaging (SPEI) is the process of constructing an image to estimate the geometry and characteristics of an object from its emitted x- and/or γ -ray radiation. Mechanical SPEI, the predominant collimation method in SPEI, employs a direct or coded aperture to restrict the solid angle of radiation incident upon the surface of a position-and-energy-resolving radiation detector [1]. The restriction of the solid angle allows for the incident trajectory of a detected photon to be estimated. The accuracy of the estimated incident trajectory and the fraction of emitted radiation allowed to pass through an aperture are inversely proportional [2]. The result is a trade off between spatial resolution and sensitivity, the limiting factor of mechanically collimated SPEI [3].

Two approaches have been explored in an attempt to address this trade off: increasing the number of Gamma cameras aimed

at the target Field Of View (FOV) [4], [5] and multiplexing of apertures in the mechanical collimator [6]. The cost associated with the first of these two approaches is substantial due to the required number and size of detector modules, processing electronics and computer hardware. The second approach utilises overlapping projections of two or more apertures to increase the sensitivity of an individual radiation detector while retaining the same spatial resolution [7]. For events that interact within the regions of overlapping aperture projections, a number of possible lines of response may be indicated, thereby reducing the individual event information in that region [8]. Any increase in sensitivity comes at a cost of the average level of information that a single measurement carries [9].

The need for a more effective way to demultiplex overlapping projections led to the development of synthetic collimation [10]. Synthetic collimation utilises multiple detection planes behind a coded aperture in combination with an application-specific version of the maximum likelihood-expectation maximisation (ML-EM) algorithm [10]. To maximise the performance of these systems, the geometrical optimisation of detector designs and system geometry is required [11]. In the case of a two-detection-plane system, the first detection plane in the stack is placed close enough to the coded aperture so that no multiplexing is present. However, finite thickness (poor depth of interaction measurement), electronic read out time of the radiation detector and image distortion associated with the geometry of the pinhole at close distances can result in an increase in image blurring. Two of the three limiting effects, finite thickness and electronic read out time, can be minimised through replacing the single radiation detector with a number of thinner devices.

The present work explores the development of a physically motivated image deblurring technique, Laplacian Erosion, to address the image distortion associated with the pinhole geometry for synthetically collimated multi-plane Gamma-cameras that utilise a number of thin radiation detectors in the non-multiplexing region. The mathematical development of the Laplacian Erosion algorithm can be found in Section II. Section III describes the Monte Carlo radiation transport model, planar image recovery methods and assessment metrics employed to assess the dependence of the developed algorithm on target detection plane and pinhole geometry using the Pixelated Emission Detector for Radioisotopes (PEDRO) [12] as a test system. The results of the algorithm's testing, a discussion and an overall conclusion of the present work follows in Sections IV, V and VI respectively.

II. LAPLACIAN EROSION

Every SPEI system exhibits some level of image blurring associated with the method of collimation. For a mechanically col-

Manuscript received March 19, 2012; revised August 09, 2012; accepted May 07, 2013. Date of publication July 19, 2013; date of current version October 09, 2013. This study was supported by the Cooperative Research Centre for Biomedical Imaging Development Ltd (CRC-BID), established and supported under the Australian Government's Cooperative Research Centres Programme. J. E. Gillam was supported by a CSIC 'Juan de la Cierva' program.

J. M. C. Brown, D. M. Paganin, and M. R. Dimmock are with the School of Physics, Monash University, Victoria 3800, Australia

[redacted] CSIC Universitat de Valencia, Valencia E-46071, Spain

Color versions of one or more of the figures in this paper are available online at <http://ieeexplore.ieee.org>.

Digital Object Identifier 10.1109/TNS.2013.2264946

limited SPEI system, the image blurring can be approximated as a symmetric Point Spread Function (PSF) incorporating the blurring factors associated with the pinhole geometry, source distribution in the imager's FOV, the offset of the detection plane from the collimator and the spatial resolution at the detection plane [13], [14].

The image data measured at a detection plane n ($D_n(x, y)$) can be expressed as:

$$D_n(x, y) = I_n(x, y) * PSF_n(x, y) \quad (1)$$

where $I_n(x, y)$ is the projection of the source distribution in the FOV onto plane n , $PSF_n(x, y)$ is a rotationally symmetric PSF that models the image blurring at plane n and $*$ denotes two-dimensional convolution.

Laplacian Erosion is a physically motivated method of image deblurring for multi-plane Gamma-cameras, conceptually similar to unsharp masking, used to reduce the blurring associated with the effects of pinhole geometry. Unlike techniques such as unsharp masking, Laplacian Erosion utilises *measured* quantities rather than purely mathematical processing methods to remove image blurring. The development of this physically motivated image deblurring technique starts from the common form of the unsharp masking algorithm [15]:

$$I(x, y) \approx D(x, y) - \alpha \nabla^2 D(x, y) \quad (2)$$

where $\nabla^2 \equiv \partial_x^2 + \partial_y^2$ is the transverse Laplacian and α is a real-valued free parameter that allows the degree of sharpening to be tuned. The multiple-plane nature of multi-plane Gamma-cameras enables the Laplacian of the image data measured at plane n to be estimated *experimentally* from the multiple image-planes collected simultaneously. As the rotationally symmetric PSF is a function of the distance between the collimator and detection plane, the multiple planes within the system record images that have been blurred to different extents.

The following proof illustrates how the Laplacian of the first detection plane in a two-detection-plane system can be estimated through a weighted subtraction. The measured images $D_1(x, y)$ and $D_2(x, y)$ are given by:

$$D_1(x, y) = I(x, y) * PSF_1(x, y), \quad (3)$$

$$D_2(x, y) = I(x, y) * PSF_2(x, y). \quad (4)$$

Here $I(x, y)$ is the ideal image of the radiotracer distribution in the FOV and $PSF_1(x, y)$ and $PSF_2(x, y)$ denote the rotationally symmetric PSFs at each detection plane. The PSFs can be modelled as Gaussian functions:

$$PSF_{1,2}(x, y) = e^{-(x^2+y^2)/2\sigma_{1,2}^2} \quad (5)$$

where $\sigma_1 < \sigma_2$. The weighted difference between the two normalised images is:

$$\alpha D_1 - \beta D_2 = I * \left[\alpha e^{-(x^2+y^2)/2\sigma_1^2} - \beta e^{-(x^2+y^2)/2\sigma_2^2} \right], \quad (6)$$

where α and β are real numbers. Fourier transformation of (6) leads to:

$$\mathcal{F}(\alpha D_1 - \beta D_2) = \mathcal{F}(I) \times \left[\alpha e^{-\sigma_1^2(u^2+v^2)/2} - \beta e^{-\sigma_2^2(u^2+v^2)/2} \right] \quad (7)$$

after application of the convolution theorem. A second order Taylor series approximation to the Gaussian then yields:

$$\mathcal{F}(\alpha D_1 - \beta D_2) = \mathcal{F}(I) \times \left[\alpha - \beta + \frac{\beta\sigma_2^2 - \alpha\sigma_1^2}{2} (u^2 + v^2) \right]. \quad (8)$$

Now let $A = (\beta\sigma_2^2 - \alpha\sigma_1^2)/2$ and $B = \alpha - \beta$, hence:

$$\mathcal{F}(\alpha D_1 - \beta D_2) = B\mathcal{F}(I) + A[u^2\mathcal{F}(I) + v^2\mathcal{F}(I)]. \quad (9)$$

The Fourier derivative theorem [16] is then applied in reverse to give:

$$\mathcal{F}(\alpha D_1 - \beta D_2) = B\mathcal{F}(I) - A \left[\mathcal{F} \left(\frac{\partial^2}{\partial x^2} I \right) + \mathcal{F} \left(\frac{\partial^2}{\partial y^2} I \right) \right], \quad (10)$$

where taking the inverse Fourier transform then yields:

$$\alpha D_1 - \beta D_2 \cong BI - A\nabla^2 I. \quad (11)$$

If α and β are set to 1 and we let $A = -1/b$, then:

$$D_1 - D_2 \approx \frac{1}{b} \nabla^2 I \quad (12)$$

where b is a normalisation constant. Therefore the Laplacian of the data at plane i can be estimated by:

$$\nabla^2 D_i(x, y) \cong [c_i D_i(x, y) - c_{i+1} D_{i+1}(x, y)] \quad (13)$$

where i is the image plane under consideration and c_i are normalisation and image resampling operators which normalise the total sum of image intensity data $D_i(x, y)$ to one. Both sets of image data are resampled and mapped to the same size and spatial resolution in image space, where the first plane, $i = 1$, is the plane with the largest amount of image blurring. The index increases plane by plane towards the plane with the least blurring.

A threshold operator \mathcal{T} may now be introduced into (13) to isolate the values of the positive components of the summand associated with the width increase of the object upon blurring. Removal of the negative components of the summand has a secondary effect of reducing the impact of amplifying statistical noise due to the intensity differences. Thus, with the definition:

$$\mathcal{T}f(x_i, y_j) = \begin{cases} f(x_i, y_j) & \text{if } f(x_i, y_j) \geq 0, \\ 0 & \text{if } f(x_i, y_j) < 0, \end{cases} \quad (14)$$

Equation (13) becomes:

$$\nabla^2 D_i(x, y) \cong \mathcal{T} [c_i D_i(x, y) - c_{i+1} D_{i+1}(x, y)]. \quad (15)$$

Equation (15) gives an experimentally informed estimate of the Laplacian of $D_i(x, y)$, which may be contrasted with the numerical methods employed in unsharp masking, that isolates the positive components associated with the width increase of the object upon blurring. For a system of n_{max} detection planes, the targeted Laplacian estimate of the width increase of the object upon blurring between detection planes can be estimated for each plane n up to n_{max} . The summation of these planes gives an experimental estimate of the transformation of the image data $D_n(x, y)$ with respect to the image with the lowest level of image blurring, $D_{n_{max}}(x, y)$, due to the rotationally symmetric PSF of the imaging system. This summation of experimental estimates of each set of image data represents a higher-order estimate of the Laplacian of the image data $D_n(x, y)$ from n to n_{max} . This summation can be given by:

$$\nabla^2 D_n(x, y) \cong \sum_{i=n}^{n_{max}} \mathcal{T} [c_i D_i(x, y) - c_{i+1} D_{i+1}(x, y)]. \quad (16)$$

The substitution of (16) into (2), including \mathcal{T} and normalising terms to rescale the image, yields:

$$I_n(x, y) \cong w_{n_{max}} \mathcal{T} \left[c_n D_n(x, y) - \sum_{i=n}^{n_{max}} \mathcal{T} [c_i D_i(x, y) - c_{i+1} D_{i+1}(x, y)] \right] \quad (17)$$

where $I_n(x, y)$ is the ideal image measured at plane n and $w_{n_{max}}$ normalises the sum of $I_n(x, y)$ to match the sum of the events in planes n to n_{max} .

The signal-to-noise limited nature of multi-plane pinhole SPEI significantly affects the estimation of the Laplacian via (16). The random nature of radioactive decay and the reduction of radiation flux incident on each plane as a function of depth

in the detection stack increase the influence of Poisson noise on the measured image data. The increase in noise degrades the accuracy to which the Laplacian of the image at each plane n can be estimated, reducing the quality of the estimate of the ideal image $I_n(x, y)$. To measure this a standard error metric, the Root Mean Square Difference (RMSD), was utilised (see Section III-C). Each time a new plane is included into the calculation, increasing $i = n_{max}$ by 1, the RMSD is calculated between the current estimate of $I_n(x, y)$ and the previous estimate $I_{n-1}(x, y)$. The index is increased until the rate of change of the RMSD changes sign; at this point Poisson noise will start to dominate the estimated Laplacian. The index is the maximum number (n_{RMSD}) of detection planes that should be used to estimate the Laplacian before noise degradation occurs. The substitution of n_{RMSD} for n_{max} in (17) results in the final form of the Laplacian Erosion algorithm:

$$I_n(x, y) \cong w_{n_{RMSD}} \mathcal{T} \left[c_n D_n(x, y) - \sum_{i=n}^{n_{RMSD}} \mathcal{T} [c_i D_i(x, y) - c_{i+1} D_{i+1}(x, y)] \right]. \quad (18)$$

III. METHOD

The Monte Carlo radiation transport modelling toolkit GEANT4 [17] was used to investigate the performance of the Laplacian Erosion algorithm for a single-pinhole collimator. Previously, a GEANT4 application was developed for optimising design and aiding in development of novel image reconstruction methods for hybrid SPEI with PEDRO [12], [18]. This GEANT4 application was employed to undertake two investigations: 1) to illustrate the performance of Laplacian Erosion as a function of the target detection plane in the test imaging system and 2) exploration of the effect of pinhole geometry on the performance of the algorithm.

A. System Model

A variant of PEDRO, with geometry shown in Fig. 1, was constructed specifically to assess the performance of Laplacian Erosion using the GEANT4 application. The PEDRO variant contains a stack of five Si Double Sided Strip Detectors (DSSDs) with a separation of 1.0 mm centred 10.5 mm behind a 2.0 mm thick single pinhole tungsten collimator. Each Si DSSD is 1.0 mm thick with a surface area of 32 mm by 32 mm, grid size of 0.1 mm and an energy resolution of 5% Full Width of Half Maximum (FWHM).

A contrast and Derenzo-like phantom, shown in Fig. 2, were selected to assess the effect of the Laplacian Erosion algorithm on the contrast and resolution, respectively. Each phantom was composed of an ideal ^{125}I radiotracer emitting 30 keV photons. The phantoms were centred 24.0 mm from the front of the collimator, filling the FOV of the rear detection plane. To avoid wasted event processing, the emission direction of the photons was confined to the same isotropically distributed cone at every position. The opening angle of the cone was set to 15° to sufficiently cover the total open cross-section of the largest pinhole

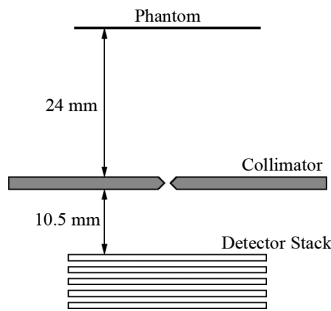


Fig. 1. The geometry of the GEANT4 Monte Carlo model of the PEDRO variant.

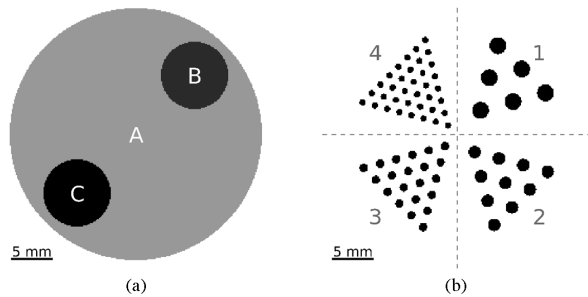


Fig. 2. The two phantoms, a contrast (a) and Derenzo like (b), employed to test the performance of Laplacian Erosion using the test multi-plane Gamma-camera PEDRO.

TABLE I
THE RELATIVE INTENSITY RATIOS, POSITION/RADIAL SEPARATION CENTRE TO CENTRE AND RADII OF EACH FEATURE WITHIN THE PHANTOMS SEEN IN FIG. 2

Phantom	Feature	Relative Intensity	Position (x, y) / Radial Separation (mm)	Radii (mm)
Contrast	A	1.0	0.0, 0.0	15.0
	B	10.0	7.0, 7.0	4.0
	C	50.0	-7.0, -7.0	4.0
Derenzo-like	1	1.0	4.0	1.0
	2	1.0	3.0	0.75
	3	1.0	2.0	0.5
	4	1.0	1.5	0.375

aperture at the edges of each phantom. At each emission location the axis of the cone was aligned with the centre of the pinhole; if a sampled emission direction did not fall within this cone the position and emission direction of the event were resampled. A total of 30×10^6 photons were emitted in this directional cone during each run. 240 runs were performed for each geometry and the data histograms were combined prior to the analysis outlined in Section III-C. The specifications of each feature within the two phantoms are shown in Table I.

In total, three different pinhole geometries were investigated. The geometries of the three pinholes, outer to inner diameter, are as follows: 1) 4.5 mm to 1.5 mm, 2) 3.0 mm to 1.0 mm and 3) 1.5 mm to 0.5 mm. For each pinhole geometry three simulations were executed; one for each phantom and a 32.0 mm^2 planar source (for the sensitivity correction). The simulations

of the planar source were used to calculate the sensitivity functions for each detection plane from a total of 6×10^9 30 keV photons. These sensitivity functions were blurred with a two-dimensional Gaussian, with three pixel standard deviation, to suppress Poisson noise and then used to correct the images measured at each detection plane.

B. Image Recovery

The image recovery process of the PEDRO variant was based on a planar energy gated pinhole projection algorithm. A single 10% energy window was applied around the centre of the 30 keV full-energy peak. An individual image representing each detector histogram was recovered, corrected for sensitivity and resampled to the same spatial resolution at the object plane. These data were used to form a set of Laplacian Eroded images, one for each plane, and two additional images: a standard and a processed summation image. The standard image was constructed from the summation of all five planes into a single image, the processed image from the sum of the five resultant images after application of the Laplacian Erosion algorithm.

C. Assessment of Reconstructed Image Quality

The two phantoms were selected to investigate the influence of Laplacian Erosion on contrast, signal to noise and spatial resolution of the reconstructed images. Procedures employed to assess the reconstructed image quality were unique to each phantom. Assessment of the Derenzo-like phantom were based on spatial resolution and required the use of line profiles along the centre of the outer triangle of each group of disks and visual assessment of the reconstructed images. For the contrast phantom three Figures of Merit (FoMs) were utilised as well as visual assessment of an image formed from the difference of each recovered image with the simulated phantom. The three FoMs were selected to assess the influence of: the ratio of measured to ideal contrast between features, Signal to Noise Ratio (SNR) and the RMSD between the recovered image and the simulated phantom. Each measure is defined below.

Contrast is defined as:

$$C = \frac{\mu_1 - \mu_2}{\mu_1 + \mu_2} \quad (19)$$

where μ_1 and μ_2 are the mean value of the area of higher intensity and local background respectively. The contrast of the features within the images were determined to their background (C_M) and compared to that of the known contrast of the true phantom (C_P) as the ratio C_M/C_P .

Signal to Noise Ratio (SNR) assesses the noise of a feature in an image. The SNR is defined as:

$$\text{SNR} = \frac{\mu}{\sigma} \quad (20)$$

where μ and σ are the mean and standard deviation of the pixel values in the feature. The SNR was assessed in the central region of each of the three features in the contrast phantom.

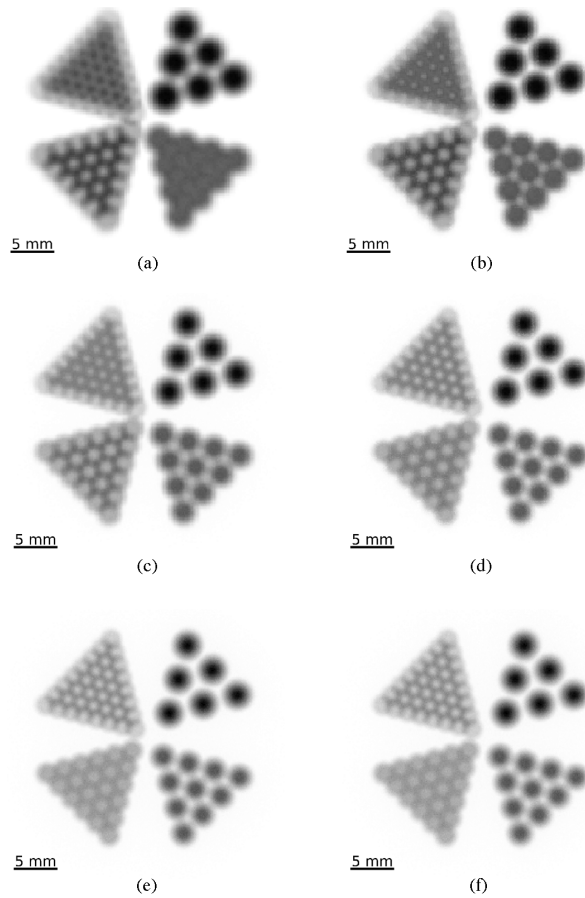


Fig. 3. The standard (left-hand side) and Laplacian Eroded (right-hand side) images recovered from the first (top), third (middle) and fifth (bottom) detection plane of the Derenzo-like phantom. An image scale indicator can be seen in the bottom left-hand side of each image, and for all images from here on.

Root Mean Square Difference (RMSD) quantifies the difference between the estimate of an object and the known object. The RMSD is defined as:

$$\text{RMSD} = \sqrt{\frac{\int \int |P_n(x, y) - I_n(x, y)|^2 dx dy}{\int \int |P_n(x, y)|^2 dx dy}} \quad (21)$$

where $P_n(x, y)$ is a normalised image of the known object and $I_n(x, y)$ is a normalised image estimate of the object.

IV. RESULTS

A. Detection Plane Dependence

1) *Derenzo-Like Phantom*: The standard and processed images recovered from the first, third and fifth detection plane of the Derenzo-like phantom can be seen in Fig. 3. Four observations can be made through the visual comparison of the standard and Laplacian Eroded images of each plane:

- the application of Laplacian Erosion enables the 0.75 mm disks in feature 2 (see Fig. 2(b)) of the phantom to be resolved in the first detection plane;
- the average level of image blurring has been reduced for the first and third detection plane;
- complicated artefacts are present in the 0.5 mm and 0.375 mm disk features of the recovered images;
- the eroded image at the fifth detection plane remains unchanged.

A comparison of the line profiles of the four different features of the Derenzo-like phantom Fig. 2(b) is shown in Fig. 4. Inspection of the line profiles for the 0.75 mm disk feature from the first detection plane, top set of profiles in Fig. 4(b), shows a clear reduction of local minima and increase of local maxima in the Laplacian Eroded profile, corresponding accurately with the features of the Derenzo-like phantom, that are not present in the standard recovered image. However, this reduction in local minima and increase of local maxima of the Laplacian Eroded profile in comparison to the Derenzo-like phantom is not isolated to the 0.75 mm disk feature of the first detection plane, with the top set of profiles in Fig. 4(a), corresponding to the 1.0 mm feature, showing a similar trend.

Comparison of the line profiles of the four different features of the phantom to the standard and Laplacian Eroded images from the third detection plane, as shown in Fig. 4, also show the trend observed in the first detection plane. However, the difference between the standard and Laplacian Eroded line profiles in the 1.0 mm disk feature is only minimal in comparison to the results of the first detection plane. This reduction and increase in signal in regions coinciding with zero and maximum intensity of the phantom is the primary goal of this image deblurring technique.

In all six images of Fig. 3 determination of the location of the disks within features 3 and 4 of the Derenzo-like phantom is counter intuitive (see Fig. 2(b)). The interplay of the PSF of each disk within their respective features creates a region that resembles a number of low activity disks in a high activity background. The centre location of each disk within its respective feature is at the centre of these low signal regions. This phenomenon is a result of the geometry of the phantom, its distance from the collimator and the geometrical configuration of PEDRO. Further occurrences of this artefact will be referred to as “*contrast inversion blurring*” and an expanded explanation of this phenomenon can be found in Appendix A.

As outlined in Section II, the process of image deblurring employed through Laplacian Erosion is based on the subtraction of an experimentally estimated Laplacian from a target image. The accuracy to which the Laplacian can be estimated via the current technique is limited by the spatial resolution of the detectors, system geometry and the location of each detection plane in the stack. Within the current system’s geometry, the contribution of image blurring at each detection plane decreases with distance from the collimator. As the fifth detection plane records the highest image spatial resolution, corresponding to the smallest level of image blurring, it sets the fundamental performance limit of Laplacian Erosion on the measured data. Thus the closer the detection plane to the collimator, the greater the improvement in image quality from Laplacian Erosion as the estimated Laplacian is of higher quality.

3338

IEEE TRANSACTIONS ON NUCLEAR SCIENCE, VOL. 60, NO. 5, OCTOBER 2013

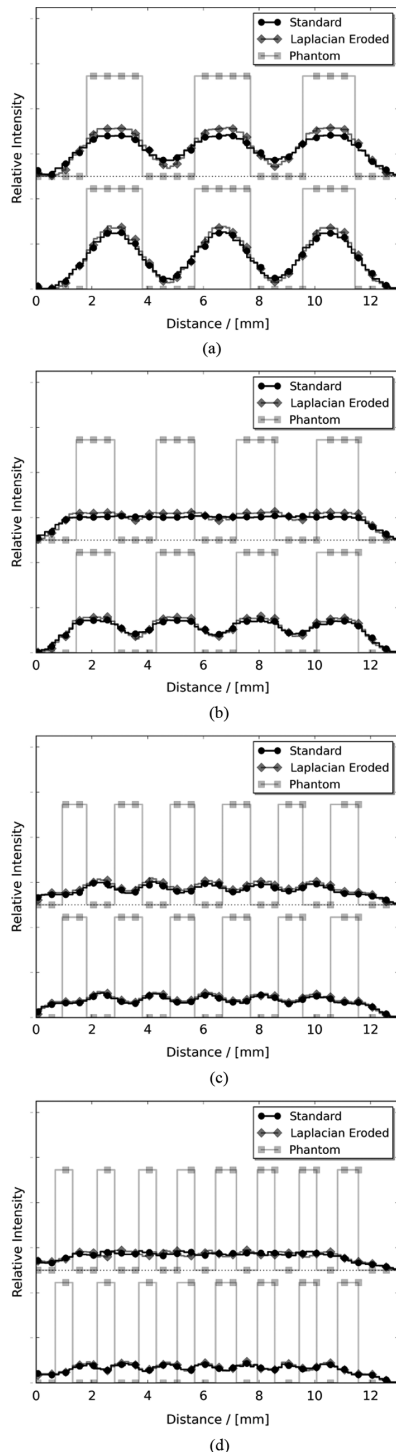


Fig. 4. A comparison of the standard and Laplacian Eroded image line profiles to the simulated phantom for the first (top) and third (bottom) detection planes. The disk radii of each feature's line profiles from top to bottom: 1.0 mm (a), 0.75 mm (b), 0.5 mm (c) and 0.375 mm (d).

2) *Contrast Phantom*: The difference images of standard and Laplacian Eroded images recovered from the first, third and fifth

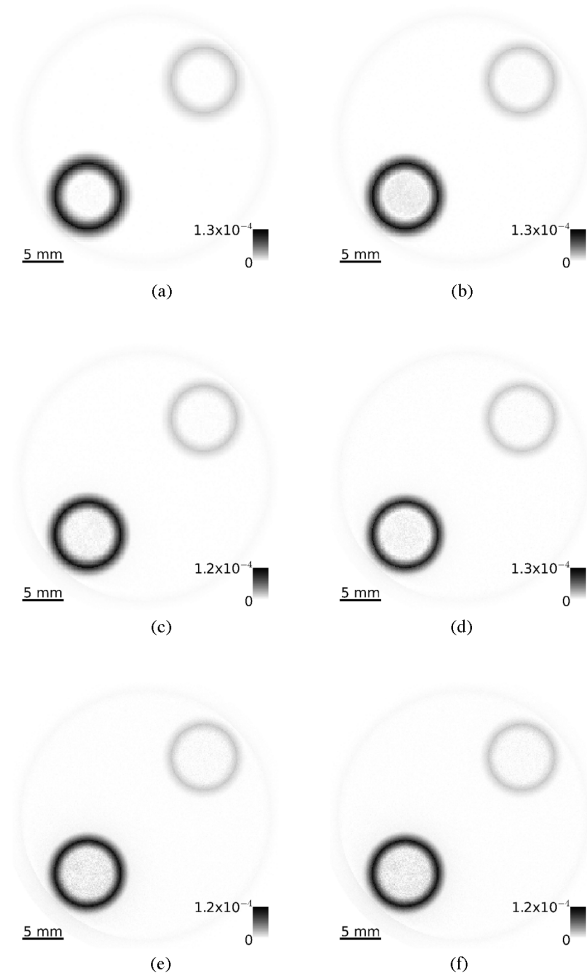


Fig. 5. The standard (left-hand side) and Laplacian Eroded (right-hand side) difference images recovered from the the first (top), third (middle) and fifth (bottom) detection planes of the contrast phantom.

detection planes to the simulated contrast phantom can be seen in Fig. 5. Visual inspection of these images yields two observations:

- reduction of the “halo” around the edge of each feature was observed;
- a higher contribution of Poisson noise was seen in the Laplacian Eroded difference images.

The reduction of the “halo” around the edge of each of the features from the standard to Laplacian Eroded image indicate a reduction in image blurring. Similar to the results from the Derenzo-like phantom, the reduction of the “halo” width in the third detection plane images are notably less than the first. Again the standard and Laplacian Eroded images from the fifth detection plane are identical.

Quantification of the contrast phantom for the first, third and fifth detection planes using the C_M/C_P , SNR and RMSD FOMs outlined in Section III-C can be found in Table II. It can be seen that the lower SNR of all three features within

TABLE II
THE SNR, C_M/C_P AND RMSD OF THE FIRST, THIRD AND FIFTH DETECTION PLANE FOR BOTH THE STANDARD AND LAPLACIAN ERODED IMAGES OF THE CONTRAST PHANTOM

Recon. Image	SNR			C_M/C_P		RMSD
	A	B	C	A to B	A to C	
P1 S	24.51	76.04	168.57	1.00	1.00	0.54
P1 LE	17.31	51.69	92.42	1.00	1.00	0.52
P3 S	13.26	39.02	86.21	0.99	1.00	0.52
P3 LE	9.70	28.19	53.61	1.00	1.00	0.50
P5 S	8.60	22.52	47.82	0.98	1.00	0.52
P5 LE	8.60	22.52	47.82	0.98	1.00	0.52

the contrast phantom, for the first and third detection plane, supported the visual observation that a higher contribution of Poisson noise was present in the Laplacian Eroded images. Examination of the relative image contrast ratios, C_M/C_P , of the standard and Laplacian Eroded images indicated that while the reduction of image blurring decreased the SNR of the image, the relative contrast between features remains unchanged. Finally, the lower RMSD values for the Laplacian Eroded images of the first and third detection plane indicates that there was a net improvement after removal of image blurring regardless of the observed decrease in SNR.

B. Pinhole Geometry Dependence

1) *Derenzo-Like Phantom*: The standard and Laplacian Eroded summation images for the three different pinhole geometries are shown in Fig. 6. Visual inspection and comparison of the recovered images yields two observations:

- all three pinhole geometries see a reduction in image blurring;
- through the application of Laplacian Erosion it is possible to observe feature structure not apparent in the standard images.

A comparison of the line profile of each feature of the simulated phantom to those of the standard and Laplacian Eroded images is shown in Fig. 7. Each sub-figure contains three sets of profiles for the large, 4.5 mm to 1.5 mm, medium, 3.0 mm to 1.0 mm, and small, 1.5 mm to 0.5 mm, diameter pinhole geometries. Inspection of the line profiles shows that for all three pinhole geometries, each feature in the Laplacian Eroded images either: more closely resembles the simulated phantom's line profiles, remains unchanged, or remains predominantly unchanged with an increased level of statistical variation.

Comparison of the standard and Laplacian Eroded images from the large diameter pinhole, see Fig. 6 (top), demonstrates the ability of Laplacian Erosion to improve the spatial resolution of multi-plane Gamma-cameras. Initially the 1.0 mm disk feature is indistinguishable for the large diameter pinhole image. Application of Laplacian Erosion improves the presentation of image information, enabling the location of individual features to be estimated. Inspection of the 1.0 mm disk feature line profiles, Fig. 7(a), shows that in the standard image no information regarding the location of the 1.0 mm disks can be obtained. This line profile exhibits the same characteristics as contrast inversion blurred features seen in Fig. 3. Inspection of the Laplacian Eroded line profile of the same features shows a reduction in the

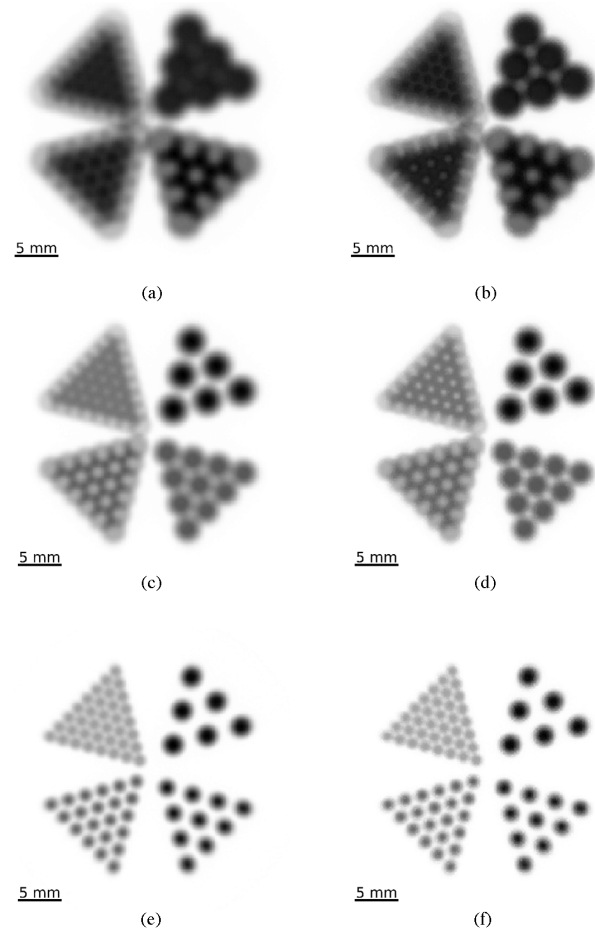


Fig. 6. The standard (left-hand side) and Laplacian Eroded (right-hand side) summation images recovered from the large, 4.5 mm to 1.5 mm, (top), medium, 3.0 mm to 1.0 mm, (middle) and small, 1.5 mm to 0.5mm, (bottom) diameter pinholes of the Derenzo-like phantom.

local minima and increase of local maxima corresponding with the respective features of the Derenzo-like phantom.

2) *Contrast Phantom*: The difference images of the standard and Laplacian Eroded images to the simulated contrast phantom for the large, medium and small diameter pinholes are shown in Fig. 8. Two observations can be made from visual inspection and quantitative analysis (see Table III) of these images:

- all three pinhole geometries see a reduction in image blurring from Laplacian Erosion;
- the performance of Laplacian Erosion is dependent on pinhole diameter.

After application of Laplacian Erosion, the width of the "halo" around the edge of each feature is reduced. This observation, in combination with the lower SNR of all three features for the Laplacian Eroded images, supports the conclusion that image deblurring through the use of Laplacian Erosion comes at the cost of image SNR. With the exception of the small diameter pinhole, the reduction in SNR does not degrade the contrast between features in the Laplacian Eroded image.

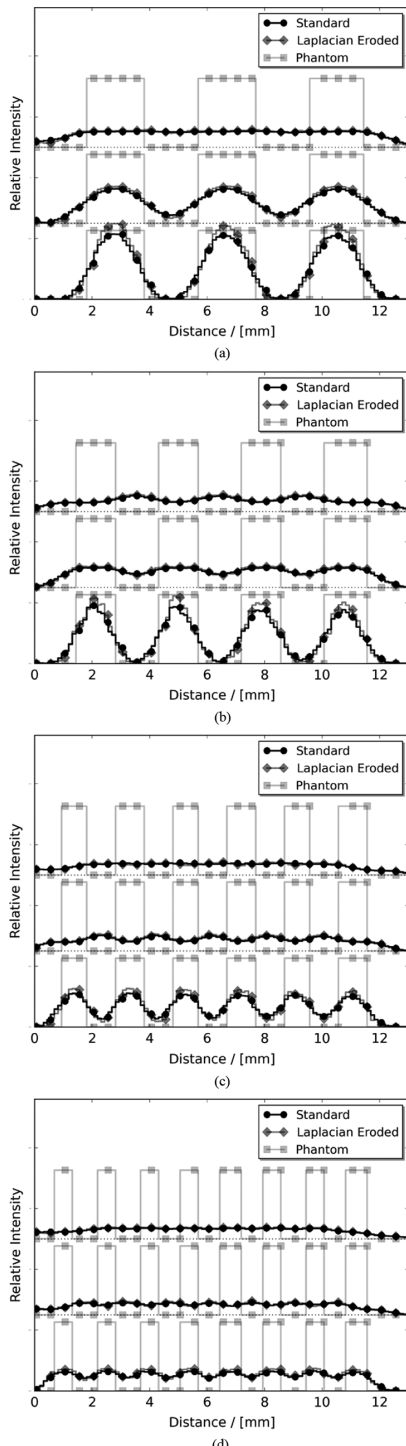


Fig. 7. A comparison of the standard and Laplacian Eroded summation image line profiles to the simulated phantom for the large, 4.5 mm to 1.5 mm, (top), medium, 3.0 mm to 1.0 mm, (middle) and small, 1.5 mm to 0.5 mm, (bottom) diameter pinholes. The disk radii of each feature's line profiles from top to bottom: 1.0 mm (a), 0.75 mm (b), 0.5 mm (c) and 0.375 mm (d).

The RMSD of the standard and Laplacian Eroded images for all three geometries can be seen in Table III. A direct relation-

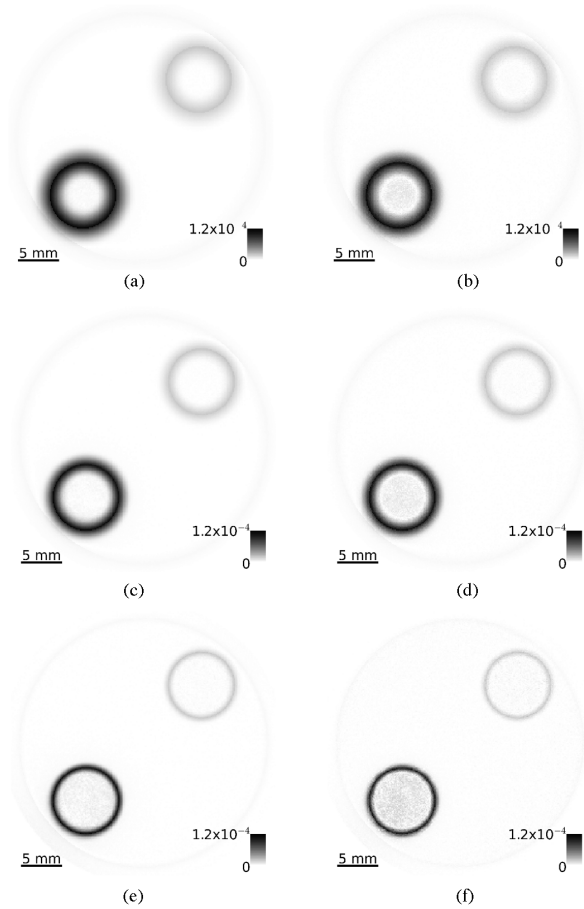


Fig. 8. The standard (left-hand side) and Laplacian Eroded (right-hand side) summation difference images recovered from the large, 4.5 mm to 1.5 mm, (top), medium, 3.0 mm to 1.0 mm, (middle) and small, 1.5 mm to 0.5 mm, (bottom) diameter pinholes of the contrast phantom.

TABLE III
THE SNR, C_M/C_P AND RMSD OF THE LARGE (Lrg), 4.5 mm TO 1.5 mm, MEDIUM (Med), 3.0 mm TO 1.0 mm, AND SMALL (Sm), 1.5 mm TO 0.5 mm, DIAMETER PINHOLE FOR BOTH THE STANDARD AND LAPLACIAN ERODED IMAGES OF THE CONTRAST PHANTOM

Recon. Image	SNR			C_M/C_P		RMSD
	A	B	C	A to B	A to C	
Lrg S	47.25	87.42	97.36	0.99	1.00	0.63
Lrg LE	16.33	39.33	67.63	1.00	1.00	0.60
Med S	32.12	101.12	196.09	1.00	1.00	0.53
Med LE	15.51	44.93	84.42	1.00	1.00	0.51
Sm S	17.76	51.38	109.18	1.00	1.00	0.41
Sm LE	7.33	19.99	41.66	1.01	1.00	0.41

ship between the pinhole diameter and performance of Laplacian Erosion can be observed. After the application of Laplacian Erosion, the RMSDs of the images improve (decrease) by 4.8%, 3.8% and 0.0% for the large, medium and small diameter pinholes respectively. Reduction in pinhole diameter has two effects which lead to the reduction in the performance of Laplacian Erosion: 1) a lower level of image blurring in measured data and 2) reduced open cross-section of the collimator restricts the amount of radiation incident on the detector stack.

These effects combine to increase the influence of Poisson noise relative to the true phantom signal measured on each detection plane in the test system. The method employed to estimate the Laplacian of each image then amplifies this noise and increases the variation in the image, reducing the SNR and damaging relative image contrast. However, the quality of the image, as assessed through the RMSD, remains unchanged.

V. DISCUSSION

Two investigations were undertaken to assess the performance of Laplacian Erosion as a function of detection plane and pinhole geometry. The first investigation showed that the integration of Laplacian Erosion into the image recovery process can reduce image blurring and recover a more accurate representation of the object for the majority of the detection planes within the test system. However, the detection plane with the highest resolution image and lowest level of image blurring will see little improvement, or degradation, due to Laplacian Erosion.

The investigation into the influence of pinhole diameter on the performance of Laplacian Erosion found that there is a direct relationship to pinhole diameter. As the pinhole diameter increased, so did the enhancement provided by Laplacian Erosion. For both test phantoms, all three pinhole geometries saw a reduction in image blurring after the application of Laplacian Erosion. As with the investigation into performance as a function of detection plane, the reduction in image blurring came at the cost of SNR. However, in the case of the small diameter pinhole the decrease in SNR resulted in a loss of image contrast and constant RMSD was observed. Depending on the specific imaging task, the reduction of image blurring at the cost of SNR and image contrast may be an acceptable trade off.

Both investigations have utilised high-statistics data sets to explore the performance of Laplacian Erosion as a function of detection plane and pinhole geometry without the influence of noise degrading the recovered images. Fig. 9 shows the respective RMSD values of the standard and Laplacian Eroded summation images of the contrast phantom for the 3.0 mm to 1.0 mm diameter pinhole geometry as a function of the fraction of total detected events. Out of the 7.2×10^9 simulated events, a total of 4.7×10^7 , 3.3×10^7 , 2.4×10^7 , 1.7×10^7 and 1.2×10^7 were detected by detection planes 1 to 5. As the total fraction of detected events increases the RMSD of the standard and Laplacian Eroded summation images with respect to the simulated phantom decreases as expected. From the crossing point of the two curves in Fig. 9, it can be seen that the gains offered by Laplacian Erosion are eliminated when only 15.0% of total simulated data are utilised.

The present work has shown the ability of Laplacian Erosion to reduce the image blurring associated with the pinhole geometry and improve edge definition of objects for single-pinhole multi-plane Gamma-cameras. The most striking illustration of the potential of Laplacian Erosion is the observed removal of “contrast inversion blurring” from the Derenzo-like phantom seen in Figs. 3 and 6. Laplacian Erosion’s ability to recover edge definition and reverse the inverted contrast of images adds additional functionality to multi-plane Gamma-cameras. Multi-

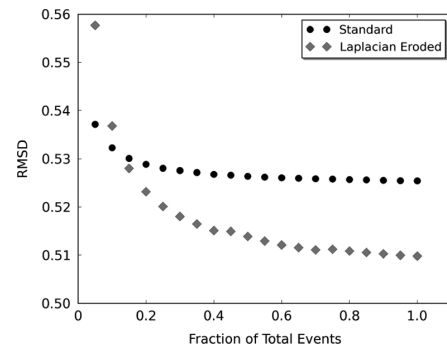


Fig. 9. RMSD values of the standard and Laplacian Eroded summation images of the contrast phantom, with respect to the ideal phantom, for the 3.0 mm to 1.0 mm diameter pinhole geometry as a function of the fraction of total detected events.

plane Gamma-cameras that apply the technique of Laplacian Erosion would be capable of choosing between two different imaging modes: SNR maximisation and improved edge definition. SNR maximisation would see the statistics of each plane included in the image reconstruction algorithm of the system without the application of Laplacian Erosion. Improved edge detection would see each plane being Laplacian Eroded before application of the system’s reconstruction algorithm. The choice of imaging mode, noise or resolution optimised, could then be selected depending on the specific imaging task. Further investigation is under way to determine the best method of integrating the technique into multi-pinhole Gamma-cameras such as SilisPECT [11] and PEDRO. Other imaging specific applications of Laplacian Erosion are also being investigated.

VI. CONCLUSION

Laplacian Erosion, a physically motivated image deblurring technique for multi-plane Gamma-cameras, has been developed and tested using a Monte Carlo radiation transport model of the prototype SPEI system PEDRO. All tested pinhole geometries saw a reduction in the level of image blurring associated with pinhole geometry. It was found that, for the test system, the performance of Laplacian Erosion was inversely and directly proportional to the detection plane offset from the collimator and pinhole diameter respectively.

The findings of the present work highlight the ability of Laplacian Erosion to reduce the level of image blurring associated with pinhole geometry in multi-plane Gamma-cameras. Further investigations are currently being undertaken to integrate this technique into the image reconstruction process of multi-plane Gamma-cameras, and explore possible application to edge detection of tumours in nuclear medicine.

APPENDIX

CONTRAST INVERSION BLURRING

The phenomenon of contrast inversion blurring can be explained using the set of images in Fig. 10. For this example a phantom of three circles of radii r , separation $4r$ and intensity I is placed at each corner of a triangle (Fig. 10(a)). In this

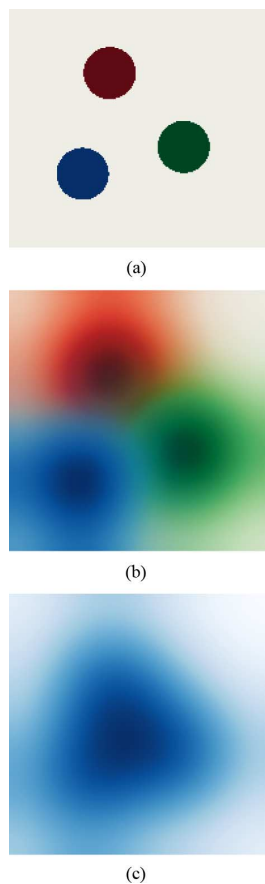


Fig. 10. A graphical description of contrast inversion blurring. (a) contains three ideal circles of radii r , separation $4r$ and intensity I , (b) the projection of each individual circle onto the detection plane of a Gamma camera, and (c) their superposition resulting in contrast inversion blurring.

example the phantom is centred 20 mm from a single detection plane, single pinhole Gamma camera. The projection of each of the three circles onto the detection plane can be seen in Fig. 10(b). The summation of the intensity of the three circles, i.e., what would be measured at the detection plane, can be seen in Fig. 10(c). Inspection of Fig. 10(c) shows that the contrast at the centre of the circles now appears as if it is the location of a single hot lesion circle, with the location of the three circles appearing as colder lesion areas.

ACKNOWLEDGMENT

The authors are grateful to Dr. T. E. Gureyev of CSIRO, Melbourne, Australia, for helpful comments and suggestions.

REFERENCES

- [1] M. A. Kupinski and H. H. Barrett, *Small-Animal SPECT Imaging*, 2nd ed. New York, NY, USA: Springer Science, 2005.
- [2] S. R. Cherry, J. A. Sorenson, and M. E. Phelps, *Physics in Nuclear Medicine*, 3rd ed. Philadelphia, PA, USA: Elsevier Science, 2003.
- [3] L. J. Meng, W. L. Rogers, N. H. Clinthorne, and J. A. Fessler, "Feasibility study of Compton scattering enhanced multiple pinhole imager for nuclear medicine," *IEEE Trans. Nucl. Sci.*, vol. 50, no. 5, pp. 1609–1617, Oct. 2003.
- [4] F. J. Beekman and B. Vastenhouw, "Design and simulation of a high resolution stationary spect system for small animals," *Phys. Med. Biol.*, vol. 49, no. 19, pp. 4579–4592, 2004.
- [5] L. R. Furenlid, D. W. Wilson, Y. C. Chen, H. Kim, P. J. Pietraski, M. J. Crawford, and H. H. Barrett, "Fast-spect II: a second-generation high-resolution dynamic spect imager," *IEEE Trans. Nucl. Sci.*, vol. 51, no. 3, pp. 631–635, Jun. 2004.
- [6] K. Vunckx, P. Suetens, and J. Nuyts, "Effect of overlapping projections on reconstruction image quality in multipinhole spect," *IEEE Trans. Med. Imag.*, vol. 27, no. 7, pp. 972–983, 2008.
- [7] S. R. Meikle, R. R. Fulton, S. Eberl, M. Dahlbom, K.-P. Wong, and M. J. Fulham, "An investigation of coded aperture imaging for small animal spect," *IEEE Trans. Nucl. Sci.*, vol. 48, no. 3, pp. 816–821, Jun. 2001.
- [8] K. Vunckx, D. Beque, M. Defrise, and J. Nuyts, "Single and multipinhole collimator design evaluation method for small animal spect," *IEEE Trans. Med. Imag.*, vol. 27, no. 1, pp. 36–46, 2008.
- [9] N. U. Schramm, G. Ebel, U. Engeland, Y. Schurrat, M. Behe, and T. M. Behr, "High resolution spect using multipinhole collimation," *IEEE Trans. Nucl. Sci.*, vol. 50, no. 3, pp. 315–320, Jun. 2003.
- [10] D. W. Wilson, H. H. Barrett, and E. W. Clarkson, "Reconstruction of two and three dimensional images from synthetic-collimation data," *IEEE Trans. Med. Imag.*, vol. 19, no. 5, pp. 412–422, 2000.
- [11] S. Shokouhi, S. D. Metzler, D. W. Wilson, and T. E. Peterson, "Multipinhole collimator design for small-object imaging with SiliSPECT: a high-resolution spect," *Phys. Med. Biol.*, vol. 54, no. 2, pp. 207–225, 2009.
- [12] M. R. Dimmock, J. E. Gillam, T. E. Beveridge, J. M. C. Brown, R. A. Lewis, and C. J. Hall, "A pixelated emission detector for radioisotopes (PEDRO)," *Nucl. Instrum. Methods Phys. Res. A*, vol. 612, no. 1, pp. 133–137, 2009.
- [13] G. J. Hine, "Evaluation of focused collimator performance II: Digital recording of line-source response," *Int. J. App. Rad. Isot.*, vol. 18, no. 12, pp. 819–823, 1967.
- [14] R. A. Moyer, "A low-energy multihole converging collimator compared with a pinhole collimator," *J. Nucl. Med.*, vol. 15, no. 2, pp. 59–64, 1973.
- [15] R. L. Easton, Jr, *Fourier Methods in Imaging*, 6th ed. West Sussex, U.K.: Wiley, 2010.
- [16] D. M. Paganin, *Coherent X-ray Optics*, 1st ed. London, U.K.: Oxford Univ. Press, 2006.
- [17] S. Agostinelli *et al.*, "Geant4: a simulation toolkit," *Nucl. Instrum. Methods Phys. Res. A*, vol. 506, no. 1, pp. 250–303, 2003.
- [18] C. V. Nguyen, J. E. Gillam, J. M. C. Brown, D. V. Martian, D. A. Nikulin, and M. R. Dimmock, "Towards optimal collimator design for the PEDRO hybrid imaging system," *IEEE Trans. Nucl. Sci.*, vol. 58, no. 3, pp. 639–650, Jun. 2011.

Part III

Fundamental Study of Advanced Compton Imaging

Towards Quantification of Advanced Compton Imaging

7.1 Introduction

As stated in Section 1.2, Advanced Compton Imaging Systems (ACISs) utilise information derived from measurement of the Compton electron to restrict the azimuthal range of a Cone of Response (CoR) centred around a plane defined by the scattered photon and Compton electron ejection vector. The extent to which the azimuthal range can be restricted is directly proportional to the measurement accuracy of the Compton electron ejection vector [2, 90, 108]. First generation ACISs, i.e. the Tracking and Imaging Gamma Ray Instrument (TIGRE) [100] and Medium Energy Gamma-ray Astronomy telescope (MEGA) [47], were composed of a tracker, a low Z multi-detector stack that was optimised for Compton scattering and measurement of Compton electron trajectories, and a calorimeter, a high Z detection block optimised to absorb the scattered photon [47, 67]. These systems were optimised such that the thickness of each position and energy resolving radiation detector in the tracker was thin enough that if a photon Compton scatters within it, the ejected Compton electron would travel through multiple detectors [47, 66]. The coordinates and energy deposited at each intersected detection element could then be utilised to determine the Compton electron ejection vector and kinetic energy [47, 66]. This approach, taken due to the limit of detection technology at the time, resulted in a minimum incident photon energy for tracking to be feasible of approximately 2 MeV [47, 66].

Recent advancements in radiation detection technology at Lawrence Berkeley National Laboratory (LBNL) (U.S.A) [105] and Kyoto University (Japan) [93] have resulted in novel radiation detectors that are capable of tracking recoil electrons in-situ (i.e. through the volume of a single position and energy resolving detector). These novel radiation detectors serve as the foundation for two second generation ACISs, one from each institution, which, in their current form, follow the same basic design as the first generation. The difference between the generations is that their tracker is composed of either a single or multiple stack of in-situ recoil electron tracking radiation detectors [61, 75].

LBNL's second generation ACIS is presently comprised of a 650 μm thick, fully-depleted Silicon scientific-grade Charge Coupled Device (CCD) with 1454 x 726 pixels of pitch 10.5 μm [40], oriented in front of a Germanium double sided strip detector [104, 105]. So far, the LBNL group has developed and experimentally benchmarked a novel in-situ recoil electron tracking algorithm to estimate two angles, α

and β , which represent the azimuthal and polar angle of the the Compton electron ejection vector with respect to the CCD pixel plane [74, 75]. During experimental testing of this tracking algorithm with the primary γ -ray line of ^{137}Cs , 662 keV, a Gaussian-like response was observed for both α and β with approximate Full Width at Half Maximums (FWHMs) of 50° and 70° respectively [75]. This initial work is the first step in LBNL's goal of creating a multiple detector tracker from several CCD layers that would be able to track the Compton electron both in-situ and across several CCD layers on a event-by-event basis [105].

Kyoto University's second generation ACIS program has been developed based around novel micro-Time Projection Chamber (μ -TPC) technology capable of measuring the three dimensional tracks of charged particles with sub-millimeter accuracy [60, 64]. These μ -TPCs, which are composed of a gas drift chamber coupled to a micro-Pixel Chamber (μ -PIC) [65], are typically located in front of, or encased in, a scintillation pixel detector array to construct an ACIS [46, 61, 92, 93, 101]. This program has, so far, developed and experimentally tested ACISs for medical imaging and γ -ray astronomy with promising results [46, 91]. Of these systems, the most advanced, SMILE-II, intended for γ -ray astronomy, has been shown to be able to track recoil electrons to within an accuracy of 200° FWHM and possesses an image space angular spatial resolution of 5.3° with a minimal background in laboratory tests at 662 keV [61].

Both radiation detector types discussed above have the potential to improve the tracking accuracy of Compton electrons and lower the minimal incident photon energy that can be tracked to around a few hundred keV [93, 105]. The following chapter presents a preliminary study of the possible improvement that can be achieved with recoil electron tracking in comparison to a standard CIS over the energy range of 250 keV to 2 MeV. A single, idealised 3D position and energy resolving radiation detector capable of in-situ recoil electron tracking, with interchangeable detection material, was implemented as the test ACIS. Four commonly employed detection materials in SPEI, High Purity Silicon (HPSi), Gaseous Argon (GAr), High Purity Germanium (HPGe) and Gaseous Xenon (GXe), were tested. Three of these materials, HPSi, GAr and GXe, correspond to those that have been utilised in the tracker detectors of the ACISs at LBNL [105] and Kyoto University [47]. For each detection material, ten different Full Width at Tenth Maximum (FWTM) recoil electron tracking accuracies over a range of 5° to 180° , assuming a normally (Gaussian) distributed tracking algorithm similar to those discussed above [61, 75], were tested.

7.2 Advanced Compton Imager Simulation, Image Recovery and Performance Assessment

Electron tracking allows for the azimuthal arc length restriction of the standard CIS cone-surface. The focus of this investigation was to quantify how electron tracking accuracy impacts overall imaging performance and point source convergence rate. To quantify these two properties, a custom Geant4 application was constructed, outlined in Section 7.2.1, of an idealised volumetric radiation detector with perfect spatial and energy resolution. Section 7.2.2 outlines the two simple cone-surface backprojection

frameworks, standard and truncated, that were utilised to recover estimates of the source distribution in image space from simulations performed with this Geant4 application. Perfect measurements were degraded directly in order to decouple imaging performance and point source convergence rate from measurement uncertainty due to detector electrode geometry and the signal processing chain. Simple backprojection allowed assessment to be performed without reference to any specific image reconstruction algorithm.

7.2.1 Geant4 Application and Simulation Description

Geant4 version 10.0 was utilised to construct a custom application of a simple point source and detector geometry in vacuum. The application comprised a point source 10 meters in front of a $100 \times 100 \times 100$ mm³ idealised volumetric detector. Four different material variations of this detection system, HPSi ($\rho = 2.33 \text{ g cm}^{-3}$), GAr ($\rho = 1.78 \times 10^{-3} \text{ g cm}^{-3}$), HPGe ($\rho = 5.32 \text{ g cm}^{-3}$) and GXe ($\rho = 5.90 \times 10^{-3} \text{ g cm}^{-3}$), were simulated with perfect spatial resolution and electronic response of the signal processing chain. Measurement of the ejected Compton electron direction vector was modelled utilising an idealised tracking algorithm. This algorithm sampled, on an interaction by interaction basis, a new ejection direction vector such that the angle between the two would fall within a normal (Gaussian) distribution of variable FWTM. Perfect gamma tracking, ordering of the interaction sequence of a single photon through the detection volume [109], was also implemented.

A total of 88 datasets of 10,000 events were generated for each material using the application described above. 80 of these datasets were generated by varying the incident photon energy and FWTM of the idealised tracking algorithm over the range of values outlined in Table 7.1. The remaining 8 data sets did not include recoil electron tracked data and served as the basis for the recovered standard CI images. The physics list G4EMSP04 was implemented as the application's default physics list as it contains the Monash University Compton scattering model, outlined in Chapter 3, that was specifically developed to simulate the ejection direction of Compton electrons in a Monte Carlo framework to a high level of precision.

7.2.2 Image Recovery

The following framework served as the basis for both the standard and truncated cone-surface backprojection algorithms. The difference between the two approaches was that the truncated algorithm implemented an additional top-hat function in azimuthal space to modulate the backprojected cone-surface. This top-hat function was centred at the intersection of the cone-surface with the negative tracked recoil electron

Parameter	Tested Value (keV and Degrees)
Energy	250, 500, 750, 1000, 1250, 1500, 1750, 2000
Angular Uncertainty (FWTM)	5, 10, 15, 30, 45, 60, 90, 120, 150, 180

Table 7.1: Tested incident photon energy and electron tracking uncertainty.

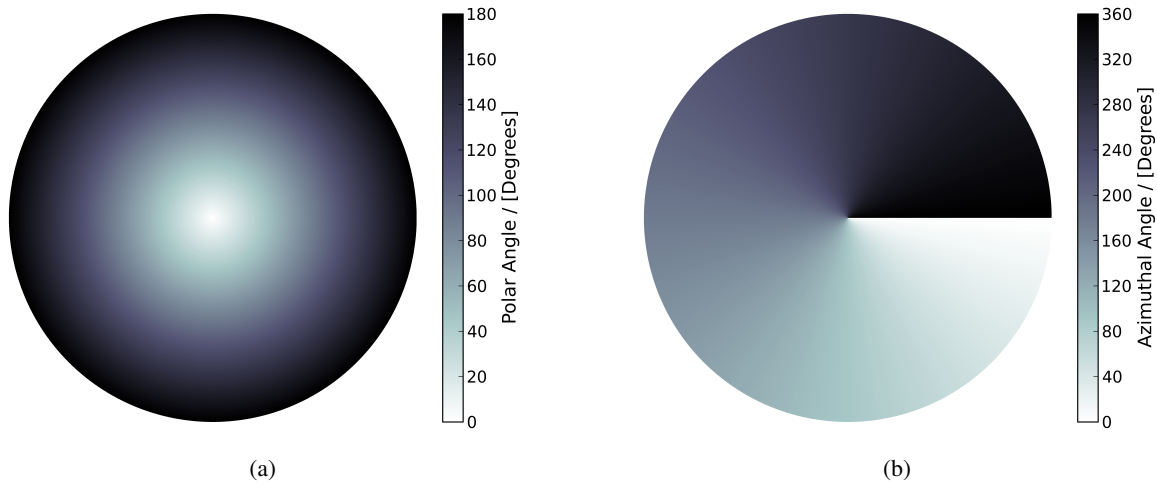


Figure 7.1: Two-dimensional spherical polar image space, polar (a) and azimuthal (b). A full polar and azimuthal angular range, 0 to 180° and 0 to 360°, is utilised for all images.

ejection vector (see Figure 1.5 in Chapter 1), and possessed an azimuthal angular width proportional to the idealised tracking algorithm's FWTM. Matching this width to the FWTM ensures that there is a greater than 99.9% chance that the true intersection plane falls within the restricted azimuthal angular range.

To remove the dependence of the recovered image quality on the source-to-detector distance, a two-dimensional spherical polar image space (Figure 7.1) was utilised. Each cone of response was constructed using the first two interaction locations to form the axis and the cone opening half-angle θ was estimated via Compton kinematics:

$$\cos \theta = 1 + mc^2 \left(\frac{1}{E_0} - \frac{1}{E_0 - E_S} \right), \quad (7.1)$$

where E_0 is the incident photon energy, E_S is the energy deposited during the first photon interaction and mc^2 is the rest-mass energy of the electron [81]. A simple cone-surface response model was implemented comprised of a single Gaussian function, i.e.:

$$f(\theta) = \exp\left(\frac{-\theta^2}{2\sigma^2}\right) \quad (7.2)$$

where θ is the normal radial distance in the image plane from the cone-surface, and σ is the sum of angular uncertainties of the estimated cone opening half-angle from finite spatial and energy measurements of the CIS [68, 69]. Due to the idealised response model of the volumetric detector, the only source of uncertainty in estimating the cone opening half-angle θ , and in turn the width of each backprojected cone-surface, is the effect of the variation in the number of electron-hole/ion pairs generated through the effect of Fano noise [27].

The variation in the number of electron-hole/ion pairs generated due to Fano noise is dependent on the energy deposited and detection material, similar to the effect of Doppler broadening [70]. This variation,

Material	Fano Factor	Electron-Hole / Ion Pair Energy (eV)
HPSi	0.1	3.76
GAr	0.17	26.2
HPGe	0.1	2.96
GXe	0.17	21.5

Table 7.2: Fano factors and electron-hole/ion pair ionisation energy for for all four tested materials. Values were taken from Knoll [50].

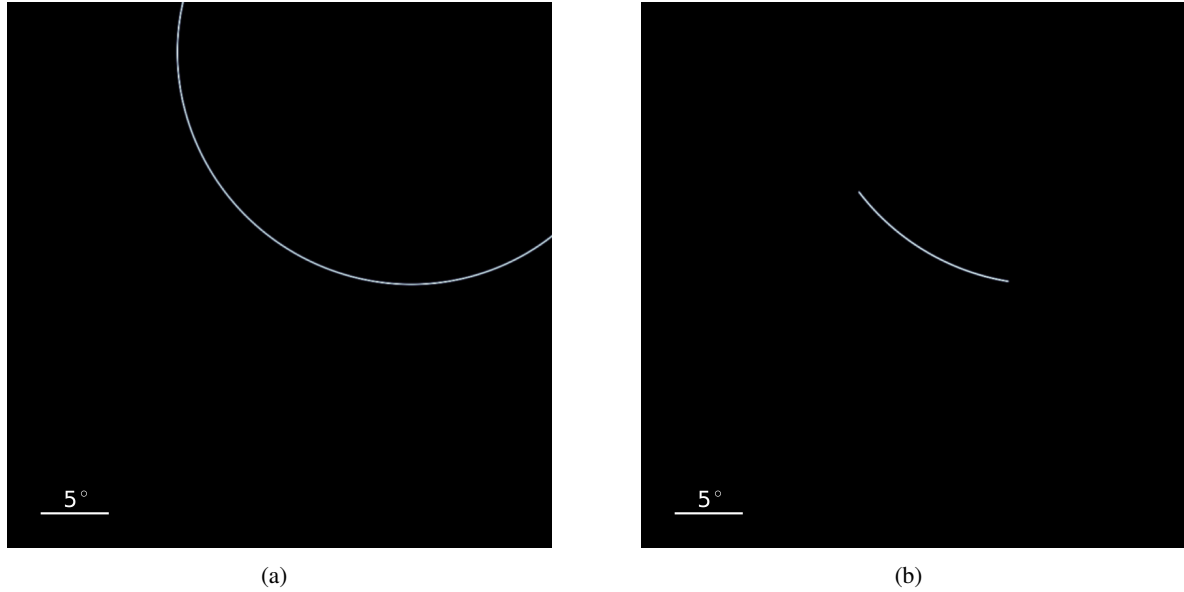


Figure 7.2: Example cone-surfaces of response for each of the cone-surface back-projection techniques, standard (a) and truncated (b). Each image space has been limited to a polar range of 0 to 20°, with the photon origin located at the direct centre of the image space.

which influences the energy response of the idealised detector, for a given detection material, can be modelled as a Gaussian-like distribution with FWHM:

$$\Delta E_{FWHM} = 2 \sqrt{2 \log_e(2) F E_S E_I} \quad (7.3)$$

where F is the Fano factor and E_I is the electron-hole/ion-pair ionisation energy for a given material [27, 50]. The values for each of the four tested materials can be found in Table 7.2. Thus the angular standard deviation of the cone-surface of response in Equation 7.2, i.e. the uncertainty in the cone opening half-angle θ estimate (Equation 7.1), can be expressed as [68]:

$$\sigma = \frac{m_0 c^2 \Delta E_{FWHM}}{2 \sqrt{2 \log_e(2)} (E_0 - E_S)^2 \sin \theta}. \quad (7.4)$$

Examples of a cone-surface of response for each of the two backprojection algorithms for the same event sequence can be seen in Figure 7.2.

7.2.3 Assessment of Recovered Image Quality and Point Source Convergence

Two Figures of Merit (FoMs) were selected to quantify the influence of increased electron tracking accuracy on recovered image quality through the assessment of the point source radial profile: the Half Width at Half Maximum (HWHM) and Half Width at Tenth Maximum (HWTM). These two FoMs define the Point Response Function (PRF) of the imaging system, assuming isotropy and homogeneity, which is a measure of the system spatial resolution and performance [5].

A single FoM was developed to quantify how electron tracking affects the rate at which, or how quickly, the simulated position and energy resolving radiation detector was able to estimate the point source's location utilising the Root Mean Square Difference (RMSD) metric, i.e.:

$$\text{RMSD} = \sqrt{\frac{\sum_{i=1}^n |P_i - R_i|^2}{\sum_{i=1}^n |P_i|^2}} \quad (7.5)$$

where P_i and R_i are the “ideal” and recovered image radial profiles of n elements respectively. Starting from a blank image space, each trial continued to backproject randomly sampled cone-surfaces, from a pool of 10,000 events, until the RMSD between successive radial profiles of the image space, treating the earlier one as the “ideal source distribution”, varied by less than 0.001. An RMSD of less than 0.001 indicates a high level of correlation between the two radial profiles and that, in turn, the simulated point source location and distribution can be determined to a high level of confidence. The convergence FoM evaluates the mean number of cone-surfaces required to reach this RMSD value from a batch of 10,000 trials for each combination of detection material, incident photon energy and electron tracking accuracy. For clarity, all three FoMs have been presented as normalised differences ($\Delta\text{FoM}_{\text{Norm}}$) between the standard ($\text{FoM}_{\text{Standard}}$) and truncated ($\text{FoM}_{\text{Truncated}}$) recovered image sets, i.e.:

$$\Delta\text{FoM}_{\text{Norm}} = \frac{\text{FoM}_{\text{Standard}} - \text{FoM}_{\text{Truncated}}}{\text{FoM}_{\text{Standard}}} \quad (7.6)$$

such that a reduction, indicating an improvement in either image quality or point source convergence, due to electron tracking, will correspond to a positive fractional difference.

7.3 Results

7.3.1 Recovered Image Quality

The FoMs for all recovered image estimates can be found in Figures 7.3 to 7.5. The standard PRF HWHM, and HWTM data as a function of detector material and incident photon energy is displayed in Figure 7.3. Figure 7.3 illustrates a proportional decrease in HWHM and HWTM with respect to the increase in incident photon energy for all four detection materials. Of the four materials, HPSi exhibits the best imaging performance, indicated by the lowest PRF HWHM and HWTM, across the simulated incident photon energy range. This is due to HPSi possessing a lower average bound atomic electron pre-collision

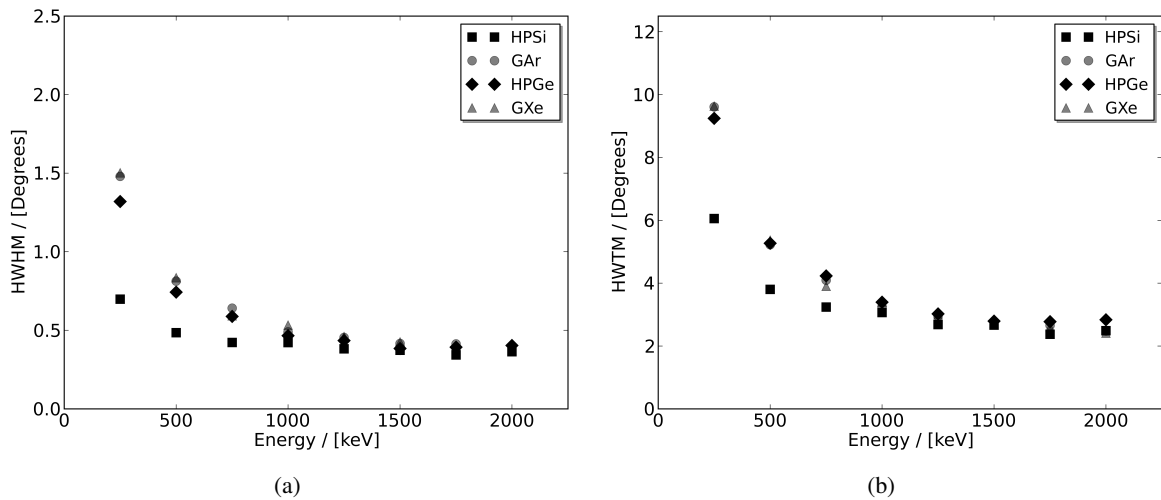


Figure 7.3: HWHM (a) and HWTM (b) values of the standard recovered image estimates for all four materials over the tested energy range.

momentum and, in turn, the impact of Doppler broadening is minimal in comparison to the other three tested materials [70, 110].

Figures 7.4 and 7.5 contain the PRF HWHM and HWTM FoM fractional differences of the truncated recovered radial profile estimates with respect to their equivalent material and incident photon energy standard, i.e. no electron tracking employed, values (see Figure 7.3). In each image the solid black line indicates the region, from right to left, where the fractional difference is greater than 0.1. The successive solid white lines from right to left indicate regions of parameter space of linearly increasing FoM fractional difference in steps of 0.1, i.e. 0.2, 0.3, etc. All four materials display a noticeable fractional difference in both the PRF HWHM and HWTM of greater than 0.1 across the tested energy range for electron tracking accuracy values below 10° and 45° respectively. For incident photon energies below 750 keV in GAr, HPGe and GXe, the observed solid line distributions are shifted outwards such that the black lines lie approximately at 15° and 90° for the PRF HWHM and HWTM FoMs respectively. An inverse relationship between the fractional differences of these two FoMs and electron tracking accuracy can be observed below these angular limits for all four materials. Additionally, an inverse relationship between fractional difference and incident photon energy is present in both FoMs for all four materials.

Figure 7.6 shows example recovered images for 500 keV photons incident on the simulated idealised HPSi and GXe detectors. In this figure three individual images, per material, are shown for electron tracking accuracies of 360° (Standard), 45° and 5° . A mirrored radial profile of the point source located at the centre of the image has been overlaid with its HWHM and HWTM, marked by a solid and dotted line respectively. Each radial profile has been plotted on a relative \log_{10} normalised scale for each detector material. Inspection of these images show that, as calculated, the PRF HWHM and HWTM decrease with electron tracking accuracy in both materials. As the electron tracking accuracy decreases, the point source distributions compress and become more localised around the location defined in the simulation.

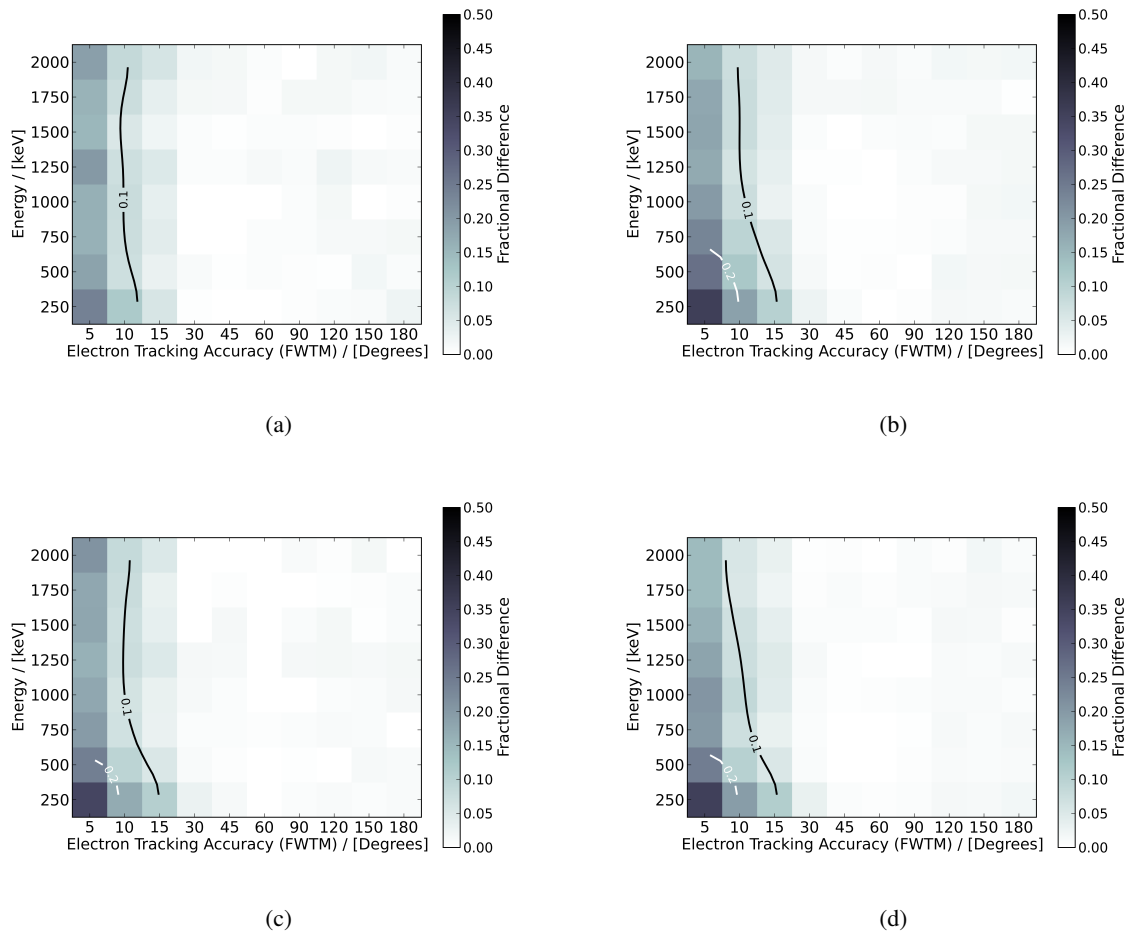


Figure 7.4: Fractional difference of PRF HWHM for HPSi (a), GAR (b), HPGe (c) and GXe (d) over the tested energy and electron tracking accuracy ranges outlined in Table 7.1. The areas bounded between the energy axis and successive solid black/white lines, from right to left, indicate fractional difference regions of greater than 0.1 and 0.2.

This compression reduces the impact of the Lorentzian tail that can be observed in each radial profile, increasing the maximum intensity at the centre of each image, and, in turn, lowering the image background corresponding with the reduction in PRF HWTM.

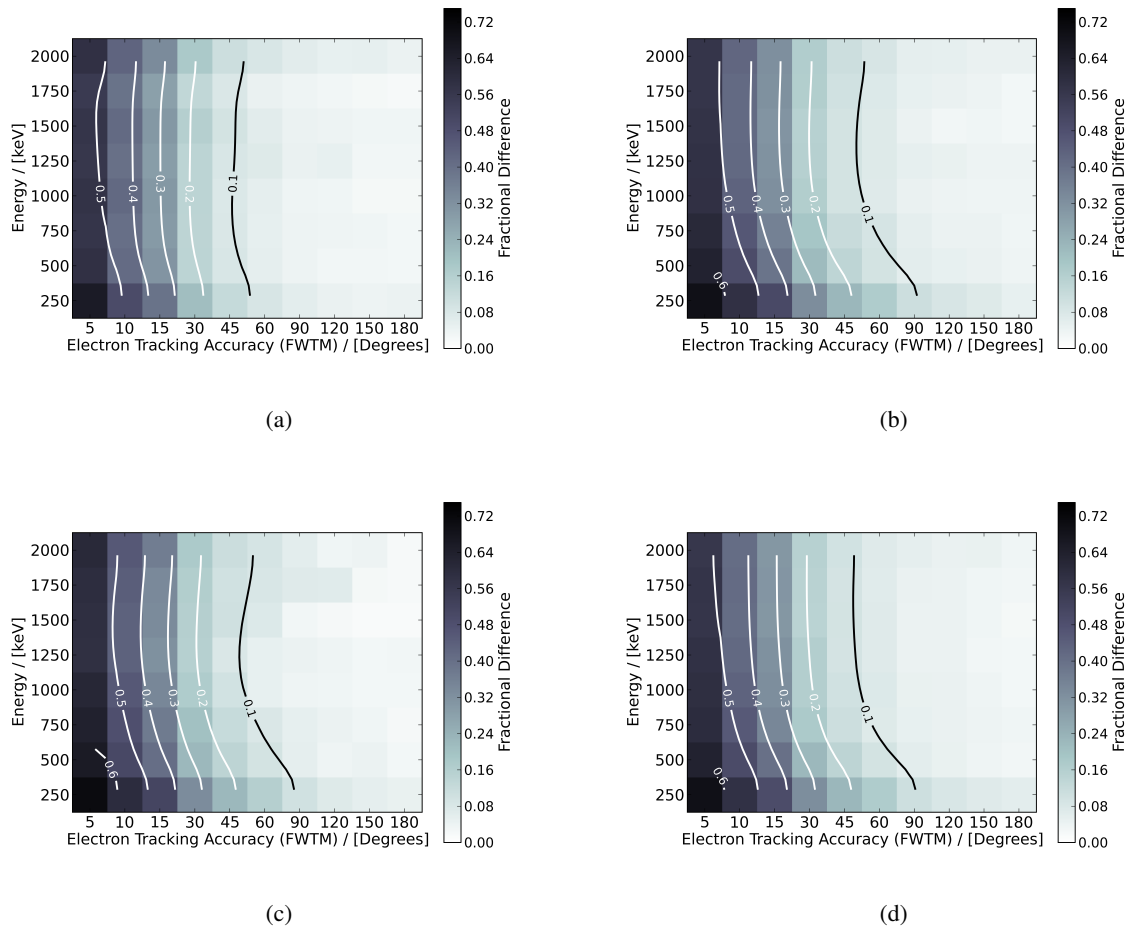


Figure 7.5: Fractional difference of PRF HWTM for HPSi (a), GAr (b), HPGe (c) and GXe (d) over the tested energy and electron tracking accuracy ranges outlined in Table 7.1. The areas bounded between the energy axis and successive solid black/white lines, from right to left, indicate fractional difference regions of greater than 0.1, 0.2, 0.3, 0.4, 0.5 and 0.6.

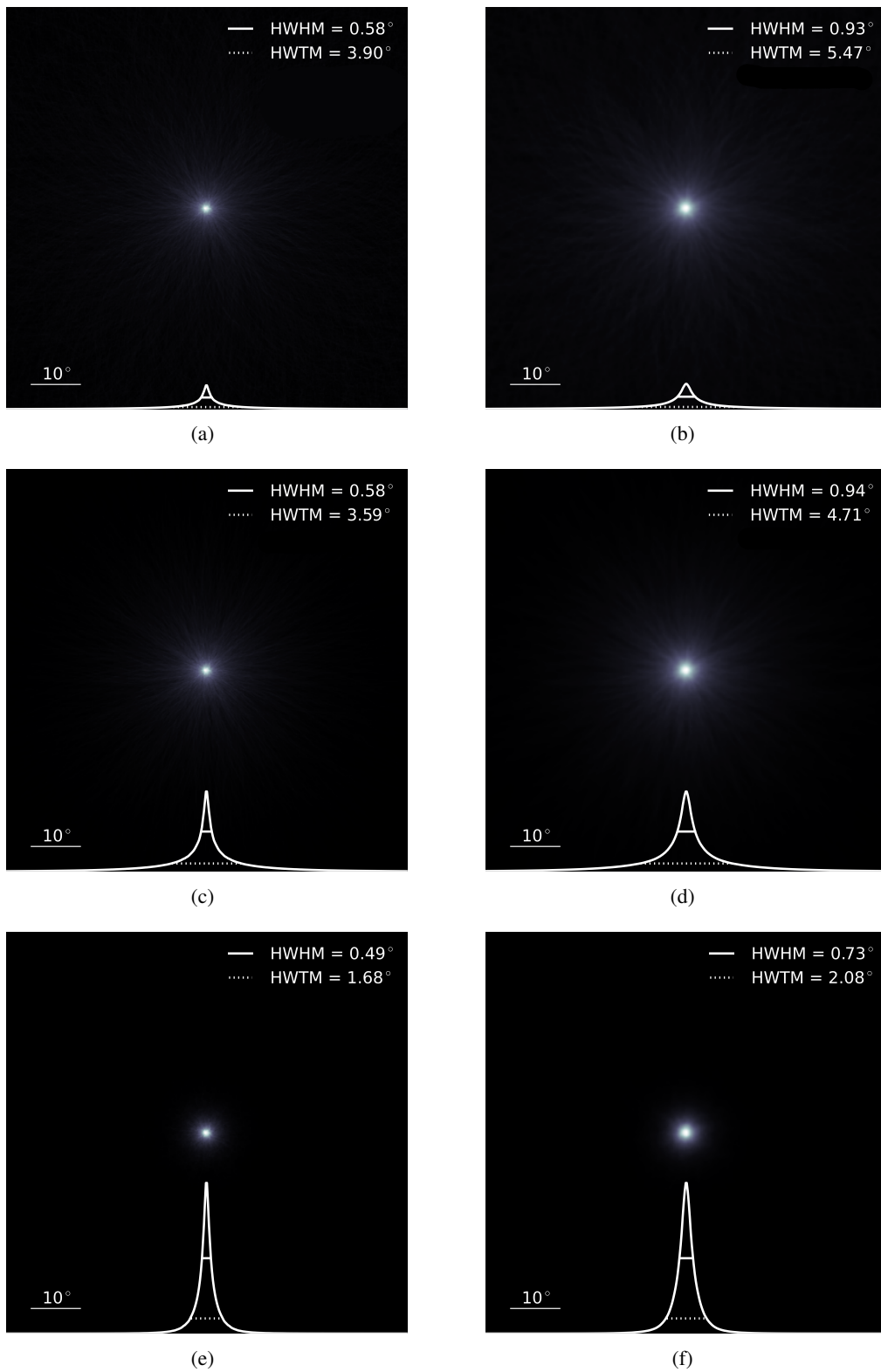


Figure 7.6: Recovered images, mirrored radial profiles, and HWHM and HWTM FoMs for 500 keV photons with electron tracking accuracies of 360° (Standard) (top row), 45° (middle row) and 5° (bottom row) for HPSi (left column) and GXe (right column).

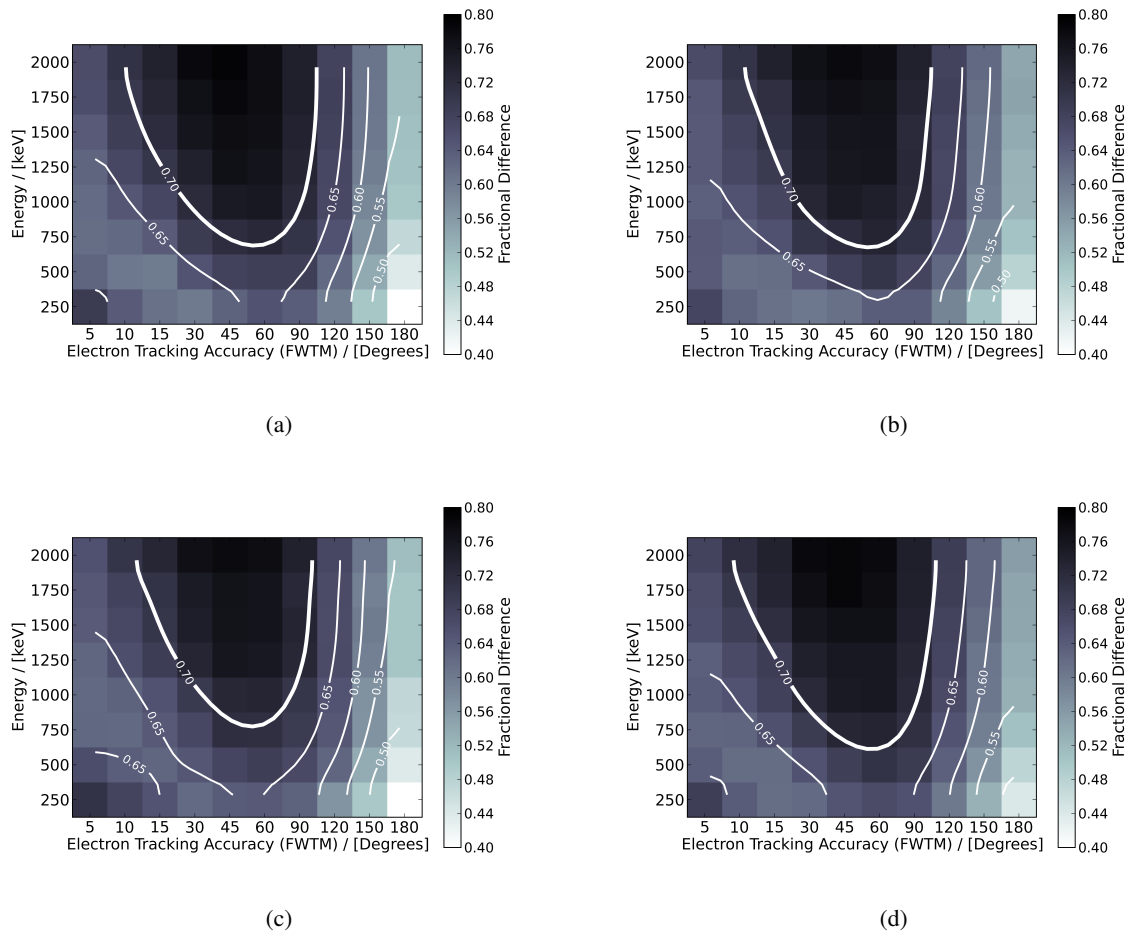


Figure 7.7: Fractional difference in radial profile convergence rate for HPSi (a), GAR (b), HPGe (c) and GXe over the tested energy and electron tracking accuracy ranges outlined in Table 7.1.

7.3.2 Point Source Convergence

Figure 7.7 shows the radial profile convergence FoM for each combination of detection material, incident photon energy and electron tracking accuracy contained in Table 7.1. All four materials display a minimum fractional difference of 0.4 in the mean number of events required for convergence, regardless of incident photon energy or electron tracking accuracy. Each figure has a bold solid white line overlaid enclosing the region, from top to bottom, in which the fractional difference in the convergence FoM is greater than 0.7. The successive solid white lines, from top to bottom, denote further regions of 0.05 reduction in the convergence FoM fractional difference with respect to the value of this region, i.e. 0.65, 0.6, 0.55, 0.5 and 0.45. Comparison of these regions illustrates that, with the exception of the enclosed 0.55 region, no clear correlation is present between detection materials. Additionally, no simple relationship with respect to the incident photon or electron tracking accuracy can be formulated due to the unique regions of increased fractional difference presented in the lower left hand area of each distribution. However, one general trend can be extracted from these distributions: an electron tracking accuracy of 45° to 60° will yield the fastest

point source radial profile convergence rate in all four materials for incident photon energies above 500 keV (see Figure 7.7).

7.4 Discussion

A preliminary investigation was undertaken to assess the impact of electron tracking accuracy on recovered image quality and point source convergence in Compton imaging. Two FoMs were implemented to assess the impact on recovered image quality: the HWHM and HWTM of each recovered image's radial profile. For the implemented simulation and image recovery frameworks, both FoMs showed that regardless of the electron tracking accuracy an increase in recovered image quality was possible. Additionally, a single FoM was used to assess the mean number of events required to estimate the simulated source distribution. No clear, simple relationship between incident photon or electron tracking accuracy and point source convergence rate was observed. However, it was discovered that for incident photon energies above 500 keV the optimal recoil electron tracking accuracy to maximise point source convergence lies between 45° to 60° , and that convergence rate increased with incident photon energy in all four materials.

The work presented in this chapter is the first step towards a larger, more detailed, study. To complete this study, both the simulation and image recovery frameworks outlined in Section 7.2 require expansion. With the assistance of Dr Andreas Zoglauer (Space Sciences Laboratory, University of California, Berkeley, USA), three extensions to these frameworks have been identified¹. These extensions are required in order to assess the validity of this investigation's observed trends. These identified extensions and their anticipated effect on the observed trends are outlined below:

1. Inclusion of the simulation of Compton electron transport throughout the active volume of the detection system and implementation of a realistic electron tracking algorithm (similar to that reported in [74, 75]). In this investigation the Compton electron ejection direction vector from the target atom was input directly into the idealised electron tracking algorithm, effectively neglecting the associated effects of small angle electron scattering on the presented results. It has been previously documented that small angle electron scattering is a major limitation in correctly determining the ejected Compton electron direction vector at low incident photon energies, i.e. below 2 MeV, and its impact is inversely proportional to ejected Compton electron kinetic energy [108]. Inclusion of these two factors is anticipated to reverse the inverse relationships between the HWHM and HWTM fractional differences and incident photon energy observed in Figures 7.4 and 7.5. It is also anticipated that the unique regions of increased point source convergence rate fractional difference observed in the lower left hand area of each distribution of Figure 7.7 will disappear.
2. Upgrading the implemented detection system model to be more realistic. This will require the addition of a number of physical factors such as: material dependent detector geometry, electrode

¹The author would like to thank Dr Andreas Zoglauer for his advice and input with respect to these outlined extensions.

layout, effective spatial resolution, strip capacitance, avalanche effects, charge collection efficiency, electronic noise and minimal energy measurement thresholds. The addition of these physical factors will further decrease the accuracy to which a recoil electron could be tracked and introduce an energy threshold below which it would be impossible for an electron to be tracked. It is anticipated that, in combination with the first set of proposed extensions, ACI will become impossible below 200 to 300 keV due to the inability to track recoil electrons from Compton scattering interactions. Additionally, the inclusion of these factors will ensure that the anticipated outcomes discussed above with respect to the observed trends in Figures 7.4, 7.5 and 7.7 occurs.

3. Expansion of the physical effects factored into the implemented event backprojection algorithms and implementation of a realistic gamma-tracking algorithm in the image recovery framework. A number of measures will need to be included into the event backprojection algorithms to incorporate the increased complexity of the simulation framework outlined above. The most important of these measures will be the substitution of the top-hat function in azimuthal space to modulate the backprojected cone-surface, utilised in this preliminary investigation, with a more physically relevant one based on the implemented realistic electron tracking algorithm performance. Whilst this is anticipated to have a noticeable effect on image contrast and point source convergence rate, the exact extent is unknown.

These three proposed extensions to the simulation and image recovery frameworks are anticipated to have a significant effect on the trends reported in Section 7.3. However, the author hypothesizes that the two following general trends will be confirmed after further investigation: 1) that increased image performance and point source convergence will be observed regardless of recoil electron tracking accuracy, and 2) the rate of point source convergence will be maximised for electron tracking accuracies of 45° to 60° FWTM for photons of incident energy greater than 500 keV.

7.5 Conclusion

A preliminary study of recoil electron tracking enhanced Compton imaging for an idealised 3D position and energy resolving radiation detector for photon energies below 2 MeV was undertaken. A custom Geant4 application was implemented and four different detection materials, HPSi, GAr, HPGe and GXe, were tested over an energy range of 250 keV to 2 MeV with electron tracking resolutions of 5° to 180° FWTM, assuming a radial Gaussian uncertainty distribution. A point source was placed in the centre of each system's FoV and an image of its distribution recovered for each combination of detection material, incident photon energy and electron tracking accuracy. Increased image performance and point source convergence was observed with respect to standard Compton imaging regardless of recoil electron tracking accuracy. Additionally, the rate of point source convergence with respect to standard Compton imaging was discovered to be maximised for electron tracking accuracies of 45° to 60° FWTM for photons of

incident energy greater than 500 keV. Further study with more detailed simulation and image recovery frameworks is required to assess the validity of these observed trends.

Concluding Remarks

This thesis has presented a total of five studies relating to the field of Single Photon Emission Imaging. These studies make significant contributions to the fields of Monte Carlo radiation transport modelling (Part I), Hybrid SPEI (Part II) and Advanced Compton Imaging (Part III).

In Part I, Chapter 3 outlined the development of an alternative Compton scattering computational model for Monte Carlo radiation transport modelling and its integration into the Monte Carlo radiation transport modelling toolkit Geant4. Using a theoretical foundation that ensured the conservation of energy and momentum in the relativistic impulse approximation, this new model, the Monash University Compton scattering model, developed energy and directional algorithms for both the scattered photon and ejected Compton electron from first principles. Assessment of the performance of G4LowEPComptonModel was undertaken in two steps: 1) comparison with respect to the two standard Compton scattering classes of Geant4 version 9.5, G4LivermoreComptonModel and G4PenelopeComptonModel, and 2) experimental comparison with respect to Compton electron kinetic energy spectra obtained from the Compton scattering of 662 keV photons off the K-shell of gold. Both studies illustrated that the Monash University Compton scattering model, and in turn G4LowEPComptonModel, is a viable replacement for the majority of computational models that have been adapted from Ribberfors' work. It was also shown that the Monash University Compton scattering model is able to reproduce the Compton scattering triply differential cross-section Compton electron kinetic energy spectra of 662 keV photons K-shell scattering off of gold to within experimental uncertainty. This model now serves as the default high accuracy low energy Compton scattering model of Geant4 as part of the G4EmStandardPhysics_option4 physics constructor.

Part II presented three studies relating to the development of the Pixelated Emission Detector for Radioisotopes (PEDRO). The first study, Chapter 4, outlined the development of a Geant4 application to be used for optimisation of PEDRO with a robust metric, the Median Distance of Closest Approach (MDCA). An initial trial was undertaken with this MDCA-Geant4 computation framework to optimise the inter-detector spacing of PEDRO operating only as a Compton imager without the coded mask at 140 keV. As the effects of energy resolution, Doppler broadening and electronic noise were added the MDCA of each isolated detector interaction event sequence increased. Furthermore, it was also determined that event sequences where the first interaction occurred in the CdTe absorption detector should be not be

reconstructed as they would lower imaging performance. These findings and the developed MDCA-Geant4 computational framework served as the basis for the two following investigations in Part II.

The second PEDRO study presented in Chapter 5 outlined the development of an automated routine for the optimisation of large-area slits in the outer regions of a coded mask which has a central region allocated for pinholes. This was undertaken with a refined version of the Geant4 application developed in Chapter 4 at 140 keV. Simulation results were blurred with realistic position and energy resolution parameters and a Bayesian interaction ordering algorithm was applied to recover a number of image estimates using cone-surface backprojection. This automatic routine was shown to allow for the large-area slits to both sample fully and extend the primary field of view (FoV) determined by the pinholes. These optimised slits enabled the truncation of the backprojected cones of response and also an increase in the success rate of the interaction ordering algorithm. Of the two configurations tested, the cylindrical geometry outperformed the square geometry, primarily because of a decrease in artifacts. Also, the cylindrical geometry provided increased sampling of the FoV due to more optimal positioning of the slits. The use of the cylindrical collimator and application of a transmission function in the reconstruction was found to improve the resolution of the system by a factor of 20, as compared to the uncollimated version of PEDRO. These findings indicate that it may indeed be possible to overcome the trade-off between spatial resolution and sensitivity inherent in SPEI through hybrid Compton-mechanical collimation.

The third, and final, PEDRO study was presented in Chapter 6. Laplacian Erosion, an image deblurring technique for multi-plane Gamma-cameras, was developed and tested for planar imaging using a further refined version of the Geant4 application outlined in Chapter 4. A contrast and Derenzo-like phantom composed of ^{125}I were both employed to investigate the dependence of detection plane and pinhole geometry on the performance of Laplacian Erosion. Three different pinhole geometries were tested. This study found that, for the test system, the performance of Laplacian Erosion was inversely proportional to the detection plane offset, and directly proportional to the pinhole diameter. All tested pinhole geometries saw a reduction in the level of image blurring associated with the pinhole geometry. However, the reduction in image blurring came at the cost of signal to noise ratio in the image. The application of Laplacian Erosion was shown to reduce the level of image blurring associated with pinhole geometry and improve recovered image quality in multi-plane Gamma-cameras for the targeted radiotracer ^{125}I . This novel, experimentally motivated, image deblurring technique is expected to reduce the level of image blurring associated with pinhole geometry in multi-plane Gamma-cameras. It is hoped that future studies will find an appropriate way to integrate this technique into the image reconstruction process of multi-plane Gamma-cameras, and explore its possible application to edge detection of tumours in nuclear medicine.

Finally, Chapter 7 of Part III presented a preliminary study of recoil electron tracking enhanced Compton imaging for an idealised 3D position and energy resolving radiation detector for photon energies below 2 MeV. A custom Geant4 application was implemented and four different detection materials, HPSi, GAr, HPGe and GXe, were tested over an energy range of 250 keV to 2 MeV with electron tracking resolutions of 5° to 180° FWTM, assuming a radial Gaussian uncertainty distribution. A point source was

placed in the centre of each system's FoV and an image of its distribution recovered for each combination of detection material, incident photon energy and electron tracking accuracy. Increased image performance and point source convergence was observed with respect to standard Compton imaging regardless of recoil electron tracking accuracy. Additionally, the rate of point source convergence with respect to standard Compton imaging was discovered to be maximised for electron tracking accuracies of 45° to 60° FWTM for photons of incident energy greater than 500 keV. Further study with more detailed simulation and image recovery frameworks is required to assess the validity of these observed trends.

These five studies are intended to serve as the basic tools/starting points for further development of Single Photon Emission Imaging systems across the fields of nuclear assay, homeland security, pre-clinical nuclear medicine and X / γ -ray astronomy. However, the developed Monash University Compton scattering model is expected have broader application across a number of fields (as indicated via the two supplemental publications in Appendices A and B). A number of projects in cellular dosimetry, microbeam radiotherapy, particle physics and radiobiology are already underway which have integrated this Compton scattering model into their research program through Geant4. An additional research project is also under development to apply the utilised theoretical framework to create a complementary photoelectric absorption model to improve the accuracy of low energy photon transport modelling in Geant4.

Bibliography

- [1] S. Agostinelli, J. Allison, K. Amako, J. Apostolakis, H. Araujo, P. Arce, M. Asai, D. Axen, S. Banerjee, G. Barrand, F. Behner, L. Bellagamba, J. Boudreau, L. Broglia, A. Brunengo, H. Burkhardt, S. Chauvie, J. Chuma, R. Chytracsek, G. Cooperman, G. Cosmo, P. Degtyarenko, A. Dell'Acqua, G. Depaola, D. Dietrich, R. Enami, A. Feliciello, C. Ferguson, H. Fesefeldt, G. Folger, F. Foppiano, A. Forti, S. Garelli, S. Giani, R. Giannitrapani, D. Gibin, J. J. Gómez Cadenas, I. González, G. Gracia Abril, G. Greeniaus, W. Greiner, V. Grichine, A. Grossheim, S. Guatelli, P. Gumplinger, R. Hamatsu, K. Hashimoto, H. Hasui, A. Heikkinen, A. Howard, V. Ivanchenko, A. Johnson, F. W. Jones, J. Kallenbach, N. Kanaya, M. Kawabata, Y. Kawabata, M. Kawaguti, S. Kelner, P. Kent, A. Kimura, T. Kodama, R. Kokoulin, M. Kossov, H. Kurashige, E. Lamanna, T. Lampén, V. Lara, V. Lefebure, F. Lei, M. Liendl, W. Lockman, F. Longo, S. Magni, M. Maire, E. Medernach, K. Minamimoto, P. Mora de Freitas, Y. Morita, K. Murakami, M. Nagamatu, R. Nartallo, P. Nieminen, T. Nishimura, K. Ohtsubo, M. Okamura, S. O'Neale, Y. Oohata, K. Paech, J. Perl, A. Pfeiffer, M. G. Pia, F. Ranjard, A. Rybin, S. Sadilov, E. Di Salvo, G. Santin, T. Sasaki, N. Savvas, Y. Sawada, S. Scherer, S. Sei, V. Sirotenko, D. Smith, N. Starkov, H. Stoecker, J. Sulikimo, M. Takahata, S. Tanaka, E. Tcherniaev, E. Safai Tehrani, M. Tropeano, P. Truscott, H. Uno, L. Urban, P. Urban, M. Verderi, A. Walkden, W. Wander, H. Weber, J. P. Wellisch, T. Wenaus, D. C. Williams, D. Wright, T. Yamada, H. Yoshida, and D. Zschiesche. Geant4—a simulation toolkit. *Nuclear Instruments and Methods in Physics Research Section A*, 506(3):250–303, 2003.
- [2] A. Akyüz, D. Bhattacharya, T. J. O'Neill, J. Samimi, and A. Zych. Enhanced performance of an electron tracking Compton gamma-ray telescope. *New Astronomy*, 9(2):127–135, 2004.
- [3] J. Allison, K. Amako, J. Apostolakis, H. Araujo, P. Arce Dubois, M. Asai, G. Barrand, R. Capra, S. Chauvie, R. Chytracsek, G. A. P. Cirrone, G. Cooperman, G. Cosmo, G. Cuttone, G. G. Daquino, M. Donszelmann, M. Dressel, G. Folger, F. Foppiano, J. Generowicz, V. Grichine, S. Guatelli, P. Gumplinger, A. Heikkinen, I. Hrivnacova, A. Howard, S. Incerti, V. Ivanchenko, T. Johnson, F. Jones, T. Koi, R. Kokoulin, M. Kossov, H. Kurashige, V. Lara, S. Larsson, F. Lei, O. Link, F. Longo, M. Maire, A. Mantero, B. Mascialino, I. McLaren, P. Mendez Lorenzo, K. Minamimoto, K. Murakami, P. Nieminen, L. Pandola, S. Parlati, L. Peralta, J. Perl, A. Pfeiffer, M. G. Pia, A. Ribon, P. Rodrigues, G. Russo, S. Sadilov, G. Santin, T. Sasaki, D. Smith, N. Starkov, S. Tanaka, E. Tcherniaev, B. Tome, A. Trindade, P. Truscott, L. Urban, M. Verderi, A. Walkden, J. P. Wellisch, D. C. Williams, D. Wright, and H. Yoshida. Geant4 developments and applications. *IEEE Transactions on Nuclear Science*, 53(1):270–278, 2006.

- [4] H. O. Anger. Scintillation camera. *Review of Scientific Instruments*, 29(1):27–33, 1958.
- [5] H. H. Barrett and K. J. Myers. *Foundations of Image Science*. John Wiley & Sons, Hoboken, U.S.A, 2004.
- [6] M. J. Berger and J. H. Hubbell. XCOM: Photon cross sections on a personal computer. Technical report, Oak Ridge Operations, Oak Ridge, U.S.A, 1987.
- [7] H. A. Bethe and W. Heitler. On the Stopping of Fast Particles and on the Creation of Positive Electrons. *Proceedings of the Royal Society London: Series A*, (146):83–112, 1934.
- [8] S. E. Boggs. Polarization constraints on gamma-ray event circles in Compton scatter instruments. *Nuclear Instruments and Methods in Physics Research A*, 503(3):562–566, 2003.
- [9] S. E. Boggs, W. Coburn, D. M. Smith, J. D. Bowen, P. Jean, J. M. Kregenow, R. P. Lin, and P. von Ballmoos. Overview of the Nuclear Compton Telescope. *New Astronomical Review*, 48(1-4):1–5, 2004.
- [10] J. M. C. Brown, M. R. Dimmock, J. E. Gillam, and D. M. Paganin. MULECS: The Monash University Low Energy Compton scattering package. *2011 IEEE Nuclear Science Symposium Conference Record*, pages 1385–1389, 2011.
- [11] M. Cañadas, P. Arce, and P. Rato Mendes. Validation of a small-animal PET simulation using GAMOS: a GEANT4-based framework. *Physics in Medicine and Biology*, 56(1):273–88, 2011.
- [12] L. L. Carter and E. D. Cashwell. *Particle-Transport Simulation with the Monte Carlo Method*. US Technical Information Centre, Energy Research and Development Administration, 1975.
- [13] E. D. Cashwell and C. J. Everett. *A Practical Manual on the Monte Carlo Method for Random Walk Problems*. Pergamon Press, 1959.
- [14] H. Casimir. Über die Intensität der Streustrahlung gebundener Elektronen. *Helvetica Physica Acta*, 6:287, 1933.
- [15] A. Castoldi, A. Galimberti, C. Guazzoni, L. Strder, and A. H. Walenta. A Novel Scatter Detector for High-Resolution SPECT Imaging With Compton Telescopes. *IEEE Transactions on Nuclear Science*, 53(6):3912–3917, 2006.
- [16] S. Chauvie, Z. Francis, S. Guatelli, S. Incerti, B. Mascialino, P. Moretto, P. Nieminen, and M. G. Pia. Geant4 Physics Processes for Microdosimetry Simulation: Design Foundation and Implementation of the First Set of Models. *IEEE Transactions on Nuclear Science*, 54(6):2619–2628, 2007.
- [17] S. R. Cherry, J. A. Sorenson, and M. E. Phelps. *Physics in Nuclear Medicine*. Elsevier Science,

Philadelphia, USA, 2003.

- [18] A. H. Compton. A Quantum Theory of the Scattering of X-rays by Light Elements. *Physical Review*, 21(5):483–502, 1923.
- [19] D. E. Cullen. A simple model of photon transport. *Nuclear Instruments and Methods in Physics Research Section B*, 101(4):499–510, 1995.
- [20] D. E. Cullen, J. H. Hubbell, and L. Kissel. EPDL97: the Evaluated Photon Data Library, “97 version”. Technical Report 6, Lawrence Livermore National Laboratory, Livermore, U.S.A, 1997.
- [21] H. Davies, H. A. Bethe, and L. C. Maximon. Theory of Bremsstrahlung and Pair Production. II. Integral Cross Section for Pair Production. *Physical Review*, 93:788–795, 1954.
- [22] M. De Napoli, C. Agodi, G. Battistoni, A. A. Blancato, G. A. P. Cirrone, G. Cuttone, F. Giacoppo, M. C. Morone, D. Nicolosi, L. Pandola, V. Patera, G. Raciti, E. Rapisarda, F. Romano, D. Sardina, A. Sarti, A. Sciubba, V. Scuderi, C. Sfienti, and S. Tropea. Carbon fragmentation measurements and validation of the Geant4 nuclear reaction models for hadrontherapy. *Physics in Medicine and Biology*, 57(22):7651–71, 2012.
- [23] A. Dell’Acqua, G. Parrou, S. Giani, P. Kent, A. Osborne, S. Ravndal, L. Silvestris, H. Fesefeldt, A. Givernaud, M. Kawaguti, S. Tanaka, K. Amako, J. Kanzaki, Y. Morita, T. Sasaki, L. Urban, Y. Nakagawa, T. Yamagata, M. Maire, P. Jacobs, S. Tonse, T. Wenaus, D. Wright, V. Grichine, H. Yoshida, P. Ward, V. Perevoztchikov, A. Breakstone, and J. Allison. Geant 4: an object-orientated toolkit for simulation in HEP. Technical Report DRDC-94-29, CERN, CERN, 1994.
- [24] N. Dogan, D. K. Wehe, and A. Z. Akcasu. A source reconstruction method for multiple scatter Compton cameras. *IEEE Transactions on Nuclear Science*, 39(5):1427–1430, 1992.
- [25] A. Einstein. Über einen die Erzeugung und Verwandlung des Lichtes betreffenden heuristischen Gesichtspunkt. *Annalen der Physik*, 17(6):132–148, 1905.
- [26] R. D. Evans. *The Atomic Nucleus*. McGraw-Hill Book Company, New York, USA, 1955.
- [27] U Fano. Ionization Yield of Radiations. II. The Fluctuations of the Number of Ions. *Physical Review*, 72(1):26–29, July 1947.
- [28] W. Feller. *An Introduction to Probability Theory and Its Applications*. John Wiley & Sons, New York, USA, 3rd edition, 1968.
- [29] M. Gavrila. Relativistic K-Shell Photoeffect. *Physical Review*, 113:514–526, 1959.
- [30] J. E. Gillam. *Development of Electronic Collimation for Nuclear Imaging*. PhD thesis, March

2007.

- [31] L. X. González, F. Sánchez, and J. F. Valdés-Galicia. Geant4 simulation of the solar neutron telescope at Sierra Negra, Mexico. *Nuclear Instruments and Methods in Physics Research Section A*, 613(2):263–271, 2010.
- [32] T. Goorley, M. James, T. Booth, F. Brown, J. Bull, L. J. Cox, J. Durkee, J. Elson, M. Fensin, R. A. Forster, J. Hendricks, H. G. Hughes, R. Johns, B. Kiedrowski, R. Martz, S. Mashnik, G. McKinney, D. Pelowitz, R. Prael, J. Sweezy, L. Waters, T. Wilcox, and T. Zukaitis. Initial MCNP6 Release Overview - MCNP6 Version 1.0. Technical Report LA-UR 13-22934, Los Alamos, USA, 2012.
- [33] S. Goudsmit and J. L. Saunderson. Multiple Scattering of Electrons. *Physical Review*, 57:24–29, 1940.
- [34] W. Greiner and J. Reinhardt. *Quantum Electrodynamics*. Springer-Verlag, Berlin, Germany, 4th edition, 2009.
- [35] M. D. Hammig and R. C. Stevenson. The degree of enhancement in a gamma-ray image gleaned from recoil-electron tracking. *2008 IEEE Nuclear Science Symposium Conference Record*, pages 2433–2439, 2008.
- [36] L. J. Harkness, A. J. Boston, H. C. Boston, R. J. Cooper, J. R. Cresswell, A. N. Grint, P. J. Nolan, D. C. Oxley, D. P. Scraggs, T. Beveridge, J. Gillam, and I. Lazarus. Optimisation of a dual head semiconductor Compton camera using Geant4. *Nuclear Instruments and Methods in Physics Research Section A*, 604(1-2):351–354, 2009.
- [37] J. He, G. J. O’Keefe, S. J. Gong, G. Jones, T. Saunder, A. M. Scott, and M. Geso. A Novel Method for Respiratory Motion Gated With Geometric Sensitivity of the Scanner in 3D PET. *IEEE Transactions on Nuclear Science*, 55(5):2557–2565, 2008.
- [38] W. Heitler. *Quantum Theory of Radiation*. Oxford University Press, London, U.K., 3rd edition, 1960.
- [39] H. Hirayama, Y. Namito, A. F. Bielajew, S. J. Wilderman, and W. R. Nelson. The EGS5 Code System. Technical Report 2005-8, Ibaraki-ken, Japan, 2007.
- [40] S. Holland. An Overview of CCD Development at Lawrence Berkeley National Laboratory. *Experimental Astronomy*, 14(2):83–89.
- [41] J. H. Hubbell and I. Øverbø. Relativistic atomic form factors and photon coherent scattering cross sections. *Journal of Physical and Chemical Reference Data*, 8(1):69, 1979.
- [42] J. H. Hubbell, W. J. Veigele, E. A. Briggs, R. T. Brown, D. T. Cromer, and R. J. Howerton. Atomic

- Form Factors, Incoherent Scattering Functions, and Photon Scattering Cross Sections. *Journal of Physical Chemistry Data*, 4(3):471–538, 1975.
- [43] S. Incerti, A. Ivanchenko, M. Karamitros, A. Mantero, P. Moretto, H. N. Tran, B. Mascialino, C. Champion, V. N. Ivanchenko, M. A. Bernal, Z. Francis, C. Villagrasa, G. Baldacchino, P. Guèye, R. Capra, P. Nieminen, and C. Zacharatou. Comparison of GEANT4 very low energy cross section models with experimental data in water. *Medical Physics*, 37(9):4692, 2010.
- [44] R. J. Jaszczak, J. Li, H. Wang, M. R. Zalutsky, and R. E. Coleman. Pinhole collimation for ultra-high-resolution, small-field-of-view SPECT. *Physics in Medicine and Biology*, 39(3):425–437, 1994.
- [45] J. A. Jauch and F. Rohrlich. *Theory of Photons and Electrons*. Addison-Wesley Publishing Company, Inc., Massachusetts, USA, 1955.
- [46] S. Kabuki, K. Hattori, R. Kohara, E. Kunieda, A. Kubo, H. Kubo, K. Miuchi, T. Nakahara, T. Nagayoshi, H. Nishimura, Y. Okada, R. Orito, H. Sekiya, T. Shirahata, A. Takada, T. Tanimori, and K. Ueno. Development of Electron Tracking Compton Camera using micro pixel gas chamber for medical imaging. *Nuclear Instruments and Methods in Physics Research Section A*, 580(2):1031–1035, 2007.
- [47] G. Kanbach, R. Andritschke, F. Schopper, V. Schönfelder, A. Zoglauer, P. F. Bloser, S. D. Hunter, J. A. Ryan, M. McConnell, V. Reglero, G. DiCocco, and J. Knödlseher. The MEGA project. *New Astronomy Reviews*, 48(1-4):275–280, February 2004.
- [48] M. Khodaverdi, A. F. Chatziioannou, S. Weber, K. Ziemons, H. Halling, and U. Pietrzyk. Investigation of different MicroCT scanner configurations by GEANT4 simulations. *IEEE Transactions on Nuclear Science*, 52(1):188–192, 2005.
- [49] O. Klein and Y. Nishina. Scattering of radiation by free electrons on the new relativistic quantum dynamics of Dirac. *Zeitschrift für Physik*, 52(11-12):853–868, 1929.
- [50] G. F. Knoll. *Radiation Detection and Measurement*. John Wiley & Sons, Hoboken, U.S.A, 4th edition, 2010.
- [51] M. A. Kupinski and H. H. Barrett. *Small-Animal SPECT Imaging*. Springer US, New York, USA, 2005.
- [52] J. W. LeBlanc, N. H. Clinthorne, C.-H. Hua, E. Nygard, W. L. Rogers, D. K. Wehe, P. Weilhammer, and S. J. Wilderman. C-SPRINT: a prototype Compton camera system for low energy gamma ray imaging. *IEEE Transactions on Nuclear Science*, 45(3):943–949, 1998.

- [53] H. W. Lewis. Multiple Scattering in an Infinite Medium. *Physical Review*, 78:526–529, 1950.
- [54] D. Liljequist, M. Ismail, F. Salvat, R. Mayol, and J. D. Martinez. Transport mean free path tabulated for the multiple elastic scattering of electrons and positrons at energies ≤ 20 MeV. *Journal of Applied Physics*, 68(7):3061–3065, 1990.
- [55] D. Liljequist, F. Salvat, R. Mayol, and J. D. Martinez. Simple method for the simulation of multiple elastic scattering of electrons. *Journal of Applied Physics*, 65(6):2431–2438, 1989.
- [56] I. Lux and L. Koblinger. *Monte Carlo Particle Transport Methods: Neutron and Photon Calculations*. CRC Press, Boston, USA, 1991.
- [57] L. J. Meng, W. L. Rogers, N. H. Clinthorne, and J. A. Fessler. Feasibility Study of Compton Scattering Enhanced Multiple Pinhole Imager for Nuclear Medicine. *IEEE Transactions on Nuclear Science*, 50(5):1609–1617, 2003.
- [58] A. Messiah. *Quantum Mechanics*. John Wiley & Son, New York, USA, 1958.
- [59] A. Mittone, F. Baldacci, A. Bravin, E. Brun, F. Delaire, C. Ferrero, S. Gasilov, N. Freud, J. Létang, D. Sarrut, F. Smekens, and P. Coan. An efficient numerical tool for dose deposition prediction applied to synchrotron medical imaging and radiation therapy. *Journal of Synchrotron Radiation*, 20(Pt 5):785–92, 2013.
- [60] K. Miuchi, H. Kubo, T. Nagayoshi, A. Ochi, R. Orito, A. Takada, T. Tanimori, and M. Ueno. Performance of the TPC with micro pixel chamber readout: micro-TPC. *IEEE Transactions on Nuclear Science*, 50(4):825–830, 2003.
- [61] Y. Mizumura, T. Tanimori, H. Kubo, A. Takada, J. D. Parker, T. Mizumoto, S. Sonoda, D. Tomono, T. Sawano, K. Nakamura, Y. Matsuoka, S. Komura, S. Nakamura, M. Oda, K. Miuchi, S. Kabuki, Y. Kishimoto, S. Kurosawa, and S. Iwaki. Development of a 30 cm-cube Electron-Tracking Compton Camera for the SMILE-II Experiment. *Journal of Instrumentation*, 9(05):C05045, 2014.
- [62] R. A. Moyer. A Low-Energy Multihole Converging Collimator Compared with a Pinhole Collimator. *Journal of Nuclear Medicine*, 15(2):59–64, 1973.
- [63] J. Myhill and G. J. Hine. *Instrumentation in Nuclear Medicine*. Academic Press, New York, USA, 1967.
- [64] T. Nagayoshi, H. Kubo, K. Miuchi, A. Ochi, R. Orito, A. Takada, T. Tanimori, and M. Ueno. Performance of large area Micro Pixel Chamber. *Nuclear Instruments and Methods in Physics Research Section A*, 513(1–2):277–281, 2003.
- [65] A. Ochi, T. Nagayoshi, S. Koishi, T. Tanimori, T. Nagae, and M. Nakamura. Development of micro

- pixel chamber. *Nuclear Instruments and Methods in Physics Research Section A*, 478(1–2):196–199, 2002.
- [66] T. J. O’Neill, F. Ait-Ouamer, I Schwartz, O. T. Tumer, R. S. White, and A. D. Zych. Compton recoil electron tracking with silicon strip detectors. *IEEE Transactions on Nuclear Science*, 39(4):629–634, 1992.
- [67] T. J. O’Neill, D. Bhattacharya, S. Blair, G. Case, O.T. Tumer, R. S. White, and A. D. Zych. The TIGRE desktop prototype results for 511 and 900 keV gamma rays. *IEEE Transactions on Nuclear Science*, 42(4):933–939, 1995.
- [68] C. E. Ordonez, A. Bolozdynya, and W. Chang. Dependence of angular uncertainties on the energy resolution of Compton cameras. *IEEE Nuclear Science Symposium Conference Record*, pages 1122–1125, 1997.
- [69] C. E. Ordonez, C. Wei, and A. Bolozdynya. Angular uncertainties due to geometry and spatial resolution in Compton cameras. *IEEE Nuclear Science Symposium Conference Record*, pages 1535–1540, 1998.
- [70] C.E. Ordonez, A Bolozdynya, and W Chang. Doppler broadening of energy spectra in Compton cameras. *IEEE Nuclear Science Symposium Conference Record*, pages 1361–1365, 1997.
- [71] S. T. Perkins, D. E. Cullen, M. H. Chen, J. H. Hubbell, J. Rathkopf, and J. Scofield. Tables and Graphs of Atomic Subshell and Relaxation Data Derived from the LLNL Evaluated Atomic Data Library (EADL), $Z = 1 - 100$. Technical Report 30, Lawrence Livermore National Laboratory, Livermore, U.S.A, 1991.
- [72] S. T. Perkins, D. E. Cullen, and S. M. Seltzer. Tables and Graphs of Electron Interaction Cross 10 eV to 100 GeV Derived from the LLNL Evaluated Electron Data Library (EEDL), $Z = 1 - 100$. Technical Report 31, Lawrence Livermore National Laboratory, Livermore, U.S.A, 1991.
- [73] I. Piqueras, F. A. Beck, E. Pachoud, and G. Duchene. A probabilistic γ -ray tracking method for germanium detectors. *Nuclear Instruments and Methods in Physics Research Section A*, 516(1):122–133, 2004.
- [74] B. Plimley, D. Chivers, A. Coffey, T. Aucott, W. Wang, and K. Vetter. Reconstruction of electron trajectories in high resolution Si devices for advanced Compton imaging. *Nuclear Instruments and Methods in Physics Research Section A*, 652(1):595–598, 2011.
- [75] B. Plimley, D. Chivers, A. Coffey, and K. Vetter. Experimental Benchmark of Electron Trajectory Reconstruction Algorithm for Advanced Compton Imaging. *IEEE Transactions on Nuclear Science*, 60(3):2308–2313, 2013.

- [76] R. H. Pratt, H. K. Tseng, C. M. Lee, L. Kissel, C. MacCallum, and M. Riley. Bremsstrahlung energy spectra from electrons of kinetic energy $1 \text{ keV} \leq T_1 \leq 2000 \text{ keV}$ incident on neutral atoms $2 \leq Z \leq 92$. *Atomic Data and Nuclear Data Tables*, 20(2):175–209, 1977.
- [77] I. Pshenichnov, A. Larionov, I. Mishustin, and W. Greiner. PET monitoring of cancer therapy with ^3He and ^{12}C beams: a study with the GEANT4 toolkit. *Physics in Medicine and Biology*, 52(24):7295–312, 2007.
- [78] L. Rädcl and C. Wiebusch. Calculation of the Cherenkov light yield from low energetic secondary particles accompanying high-energy muons in ice and water with Geant4 simulations. *Astroparticle Physics*, 38:53–67, 2012.
- [79] R. Ribberfors and K. Berggren. Incoherent-x-ray-scattering functions and cross sections $(d\sigma/d\Omega')_{incoh}$ by means of a pocket calculator. *Physical Review A*, 26(6):3325–3333, 1982.
- [80] W. L. Rogers, N. H. Clinthorne, and A. Bolozdynya. Chapter 19 - Compton Cameras for Nuclear Medical Imaging. In *Emission Tomography*, pages 383–419. Academic Press, San Diego, USA, 2004.
- [81] R. C. Rohe and J. D. Valentine. An energy-subtraction Compton scatter camera design for in vivo medical imaging of radiopharmaceuticals. *IEEE Transactions on Nuclear Science*, 43(6):3256–3263, 1996.
- [82] F. Salvat, J. M. Fernandez-Varea, and J. Sempau. *PENELOPE-2011: A Code System for Monte Carlo Simulation of Electron and Photon Transport*. Nuclear Energy Agency, Spain, 2011.
- [83] S. M. Seltzer and M. J. Berger. Bremsstrahlung spectra from electron interactions with screened atomic nuclei and orbital electrons. *Nuclear Instruments and Methods in Physics Research Section B*, 12(1):95–134, 1985.
- [84] S. M. Seltzer and M. J. Berger. Bremsstrahlung energy spectra from electrons with kinetic energy 1 keV–10 GeV incident on screened nuclei and orbital electrons of neutral atoms with $Z = 1-100$. *Atomic Data and Nuclear Data Tables*, 35(3):345–418, 1986.
- [85] M. Singh. An electronically collimated gamma camera for single photon emission computed tomography. I. Theoretical considerations and design criteria. *Medical Physics*, 10(4):421–427, 1983.
- [86] M. Singh and D. Doria. An electronically collimated gamma camera for single photon emission computed tomography. II. Image reconstruction and preliminary experimental measurements. *Medical Physics*, 10(4):428–435, 1983.

- [87] J. Spanier and E. M. Gelbard. *Monte Carlo Principles and Neutron Transport Problems*. Dover Publications, Mineola, USA, 2008.
- [88] J. Spiga, E. A. Siegbahn, E. Bräuer-Krisch, P. Randaccio, and A. Bravin. The GEANT4 toolkit for microdosimetry calculations: Application to microbeam radiation therapy (MRT). *Medical Physics*, 34(11):4322, 2007.
- [89] H. Tajima, T. Nakamoto, T. Tanaka, S. Uno, T. Mitani, E. C. Silva, Y. Fukazawa, T. Kamae, G. Madejski, D. Marlow, K. Nakazawa, M. Nomachi, Y. Okada, and T. Takahashi. Performance of a low noise front-end ASIC for Si/CdTe detectors in Compton gamma-ray telescope. *IEEE Transactions on Nuclear Science*, 51(3):842–847, 2004.
- [90] A. Takada, K. Hattori, H. Kubo, K. Miuchi, T. Nagayoshi, H. Nishimura, Y. Okada, R. Orito, H. Sekiya, A. Tada, and T. Tanimori. Development of an advanced Compton camera with gaseous TPC and scintillator. *Nuclear Instruments and Methods in Physics Research Section A*, 546(1–2):258–262, 2005.
- [91] A. Takada, H. Kubo, H. Nishimura, K. Ueno, K. Hattori, S. Kabuki, S. Kurosawa, K. Miuchi, E. Mizuta, T. Nagayoshi, N. Nonaka, Y. Okada, R. Orito, H. Sekiya, A. Takeda, and T. Tanimori. Observation of Diffuse Cosmic and Atmospheric Gamma Rays at Balloon Altitudes with an Electron-tracking Compton Camera. *The Astrophysical Journal*, 733(1):13, 2011.
- [92] A. Takada, H. Kubo, H. Nishimura, K. Ueno, T. Tanimori, K. Miuchi, K. Tsuchiya, S. Kabuki, K. Hattori, S. Kurosawa, C. Ida, S. Iwaki, N. Nonaka, and E. Mizuta. The Observation of Diffuse Cosmic and Atmospheric Gamma Rays with an Electron-Tracking Compton Camera Loaded on a Balloon. *Journal of the Physical Society of Japan*, 78(A):161–164, 2009.
- [93] T. Tanimori, H. Kubo, K. Miuchi, T. Nagayoshi, R. Orito, A. Takada, A. Takeda, and M. Ueno. MeV γ -ray imaging detector with micro-TPC. *New Astronomy Reviews*, 48(1–4):263–268, 2004.
- [94] The Geant4 Collaboration. *Geant4 Physics Reference Manual*. CERN, 2013.
- [95] The Geant4 Collaboration. *Geant4 User's Guide for Application Developers*. CERN, 2013.
- [96] R. W. Todd, J. M. Nightingale, and D. B. Everett. A proposed gamma camera. *Nature*, 251(5471):132–134, 1974.
- [97] Y.-S. Tsai. Pair production and bremsstrahlung of charged leptons. *Review of Modern Physics*, 46:815–851, 1974.
- [98] Y.-S. Tsai. Erratum: Pair production and bremsstrahlung of charged leptons. *Review of Modern Physics*, 49:421–423, 1977.

- [99] H. K. Tseng and R. H. Pratt. Exact Screened Calculations of Atomic-Field Bremsstrahlung. *Physical Review A*, 3:100–115, 1971.
- [100] O. T. Tumer, A. Akyuz, D. Bhattacharya, S. C. Blair, G. L. Case, D. D. Dixon, C.-J. Liu, T. J. O’Neill, J. Samimi, R. S. White, and A. D. Zych. The TIGRE instrument for 0.3-100 MeV gamma-ray astronomy. *IEEE Transactions on Nuclear Science*, 42(4):907–916, 1995.
- [101] K. Ueno, T. Mizumoto, K. Hattori, N. Higashi, S. Iwaki, S. Kabuki, Y. Kishimoto, S. Komura, H. Kubo, S. Kurosawa, Y. Matsuoka, K. Miuchi, K. Nakamura, H. Nishimura, J. Parker, Y. Sato, T. Sawano, A. Takada, and T. Tanimori. Development of the balloon-borne sub-MeV gamma-ray Compton camera using an electron-tracking gaseous TPC and a scintillation camera. *Journal of Instrumentation*, 7(1):C01088, 2012.
- [102] L. Urban. A Model for Multiple scattering in Geant4. Technical Report 2006-077, CERN, 2006.
- [103] J. van der Marel and B. Cederwall. Backtracking as a way to reconstruct Compton scattered γ -rays. *Nuclear Instruments and Methods in Physics Research Section A*, 437(2-3):538–551, 1999.
- [104] K. Vetter, M. Burks, and L. Mihailescu. Gamma-ray imaging with position-sensitive HPGe detectors. *Nuclear Instruments and Methods in Physics Research Section A*, 525(1-2):322–327, June 2004.
- [105] K. Vetter, D. Chivers, B. Plimley, A. Coffey, T. Aucott, and Q. Looker. First demonstration of electron-tracking based Compton imaging in solid-state detectors. *Nuclear Instruments and Methods in Physics Research Section A*, 652(1):599–601, 2011.
- [106] V. Votruba. Pair Production by γ -Rays in the Field of an Electron. *Physical Review*, 73:1468, 1948.
- [107] E. A. Wulf, B. F. Philips, W. N. Johnson, R. A. Kroeger, J. D. Kurfess, and E. I. Novikova. Germanium strip detector compton telescope using three-dimensional readout. *IEEE Transactions on Nuclear Science*, 50(4):1182–1189, 2003.
- [108] A. Zoglauer. *First Light for the Next Generation of Compton and Pair Telescopes*. PhD thesis, 2005.
- [109] A. Zoglauer, S. E. Boggs, R. Andritschke, and G. Kanbach. Recognition of Compton scattering patterns in advanced Compton telescopes. *Mathematics of Data/Image Pattern Recognition, Compression, Coding and Encryption X, SPIE*, (6700), 2007.
- [110] A. Zoglauer and G. Kanbach. Doppler broadening as a lower limit to the angular resolution of next-generation Compton telescopes. In *X-Ray and Gamma-Ray Telescopes and Instruments for Astronomy*, volume 4851, pages 1302–1309. SPIE, 2003.

Appendices: Geant4 Collaboration Papers

Appendix A

Geant4 electromagnetic physics: improving simulation performance and accuracy

V. N. Ivanchenko, S. Incerti, J. Allison, A. Bagulya, J. M. C. Brown, C. Champion, S. Elles, Z. Francis, V. Grichine, A. Ivantchenko, J. Jacquemier, M. Karamitros, M. Maire, A. Mantero, J. P. Marques, L. Pandola, M. Raine, D. Sawkey, A. Schaelicke, M. Schenk, A. Taborda and L. Urban

Published in Proceedings of the International Conference on Supercomputing in Nuclear Applications and Monte Carlo, 2013

DOI: 10.1051/snamc/201403101

Reproduced here with kind permission from EDP Sciences

Joint International Conference on Supercomputing in Nuclear Applications and Monte Carlo 2013 (SNA + MC 2013)
La Cité des Sciences et de l'Industrie, Paris, France, October 27-31, 2013

Geant4 electromagnetic physics: improving simulation performance and accuracy

V. N. Ivanchenko^{1,2,3*}, S. Incerti⁴, J. Allison³, A. Bagulya⁵, J. M. C. Brown⁶, C. Champion⁴, S. Elles⁷, Z. Francis⁸,
V. Grichine⁵, A. Ivantchenko^{1,3}, J. Jacquemier⁷, M. Karamitros⁴, M. Maire^{3,7}, A. Mantero⁹, J. P. Marques^{10,11}, L. Pandola¹²,
M. Raine¹³, M. A. Reis^{10,14}, G. Santin¹⁵, D. Sawkey¹⁶, A. Schaelicke¹⁷, M. Schenk¹⁸, A. Tabora^{10,14}, L. Urban³
and T. Yamashita¹⁹

on behalf of the Geant4 Collaboration

¹ CERN, CH1211 Geneva 23, Switzerland

² Ecoanalytica, 119899 Moscow, Russia

³ Geant4 Associates International Ltd, United Kingdom

⁴ Université Bordeaux I, CNRS/IN2P3, CENBG, 33175 Gradignan, France

⁵ Lebedev Physics Institute, 119991 Moscow, Russia

⁶ Monash University, School of Physics, Melbourne, Australia,

⁷ LAPP, 74941 Annecy-le-vieux, France

⁸ Université Saint Joseph, Faculty of Science, Department of Physics, Beirut, Lebanon

⁹ INFN-Genova, 16146 Genova, Italy

¹⁰ Centro de Física Atómica da Universidade de Lisboa, 1649-003 Lisboa, Portugal

¹¹ Departamento de Física da Faculdade de Ciências, Universidade de Lisboa, Campo Grande, Ed. C8, 1749-016 Lisbon, Portugal

¹² INFN-LNGS, 67100 Assergi, Italy

¹³ CEA, DAM, DIF, F-91297 Arpajon, France

¹⁴ IST/ITN, Instituto Superior Técnico, Universidade de Lisboa, Campus Tecnológico e Nuclear, 2686-953 Sacavém, Portugal

¹⁵ ESA/ESTEC, 2200 AG Noordwijk, The Netherlands

¹⁶ Varian Medical Systems, Palo Alto, CA 94304, USA

¹⁷ Helmholtz-Zentrum Berlin für Materialien und Energie GmbH, 12489 Berlin, Germany

¹⁸ The University of Bern, LHEP, CH-3012 Bern, Switzerland

¹⁹ Hyogo Ion Beam Medical Center, Tatsuno, Japan

* Corresponding Author, E-mail: [REDACTED]

The most recent upgrades of the electromagnetic (EM) physics “standard” and “low energy” sub-libraries of the general purpose Geant4 Monte Carlo simulation toolkit are described. These upgrades are relevant to different application domains including high energy physics, medical physics and space science. Validation results are presented and discussed.

KEYWORDS: *Monte Carlo, Geant4, electromagnetic physics.*

I. Introduction

The Geant4 Monte Carlo general purpose toolkit^{1,2)} includes a large variety of physics models for the simulation of particle transport in matter. It covers a wide spectrum of application domains, including simulation of high energy physics experiments, beam transport, nuclear physics, radiation medicine, cosmic rays and radiation in space. Electromagnetic (EM) physics sub-libraries^{3,4)} of the toolkit are used practically in all types of simulations and determine the accuracy of many simulation predictions.

In this work we report on recent progress in electromagnetic physics in the Geant4 public release 9.6 (available since December 2012) and beta version of the new release 10.0 (available since June 2013). Some models and interfaces were upgraded, and new models have been added. The unification of all EM model interfaces has been completed.

A new sub-library “dna” was created. A migration for EM models and processes was done for compatibility with Geant4 multi-threading (MT)⁵⁾. This paper presents both an overview of these new features, and new validation results.

II. Photon models

Models for photon interactions have been reviewed and improved. The interfaces to the angular generators were unified. All photo-electric effect and Compton scattering models were migrated to a common interface for the de-excitation module⁶⁾, allowing the sharing of internal physics tables of photon models/processes between threads in MT mode.

A new model^{7, 8)} (*G4LowEPComptonModel*) for Compton scattering has been developed by the Monash University group (Australia). This model was created to address the

limited accuracy of approximations utilised in sampling the ejected Compton electron direction seen in Geant4 and other photon transport simulation software⁹⁻¹³). It was developed from first principles¹⁴) utilising a two-body fully relativistic three-dimensional scattering framework in the Relativistic Impulse Approximation for bound atomic electrons. Comparison of this new model with respect to the Compton scattering models of Livermore and Penelope shows a high level of agreement between the photon scattering algorithms of all three models⁸). However, the ejected Compton electron angular distributions of the Monash model exhibit a more realistic distribution than those of the Livermore and Penelope Compton scattering models⁸). An example of the extent of this difference can be seen in Fig. 1 which shows 2-D distribution for electron polar angle respect to the primary photon and azimuthal angle respect to the photon scattering plane. Experimental validation of the Monash Compton scattering model for the K-shell Compton scattering of 662 keV photons in gold is reported in Ref.⁸).

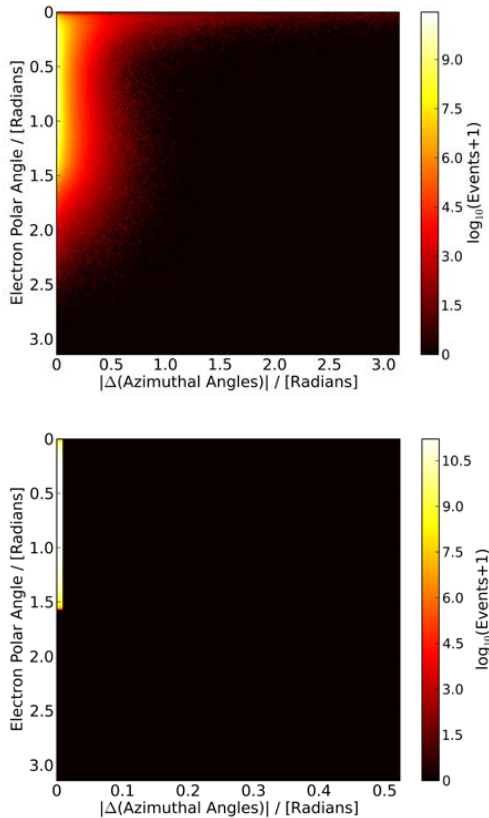


Figure 1: The Monash (top) and Penelope (bottom) model two-dimensional log intensity histograms of the ejected Compton electron angles for Cu at 500 keV photon beam.

Data management and sampling algorithms of the low energy Livermore models, including Rayleigh scattering, gamma conversion, photo-electric effect, and partial Compton scattering, have been optimised. These models are

based on the EPDL data library¹⁵) which is transformed into Geant4 G4LEDATA data sets. Internal data inside Livermore models were moved to standard Geant4 *G4PhysicsVector* and *G4ElementData* formats allowing sharing of these data between threads in MT mode. Low-energy limits were reduced to real EPDL values. High energy limits were extended by usage of asymptotic formulas for cross sections. Sampling algorithms for final states have been significantly updated. In particular, the Livermore Rayleigh scattering model is now 1000 times faster for energies above 100 keV, and can now be used in standard EM physics constructors. CPU performance of other Livermore models was also improved. In all Compton scattering and photo-electric effect models, a new general interface for de-excitation is introduced (see section VI). A summary of all recommended Geant4 photon models is shown in Table 1. The main difference between models is the sampling of the final state, at the same time the cross sections are similar for energies where compared models are applicable. Validation¹⁶) of cross sections was performed versus NIST and other evaluated data-bases.

Model	E_{\min}	E_{\max}	CPU
G4LivermoreRayleighModel	100 eV	10 PeV	1.2
G4PenelopeRayleighModel	100 eV	10 GeV	0.9
G4KleinNishinaCompton	100 eV	10 TeV	1.4
G4KleinNishinaModel	100 eV	10 TeV	1.9
G4LivermoreComptonModel	100 eV	10 TeV	2.8
G4PenelopeComptonModel	10 keV	10 GeV	3.6
G4LowEPCComptonModel	100 eV	20 MeV	3.9
G4BetheHeitlerModel	1.02 MeV	100 GeV	2.0
G4PairProductionRelModel	10 MeV	10 PeV	1.9
G4LivermoreGammaConversionModel	1.02 MeV	100 GeV	2.1
G4PenelopeGammaConversionModel	1.02 MeV	10 GeV	2.2
G4PEEFluoModel	1 keV	10 PeV	1
G4LivermorePhotoElectricModel	10 eV	10 PeV	1.1
G4PenelopePhotoElectricModel	10 eV	10 GeV	2.9

Table 1: List of recommended Geant4 photon models, applicability range, and relative CPU time for sampling of final state for 1 MeV gamma in Aluminum (10 MeV for gamma conversion) normalized to G4PEEFluoModel time.

III. Ionisation models

Models of ionisation are an essential part of charged particle transport code. Geant4 predicts hadron and ion transport with good accuracy¹⁷). Standard validation versus measurement is demonstrated in Fig.2 for protons in water for Geant4 10.0 beta. Note that for this Geant4 version management of internal tables for energy loss and range was changed due to the migration to MT providing sharing of all tables between threads. This internal reorganisation of tables does not affect physics results but slightly improves CPU and memory usage.

There are currently two models of energy loss straggling: the standard sub-library model (*G4UniversalFluctuations*) based on an empirical parameterisation¹⁹) and the photo-absorption ionisation model²⁰) (PAI) which considers all ionisation collisions. The first model is the default, and the PAI model is recommended for accurate simulation in sensitive volumes.

Recently these models were updated in order to be applicable to thin solid targets and gaseous detectors. The results of comparison with the ALICE TPC test-beam data^{21,22)} (Fig.3) demonstrate that both models can provide satisfactory results; however, the PAI model is stable versus step size while the default model needs optimisation of step limits. The alternative PAI-Photon model for this case demonstrates the same performance as the PAI model. The PAI-Photon model samples not only delta-rays but also X-rays.

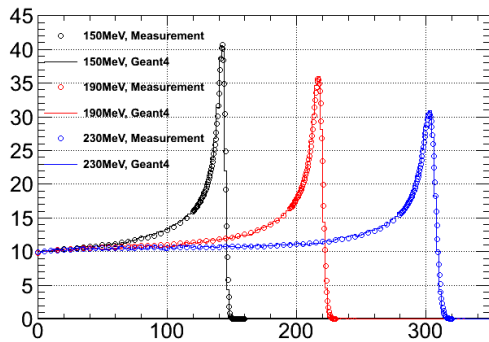


Figure 2: Proton Bragg peak shape in water (millimeters) for different energies of proton beam: histogram – simulation, open circles – data¹⁸⁾, 0.1 mm cut, Opt3 EM Physics List is used.

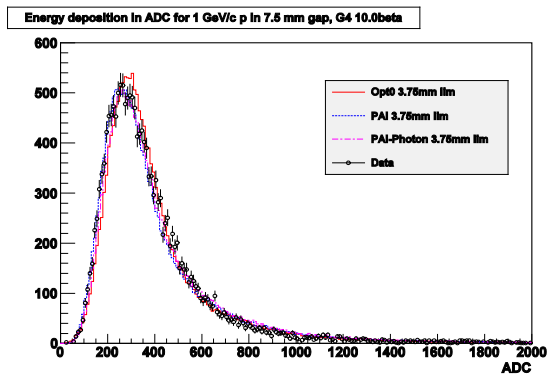


Figure 3: Proton energy deposition in gas gap in ADC counts: histogram – simulation, open circles – data^{21,22)}, 1 mm cut, step limit is equal to half gap thickness, beam momentum is 1 GeV/c, gas mixture Ne-CO₂-N₂; ADC scale for simulation was normalized on the PAI model peak position.

New microdosimetry processes^{23, 24)} based on the dielectric formalism have been developed at CEA (France) specifically to model the transport and generation of very low energy (down to 5 eV) electrons by incident electrons, protons and heavy ions in silicon. The aim of these developments is to study the effect of ionizing radiation in highly integrated microelectronic components²⁵⁾. The size of current and

future devices indeed requires a description of the deposited energy distribution at nanometric dimensions. For that, each ionisation collision should be simulated and condensed history algorithms (continues energy loss and multiple scattering) should not be applied. These new processes are fully included in the Geant4 public distribution since the 9.6 beta version, under the name “MuElec”¹⁾.

The list of physical interactions per particle type that can be modeled using the “MuElec” processes and models is reported in Table 2. The corresponding process classes, model classes, low and high energy limits of applicability of models, and energy threshold below which the incident particle is killed (stopped and the kinetic energy is locally deposited) are also listed. All models are interpolated. For now, they are valid for Silicon only (requiring the use of the «G4_Si» Geant4-NIST material). Developments for other materials are foreseen.

Since the first version of “MuElec” described in refs.^{23, 24)} and released in 9.6 beta, the energy range of applicability has been extended from 50 keV up to 100 MeV for electrons and from 23 MeV/u up to 1 GeV/u for protons and heavy ions (release 9.6 and 10.0beta). Further extension is under progress to go up to 10 GeV/u for protons and heavy ions, while improving the proton stopping power evaluation (shown to be overestimated²⁵⁾). These improvements are summarized in Fig.4 which shows the relative difference of stopping powers calculated with SRIM²⁶⁾ (software of reference for stopping power calculations), the first version of “MuElec” and the future one, compared to the PSTAR database²⁷⁾. A full description of these new developments will be given in a dedicated publication²⁸⁾. They are expected to be introduced in Geant4 in release 10.0.

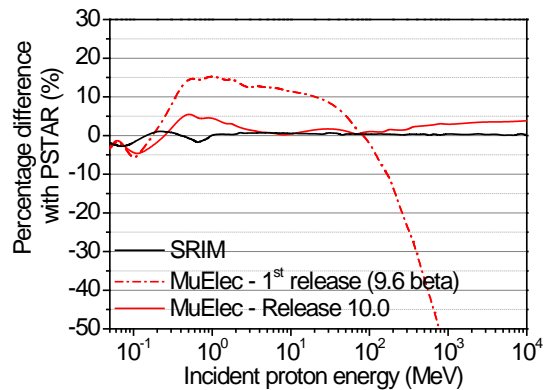


Figure 4: Percentage difference with PSTAR database²⁷⁾ as a function of the incident proton energy for stopping powers calculated with the first version of MuElec (Geant4 release 9.6 beta) and the future one (release 10.0). The SRIM²⁶⁾ comparison with PSTAR is also represented.

¹⁾ “MuElec” stands for micro(μ)-electronics. The name will be changed to “MicroElec” in the release 10.0 of Geant4, to avoid any confusion with muon processes.

Process	Geant4 process class	Geant4 model class	E_{\min}	E_{\max}
Electrons				
Elastic scattering	G4MuElecElastic	G4MuElecElasticModel	5 eV (*)	100 MeV
Ionisation	G4MuElecInelastic	G4MuElecInelasticModel	16.7 eV	100 MeV
Protons and ions				
Ionisation	G4MuElecInelastic	G4MuElecInelasticModel	50 keV/u	1 GeV/u

Table 2: “MuElec” physical interactions per particle type, and corresponding Geant4 processes and models, with energy ranges of applicability; (*) denotes a tracking cut below this energy.

IV. Bremsstrahlung

The relativistic Landau-Pomeranchuk-Migdal effect (LPM) is taken into account at high energies in ultra-relativistic bremsstrahlung and gamma conversion models using a recent theory which was verified versus experimental data²⁹⁾. At moderate energies, a new *G4SeltzerBergerModel* was created within the standard EM sub-library³⁰⁾. This model uses a parameterisation based on evaluated data tables³¹⁾ of Seltzer and Berger. For these new models computation³⁾ of restricted energy loss and restricted cross sections is performed using numerical integration instead of empirical parameterisations used in previous models of the standard sub-library.

V. Multiple and single scattering

In recent years a set of Geant4 multiple scattering and single scattering models³²⁾ was established. These models are tuned per particle type and application domain. In particular, single scattering models are useful for the sampling of charged particle transport in thin layers or low-density media. New single scattering models^{33, 34)} for space applications are available with Geant4 9.6.

Multiple scattering models determine CPU performance and accuracy of particle transport. For Geant4 9.6 sampling of scattering was moved from post-step to along-step before sampling of energy loss and straggling. This design change is an essential step in order to provide the possibility of sampling the lateral displacement of a charged particle on geometry boundary. For backward compatibility in Geant4 9.6 and in previous releases several versions of the Urban model³⁵⁾ were delivered. Recent tuning of the model and analysis of validation results allows consolidation of the model into only one version for the release 10.0 (*G4UrbanMscModel*).

The validation was performed using the EM testing suite³⁶⁾ which has been significantly extended for multiple and single scattering models^{29, 30)}. For electrons, multiple scattering models were tested by comparing simulations to electron scattering benchmark measurements³⁷⁾. The code used for the simulations is the *electronScattering2* extended example³⁸⁾, available in the Geant4 distribution. Scattering from various thicknesses of 7 different materials with atomic numbers ranging from 4 to 79, for incident electron energies of 13 and 20 MeV, was simulated. The width of the central portion of the scattering peak was compared to measured values. This width was determined by a Gaussian fit to the part of the curve above $1/e$ of the peak height. These widths obtained from simulation, divided by the measured widths,

are shown in Fig.5 for the standard EM Physics List *standard_option4* (Opt4). For 30 out of 35 points, widths are within 2% of the experimental value (the experimental uncertainty was 1%), with the worst disagreement of 3.5% for carbon.

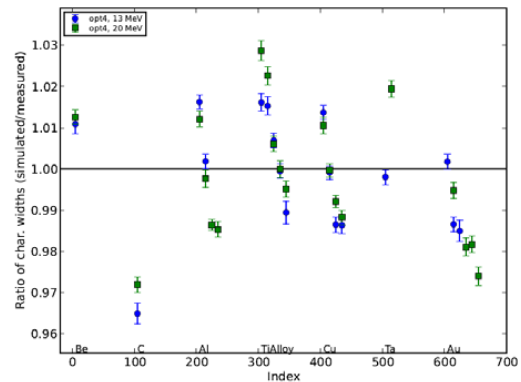


Figure 5: Ratio of simulated to measured scattering peak widths, as a function of scattering foil index. The index increases with increasing atomic number. The standard physics list Opt4 was used.

The overall goodness of fit was calculated using the chi-square method. This parameter takes into account the agreement at large scattering angles in addition to the central peak. The measured data were reported in N angular bins normalized to the first bin. Because of this, the simulated histograms were renormalized to minimize χ^2/N . Results are presented in Fig.6 for the Opt4 Physics List.

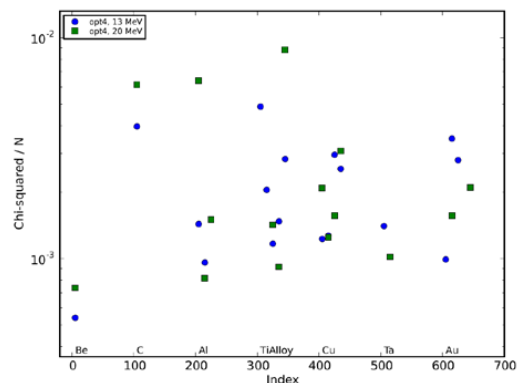


Figure 6: The value χ^2/N , used to compare the goodness of the simulation over the full range of measured scattering angles.

Thus, for electron transport the final version of the Urban model is the most accurate. Previous versions³⁸⁾ demonstrated worse agreement. For other particle types and for high energies, the alternative combined approach^{29, 30, 32)} of the WentzelVI (WVI) multiple scattering model combined with the single scattering model has several advantages compared to the Urban model. First of all, these display the correct Rutherford tail of angular distribution for large scattering angles at any projectile energy, and a smaller dependence of the simulation results on step size. For low energy muons, it is confirmed by comparison with MuScat experimental data³⁹⁾. In Fig.7 values of χ^2/N are shown for 10 different targets and for sum over all available targets.

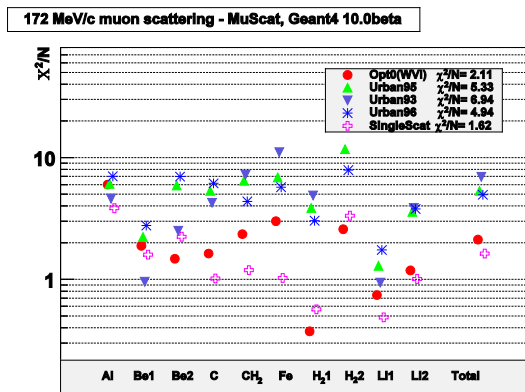


Figure 7: Comparison of simulation of muon scattering in different targets versus data³⁹⁾. The value χ^2/N for different versions of Urban model, WentzelVI model (WVI) and single scattering model. In the default EM Physics List Opt0 a combination WVI and single scattering is used.

Another new high energy benchmark provides comparison of transfer displacement of muon tracks⁴⁰⁾ from Z-boson decay in muon system of L3 detector at CERN LEP collider. Experimental data compared with simulation predictions are shown in Table 3 which demonstrates that WVI and single scattering models are significantly closer to the data than old Urban models. Note that this benchmark is done using simplified geometry of the L3 detector. The most recent version of Urban model prediction is practically similar to the WVI prediction. Thus analysis of all available multiple scattering benchmarks allow to remove all old versions of the Urban model and release with Geant4 10.0 the most accurate one.

Model	Displacement (mm)
Urban90	7.639 ± 0.095
Urban93	6.989 ± 0.083
Urban95	6.630 ± 0.080
Urban96	6.442 ± 0.080
WentzelVI+Single Scattering	6.404 ± 0.079
Data ⁴⁰⁾	6.078 ± 0.028

Table 3: RMS of 45.6 GeV muon displacement in the muon system of L3 detector at the LEP collider.

VI. Atomic de-excitation

Since Geant4 9.6 all EM models and the radioactive decay model use the same common atomic de-excitation interface⁶⁾ which allows the simulation of radiative and non-radiative atomic relaxation (fluorescence X-rays and Auger electrons emission). Consequently, the de-excitation module is usable in all Geant4 electromagnetic physics constructors and is steered via standard Geant4 command line interface (UI) or via C++ interface. In particular, de-excitation module can be used for the simulation of fluorescence spectra obtained in particle induced X-ray emission (PIXE) elemental ion beam analysis experiments. In a recent study⁴¹⁾, sample targets were irradiated with a 3 MeV proton beam and the de-excitation spectra were detected using a Si(Li) detector. The obtained results were compared with Geant4 simulated X-ray spectra. Validation was done for mono-elemental samples of Si, Al, Cu and Fe and more complex reference samples containing more than ten elements, e.g. B-EN and stainless steel (see details in⁴¹⁾). Figure 8 shows an example of comparison of the copper K-shell de-excitation simulated with Geant4 and the experimental data.

In the updated de-excitation module PIXE simulation is performed generically using shell ionisation cross sections interface. Models of ionization are responsible only for simulation of energy loss and delta-electron emission. Users may define cross section class per particle type, with default cross sections provided. For hadrons and heavy ions, original shell cross sections are not available; in that case scaling from the proton one is used. Additional shell ionisation cross sections for incident protons and alpha particles for K, L and M shells have been recently added for the simulation of PIXE. These models cover the 100 keV – 100 MeV incident energy range for K and L shells and for Z=6 to Z=92 target atomic numbers, and the 100 keV – 10 MeV range for M shells and for Z>61 up to Z=92 elements^{42, 43)}. These models, as well as the already existing set of empirical models and analytical models⁶⁾, are fully selectable using UI commands in Geant4 applications.

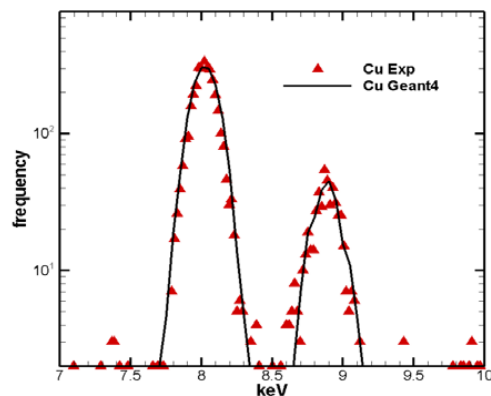


Figure 8: Energy of photons (K-shell radiation) from 3 MeV proton beam off thin copper target: red markers - experimental data; line - Geant4 simulation. Livermore EM physics list was used. Detector resolution is taken into account.

VII. Geant4 DNA processes and models

Since 2007, Geant4 is being extended in the framework of the Geant4-DNA project⁴⁴⁾ in order to provide an open-source platform able to simulate early DNA damage resulting from irradiation of biological samples, such as biological cells. All these Geant4-DNA developments are included in the new “dna” electromagnetic sub-library of Geant4. The simulation is based on a succession of the following three stages:

- the “physical” stage where the interaction between ionizing radiation and the biological medium is simulated;
- the “physico-chemical” stage where water - the main component of biological materials - impacted by ionizing radiation from previous stage may dissociate into new chemical species;
- the “chemical” stage where chemical species may react either with each other, producing a temporal evolution of their concentrations, or with biological molecules such as DNA, leading to DNA damage.

For the “physical” stage, the Geant4-DNA extension provides a set of processes and models, which can reach the eV scale and simulate all discrete interactions in liquid water. Table 4 shows the list of processes and models currently available in Geant4-DNA.

In the context of the Geant4-DNA project, a prototype for simulating radiation chemistry of liquid water in Geant4 is currently being developed^{45,46)}. This module aims at simulating, at the biological cell scale, the chemical reactions occurring in the “chemical” stage from 1 picosecond up to 1 microsecond after irradiation. Its first version is based on the particle-continuum representation where each chemical species is explicitly simulated and the solvent is treated as a continuum and uses the diffusion-controlled reaction model. A full description of the implemented method and model can be found in ref.⁴⁶⁾.

To benchmark radiochemistry codes, one of the criteria often used is the so-called time-dependent radiochemical yield. It corresponds, for a given chemical species, to the number of molecules available in the liquid water medium at a given time and for 100 eV of deposited energy:

$$G(t) = N(t)/100 \text{ eV.}$$

The time-dependent radiochemical yields of the two main radical species, namely the hydroxyl radical and the solvated electron, are reported for the case of irradiation with 1 MeV electrons. The simulated setup is an infinite water box. The radiochemical yields are computed for each single primary particle independently. When the primary particle has deposited more than 10 keV, it is withdrawn from the simulation. All its secondary electrons are followed until thermalization (i.e. when they reach the energy given by the medium’s temperature, around 25 meV in our case) and solvation. The simulation of the “chemical” stage was done using the parameters given in⁴⁷⁾ and the simulation method described in⁴⁸⁾. The results are presented in Fig.9. A full discussion of those results is given in⁴⁹⁾.

We expect to deliver a first example user application called “dnachemistry” that will detail how to enable the chemistry

stage of Geant4-DNA in the Geant4 release version 10.0 in December 2013. This example will show the user how to follow in time the evolution of the chemical reactions resulting from water irradiation.

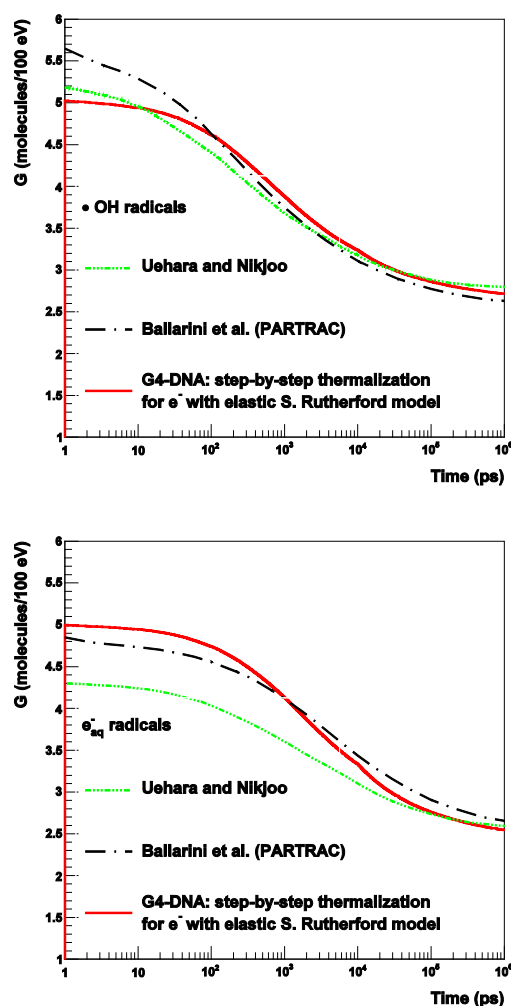


Figure 9: Time-dependent radiochemical yields for hydroxyl radicals (top) and solvated electrons (bottom). The red line is obtained using Geant4-DNA and is compared to the results in black obtained from Ballarini et al. (using the PARTRAC software)⁴⁸⁾ and to the results in green obtained from Uehara and Nikjoo⁴⁹⁾.

VIII. Built-in biasing options

For the first time, built-in EM biasing options are available inside the Geant4 toolkit. Geant4 version 9.6 includes: cross section biasing, forced interactions, splitting of final state, and Russian roulette. These biasing options may be enabled via UI command or C++ interfaces and can be applied on top of any EM Physics configurations. Cross section biasing may be useful to study the effects of uncertainty of EM cross sections on EM shower shape or other observables. Forced

interaction method is implemented only for the limited use-case of thin target assuming that forced interaction happens uniformly in the volume of interest and no correction is applied to secondary particle weight.

The other two methods are classical variance reduction techniques used to speed up simulation. Secondary particle splitting allows enhance secondary particle spectra in an area of interest. Russian roulette method is applicable for the case when too many secondary particles are produced (EM shower), so only a fraction of secondary particles is tracked with increased weight of each tracked particle.

The secondary particle splitting has been implemented in view of medical and other applications. The user may request that each interaction produce N secondaries, each of weight $1/N$. Each secondary is chosen independently from the relevant distributions. The energy and momentum of the primary particle after scattering are determined from the first secondary (this preserves straggling). The splitting is configurable by Geant4 EM process type, geometry region, and energy interval for secondary particles.

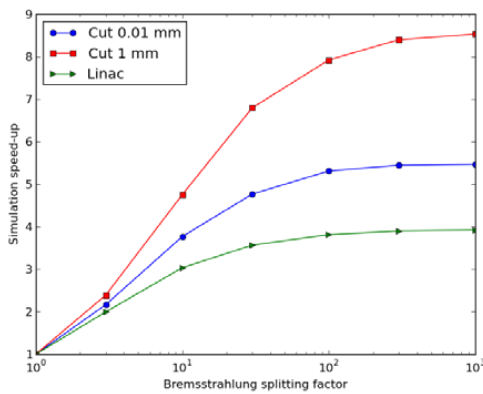


Figure 10: Relative speed-ups for the simulations, as a function of bremsstrahlung splitting factor. The product of number of incident particles and bremsstrahlung splitting factor was kept constant for each series of simulations. For curves labeled 'Cut', 6 MeV electrons are shot onto a W target. Production cuts of 0.01 and 1 mm were used, as labeled. For the curve labeled 'Linac', a medical linear accelerator was simulated.

An example application involves medical linear accelerators with photon beams produced by bremsstrahlung. A large fraction of the simulation time can be spent simulating electron transport in the bremsstrahlung target. This may be reduced by creating multiple photons for each bremsstrahlung event. Fig.10 shows the speed-up of simulations, when the product of number of incident particles and the bremsstrahlung splitting factor is kept constant. Two geometries were considered: one was a 2 mm thick W target, with a 6 MeV incident electron beam. The second was a medical linear accelerator⁵⁰⁾ operated at 6 MV (6.18 MeV incident electron beam). Relative simulation times decreased for both geometries with increasing bremsstrahlung splitting factors, up to a maximum improvement in speed of 8.5. The improvement in speed was greater for the simple geometry, reflecting the time spent

transporting photons in the more complex geometry of the medical linear accelerator. Similarly, reducing the production cuts decreased the effectiveness of bremsstrahlung.

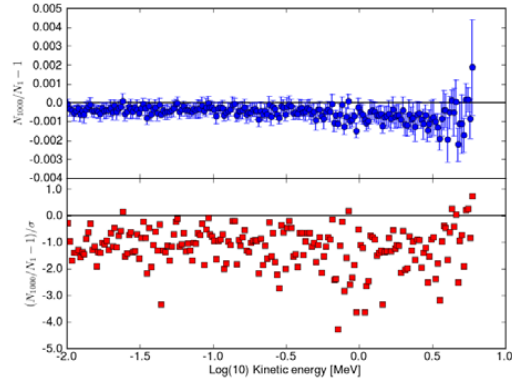


Figure 11: Ratio of number of photons (N) created for the simulation with splitting factor of 1000, to that with splitting factor 1, as a function of the kinetic energy of the photon. Lower curve shows the ratio relative to the statistical precision (σ).

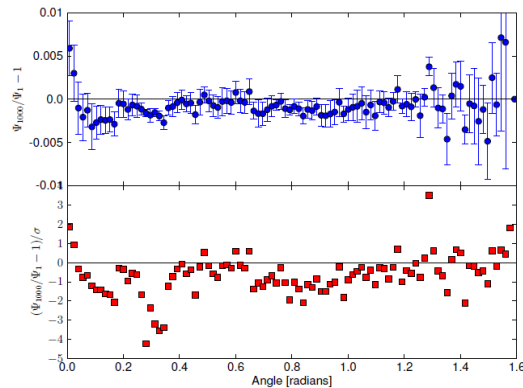


Figure 12: Ratio of the energy fluence (ψ) of photons leaving the target for simulations with bremsstrahlung splitting factors of 1000 and 1, as a function of the angle. Lower curve shows the ratio relative to the statistical precision (σ).

The accuracy of the bremsstrahlung splitting was evaluated by comparing the photons generated from simulations with different bremsstrahlung splitting factors. The example code *TestEm5* from Geant4 distribution was used, with a geometry consisting of a pencil beam of 6 MeV electrons on a 3 mm thick W target. Bremsstrahlung splitting factors of 1 (no splitting) and 1000 were used. The energy of the photons at their creation, plus the energy fluence, differential in angle, of photons exiting the target was recorded. All photons were considered, not just those created by bremsstrahlung. The ratio of these quantities for these two different bremsstrahlung splitting factors is expected to be 1. In Fig.11 the ratio of the number of photons per energy bin is shown. Results with the two different bremsstrahlung

splitting factors agreed to better than 0.05%. The lower panel of the figure shows the difference relative to the statistical uncertainty. In Fig.12 the energy fluence per angle bin is shown, and the agreement is 0.1% over most of the angular region. Agreement for both values is equal to the statistical uncertainty.

IX. Infrastructure of electromagnetic physics

With the release 9.6 the unification of all EM physics sub-libraries has been achieved for “standard”, “low-energy”, and “dna” sub-libraries. This allows combining models from different sub-libraries in EM physics constructors. For Geant4 9.6 in EM components⁴⁾ of physics lists have been updated. In all EM constructors (except standard Opt3) the WentzelVI multiple scattering model is used for electrons and positrons above 100 MeV, and for muons and hadrons at all energies. The Urban model is used below 100 MeV for electrons and positrons, and for all energies for ions. In standard Opt3 constructor Urban model is used for all particles at all energies. In all EM constructors the ultra-relativistic gamma conversion model is applied above 80 GeV. This model takes into account LPM effect providing more accurate high energy cross section.

A new physics constructor (standard Option4) has been designed in order to provide the most accurate EM physics to Geant4 users. For that, step limitation parameters are optimised per particle type and the most accurate models for gamma and electron transport from the “standard” and “low-energy” sub-libraries are used.

For the version 10.0 EM processes and models are adopted for the MT approach⁵⁾: tables of energy loss, ranges, and cross sections are filled at initialisation time in the master thread and are available in the run time shared between all worker threads. This was achieved by migration of material property classes, 1-D and 2-D physics vector classes of Geant4 to read-only run time mode.

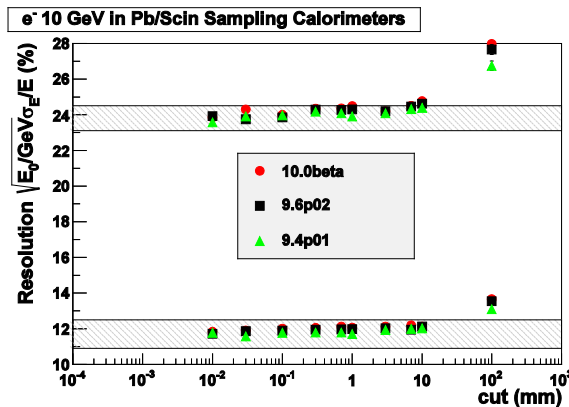


Figure 13: Energy resolution of two sampling Lead/Scintillator calorimeters for 10 GeV electrons: points – Geant4 simulation for different versions of the toolkit, hashed area – one standard deviation for the data^{51, 52)}.

In Fig.13 resolution of two sampling calorimeters^{51, 52)} versus cut in range value³⁾ and Geant4 version is shown. A recommended cut in range for typical high energy calorimeters is 1 mm – Geant4 simulated energy resolution is at a plateau while CPU performance is acceptable. For lower cut values required CPU time significantly increased. This plot illustrates good agreement of Geant4 simulation predictions with the data and stability of simulation results for high energy physics applications between Geant4 versions.

X. Summary

With the Geant4 version 9.6 the program of design change toward modularisation³⁾ and unified interfaces⁴⁾ was completed. This allowed straightforward migration of EM physics sub-libraries to Geant4 MT⁵⁾ and continues development of new high-energy, low-energy and DNA models. Geant4 EM physics is used successfully in many application domains, in particular, for simulation of experiments at Large Hadron Collider at CERN for discovery of Higgs boson^{53, 54)}.

Acknowledgment

This work was supported in part by ESA TRP contracts 22712/09/NL/AT, 22839/10/NL/AT, and 4000107387/12/NL/AK.

References

- 1) S. Agostinelli et al., “Geant4 – a simulation toolkit,” *Nucl. Instr. Meth. A*, **506**, 250 (2003).
- 2) J. Allison et al., “Geant4 developments and applications,” *IEEE Trans. Nucl. Sci.*, **53**, 270 (2006).
- 3) J. Apostolakis et al., “Geometry and physics of the Geant4 toolkit for high and medium energy applications,” *Rad. Phys. Chem.*, **78**, 859 (2009).
- 4) V.N. Ivanchenko et al., “Recent improvements in Geant4 electromagnetic physics and interfaces,” *Progress in Nuclear Science and Technology*, **2**, 898-903 (2011).
- 5) S. Ahn, J. Apostolakis, M. Asai, D. Brandt, G. Cooperman, G. Cosmo, A. Dotti, X. Dong, A. Novak and S. Y. Jun “Geant4-MT: bringing multi-threaded Geant4 into production”, in these proceedings.
- 6) A. Mantero, H. Ben Abdelouahed, C. Champion, Z. El Bitar, Z. Francis, P. Guèye, S. Incerti, V. Ivanchenko, M. Maire, “PIXE simulation in Geant4,” *X-Ray Spectrometry*, **40**, 135-140 (2011).
- 7) J.M.C. Brown, M.R. Dimmock, J.E. Gillam, D.M. Paganin, “MULECS: The Monash University Low Energy Compton scattering package,” *proceedings of the Nuclear Science Symposium and Medical Imaging Conference (NSS/MIC) 2011*, pp. 1385-1389 (2011).
- 8) J.M.C. Brown, M.R. Dimmock, J.E. Gillam, D.M. Paganin, “A low energy bound atomic electron Compton scattering model for Geant4,” *Nucl. Instr. Meth. A*, in Review.
- 9) Y. Namito S. Ban and H. Hirayama, “Implementation of Doppler broadening of a Compton scattering photon into EGS4 code,” *Nucl. Instr. Meth. A*, **349**, 489-494 (1994).
- 10) D. Brusa, G. Stutz, J. A. Riveros, J. M. Fernandes-Varea and F. Salvat, “Fast sampling algorithm of the simulation of

- photon Compton scattering," *Nucl. Instr. Meth. A*, **379**, 167-175 (1996).
- 11) I. Kawrakow, D. W. O. Rogers, "The EGSnrc Code System: Monte Carlo Simulation of Electron and Photon Transport," NRCC Report PIRS-701, NRC, Ottawa, 2001.
 - 12) RSICC Computer Code Collection, MCNPX 2.4.0," Report CCC-715, LANL, Los Alamos, 2002.
 - 13) M. R. Kippen, "The GEANT low energy Compton scattering (GLESC) package for the use in simulating advanced Compton telescopes," *New Astro. Reviews*, **48**, 221-225 (2004).
 - 14) R. Ribberfors, "Relationship of the relativistic Compton cross section to the momentum distribution of bound electron states," *Phys. Rev. B*, **12**, 2067-2074 (1975).
 - 15) D. Cullen, J.H. Hubbell, L. Kissel, "The evaluated photon data library," Report UCRL-50400, Vol.6 (1997).
 - 16) G.A.P. Cirrone et al., "Validation of the Geant4 electromagnetic photon cross-sections for elements and compounds," *Nucl. Instr. Meth. A*, **618**, 315-322 (2010).
 - 17) A. Lechner, V. N. Ivanchenko, J. Knobloch, "Validation of recent Geant4 physics models for application in carbon ion therapy," *Nucl. Instrum. and Meth. B*, **268**, 2343-2354 (2010).
 - 18) Y. Kumazaki, T. Akagi, T. Yanou, D. Suga, Y. Hishikawa, T. Teshima, "Determination of the mean excitation energy of water from proton beam ranges", *Radiation Measurements*, **42**, 1683 – 1691 (2007).
 - 19) K. Lassila-Perini, L.Urban, "Energy loss in thin layers in GEANT," *Nucl. Instr. Meth. A*, **362**, 416 (1995).
 - 20) V. Grichine et al., "An implementation of ionisation energy loss in very thin absorbers for the Geant4 simulation package," *Nucl. Instr. Meth. A*, **453**, 597-605 (2000).
 - 21) D. Antonchuk et al., "Performance studies with an ALICE TPC prototype," *Nucl. Instr. Meth. A*, **565**, 551-560 (2006).
 - 22) P. Christiansen, "Particle Identification Studies with an ALICE Test TPC," *Int. J. Mod. Phys. E*, **16**, 2457-2462 (2007).
 - 23) A. Valentin, M. Raine, J.-E. Sauvestre, M. Gaillardin and P. Paillet, "Geant4 physics processes for microdosimetry simulation: very low energy electromagnetic models for electrons in silicon," *Nucl. Instr. Meth. B*, **288**, 66-73 (2012).
 - 24) A. Valentin, M. Raine, M. Gaillardin and P. Paillet, "Geant4 physics processes for microdosimetry simulation: very low energy electromagnetic models for protons and heavy ions in silicon," *Nucl. Instr. Meth. B*, **287**, 124-129 (2012).
 - 25) M. Raine, A. Valentin, M. Gaillardin and P. Paillet, "Improved simulation of ion track structures using new Geant4 models - Impact on the modeling of advanced technologies response ", *IEEE Transactions on Nuclear Science*, vol. 59, pp. 2697-2703, 2012.
 - 26) SRIM [Online]. Available: <http://www.srim.org>
 - 27) M. J. Berger, J. S. Coursey, M. A. Zucker and J. Chang, "NISTIR-4999: Stopping power and range tables for electrons, protons and helium ions", NIST Reports, 2005.
 - 28) M. Raine, M. Gaillardin and P. Paillet, "Geant4 physics processes for Silicon microdosimetry simulation: improvements and extension of the energy-range validity up to 10 GeV/nucleon", *Nucl. Instr. Meth. B*, to be published.
 - 29) A. Schaelicke, A. Bagulya, O. Dale, F. Dupertuis, V. Ivanchenko, O. Kadri, A. Lechner, M. Maire, M. Tsagri and L. Urban, "Geant4 electromagnetic physics for the LHC and other HEP applications," *J. Phys: Conf. Ser.*, **331**, 032029 (2011).
 - 30) J. Allison, J. Apostolakis, A. Bagulya, C. Champion, S. Elles, F. Garay, V. Grichine, A. Howard, S. Incerti, V. Ivanchenko, J. Jacquemier, M. Maire, A. Mantero, P. Nieminen, L. Pandola, G. Santin, D. Sawkey, A. Schaelicke, and L.Urban, "Geant4 electromagnetic physics for high statistic simulation of LHC experiments," *J. Phys: Conf. Ser.*, **396**, 022013 (2012).
 - 31) S.M. Seltzer and M. J Berger, "Bremsstrahlung spectra from electron interactions with screened atomic nuclei and orbital electrons," *Nucl. Instrum. Meth. B*, **12**, 95 (1985).
 - 32) V.N. Ivanchenko, O. Kadri, M. Maire and L. Urban, "Geant4 models for simulation of multiple scattering", *J. Phys., Conf. Ser.*, **219**, 032045 (2010).
 - 33) M. J. Boschini, et al., "Nuclear and non-ionizing energy-loss for Coulomb scattered particles from low energy up to relativistic regime in space radiation environment". In: Giani, S., Leroy, C., Rancoita, P.G. (Eds.), Proceedings of the 12th ICATPP, 7–8 October 2010, Villa Olmo, Como, Italy. World Scientific, Singapore, pp. 9–23, ISBN: 978-981-4329-02-6 (2010).
 - 34) M. J. Boschini et al., "An expression for the Mott cross section of electrons and positrons on nuclei with Z up to 118," *Rad. Phys. Chem.*, **90**, 39-66 (2013).
 - 35) L. Urban, "A multiple scattering model in Geant4," Preprint CERN-OPEN-2006-077 (2006).
 - 36) J. Apostolakis, A. Bagulya, S. Elles, V.N. Ivanchenko, J. Jacquemier, M. Maire, T. Toshito and L. Urban, "Validation and verification of Geant4 standard electromagnetic physics," *J. Phys: Conf. Ser.*, **219**, 032044 (2010).
 - 37) C. Ross et al., "Measurement of multiple scattering of 13 and 20 MeV electrons by thin foil," *Med. Phys.*, **35**, 4121 (2008).
 - 38) B.A. Faddegon et al., "The accuracy of EGSnrc, Geant4 and PENELOPE Monte Carlo systems for the simulation of electron scatter in external beam radiotherapy," *Phys. Med. Biol.*, **54**, 6151 (2009).
 - 39) D. Attwood et al., "The scattering of muons in low-Z materials," *Nucl. Instr. Meth. B*, **251**, 41 (2006).
 - 40) P. Arce et al. "Multiple scattering in GEANT4. A comparison with Moliere theory and L3 detector data", Proceedings of MC-2000 Conference, EXP CERN-LEP-L3, (2000).
 - 41) Z. Francis, M. El Bast, R. El Haddad, A. Mantero, S. Incerti, V. Ivanchenko, Z. El Bitar, C. Champion, M.A. Bernal, M. Roumie, "A comparison between Geant4 PIXE simulations and experimental data for standard reference samples," *Nucl. Instr. Meth. B*, in press (2013).
 - 42) A. Taborda, P. C. Chaves, M. A. Reis, "Polynomial approximation to universal ionisation cross-sections of K and L shells induced by H and He ion beams," *X-Ray Spectrometry*, **40**, 127-134 (2011).
 - 43) A. Taborda, P. C. Chaves, M. L. Carvalho, M. A. Reis, "Polynomial approximation to universal M-shell ionisation cross-sections induced by H+ and He2+ ions," *X-Ray Spectrometry*, **42**, 177-182 (2013).
 - 44) S. Incerti, G. Baldacchino, M. Bernal, R. Capra, C. Champion, Z. Francis, P. Guèye, A. Mantero, B. Mascialino, P. Moretto, P. Nieminen, C. Villagrasa, C. Zacharatou, "The Geant4-DNA Project," *International Journal of Modeling, Simulation, and Scientific Computing*, **01**, 157-178 (2010).
 - 45) M. Karamitros, A. Mantero, S. Incerti, G. Baldacchino, P. Barberet, M. Bernal, R. Capra, C. Champion, Z. El Bitar, Z. Francis, W. Friedland, P. Guèye, A. Ivanchenko, V. Ivanchenko, H. Kurashige, B. Mascialino, P. Moretto, P. Nieminen, G. Santin, H. Seznec, H. N. Tran, C. Villagrasa, C. Zacharatou, "Modeling radiation chemistry in the Geant4 Toolkit," *Progress in Nuclear Science and Technology*, **2**, 503-508 (2011).
 - 46) M. Karamitros, S. Luan, M.A. Bernal, J. Allison, G. Baldacchino, M. Davidkova, Z. Francis, W. Friedland, V. Ivantchenko, A. Ivantchenko, A. Mantero, P. Nieminen, G. Santin, V. Stepan, N.H. Tran, S. Incerti, "Improving

- computational performance of the chemistry module of Geant4-DNA,” submitted (2013).
- 47) V. Breton, C. Champion, Z. El Bitar, M. Karamitros, S. B. Lee, L. Maigne, Y. Perrot, Q. T. Pham, J. I. Shin, H. N. Tran, S. Incerti, “Extended Geant4 at the physics-medicine-biology frontier”, submitted (2013).
- 48) S. Uehara, H. Nikjoo, “Monte Carlo Simulation of Water Radiolysis for Low-energy Charged Particles”, *Journal of Radiation Research*, **47**, 69-81 (2006).
- 49) F. Ballarini, M. Biaggi, M. Merzagora, A. Ottolenghi, M. Dingfelder, W. Friedland, P. Jacob, H.G. Paretzke, “Stochastic aspects and uncertainties in the prechemical and chemical stages of electron tracks in liquid water: a quantitative analysis based on Monte Carlo simulations,” *Radiation and Environmental Biophysics*, **39**, 179-188 (2000).
- 50) M. Constantin et al., “Modeling the TrueBeam linac using a CAD to Geant4 geometry implementation: Dose and IAEA-compliant phase space calculations,” *Med. Phys.*, **38**, 4018 (2011).
- 51) E. Bernardi E et al, „Performance of a compensating lead-scintillator hadronic calorimeter,“ *Nucl. Instrum. Meth. A*, **262**, 229-242, (1987).
- 52) G. D’Agostini et al., “Experimental study of uranium plastic scintillator calorimeters,“ *Nucl. Instrum. Meth. A*, **274**, 134, (1989).
- 53) ATLAS Collaboration, “Observation of a new particle in the search for the Standard Model Higgs boson with the ATLAS detector at the LHC”, *Phys. Lett. B* **716**, 1-29, (2012).
- 54) CMS Collaboration, “Observation of a new boson at a mass of 125 GeV with the CMS experiment at the LHC”, *Phys. Lett. B*, **716**, 30-61, (2012).

Process	Geant4 process class	Geant4 model class	E _{min}	E _{max}
Electrons				
Elastic scattering	G4DNAElastic	G4DNAScreenedRutherfordElasticModel	9 eV(*)	1 MeV
		G4DNACHampionElasticModel	7.4 eV(*)	1 MeV
Excitation	G4DNAExcitation	G4DNABornExcitationModel	9 eV	1 MeV
Ionisation	G4DNAIonisation	G4DNABornIonisationModel	11 eV	1 MeV
Vibrational excitation	G4DNAVibExcitation	G4DNASancheExcitationModel	2 eV	100 eV
Attachment	G4DNAAttachment	G4DNAMeltonAttachmentModel	4 eV	13 eV
Protons				
Excitation	G4DNAExcitation	G4DNAMillerGreenExcitationModel	10 eV	500 keV
		G4DNABornExcitationModel	500 keV	100 MeV
Ionisation	G4DNAIonisation	G4DNARuddIonisationModel	100 eV(*)	500 keV
		G4DNABornIonisationModel	500 keV	100 MeV
Charge decrease	G4DNAChargeDecrease	G4DNADingfelderChargeDecreaseModel	100 eV	100 MeV
Hydrogen				
Excitation	G4DNAExcitation	G4DNAMillerGreenExcitationModel	10 eV	500 keV
Ionisation	G4DNAIonisation	G4DNARuddIonisationModel	100 eV(*)	100 MeV
Charge increase	G4DNAChargeIncrease	G4DNADingfelderChargeIncreaseModel	100 eV	100 MeV
Neutral helium ionised twice				
Excitation	G4DNAExcitation	G4DNAMillerGreenExcitationModel	1 keV	400 MeV
Ionisation	G4DNAIonisation	G4DNARuddIonisationModel	1 keV(*)	400 MeV
Charge decrease	G4DNAChargeDecrease	G4DNADingfelderChargeDecreaseModel	1 keV	400 MeV
Neutral helium ionised once				
Excitation	G4DNAExcitation	G4DNAMillerGreenExcitationModel	1 keV	400 MeV
Ionisation	G4DNAIonisation	G4DNARuddIonisationModel	1 keV(*)	400 MeV
Charge decrease	G4DNAChargeDecrease	G4DNADingfelderChargeDecreaseModel	1 keV	400 MeV
Charge increase	G4DNAChargeIncrease	G4DNADingfelderChargeIncreaseModel	1 keV	400 MeV
Neutral helium				
Excitation	G4DNAExcitation	G4DNAMillerGreenExcitationModel	1 keV	400 MeV
Ionisation	G4DNAIonisation	G4DNARuddIonisationModel	1 keV(*)	400 MeV
Charge increase	G4DNAChargeIncrease	G4DNADingfelderChargeIncreaseModel	1 keV	400 MeV
C, N, O, Fe ions				
Ionisation	G4DNAIonisation	G4DNARuddIonisationExtendedModel	1 keV(*)	400 MeV

Table 4: List of Geant4 very low energy processes and models available in the Geant4-DNA extension (Geant4 version 9.6p02) for track structure simulation in liquid water during the “physical” stage. Low and high-energy limit applicability of models are shown. (*) denotes a tracking cut below the corresponding kinetic energy.

Appendix B

Recent developments in Geant4

M. Asai, A. Dotti, M. Verderi, D. H. Wright and The Geant4 Collaboration (inc. J. M. C. Brown)

In Press, Annals of Nuclear Energy, 2014

DOI: 10.1016/j.anucene.2014.08.021

Reproduced here with kind permission from Elsevier Inc.

ARTICLE IN PRESS

Annals of Nuclear Energy xxx (2014) xxx–xxx



Contents lists available at ScienceDirect

Annals of Nuclear Energy

journal homepage: www.elsevier.com/locate/anucene

Recent developments in Geant4

Makoto Asai^a, Andrea Dotti^a, Marc Verderi^b, Dennis H. Wright^{a,*}, The GEANT4 Collaboration^aSLAC National Accelerator Laboratory, Stanford, CA, USA^bIN2P3 Laboratoire Leprince-Ringuet, Paris, France

ARTICLE INFO

Article history:

Received 29 April 2014

Accepted 12 August 2014

Available online xxx

Keywords:

Monte Carlo

Multi-threading

Physics modeling

GUI

ABSTRACT

During the last two to three years extensive development of the GEANT4 simulation toolkit has occurred, which will culminate in a major release at the end of 2013. This development includes the adoption of multi-threading, the extension and improvement of physics models, improvements to the geometry modeler with a revised implementation of most geometrical primitives, advances in visualization and graphical user interfaces (GUI), the move from GNU make to CMake and the extension and automation of the GEANT4 testing suite. The reasons for and implementation of multi-threading will be discussed. Certain electromagnetic and hadronic model extensions will also be discussed along with their effects on calorimeter results. Finally, visualization and GUI improvements will be highlighted along with the new configuration, build and testing systems.

© 2014 Elsevier Ltd. All rights reserved.

1. Introduction

Perennial demands for improved physics modeling, the need for faster and more efficient simulations, and the desire to keep pace with modern hardware and software trends have all led to numerous improvements in the GEANT4 toolkit (Agostinelli et al., 2003; Allison et al., 2006) over the past two to three years.

Faster simulations can be achieved by exploiting the trend toward increasing numbers of cores per chip. In GEANT4 this is done by adopting multi-threading. We discuss the resulting changes to the kernel, the geometry package and other GEANT4 categories, which are extensive enough to warrant a major release of GEANT4 by the end of 2013.

Requests to improve physics simulations, in particular for hadronic showers, have come mostly from the high energy physics community. Hence the concentration on parton string and cascade models which has improved the agreement of simulations with calorimeter data. Significant input from the space and medical communities has led to improvements in low and medium energy models. We cover here electromagnetic and hadronic processes and note that improvements in physics models almost always imply increased computing time. It is hoped that these increases can be offset by employing more cores via multi-threading.

Algorithms of most geometrical primitives utilized by the geometry modeler have been deeply reviewed in the last couple

of years. We will describe the major improvements and new features introduced.

To aid in the interpretation of simulated results, GEANT4 offers an array of visualization options and graphical user interfaces, most of which have seen significant advances recently. A few of these are highlighted below.

Finally we discuss the upgrade of build and testing tools. The move from GNU make to CMake has resulted in a more versatile configure and build system and a more powerful developer environment. An extensive testing suite has been developed with a number of online tools for running, monitoring and validating results of system tests.

2. The Geant4 kernel

2.1. Incorporating Geant4-MT in the Geant4 production release

To make efficient use of multi-core processors and reduce the memory footprint of the simulation we have developed a version of GEANT4 which uses multi-threading (MT for short) to share a substantial part of data between threads. Two GEANT4-MT prototypes were released in 2011 and 2012. In the next major release the multi-threaded code will be merged into the main source code. By design the memory savings in GEANT4-MT (Dong et al., 2010, 2012) are obtained by sharing the majority of the geometry descriptions and the tables of the physics processes among the threads; threads are otherwise independent. Each thread is responsible for simulating one or more full events, thus implementing event-level parallelism. Measurements performed with the

* Corresponding author. Address: SLAC National Accelerator Laboratory, 2575 Sand Hill Road, Menlo Park, CA 94025, USA. Tel.: +1 [redacted]
E-mail address: [redacted] (D.H. Wright).

<http://dx.doi.org/10.1016/j.anucene.2014.08.021>

0306-4549/© 2014 Elsevier Ltd. All rights reserved.

GEANT4-MT prototype demonstrate (Figs. 1 and 2) that this approach scales well with the number of threads.

To ensure the long-term maintainability of the code, and to allow the code to evolve towards newly emerging technologies, GEANT4-MT is based on the POSIX thread standard. This has allowed the code to be ported to different operating systems, including Mac OS X, and also to newly emerging technologies, such as the Intel Xeon Phi co-processor. This latter aspect is interesting since these co-processors allow the use of a large number of threads, and enable testing of the scalability of the system. We have reached an efficiency in linearity of more than 80% with about 200 threads on Intel Xeon Phi (Ahn et al., 2013).

An important constraint and driving consideration in the design of GEANT4-MT is that the effort required for application developers to port an application to GEANT4-MT is small. Our criterion is that this extra effort should be a small fraction of the total development effort. In addition, the effort required to maintain the required code modifications should be small. For a simple or standalone GEANT4 application, i.e. one which does not depend on a large external framework, the effort to make the first port of an application should be of the order of a few hours' work.

The process of porting a GEANT4 application to multi-threading involves the inspection and potentially the adaptation of a small set of methods, which are the responsibility of an application developer. The key parts that require intervention are classes in which the user examines the internal state of the simulation at the end of every step, track or event, and records observables which will be output (*SensitiveDetector*).

GEANT4-MT has been integrated with the main GEANT4 code base and will become publicly available with Version 10. For a detailed description of multi-threading capabilities in GEANT4 and benchmarks performed so far see Ahn et al. (2013).

2.2. Geometry

The GEANT4 geometry modeler has undergone a deep review in different areas. The integration of multi-threading capabilities into the toolkit and the stringent requirement to allow for sharing of all geometrical information in a multi-threaded run, has required the adaptation of a few key classes to clearly separate the read-only part from data which can change during the generation of an event, and therefore should be treated privately by each single working thread. See Ahn et al. (2013) for details.

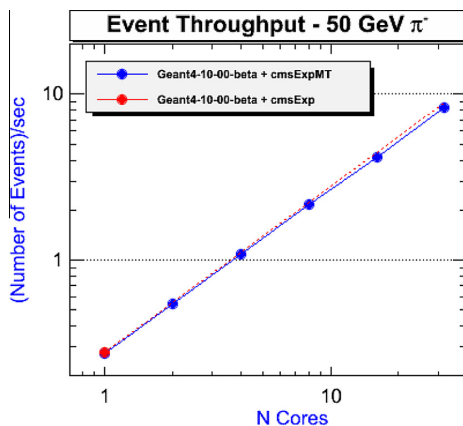


Fig. 1. Linearity of speed-up as a function of the number of threads. For reference, results obtained with the sequential version of GEANT4 are shown in red. (For interpretation of the references to color in this figure legend, the reader is referred to the web version of this article.)

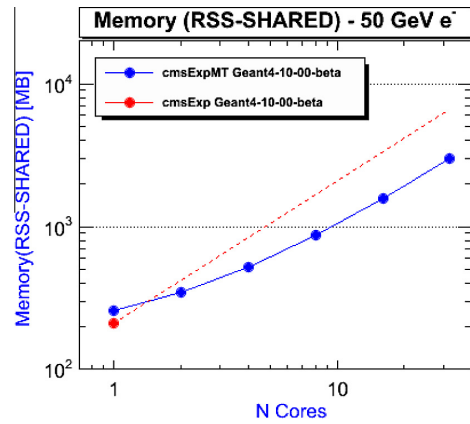


Fig. 2. Linearity of memory use as a function of the number of threads. For reference, results obtained with the sequential version of GEANT4 are shown in red. (For interpretation of the references to color in this figure legend, the reader is referred to the web version of this article.)

In addition to the modifications strictly related to thread safety, several new features and improvements have been introduced and are planned for the geometry for the next major release of GEANT4.

It is now possible to define volumes with material in parallel geometry layers. The volumes created can complement or overlap the standard geometry setup used for tracking. All geometries and all geometrical regions are now scanned for their own material. This new capability, *layered mass geometry*, was introduced in release 9.5 and allows for the definition of one or more additional layers for the mass geometry. This is an enhancement of the existing functionality for parallel specialized geometries (Apostolakis et al., 2008), which has been in use for scoring, fast simulation, shower parameterization and event biasing. Interesting applications could be the definition of sampling calorimeters, where the geometry could be layered according to different levels of detail for different particle types, or in medical physics applications like brachytherapy (Asai et al., 2012).

An important effort was begun in the last couple of years, based on the AIDA (AIDA, 2012) initiative, to write a new software library for the modeling of geometrical primitives (solids), starting from the existing implementations in GEANT4 and in the Root geometry package (Gayer et al., 2012).

This work, which is now nearly completed, consists in reviewing at the algorithmic level most of the primitives and provides an enhanced, optimized and well-tested implementation to be shared among software packages. In most cases considerable performance improvement was achieved. For example, the time required to compute intersections with the tessellated solid was dramatically reduced with the adoption of spatial partitioning for composing facets into a 3D grid of voxels.

Such techniques allow speedup factors of a few thousand for relatively complex structures having of order 100K to millions of facets, which is typical for geometry descriptions imported from CAD drawings (see Fig. 3). Consequently, it is now possible to use tessellated geometries for tuning the precision in simulation by increasing the mesh resolution, something that was not possible before. This development has been included in the GEANT4 distribution since release 9.6.

In addition to a full set of highly optimized primitives and a tessellated solid, the library includes a new "multi-union" structure implementing a composite set of solids (several or many) to be placed in 3D space. This differs from the simple technique based on Boolean unions, with the aim of providing excellent scalability

ARTICLE IN PRESS

M. Asai et al. / Annals of Nuclear Energy xxx (2014) xxx–xxx

3

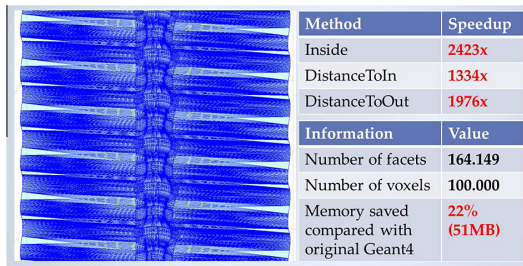


Fig. 3. Performance of the new tessellated solid measured on a sample of 164K facets from CAD drawings of the LHCb VELO foil, compared to the old implementation.

on the number of constituent solids. The multi-union adopts a similar voxelization technique to partition 3D space, allowing dramatically improved speed and scalability over the original implementation based on Boolean unions. A scalability plot is shown in Fig. 4. This new library is planned for inclusion in the next major release of GEANT4 as an optional component.

3. Physics

3.1. Physics lists

In GEANT4, physics processes and the models and cross sections that implement them are collected, instantiated and assigned to particle types in “physics lists”. In principle it is the user’s responsibility to implement the physics list classes and make sure that the physics appropriate to a given application is included. However, this is often a difficult task and several fully implemented physics lists have been provided to aid the user.

Because few models handle the physics of a given particle at all energies, and because GEANT4 offers several alternate models and cross sections, the physics lists became complex and their number increased along with the number of applications. Recently this complexity was somewhat reduced by extensions of existing physics models (see next two sections) which allowed fewer models to cover more particles and larger energy ranges. Improvements in the quality of physics models and cross sections also allowed older models to be removed, thus reducing the number of options to choose from. As a result, the number of prepared physics lists offered was reduced from 40 to 17, while still covering the same physics. Of the remaining 17 lists, several, including FTTP.BERT,

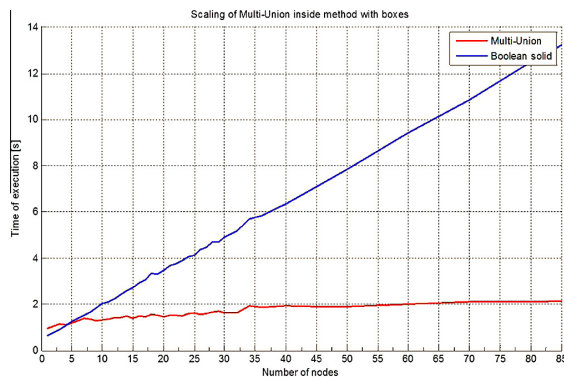


Fig. 4. New multi-union replaces linear scalability with logarithmic for performance-critical methods such as Inside().

QGSP.BERT and QBBC, are regularly tested and validated against LHC calorimeter data.

Significant variations on the above physics lists are allowed through the use of the G4PhysListFactory class. Users may thus specify a base physics list, such as FTTP.BERT, and substitute various electromagnetic physics options depending on their applications. These options include the relatively low energy Livermore and Penelope set of processes, a fast and general but approximate set, and the default set which covers all energies.

3.2. Electromagnetic physics

The GEANT4 set of electromagnetic (EM) physics processes and models is a key component of the toolkit, covering a wide spectrum of application domains, including simulation of high energy and nuclear physics experiments, beam transport, medical physics, cosmic ray interactions and radiation effects in space. EM physics sub-packages (Agostinelli et al., 2003; Apostolakis et al., 2009; Ivanchenko et al., 2011) of the toolkit are used in practically all types of simulation and determine the accuracy of many simulation predictions. GEANT4 EM physics includes models for high energy up to 10 PeV, for moderate energies which are important for all types of applications, low-energy models working down to 100 eV and very low energy models developed in the framework of the GEANT4-DNA project. With the 9.6 release of (December 2012), the unification of interfaces (Ivanchenko et al., 2011) for all EM physics sub-packages was completed. Recent developments and results for GEANT4 EM are discussed in Ivanchenko et al. (2013), while only a short description is presented below.

3.2.1. EM infrastructure

GEANT4 EM physics processes are organized into “constructors” which represent different options to be included in the physics lists. These constructors were updated in release 9.6, and have several physics models in common. One of these is the WentzelVI multiple scattering model (Ivanchenko et al., 2010) which is used for e^+ and e^- above 100 MeV. Another is an ultra-relativistic gamma conversion model (Schaelicke et al., 2011) applied above 80 GeV.

A new physics constructor (so-called “option4”) was designed to provide the most accurate set of EM physics models to users. In this option, step limitation parameters are optimized per particle type and the most accurate models for gamma and electron transport from the “standard” and “low-energy” sub-categories are used.

For the first time, built-in biasing options are available in GEANT4; these options include cross section biasing, forced interactions, splitting of final state, and Russian roulette. These options may be activated per process, per particle type, and per geometry region by either C++ or command line user interfaces.

3.2.2. Standard models

New models have been developed for bremsstrahlung and gamma conversion (Schaelicke et al., 2011; Allison et al., 2012). For high energies, relativistic LPM effects are included by using recent theoretical analyses and verified versus experimental data. For low and moderate energies, a parameterization based on evaluated data tables (Seltzer and Berger, 1985) was introduced. For all models, computation of restricted energy loss and restricted cross sections (Apostolakis et al., 2009) is performed using numerical integration instead of the empirical parameterizations used in previous models.

Multiple and single scattering models (Ivanchenko et al., 2010) were further tuned. In release 9.6, the sampling of scattering was moved from post-step to along-step before the sampling of energy loss and straggling. This design change is an essential step in order

to provide the possibility of sampling the lateral displacement of a charged particle on a geometrical boundary; it is planned for the 10.0 release. Also, a consolidation of the Urban model of multiple scattering has been achieved, so that with release 10.0 only one version of the model will be delivered. The EM testing suite (Apostolakis et al., 2010) has been significantly extended for multiple and single scattering models (Schaelicke et al., 2011; Allison et al., 2012).

3.2.3. Low energy models

The alternative “low energy” sub-category of EM processes can describe interactions of electrons, gammas and positrons including the simulation of atomic deexcitation processes (fluorescence and Auger emission). In particular in this unification effort, all evaluated “Livermore” sets of models describing the interactions of gammas have been reviewed. These models include the photoelectric effect, Rayleigh scattering and gamma conversion. The data management and sampling algorithms of the corresponding classes have been optimized. In addition, a new model for Compton scattering (Brown et al., 2011) has been introduced in order to improve the accuracy of the Compton electron direction computation below 2 MeV. Also available are analogues of these models which handle polarization and extend upwards in energy to 100 GeV in some cases (DePaola, 2003, 2009; DePaola and Leguizamon, 2009).

The interface for simulating radiative and non-radiative atomic de-excitation has been updated so that it can be used transparently by both sub-categories of electromagnetic processes and can easily be controlled using macro commands (Mantero et al., 2011). This new interface also proposes an additional set of shell ionization cross sections for incident protons and alpha particles, covering K and L shells in the range 0.1–100 MeV, and M shells in the range 0.1–10 MeV, for a selection of target materials. These cross sections were calculated in the ECPSSR framework (Taborda et al., 2011, 2013).

Finally, a set of microdosimetry processes and models, based on the dielectric formalism (Valentin et al., 2012a,b), has been developed specifically for the simulation of electron, proton and ion discrete interactions in silicon, for microelectronics applications.

3.2.4. DNA processes and models

The “DNA” sub-category of GEANT4 is able to simulate the discrete interactions of electrons, protons, neutral hydrogen, alpha particles and their charged states, and a few ions (C, N, O, Fe) for microdosimetry applications in liquid water, in the framework of the “GEANT4-DNA” project (Incerti et al., 2010; Francis et al., 2011). In particular, electron elastic scattering is simulated in the partial wave formalism down to about 7 eV (Champion et al., 2012a). With the unified EM class design, these very low energy processes can be combined with other EM processes (Ivanchenko et al., 2011, 2012). In addition, processes and models were developed using the Classical Trajectory Monte Carlo approach for the simulation of proton and neutral hydrogen interactions in liquid water and the DNA nucleobases, adenine, thymine, guanine and cytosine (Champion et al., 2013, 2012b). Once fully verified, they will be released in GEANT4.

3.2.5. Validation of electromagnetic physics

Validation of EM physics is performed on several levels. Because EM physics is used in practically all tests and examples, the Geant4 integration test system (see Section 5) routinely checks all EM physics models. A specific EM validation suite (Apostolakis et al., 2010) runs on a regular basis (Ivanchenko et al., 2011, 2013, 2010; Schaelicke et al., 2011; Allison et al., 2012) for each reference version of Geant4. Dedicated validations of cross sections, stopping powers, and atomic transition energies versus evaluated data and

theory are being done (Cirrone et al., 2010; Seo et al., 2011; Pia et al., 2011; Batic et al., 2011, 2012, 2013) by Geant4 developers and various user groups. In parallel with main development EM physics, an alternative library for proton induced X-ray emission has been created and validated (Pia et al., 2009).

Geant4 EM physics validation is performed in various application domains by different user communities who have built their software on top of Geant4, in particular GATE (Jan et al., 2011), GAMOS (Canadas et al., 2011) and GRAS (Ibarmia et al., 2013).

There are also many validation results obtained by different user groups. As an example a recent validation of therapeutic ion beam simulations was done by Lechner et al. (2010) and Mishustin et al. (2010).

3.3. Hadronic physics

Recent work on GEANT4 hadronic physics has spanned the energy range from sub-thermal neutron propagation to the scattering of TeV hadrons from nuclei. Much of this work was driven by the simulation requirements of LHC detector groups needing detailed treatment of shower development and propagation.

At the high energy end, the Fritiof (Andersson et al., 1987) (FTF) parton string model has undergone almost continuous development for the last two years. The most important improvement has been its extension to lower energies, down to 2–3 GeV for mesons and baryons, and down to zero for anti-baryons. Diffraction processes have been significantly improved. The tuning of the model parameters has been refined to better describe thin-target scattering data. Finally, nucleus-nucleus interactions can be also simulated by the model.

At medium energies (200 MeV to 10 GeV) progress has been made on two intra-nuclear cascade models. The INCL cascade (Kaitaniemi et al., 2011) was introduced into GEANT4 several years ago as an alternative to the Bertini and Binary (Folger et al., 2004) cascade codes. It had its origins in the Liege intra-nuclear cascade and was translated from its original Fortran into C++. It has recently been replaced by the completely re-designed and upgraded INCL++. INCL++ (and INCL) is a more data-driven approach to the intra-nuclear cascade than the Bertini or Binary codes and includes such features as light cluster formation at the end of the cascade phase. After the precompound phase the native GEANT4 de-excitation code is used to complete the reaction. In addition to the usual pion and nucleon projectiles, the model can now handle light ion projectiles up to ^{12}C , and is valid for incident energies up to 3 GeV.

The GEANT4 Bertini-style cascade (Heikkinen et al., 2003) continues to be extended and improved. It can now be invoked for all long-lived hadron species and has recently been extended to other particle types such as gammas from 10 MeV to 10 GeV incident energy, electrons and positrons of 10 GeV and below, and stopped muons. The code has been extended to provide interfaces to models outside its range of applicability. For the case of high energy interactions where the Fritiof model is used, secondaries from the first interaction are often too high in energy to be passed to a nuclear precompound model. In this case an intra-nuclear cascade model would be a better choice and the FTF–Bertini interface has been developed for this purpose. Another interface was developed which allows the Bertini-style cascade to bypass its own precompound and de-excitation codes and use the native GEANT4 precompound and de-excitation models (Quesada et al., 2010) instead. Using this interface produces superior results at energies below 75 MeV.

A precise treatment of the elastic, inelastic and capture processes of neutrons from sub-thermal to 20 MeV has a large effect in shielding applications and on some calorimeter observables such as energy deposition and time structure. Two GEANT4 models

ARTICLE IN PRESS

M. Asai et al. / *Annals of Nuclear Energy* xxx (2014) xxx–xxx

5

which treat neutrons in this regime are the High Precision (HP) and LEND. The HP models are data-driven codes based on the G4NDL database, which in turn is based on the ENDF/B-VII database (Chadwick et al., 2011). In the past, data in G4NDL was taken from eight different databases, including ENDF, JENDL, JEFF, ENDL, MENDL and CENDL. This caused confusion when the origin of any part of the data was required. This problem was recently resolved by basing G4NDL entirely on ENDF/B-VII and making the other databases available in their entirety as alternatives.

LEND models were developed as an alternative to the HP models and are based on the GIDI (General Interaction Data Interface) developed at Livermore. In the future, ENDF, JEFF, JENDL and ENDL will be converted to this format. An advantage of the LEND models over the standard HP models is speed. Due to the pre-calculation of Doppler broadening, a factor of five improvement has been seen in some applications. It is noted here that the HP models do have an option to ignore Doppler broadening which increases their speed.

Radioactive decay is another low energy GEANT4 model. It is based on the ENSDF (National Nuclear Data Center, 2013) database and can handle the beta, alpha, isomeric transition and electron capture reactions for 2248 isotopes. This includes 534 nuclear states that now have precise beta decay spectra due to the recent addition of the 1st, 2nd and 3rd unique forbidden shapes. Directional biasing of nuclei was also added as a means of speeding up certain reactions. Independent validations and improvements of this model can be found in Hauf et al. (2013a,b).

The production and propagation of isomers and metastable states is currently under development and will be released with GEANT4 version 10. Also at that time, the radioactive decay and

photo-evaporation databases, updated to ENSDF August 2012, will be released.

Two long-standing GEANT4 models have been deprecated as they have been replaced by more performant codes. These are the Chiral Invariant Phase Space (Degtyarenko et al., 2000a,b) and the Low and High Energy Parameterized (LHEP) models. Essential pieces of the CHIPS code have been extracted and refactored into new classes so its modeling capabilities have not entirely disappeared. The LHEP models are re-engineered C++ versions of the Gheisha Fortran code (Fesefeldt, 1985) and were the first hadronic models in GEANT4. However, they were highly parameterized and did not treat individual interactions in detail. In fact, they did not conserve energy or momentum on an event-by-event basis.

As a result of these deprecations, several new stopped particle interaction models were developed to replace the old ones. Models handling pion, kaon and sigma absorption are now based on the Bertini-style cascade. Although it has not historically been used for stopped particles, the Bertini code performs rather well in this case because it bypasses the cascade and goes straight to its precompound model to generate the necessary particle-hole states. Similarly, the FTF model is usually never used for stopped particles because there is no energy available for string formation. However with proton-antiproton annihilation, 2 GeV are available and low-mass strings can be produced. As a result this model is now used for antiproton absorption. A new stopped muon absorption model was also developed as an alternative to the model currently used in most physics lists, which was known to poorly reproduce the resultant neutron spectra. The new model, also based on the Bertini cascade, does an excellent job reproducing the neutron spectra as shown in Fig. 5.

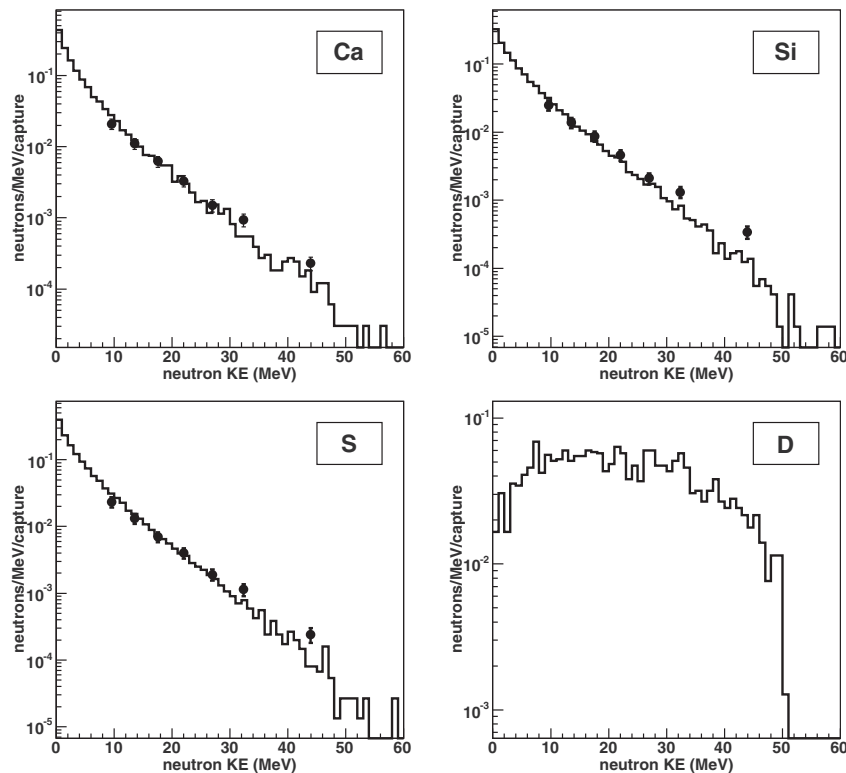


Fig. 5. Comparison of neutron energy spectra from muon capture with Bertini-based capture model (upper curves) and CHIPS-based capture model (lower curves).

3.4. Calorimeter response

One of the most challenging aspects of detector simulation for high energy physics is the simulation of jets, isolated electrons and gammas. The energy of these objects is well-measured in calorimeters.

The simulation of showers in calorimeters requires all physics processes to be correctly simulated to allow for the precise description of the main observables: response, resolution, lateral and longitudinal shower shapes.

Significant efforts have been made to improve the description of EM shower shapes: the bremsstrahlung and multiple scattering descriptions were reviewed and improved, having been identified as key components in defining EM shower shapes. Calorimeters are sensitive to the precise simulation of electron and gamma transport in the MeV energy region. Therefore significant validation and benchmarking is being carried out for medium and low energy electrons and gammas. A comprehensive description of recent improvements of the GEANT4 EM module can be found in Allison et al., 2012). The general agreement of GEANT4 predictions with experimental data collected at the LHC is better than one percent (Abat et al., 2011).

The extensive validation of GEANT4 physics against LHC test-beam calorimeter data has shown that the most critical models for the description of hadronic showers are:

- Parton string models at high energy (in this case the recommended model for calorimeter simulations is the Fritiof model (Andersson et al., 1987).
- Cascade models at intermediate energies (from a few hundred MeV up to about 10 GeV, the recommended model in this energy regime is the Bertini intra-nuclear cascade (Heikkinen et al., 2003).
- A pre-equilibrium and evaporation model at low energies (below a few hundred MeV, the recommended model in this energy regime is G4Precompound (Quesada et al., 2010).

For the response function the agreement between simulation and data for hadron-induced showers is at the level of a few percent, but shower shapes and resolution are less precisely described and show an agreement at the level of 10–20%. The response to pion beams is shown as a function of the particle energy for different GEANT4 physics lists. Fig. 6 shows the comparison between the predictions of GEANT4 simulations and test-beam data collected by the ATLAS collaboration (Adragna et al., 2009). Note that the data have been rescaled to take into account the simpler geometrical structure considered in our simulation (Dotti et al., 2011).

The older QGSP.BERT_HP list uses our implementation of the quark-gluon string model coupled with parametrized models and the high precision neutron model for the treatment of low energy neutrons. Note that while the HP model does not play an important role in describing the response in calorimeters, it is important for other calorimetric observables such as the time structure of the showers and lateral development in neutron-rich materials.

4. Visualization and GUI

The GEANT4 Visualization System (Allison et al., 2013) is a multi-driver graphics system designed to serve the GEANT4 Simulation Toolkit. It is aimed at the visualization of GEANT4 data, primarily detector descriptions and simulated particle trajectories and hits. It can handle a variety of graphical technologies simultaneously and interchangeably, allowing the user to choose the visual representation most appropriate to requirements, for example:

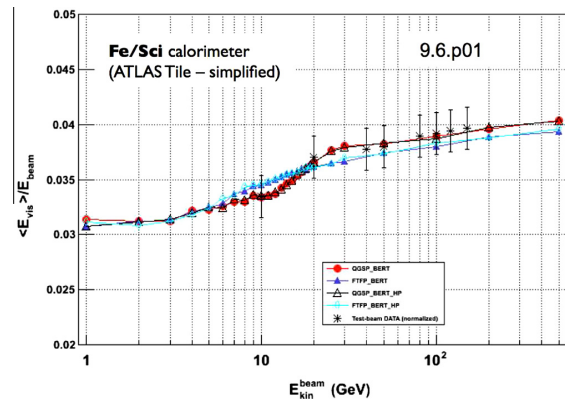


Fig. 6. Comparison between test-beam data (see text) and GEANT4 for the simulation of high energy pions as a function of beam energy. Different physics lists are shown.

- Very quick response in surveying successive events.
- High-quality output for presentation and documentation.
- Flexible camera control for debugging detector geometry and physics.
- Selection of visualizable objects.
- Interactive picking of graphical objects for attribute editing or feedback to the associated data.
- Highlighting incorrect intersections of physical volumes, and
- Co-working with graphical user interfaces.

Because it is very difficult to respond to all of these requirements with only one built-in visualizer, the Graphics Interface was developed to support multiple graphics drivers over several complementary graphics technologies to satisfy a wide variety of users' needs. This may use a graphics library directly, communicate with an independent process via pipe or socket, or simply write an intermediate file for a separate viewer.

The current distribution of Geant4 contains, at the latest count, 14 drivers of various sorts. They are listed in Fig. 7 along with their capabilities. Those which need external libraries or packages may only be activated at the compilation step if the corresponding external system is installed.

In addition, in principle, the user may extend this list by implementing his/her own driver to the specification of the abstract interface. A user may draw to the basic abstract interfaces, either in C++ code or, more usually, via visualization commands through a user interface, and expect it to be rendered in one of a number of different ways: to a computer screen (graphic drivers) or to a file for subsequent browsing (file-writing drivers).

The workhorse of the Geant4 Visualisation System is the set of OpenGL drivers. In particular, recent work has focused on our implementation of OpenGL within the context of the popular platform-independent GUI toolkit, Qt. The Geant4 Qt visualization/GUI solution allows the user to rotate and zoom the view, to toggle visibility of various viewed objects, and to interrogate detailed information about geometry, trajectories and hits. The same interface allows the user to control the overall simulation, even customizing the GUI with the user's own action buttons.

Other recent work on Geant4's OpenGL implementations has improved speed of rendering and exploited OpenGL's native ability to generate high quality PostScript renderings. For a wide variety of graphics drivers, Geant4 now offers improved view annotation features such as text, arrows, rulers, axes, date stamps, logos, etc.

The full set of Geant4 graphics drivers includes:

ARTICLE IN PRESS

M. Asai et al. / Annals of Nuclear Energy xxx (2014) xxx–xxx

7

Driver	Categorie	Variant	Picking	Hight Quality print	Interactive	Browse geom. Hearichle	Direct access to G4	Make movies	Web
OpenGL	Graphic	X							
		Xm							
		Qt							
OpenInventor	Graphic	Win32							
HepRepFile	File-writing								
RayTracer	File-writing								
Dawn	File-writing								
VRML	File-writing								
gMocren	File-writing								
ASCII Tree	File-writing								

Fig. 7. Visualization drivers and their capabilities.

- Qt – a rich vis/GUI interface for manipulation not just of visualization but of the entire simulation process.
- Open Inventor – including a newer variant that is specialized to visualization of accelerators, letting the viewer “fly” along a beamline.
- HepRep – renders in XML format to be read into a HepRep browser such as HepRApp (perl, <http://www.slac.stanford.edu/perl/heprep>).
- RayTracer – uses Geant4’s own tracking to render geometry to a jpeg file.
- DAWN – produces a file suitable for browsing with DAWN (Tanaka and Kawaguti, 1997).
- VRML – produces a file suitable for browsing with a VRML browser).
- gMocren (Kimura, <http://geant4.kek.jp/gMocren>), used typically to visualize radiation therapy dose data, and
- ASCII Tree – dumps the geometry tree to standard output and lists the physical volume name.

A particular feature of OpenGL is that one may store GL commands in a “display list” that may be efficiently rendered by a graphics processing unit. The most sophisticated is the OpenGL Qt (Garnier, <http://geant4.in2p3.fr/spip.php?article60&lang=en>) driver (Fig. 8) which offers a huge amount of interactivity, including rotation, pan and zoom, picking, drawing style, projection style, etc. The Qt user interface, includes an interactive help system and an interactive portrayal of the scene, including the geometry hierarchy, through which one can change the color and visibility of individual screen objects.

5. Configuration and testing

5.1. Configuring and building Geant4 with CMake

Geant4 as installed consists of a set of C++ headers and binary libraries, plus data resource files for physics models. This is typical for a midsize to large C++ toolkit, and like others in this class, configuring and building Geant4 from source has to take care of.

- Portability to Linux, OS X and Windows.
- Different build modes, e.g. Optimized or Debug.
- Optional toolkit components, e.g. GDML support.
- Use of third party APIs, e.g. CLHEP.

Up to version 9.5.0, Geant4 used the Perl dist system (Perl dist, <http://sourceforge.net/projects/dist/>) to perform build configuration, and GNU make (<http://www.gnu.org/software/make/>) to compile, link and install. The set of GNU make files provided could also be used to build applications against Geant4. Whilst this

system worked well for many years, it suffered from several deficiencies:

- A POSIX layer, such as Cygwin, was required on Windows platforms.
- Environment variables were used to store configuration options, making builds prone to error and often difficult to debug.
- Dist/Metaconfig scripts required a high level of maintenance to enable portability across platforms.
- Application developers only had the GNU make system available.

Modern build tools were therefore reviewed and the CMake system (Kitware CMake, 2012) was selected. The SCons and GNU Autotools systems were also considered, but rejected due to portability and maintenance considerations (Morgan, 2008).

CMake provides cross-platform support by design, and uses simple and easy-to-maintain scripts to generate build files for native tools such as Makefiles or Projects for Xcode/Visual Studio. It also provides many checks for system, compiler and third party API requirements directly, with further checks being easy to implement via the CMake scripting language. Build configuration is performed by running CMake from the command line or via a graphical interface to generate the native tool scripts. These scripts are then run with the native tool to build and if required, install, Geant4. This provides both easy, native builds for users, and flexible builds for developers under the development environment of their choice.

A full CMake build system for Geant4 was released with version 9.5.0, and has proved popular with users and developers. The number of problems with installation reported to the user forums has decreased, and those that have been easier to resolve due to CMake’s error reporting and caching of the configuration state in a dedicated file. Updates to support new platforms, compilers or other options have also been quick and easy to implement.

The development of the CMake system has continued to add functionality to help both users and developers. Data resources needed by some physics processes can now be downloaded and installed as part of the toolkit build, minimizing the number of installation tasks. Additional tools for application developers have been provided to enable them to build applications using CMake, GNU Make using the original Geant4 build system, or any tool capable of interfacing with a POSIX shell. In addition to build configuration, CMake provides the capability to generate source bundles and binary packages of the toolkit in formats such as rpm or exe. Work in this area is continuing, and concentrating on the Windows platform.

Usage of CMake has also allowed a radical upgrade to the testing of Geant4. The CTest tool provided by CMake, combined with the web based CDash system, provides a framework for continuous

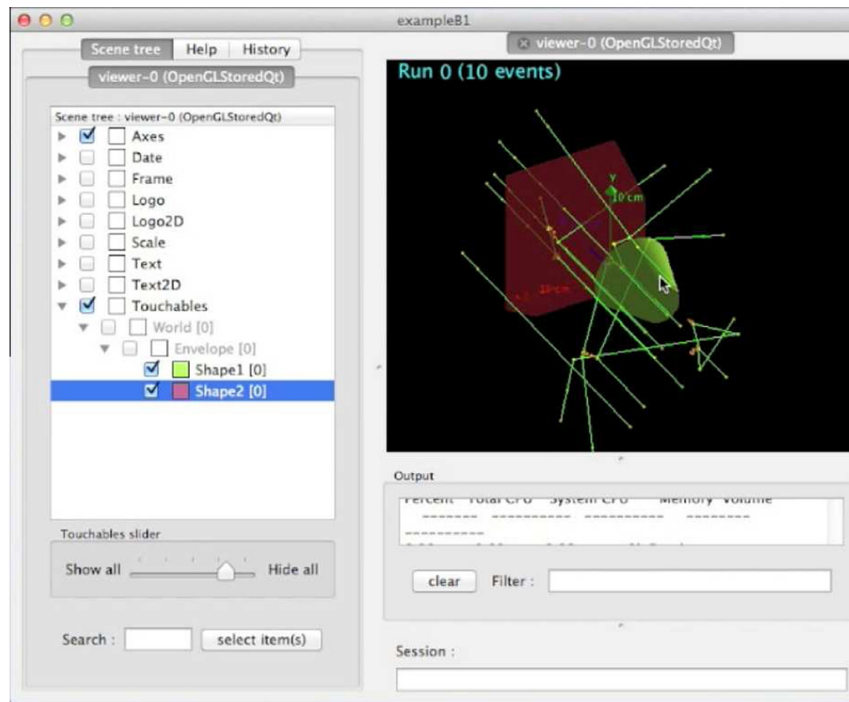


Fig. 8. Screen shot of Qt GUI.

integration of Geant4. The following section describes this system and its capabilities.

5.2. Testing Geant4 development

Geant4 is developed in a distributed way, each subpackage being updated and maintained by one or several collaborators. Testing the updates is a continuous process and consists of three main activities:

- Integration testing.
- Performance monitoring and improvement and
- Validation of physics performance.

Integration testing is run daily, or even continuously, while performance monitoring and validation of physics performance is performed for monthly Collaboration internal releases.

5.2.1. Integration testing

Integration testing checks that new or modified code in the code repository does not cause problems on any of the supported systems. We test Geant4 on Linux, Mac, and Windows using multiple compilers and OS versions, and using different configurations of GEANT4, summing up to about 20 different combinations tested. With the migration to the CMake-based build system, we adapted the testing system to use the CTest tool (Kitware CTest, 2012) designed to co-work seamlessly with CMake. The current setup is implemented using a client–server system, with a server starting and monitoring jobs on clients using Electric Commander software (ElectricComander, 2012), and clients sending results to a web-based software testing server running CDash software (Kitware CDash, 2012). The jobs started by Electric Commander on a client run a script to set the environment, check-out or update the source

code, and build libraries and tests using the CTest testing tool. As a result, much of the running and monitoring of testing is done via web interfaces of Electric Commander and the CDash web pages.

This automation made it possible to share the workload within the collaboration via testing shifts. A collaborator on shift selects which changes are to be included in a nightly test run and at a later time checks that test results do not show problems resulting from the changes. Currently about 200 test cases are run, which include most of the GEANT4 examples, tests checking specific parts of GEANT4, and a few general setups.

In addition, the automation allows us to start an incremental build running a reduced set of tests using a reduced set of compilers and Geant4 configurations whenever we find modified code. This allows developers to have prompt feedback on modified code, and acts as a filter for the full nightly build.

5.2.2. Performance monitoring

Performance monitoring provides general benchmarking and profiling information of GEANT4 software to the developers through code development cycle. It is also designed to identify problems and opportunities for code improvement and optimization. Results from profiling and benchmarking runs on development releases (reference, candidate, and public releases) are submitted to the responsible developers, and posted to a publicly available web-site (FNAL-G4P, 2010).

A set of tools for collecting, managing and analyzing data is used for both CPU and memory performance measurements. It includes generic timing tools (POSIX timer, usage), FAST profiler (FNAL-FAST, 2010) for profiling CPU performance, and IgProf (Eullisse and Tuura, 2002) for measuring memory footprint. GEANT4 applications with different combinations of event samples and physics lists are profiled on a batch system which consists of a 5 × 32 core AMD Opteron Processor. A semi-automated

ARTICLE IN PRESS

M. Asai et al. / *Annals of Nuclear Energy* xxx (2014) xxx–xxx

9

post-analysis generates various performance observables (plots, tables, and web-based navigation) for visual scans and further investigation.

As a GEANT4 version with *event level* multi-thread capabilities is being commissioned, the computing monitoring task has been extended to meet the new requirements. Besides conventional tools that are used for profiling sequential applications, multi-thread-capable performance evaluation tools such as HPCToolkits (Rice University, 2000), OpenSpeedshop (Open Speedshop, 2012) and TAU (University of Oregon, 1997), which are widely used in the high performance computing community, are tested for both sequential and multi-threaded modes. To quantify the scalability with the number of computational threads of the multi-threaded application, event throughput and memory gains are measured for selected samples. Opportunities for code optimization and performance improvements are continuously sought, resulting in the evolution and refinement of GEANT4 performance monitoring.

5.2.3. Validation of physics performance

Periodically – at least once per month, in correspondence with a new GEANT4 development release, or for a new release of Geant4 – a set of tests are run on the Grid to check whether there are changes on physics observables with respect to a reference version of GEANT4 (Dotti, 2012). The variables that are considered are those that describe hadronic showers in calorimeters: visible energy, energy resolution, longitudinal and lateral shower shapes. A set of simplified hadronic calorimeters – with the same absorber and active materials, and respective thicknesses, as for the real calorimeters of the LHC experiments – is used in the tests, for different combinations of beam particle energies and beam particle types. The CPU effort needed to complete the entire set of tests requires the use of the Grid. As final results of these tests, plots of physics observables as a function of the beam energy are produced, comparing two or more versions of GEANT4. If significant differences are seen in any of these plots, investigations are then carried out to understand which changes in the code – typically developments in the physics models – are responsible.

6. Summary

During the past two to three years, the capabilities of GEANT4 have been extensively augmented. Improvements in the kernel, geometry, physics, visualization, user interfaces, testing and build system have resulted in a more efficient and powerful toolkit. Highlights of these improvements include.

- The implementation of event-level parallelism through multi-threading which allows efficient and scalable use of on-board cores.
- An improved geometry modeler which incorporates multi-threading capabilities and the stringent requirement that all geometrical information must be shared in a multi-threaded run.
- Augmented electromagnetic and hadronic physics models which have improved the reproduction of showers in calorimeters, and further extended the reach of GEANT4 physics into medical and space applications and other experimental domains.
- The implementation of OpenGL within the context of the Qt GUI toolkit, providing the user a rich set of options for displaying geometry, trajectories and hits, and faster, high-quality renderings.
- An automated performance monitoring system, including benchmarking and profiling, which employs online tools to analyze both sequential and multi-threaded applications, and

- A CMake system which provides cross-platform support for the building of the GEANT4 toolkit, its applications and the data files required by various physics models.

These developments will be included in the next major GEANT4 release scheduled for the end of 2013.

References

- Abat, E. et al., 2011. Photon reconstruction in the ATLAS inner detector and liquid argon barrel calorimeter at the 2004 combined test beam. *J. Instrum.* 6-04, P04001.
- Adragna, P. et al., 2009. *Nucl. Instrum. Methods A* 606-3, 362.
- Agostinelli, S. et al., 2003. *Nucl. Instrum. Methods A* 506, 250.
- Ahn, S. et al., 2013. Geant4-MT: bringing multi-threaded Geant4 into production. In: Proceedings of the Joint International Conference on Supercomputing in Nuclear Applications and Monte Carlo, Paris.
- AIDA, 2012. <<http://cern.ch/aida/>>.
- Allison, J. et al., 2006. *IEEE Trans. Nucl. Sci.* 53 (1), 270.
- Allison, J. et al., 2012. Geant4 electromagnetic physics for high statistics simulation of LHC experiments. *J. Phys.: Conf. Ser.* 396, 022013.
- Allison, J., Garnier, L., Kimura, A., Perl, J., 2013. The Geant4 visualization system – a multi-driver graphics system. *Int. J. Model. Simul. Sci. Comput.* 4 (Suppl. 1), 1340001.
- Andersson, B. et al., 1987. *Nucl. Phys. B* 281-1/2, 289.
- Apostolakis, J. et al., 2008. Parallel geometries in Geant4: foundation and recent enhancements. *IEEE Nucl. Sci. Symp. Conf. Record*, 883.
- Apostolakis, J. et al., 2009. *Radiat. Phys. Chem.* 78, 859.
- Apostolakis et al., 2010. Validation and verification of Geant4 standard electromagnetic physics. *J. Phys.: Conf. Ser.* 219, 032044.
- Asai, M. et al., 2012. *Phys. Med. Biol.* 57 (19), 6269.
- Batic, M., Pia, M.G., Saracco, P., 2011. *IEEE Trans. Nucl. Sci.* 58, 3269.
- Batic, M., Hoff, G., Pia, M.G., Saracco, P., 2012. *IEEE Trans. Nucl. Sci.* 59, 1636.
- Batic, M., Hoff, G., Pia, M.G., Saracco, P., Weidenspointner, G., 2013. *IEEE Trans. Nucl. Sci.* 60, 2934.
- Brown, J.M.C., Dimmock, M.R., Gillam, J.E., Paganin, D.M., 2011. MULECS: The Monash University low energy Compton scattering package. In: Proceedings of the Nuclear Science Symposium and Medical Imaging Conference (NSS/MIC), pp. 1385.
- Canadas, M., Arce, P., Rato Mendes, P., 2011. *Phys. Med. Biol.* 56, 273.
- Chadwick, M.B. et al., 2011. *Nucl. Data Sheets* 112, 2887.
- Champion, C., Incerti, S., Tran, H., El Bitar, Z., 2012a. *Nucl. Instrum. Methods B* 273, 98.
- Champion et al., 2012b. *Int. J. Radiat. Biol.* 88, 62.
- Champion et al., 2013. *Nucl. Instrum. Methods B* 306, 165.
- Cirrone et al., 2010. *Nucl. Instrum. Methods A* 618, 315.
- Degtyarenko, P.V., Kossov, M.V., Wellisch, H.-P., 2000a. *Eur. Phys. J. A* 8, 217.
- Degtyarenko, P.V., Kossov, M.V., Wellisch, H.-P., 2000b. *Eur. Phys. J. A* 9, 411.
- Depaola, G.O., 2003. *Nucl. Instrum. Methods A* 512, 619.
- Depaola, G.O., 2009. *Nucl. Instrum. Methods A* 611, 84.
- Depaola, G.O., Leguizamón, G.N., 2009. *X-Ray Spectrom.* 38, 519.
- Dong, X. et al., 2010. Multithreaded Geant4: semi-automatic transformation into scalable thread-parallel software. *Euro-Par 2010 – Parallel Proc.* 6272, 287.
- Dong, X. et al., 2012. Creating and improving multi-threaded Geant4. *J. Phys.: Conf. Ser.* 396, 052029.
- Dotti, A. et al., 2011. Description of hadron-induced showers in calorimeters using the Geant4 simulation toolkit. In: Nuclear Science Symposium and Medical Imaging Conference (NSS/MIC), pp. 2128–2134.
- Dotti, A., 2012. Validation of Geant4 releases with distributed resources. *J. Phys.: Conf. Ser.* 396-3, 032033.
- Electric Commander, 2012. <<http://www.electric-cloud.com/products/electriccommander.php>>.
- Eullisse, G. and Tuura, L., 2002. IgProf. <<http://igprof.org/index.html>>.
- Fesefeldt, H., 1985. GHEISHA, RWTH Aachen report PITHA 85/2.
- FNAL-FAST, 2010. FAST Project. <<https://cdvcs.fnal.gov/redmine/projects/fast>>.
- FNAL-G4P, 2010. Geant4 Profiling and Benchmarking. <<https://oink.fnal.gov/perfanalysis/g4p>>.
- Folger, G., Ivanchenko, V., Wellisch, H.-P., 2004. *Eur. Phys. J. A* 21, 404.
- Francis et al., 2011. *Appl. Radiat. Isot.* 69, 220.
- Garnier, L., Qt driver tutorial. <<http://geant4.in2p3.fr/spip.php?article60&lang=en>>.
- Gayer, M. et al., 2012. New software library of geometrical primitives for modeling of solids used in Monte Carlo Detector Simulations. *J. Phys.: Conf. Ser.* 396, 052029.
- Hauf, S. et al., 2013a. *IEEE Trans. Nucl. Sci.* 60, 2966.
- Hauf, S. et al., 2013b. *IEEE Trans. Nucl. Sci.* 60, 2984.
- Heikkinen, A., Stepanov, N., Wellisch, J.P., 2003. Bertini intra-nuclear cascade implementation in Geant4. In: Computing in High Energy Physics 2003, La Jolla, California, USA.
- Ibarmia, S. et al., 2013. *IEEE Trans. Nucl. Sci.* 60, 2486.
- Incerti, S. et al., 2010. *Med. Phys.* 37, 4692.
- Ivanchenko, V.N., Kadri, O., Maire, M., Urban, L., 2010. Geant4 models for simulation of multiple scattering. *J. Phys.: Conf. Ser.* 219, 032045.
- Ivanchenko, V.N. et al., 2011. *Prog. Nucl. Sci. Technol.* 2, 898.

ARTICLE IN PRESS

10

M. Asai et al./Annals of Nuclear Energy xxx (2014) xxx–xxx

- Ivanchenko, V.N. et al., 2012. Nucl. Instrum. Methods B 273, 95.
- Ivanchenko, V.N. et al., 2013. In: Proceedings of the Joint International Conference on Supercomputing in Nuclear Applications and Monte Carlo, Paris.
- Jan, S. et al., 2011. Phys. Med. Biol. 56, 881.
- Kaitaniemi, P., Boudard, A., Leray, S., Cugnon, J., Mancusi, D., 2011. Prog. Nucl. Sci. Technol. 2, 788.
- Kimura, A., gMocren – a volume visualizer for Geant4 medical simulation, <<http://geant4.kek.jp/gMocren>>.
- Kitware CDash, 2012. <<http://www.cdash.org>>.
- Kitware CMake, 2012. <<http://www.cmake.org>>.
- Kitware CTest, 2012. <http://cmake.org/Wiki/CMake/Testing_With_CTest>.
- Lechner, A., Ivanchenko, V.N., Knobloch, J., 2010. Nucl. Instrum. Methods B 268, 14.
- Mantero, A. et al., 2011. X-Ray Spectrom. 40, 135.
- Mishustin, I., Pshenichnov, I., Greiner, W., 2010. Eur. Phys. J. D 60, 109.
- Morgan, B., 2008. 14th Geant4 Users and Collaboration Workshop, <<https://indico.cern.ch/getFile.py/access?contribId=138&sessionId=58&resId=0&materialId=slides&confId=44566>>.
- National Nuclear Data Center, 2013. <<http://www.nndc.bnl.gov/ensdf>>, Evaluated Nuclear Structure Data Files.
- Open Speedshop, 2012. <<http://www.openspeedshop.org/wp/>>
- Perl dist, Tools for the development and distribution of portable software on Unix platforms, <<http://sourceforge.net/projects/dist/>>.
- Perl, J., HepRep: a Generic Interface Definition for HEP Event Display Representables, <<http://www.slac.stanford.edu/perl/heprep>>.
- Pia, M.G. et al., 2009. IEEE Trans. Nucl. Sci. 56, 3614.
- Pia, M.G., Seo, H., Batic, M., Begalli, M., Kim, C.H., Quintieri, L., Saracco, P., 2011. IEEE Trans. Nucl. Sci. 58, 3246.
- Quesada, J.M. et al., 2010. Recent developments in pre-equilibrium and de-excitation models in Geant4. In: Joint International Conference on Supercomputing in Nuclear Applications and Monte Carlo 2010, Tokyo, Japan.
- Rice University, 2000. HPCToolkits, <http://hpctoolkit.org/index.html>.
- Schaelicke, A. et al. et al., 2011. Geant4 electromagnetic physics for the LHC and other HEP applications. J. Phys.: Conf. Ser. 331, 032029.
- Seltzer, S.M., Berger, M.J., 1985. Nucl. Instrum. Methods B12, 95.
- Seo, H., Pia, M.G., Saracco, P., Kim, C.H., 2011. IEEE Trans. Nucl. Sci. 58, 3219.
- Taborda, A., Chaves, P.C., Reis, M.A., 2011. X-Ray Spectrom. 40, 127.
- Taborda, A., Chaves, P.C., Carvalho, M.L., Reis, M.A., 2013. X-Ray Spectrom. 42, 77.
- Tanaka, S., Kawaguti, M., 1997. DAWN for Geant4 visualization. In: Proceedings of the CHEP97 Conference, Berlin, Germany; For documentation, see <http://geant4.kek.jp/tanaka/DAWN/About_DAWN.html>.
- University of Oregon, 1997. TAU. <<http://www.cs.uoregon.edu/research/tau/home.php>>.
- Valentin, A., Raine, M., Gaillardin, M., Paillet, P., 2012a. Nucl. Instrum. Methods B 287, 124.
- Valentin, A., Raine, M., Sauvestre, J.-E., Gaillardin, M., Paillet, P., 2012b. Nucl. Instrum. Methods B 288, 66–73.